Translational Spectroscopy of the Metastable Products of Electron Impact Dissociative Excitation

by

Sarah M. Barnett

A thesis submitted in partial
fulfilment for the degree of
Doctor of Philosophy

University of London

1992

ProQuest LLC.
789 East Eisenhower Parkway
P.O. Box 1346
Ann Arbor, MI 48106 – 1346

Abstract

In molecular dissociation processes the fragments may be produced with kinetic energies exceeding the thermal energy of the parent gas molecules. The fragments will therefore be highly chemically reactive. The fragments may also be produced in electronically excited states, including those forbidden in electric dipole transitions. These states, metastable states, must decay through magnetic dipole or electric quadrupole transitions and are long-lived. The metastable fragments are therefore both fast-moving and long-lived and may travel large distances before decaying. Metastable dissociation fragments are thus important in the energy transfer processes of complex systems such as planetary atmospheres, lasers, gas discharges and plasmas. The Martian emission spectrum is dominated by the electric dipole forbidden transition $CO(a^3\pi - X^1\Sigma^+)$, the Cameron bands, in which the upper state is populated predominantly by electron impact dissociative excitation of carbon dioxide. In this work, metastable fragments produced by electron impact dissociation of nitrous oxide, carbon monoxide, carbon dioxide and carbonyl sulphide have been studied by the technique of translational spectroscopy. A low work function metastable surface detector was used to study the low lying metastable states of molecular nitrogen, $N_2(A^3\Sigma^+{}_u)$, and carbon monoxide, $CO(a^3\pi)$. A channel electron multiplier was used for the selective detection of metastable $O(^5S)$ atoms. The kinetic energy distributions of the product fragments were derived from the time of flight spectra obtained and from these the nature of the dissociation process could be investigated.

Contents

Chapter One Introduction

Chapter Two Review of Methods of Detection of Metastable Species

Chapter Three The Vacuum System and Electron Gun

Chapter Four The Technique of Translational Spectroscopy

Chapter Five Calibration of Detectors

Chapter Six Dissociative Excitation of $N_2(a^1\pi_g)$ and $N_2(A^3\Sigma^+{}_u)$ from Nitrous Oxide

Chapter Seven **Dissociative Excitation of CO($a^3\pi$) and O(^5S) from Carbonyl Sulphide. Carbon Dioxide and Carbon Monoxide**

List of Figures

List of Tables

Acknowledgments

Dr W. R. Newell, for his supervision throughout this work and his constant flow of new ideas.

Dr N. J. Mason, for his guidance and support.

Messrs E. J. C. Oldfield and I. Rangué, for their expert technical assistance and without whom this work would not have been finished.

Dr A. C. H. Smith, Dr J. Tennyson and Dr P. Storey for their interest in this work.

Dr W. M. Johnstone, for his invaluable assistance in the preparation of this thesis and Dr J. H. Sanderson and Ms J. M. Furlong, for all their help.

My mother, for her endless encouragement.

Michael Chyriwsky, for numerous helpful suggestions.

The Science and Engineering Research Council, for a post graduate studentship, number 88302362 and the Department of Physics and Astronomy, for financial support.

Chapter One

Introduction

> *It will be found that everything depends on the composition of the forces with which the particles of matter act upon one another; and from these forces, as a matter of fact, all phenomena of Nature take their origin.*
>
> *R.J. Boscovich (1763)*

1.1 Introduction

Electron collisions with atoms and molecules have been the subject of experimental and theoretical studies for over half a century. Elastic collisions of electrons with atoms and with simple diatomic molecules may be described theoretically by the R-matrix method (Burke et al 1987) which has developed from the early quantum mechanical treatment of electron-atom scattering (Born 1926, Massey and Mohr 1932). A large volume of experimental data complements such theoretical calculations. Inelastic electron-molecule scattering processes are more difficult to treat theoretically and most information concerning the excitation and ionisation of molecules has been derived from experimental studies, especially from electron impact spectroscopy.

The least studied electron-molecule collision process is dissociation. In dissociation, the molecule is first excited to an unbound potential energy level or to the repulsive part of a bound potential energy level before dissociating. The atomic or molecular dissociation products may be ground state neutrals, excited neutrals or ions. This work is concerned with electron impact dissociative excitation in which one or more of the fragments are produced in long-lived or 'metastable' states. Since the fragments are produced with high kinetic energies these metastable fragments may travel large distances before decaying and are therefore important in many different energy transfer processes.

In this work, the metastable fragments produced by electron impact dissociation of nitrous oxide, carbon monoxide, carbon dioxide and carbonyl sulphide have been studied by the technique of translational spectroscopy. In this first chapter, the classification of molecular states, molecular bonding and the process of dissociative excitation are discussed together with a brief review of previous experimental and theoretical studies. The study of low-lying metastable states produced by dissociative excitation necessitated the development of a tantalum surface detector which uses the principle that an incident metastable atom or molecule is capable of causing secondary electron emission from the surface. In chapter two, the effect of impurities on the surface and the mechanisms by which secondary electron emission occur are described together with a review of alternative techniques used in the detection of metastable species. The design of the detectors used in this work and the results of their calibration by the observation of the direct electron impact excitation of molecular nitrogen and carbon monoxide are presented in chapter five.

The basic experimental apparatus is described in chapter three, including descriptions of the vacuum system and the design and operation of the electrostatic lenses producing the electron beam. The technique of translational spectroscopy, the dynamics of the target gas beam and the momentum transferred from the electron to the atom or molecule during non-dissociative collisions are discussed in chapter four. The dissociative excitation of metastable states of molecular nitrogen from nitrous oxide is described in chapter six. Chapter seven discusses the present results for electron impact dissociation of carbon monoxide, carbon dioxide and carbonyl sulphide. In chapter eight, ideas for future work are suggested.

1.2 Classification of Molecular States

The energy of an electron in an atomic orbital depends on four quantum numbers: n, the average distance from the nucleus; l, orbital angular momentum; s, spin angular momentum; j, the coupling of l and s. The axis along which the components of orbital angular momentum and spin angular momentum are taken may be defined in any convenient direction and the components of l and s along this axis are denoted by m_l and m_s respectively. The angular momenta of several electrons in an atom may be combined in different ways, producing different classifications of the atomic state.

In a diatomic molecule the quantum numbers describing the electron are similar: n specifies the size of the orbital and determines its energy; l specifies the orbital angular momentum. Due to the electrostatic field along the internuclear axis, the orbital angular momentum is quantised along this axis. Therefore the axial component of the orbital angular momentum is more important in molecules than the orbital angular momentum itself. The axial components of the orbital angular momentum are denoted by λ where $\lambda = |l_z|$.

In atoms, lower case Roman letters are used to designate values of l while in molecules small Greek letters denote values of λ:

atoms	l	=	0,	1,	2,	3,
			s,	p,	d,	f,
molecules	l_z	=	0,	±1,	±2,	±3,
	λ	=	0,	1,	2,	3,
			σ,	π,	δ,	ϕ,

In atoms, the total orbital angular momentum, l, is given by the sum of the angular momenta of the constituent electrons, i.e. $l = \Sigma\, l_i$. In molecules, since the total orbital angular momentum is quantised along the internuclear axis, it is more convenient to use the axial component, Λ, defined by $\Lambda = |\Sigma\, \lambda_i|$.

Upper case Roman letters and capital Greek letters are used to denote l and Λ respectively:

atoms	L	=	0,	1,	2,	3,
			S,	P,	D,	F,
molecules	Λ	=	0,	1,	2,	3,
			Σ,	Π,	Δ,	Φ,

In molecules the spin-axial coupling is weak, i.e. the electrons in molecular orbitals are not strongly influenced by the electrostatic field along the internuclear axis, so it is sufficient to use the same notation as for the electronic spin in atoms, however the projection of the spin onto the nuclear axis may be denoted by Σ and by analogy with the atomic case, the total angular momentum is Ω where $\Omega = \Lambda + \Sigma$.

The notation for molecular states is analogous to that for atomic states:

atoms $^{(2s+1)}L_{J}$
molecules $^{(2s+1)}\Lambda_{(g/u)\Omega\pm}$

The 'g' and 'u' suffices in the molecular notation describe the symmetry of the molecule and will be discussed in section 1.3.2.

1.3 Molecular Bonding

To understand the potential energy levels in molecules and their dissociation, it is necessary to give a description of molecular bonding. Four quantum mechanical principles are important when discussing atomic and molecular bonding,

1. An electron may only possess discrete quanta of energy.
2. The motion of electrons can be described as wave motion.
3. It is not possible to determine simultaneously both the position of an

electron and its momentum, the Heisenberg Uncertainty Principle.

4. Each bonding orbital is occupied by two electrons of opposite spin, the Pauli Exclusion Principle.

The spatial distribution and the energy of electrons in atoms obey well defined laws and may be calculated from the Schrodinger equation and expressed in terms of a three dimensional wave function, or orbital, ϕ, which depends on the quantum numbers n, l, m and the electron spin, s. Definite rules determine which orbitals are occupied and which transitions between orbitals are allowed.

In molecules, the orbitals extend over two or more nuclei. The shape and energy of these orbitals can also be calculated from the Schrodinger equation and expressed in terms of three quantum numbers, n, λ and Λ.

The Schrodinger equation describing molecules is complicated. For a system of electrons and nuclei interacting through Coulombic attraction and repulsion the Hamiltonian may be written as

$$H = \sum_{\alpha} \frac{p_{\alpha}^{2}}{2M_{\alpha}} + \sum_{i} \frac{p_{i}^{2}}{2m} + V\,(Q_{\alpha},q_{i})$$

where the first term is the kinetic energy operator for the αth nucleus of mass M_{α}; the second term the kinetic energy operator for the ith electron of mass m; Q_{α} the set of nuclear coordinates and q_i the set of electronic coordinates. $V(Q_{\alpha},q_i)$ is the potential energy of the entire system of electrons and nuclei and consists of all the Coulomb interactions between all pairs of charges.

The system potential energy is given by

$$V\,(Q_{\alpha},q_{i}) = \sum_{i<j} \frac{e^{2}}{r_{ij}} + \sum_{\alpha<\beta} \frac{Z_{\alpha}Z_{\beta}e^{2}}{r_{\alpha\beta}} - \sum_{i,\alpha} \frac{Z_{\alpha}e^{2}}{r_{i\alpha}}$$

in which the first term represents the sum of all interactions between pairs of electrons, the second, the sum of all interactions between pairs of nuclei and the third, the sum of all interactions between electrons and nuclei.

1.3.1 Molecular Orbital Theory

The calculation of the shape of the molecular orbitals from the Schrodinger equation is complicated. A good approximation is to consider the molecular orbitals as a linear combination of the atomic orbitals (LCAO) of the constituent atoms. For a diatomic molecule, the individual atomic orbitals, ϕ_1 and ϕ_2, may be combined in two different ways to form two different molecular orbitals:

$$\Phi^{B}_{MO} = \Phi_1 + \Phi_2$$
$$\Phi^{A}_{MO} = \Phi_1 - \Phi_2$$

One of the molecular orbitals formed is of a lower energy than the individual atomic orbitals and is described as the 'bonding molecular orbital'. The other has a higher energy and is termed an 'anti-bonding molecular orbital'. In diatomic molecules, the bonding molecular orbital is characterised by a charge distribution between the two nuclei, close to the internuclear axis. Two electrons of opposite spin occupy the orbital and are said to form a single bond. A σ-bond is associated with σ-orbitals and possesses cylindrical symmetry about the axis but has no angular momentum along the internuclear axis. A π-bond is associated with π-orbitals, is antisymmetric in a plane parallel to, and containing, the internuclear axis and has a positive and a negative lobe. A double bond consists of a σ-bond and a π-bond, while a triple bond consists of two π-bonds in perpendicular orientation and a σ-bond.

1.3.2 Bonding in Molecular Hydrogen

To illustrate the above description of molecular bonding, it is useful to consider the bonding in the simplest of diatomic molecules, molecular hydrogen.

a) 1s Bonding

Consider two hydrogen atoms approaching one another. A hydrogen atom has one electron associated with the orbital of lowest energy, the 1s orbital. This orbital is spherically symmetric about the nucleus with the probability of an electron being at a particular distance from the nucleus being the same in all directions. As the two hydrogen atoms approach one another, the 1s orbitals of each atom overlap, with the result that two molecular orbitals are formed. The two 1s orbitals may be combined in two ways:

$$\phi^B_{H2} = \phi_{1s} + \phi_{1s}$$
$$\phi^A_{H2} = \phi_{1s} - \phi_{1s}$$

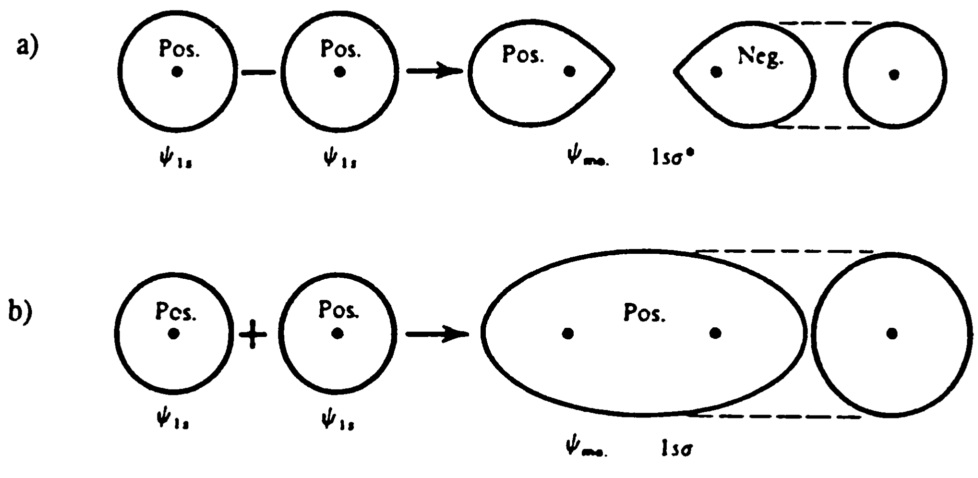

Figure 1.1 Bonding in molecular hydrogen, formation of the bonding $1s\sigma_g$ orbital and the antibonding $1s\sigma_u^*$ orbital.

Consider the first case, in which the atomic orbitals are added. The wavefunction ϕ_{1s} is positive everywhere, therefore when two 1s orbitals overlap the value of the molecular wavefunction is increased. The shape of the molecular orbital, ϕ^{B}_{H2}, is an ellipsoid, figure 1.1a. The electronic charge between the two nuclei keeps the nuclei together and a bond is formed. This molecular orbital is the bonding orbital and is denoted by $1s\sigma_g$.

Consider the second combination of atomic orbitals. The two ϕ_{1s} orbitals will cancel between the nuclei. The value of ϕ^{A}_{H2} will therefore be zero between the nuclei, positive around one nucleus and negative around the other, figure 1.1b. The electronic charge is greatest outside the nuclei and enhances the nuclear repulsion. This molecular orbital is therefore an anti-bonding orbital and is labelled $1s\sigma_u^*$.

In the labelling of these molecular orbitals, σ indicates that the orbitals are symmetric about the internuclear axis. The orbital of higher energy is denoted by an asterisk.

The g and u suffixes denote the symmetry of the molecule under inversion through the centre of symmetry. If the diatomic molecule is homonuclear, i.e. consists of two identical atoms, then the mid-point of the internuclear axis is a centre of symmetry. At any point in such a molecule, the conditions encountered will be exactly the same as at a point diagonally opposite through the centre of symmetry. This is known as 'inversion'. The wavefunction describing the system may or may not be changed in sign by inversion.

Consider the $1s\sigma_g$ and $1s\sigma_u^*$ molecular orbitals in hydrogen. Inversion in the $1s\sigma_g$ orbital causes no change in the sign of the wavefunction since ϕ^{B}_{H2} is positive everywhere. This orbital is therefore completely symmetrical, is described as 'even' and denoted by the suffix 'g' which derives from the german *gerade* meaning even. In the molecular orbital $1s\sigma_u^*$ there will be a change in the sign of the wavefunction following inversion. The orbital is thus antisymmetrical or 'odd' and labelled 'u' from the german for odd, *ungerade*.

If the diatomic molecule is heteronuclear, that is, the constituent atoms are different as in carbon monoxide, inversion has no meaning and the designation of 'g' or 'u' symmetry is unnecessary. However, in triatomic molecules such as carbon dioxide containing two identical atoms, inversion must again be considered in the description of the energy levels.

b) 2s bonding

The second lowest atomic orbital in hydrogen is the 2s orbital. Two 2s orbitals may be combined in the same way as two 1s orbitals:

$$\begin{aligned} \phi^{B}{}_{H2} &= \phi_{2s} + \phi_{2s} \\ \phi^{A}{}_{H2} &= \phi_{2s} - \phi_{2s} \end{aligned}$$

The addition of the individual atomic orbitals results in a bonding orbital, $2s\sigma_g$, while the second case results in an anti-bonding orbital, $2s\sigma^{*}{}_{u}$. These molecular orbitals are identical in shape to the $1s\sigma_g$ and $1s\sigma^{*}{}_{u}$ orbitals but are larger and higher in energy.

c) 2p Bonding

The next atomic orbital in terms of energy is the 2p orbital. The shape of a p-orbital is a dumb-bell, figure 1.2. Two p-orbitals can therefore overlap in different ways depending on their orientation.

Choosing the internuclear axis of the molecule as the z-axis, the 2p orbital may be described as being parallel to this axis, $2p_z$, of perpendicular to it, $2p_y$. The orbitals may then be combined as follows:

$$\begin{aligned} \phi^{A1}{}_{H2} &= \phi_{2pz} + \phi_{2pz} \\ \phi^{B1}{}_{H2} &= \phi_{2pz} - \phi_{2pz} \\ \phi^{A2}{}_{H2} &= \phi_{2py} - \phi_{2py} \\ \phi^{B2}{}_{H2} &= \phi_{2py} + \phi_{2py} \end{aligned}$$

These combinations are shown graphically in figure 1.2. The labelling of the molecular orbitals follows the same convention as for combinations of s-orbitals. When the resultant molecular orbital is cylindrically spherical about the internuclear axis, the orbital is labelled σ. In the combination of the $2p_y$ states, the end-view of the molecular orbital is reminiscent of a p-orbital, the molecular orbital is thus labelled π. The $2p\sigma_u^*$ and $2p\pi_g^*$ are clearly anti-bonding orbitals while $2p\sigma_g$ and $2p\pi_u$ are bonding orbitals.

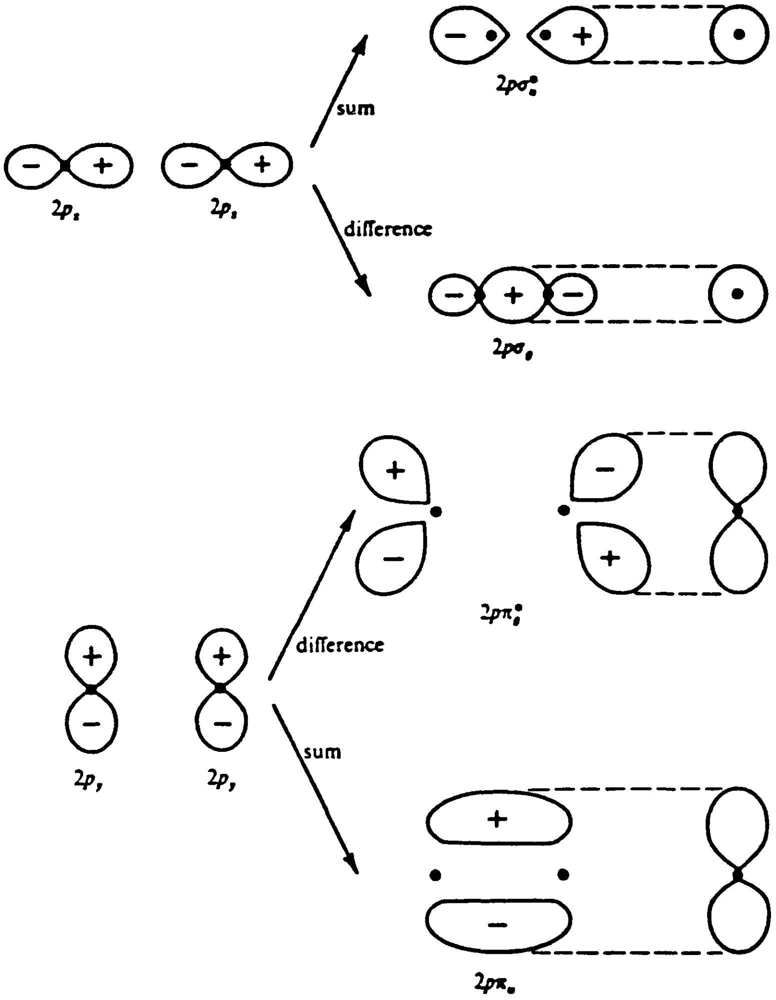

Figure 1.2 Combination of two 2p orbitals in the bonding of molecular hydrogen.

1.3.3 Energy Levels of Molecular Orbitals

The energy levels of the molecular orbitals of small molecules such as N_2 and O_2 are as shown in figure 1.3a. In smaller molecules such as Li_2, Be_2 and B_2, the $2s\sigma_u^*$, $2p\sigma_g$ and $2p\pi_u$ orbitals overlap while in molecular hydrogen the orbitals derived from the combination of 2s orbitals lie between those from the combination of 2p orbitals, figure 1.3b, since in atomic hydrogen the 2s and 2p levels are degenerate.

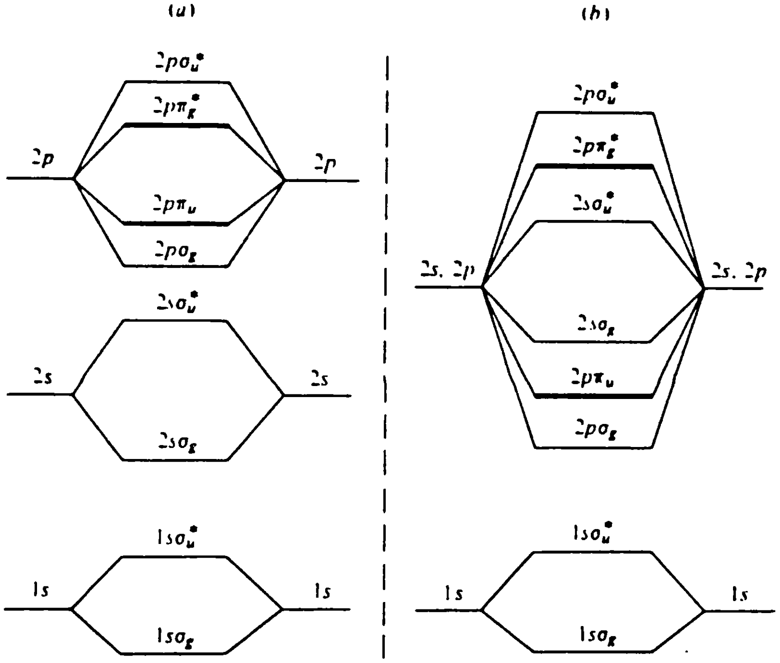

Figure 1.3 Energy levels in a) molecules such as O_2 and N_2 and b) molecular hydrogen.

1.3.4 Bonding in Polyatomic Molecules

In polyatomic molecules there are three or more nuclei and at least two internuclear axes. There are, therefore, a greater number of vibrational modes and more allowed transitions and since there are fewer forbidden transitions, polyatomic molecules have fewer metastable electronic states. The potential energy of the molecule can no longer be represented in two dimensions as a function of internuclear separation, but must be considered as a potential surface over the whole molecule. The molecular orbitals of polyatomic molecules are said to be symmetrised as they are influenced by other bonds in the molecule, and delocalised since they embrace more than one nucleus.

Consider the bonding in a hydride, H_2A, in which A is an atom having three p-orbitals available for bonding. There are two possibilities for bonding, that each H(1s) orbital interacts with a separate p-orbital or that each H(1s) orbital interacts with a different lobe of the same p-orbital, figure 1.4.

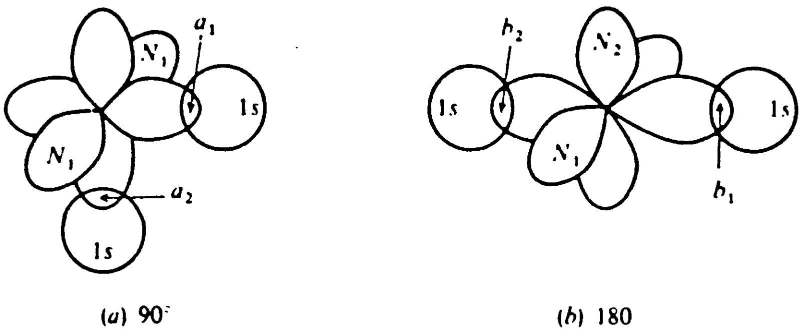

Figure 1.4 Bonding in the hydride H_2A, H(1s) orbitals interact with a) different p-orbitals and b) the same p-orbital.

In the first case the bond angle is 90°, a_1 and a_2 are the bonding molecular orbitals and there is one non-bonding orbital, N_1. The s-orbital of the atom A is non-bonding. In the second case, the bond angle is 180°, b_1 and b_2 are the bonding orbitals formed and there are two non-bonding p-orbitals, N_1 and N_2. Note that in this case, the two hydrogen electrons are in the same bonding orbital and not paired with electrons donated from the atom A.

The near degeneracy of the 2s and 2p orbitals means that they can mix, this process is known as hybridisation. Atom A mixes its s-orbital with one of the p-orbitals forming two new hybrid orbitals at 180° to each other. The hybrid orbitals are atomic orbitals because the s and p-orbitals which mix are from the same atom. Since the hybrid orbitals form stronger bonds than the unmixed orbitals, it is energetically favourable in some cases for hybridisation to occur.

Consider for example the water molecule. The configurations in the constituent atoms are H(1s) and $O(1s^2 2s^2 2p^4)$. The oxygen atom contributes six electrons to the bonding orbitals while each hydrogen atom contributes one electron. Hybridisation of the bonding orbitals occurs resulting in four hybrid orbitals arranged in a regular tetrahedron at 109° 28' to each other. This is termed sp^3 hybridisation since one s-orbital and three p-orbitals are involved. The hybrid orbitals may be written as

$$\begin{aligned}
\phi_1 &= \tfrac{1}{2}\,(s + p_x + p_y + p_z)\\
\phi_2 &= \tfrac{1}{2}\,(s + p_x - p_y - p_z)\\
\phi_3 &= \tfrac{1}{2}\,(s - p_x + p_y - p_z)\\
\phi_4 &= \tfrac{1}{2}\,(s - p_x - p_y + p_z)
\end{aligned}$$

In two of these orbitals an electron from one of the hydrogen atoms is paired with a p-electron from the atomic oxygen, while in the other two are 'lone pairs', pairs of electrons originating from the 2s and one 2p orbital in the oxygen atom. The repulsive force of the lone pairs, however, pushes the bonding orbitals closer together resulting in an angle of 105° between the hydrogen atoms.

Other hybrid orbitals may be formed. In sp^2 hybridisation, involving one s-orbital and two p-orbitals, the orbitals may be written

$$\begin{aligned}
\phi_1 &= \frac{1}{3}s + \frac{2}{3}p_x\\
\phi_2 &= \frac{1}{3}s - \frac{1}{6}p_x + \frac{1}{2}p_y\\
\phi_3 &= \frac{1}{3}s - \frac{1}{6}p_x + \frac{1}{2}p_y
\end{aligned}$$

The directions of the bonds lie in the same plane, the angle between any two bonds being 120°.

In sp hybridisation, one s-orbital and one p-orbital mix to form the orbitals,

$$\phi_1 = \alpha s + \sqrt{(1 - \alpha^2)}\, p_z$$
$$\phi_2 = \sqrt{(1 - \alpha^2)}\, s - \alpha p_z$$

where $0 \leq \alpha \leq 1$. The directions of maximum density in this case lie along the z-axis.

1.4 Potential Energy Curves

Atoms in a molecule do not remain in fixed positions but vibrate about some mean position causing changes in the internuclear distance and thus in the total energy of the molecule. The energy of the molecule is usually represented as a function of the internuclear distance. The potential energy of a diatomic molecule in a bound state has a minimum at some equilibrium distance, such curves, termed Morse curves, may be described by a purely empirical function. The potential energy curve for an unbound or repulsive state of a diatomic molecule has no minimum.

This may be illustrated by the states of molecular hydrogen. The variation of the energy of the $1s\sigma_g$ and $1s\sigma_u^*$ molecular orbitals with internuclear distance is shown diagrammatically in figure 1.5. The potential energy of the bonding orbital, or bound state, follows the typical Morse curve for a diatomic molecule, the minimum indicates bond formation between the constituent atoms. The antibonding orbital, or unbound state, has no potential energy minimum.

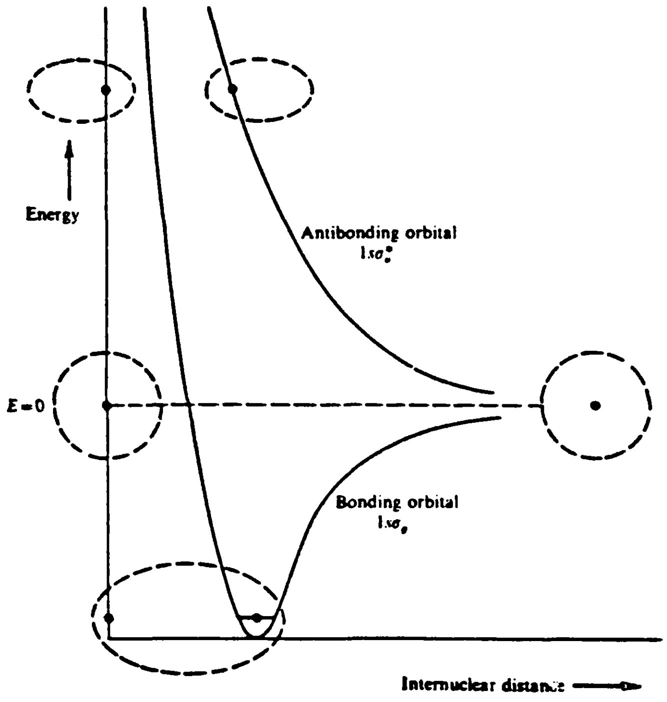

Figure 1.5 Variation of potential energy with internuclear distance for the $1s\sigma_g$ and $1s\sigma_u^*$ molecular orbitals in hydrogen.

1.5 Forbidden Transitions and Metastable States

1.5.1 Electric Dipole Transitions

The transition probability for the spontaneous emission of electric dipole radiation in a one-electron atom is given by

$$A_{E1} = \frac{\omega_{ki}^{3}}{3\pi\varepsilon_0\hbar c^3}\ \frac{1}{g_k} \sum_{m_i,m_k} |<km_k|er|im_i>|^2 \qquad 1.1$$

in which the initial and final states are denoted by i and k respectively, g_k is a statistical weight introduced to account for the degeneracy of the upper level.

This derivation assumes that the spatial extent of the electron charge distribution in the atom is small compared with the wavelength of the light emitted. If this is valid, phase differences in the contributions to the emitted electromagnetic wave from different regions in the atom may be neglected. This is the 'electric dipole approximation' in which only the first term of the expansion

$$\exp(-ik.r) = 1 - ik.r + ½(ik.r)^2 - .... \qquad 1.2$$

is required.

When the matrix element in equation 1.1 is finite the emitted radiation is electric dipole radiation. However, if the matrix element is zero the relative phases of the contributions from different regions in the atom cannot be neglected and higher terms in the expansion 1.2 must be included. The second term represents magnetic dipole radiation and the third term electric quadrupole radiation.

Excited atoms and molecules decay via electric dipole transitions after typically 10^{-8}s. Electronically excited states which cannot decay through electric dipole transitions must lose their energy by an electric quadrupole or magnetic dipole transition. It will be demonstrated in sections 1.5.2 and 1.5.3 that the lifetimes of the atoms or molecules in such states are typically $>50\mu s$. Such states are known as metastable states because of their long lifetimes.

1.5.2 Magnetic Dipole Transitions

The second term in the expansion of exp (-ik.r) in equation 1.2 gives rise to magnetic dipole radiation.

The power radiated by a classical oscillating magnetic dipole is

$$P_{M1} = \frac{\mu_0 k^4 c}{12\pi} |\mu|^2 \qquad 1.3$$

where μ is the magnetic moment operator.

The quantum mechanical expression for the magnetic dipole transition probability, A_{M1}, is given by

$$A_{M1} = \frac{4P_{M1}}{\hbar \omega_{ki}} \qquad 1.4$$

and μ is given by

$$\frac{\mu}{2} = \int \Phi_k \ \mu \ \Phi_i \, d\tau \qquad 1.5$$

Substituting 1.4 and 1.5 in 1.3 gives

$$A_{M1} = \frac{\mu_0 \omega_{ki}^3}{3\pi\hbar c^3} \frac{1}{g_k} \sum_{m_i, m_k} |<km_k|\mu|im_i>|^2 \qquad 1.6$$

The magnetic moment operator μ is given by

$$\begin{aligned}\mu &= \frac{-eh}{2m}\,(l + 2s)\\ &= -\mu_B\,(l + 2s)\end{aligned}$$

For a many electron atom, the single electron operator in 1.6 is replaced by a summation over the valence electrons, giving

$$\mu = -\mu_B\,(L + 2S)$$

From 1.1 and 1.6, the ratio of the transition probability for magnetic dipole radiation to electric dipole radiation is given approximately by

$$\frac{A_{M1}}{A_{E1}} = \frac{1}{c^2}\left(\frac{\mu}{er}\right)^2 = \left(\frac{Z\alpha}{2}\right)^2 \sim 10^{-5}$$

where Z is the nuclear charge and α is a fine structure constant such that

$$\alpha = \frac{e^2}{4\pi\varepsilon_0\hbar c} \sim \frac{1}{137}$$

Thus if the electric dipole transition probability is $\sim 10^8 s^{-1}$, the magnetic dipole transition probability is $\sim 10^3 s^{-1}$ and if electric dipole transitions are allowed, the effect of the magnetic dipole transition on the lifetime of the state will be negligible. If electric dipole radiation is forbidden, the lifetime of the state will depend solely on the magnetic dipole transition probability. The lifetime will thus be $\sim 10^{-3}$s, hence the term 'metastable'.

1.5.3 Electric Quadrupole Transitions

The expression for the vector potential A(**r**,t) of an oscillating distribution of current and charge contains contributions from both magnetic dipole and electric quadrupole distributions. These are therefore expected to radiate at similar rates and consequently electric quadrupole radiation must be considered in addition to magnetic dipole radiation.

The power radiated by a classical electric quadrupole source is

$$P_{E2} = \frac{ck^6}{1440\pi\varepsilon_0} \sum_{\alpha,\beta} |Q_{\alpha\beta}|^2 \qquad 1.7$$

where $Q_{\alpha\beta}$ are the components of the electric quadrupole moment tensor.

The electric quadrupole transition probability is obtained in a similar way as for magnetic quadrupole radiation, giving

$$A_{E2} = \frac{\omega_{ki}^5}{360\pi\varepsilon_0\hbar c^5} \frac{1}{g_k} \sum_{m_i,m_k} |<km_k|-e\,\Sigma(3r_\alpha r_\beta - r^2\delta_{\alpha\beta})|im_i>|^2 \qquad 1.8$$

where r_α and r_β are the Cartesian components of the electron position vector r and $\delta_{\alpha\beta}$ is the delta function.

For a many electron system the electric quadrupole operator is

$$Q = -e \sum (3r_i r_i - r_i^2 \phi)$$

where ϕ is the unit tensor.

The ratio of the transition probability for electric quadrupole radiation compared with that for electric dipole radiation is given by

$$\frac{A_{E2}}{A_{E1}} = \frac{3}{40}\left(\frac{\omega r}{c}\right)^2 = \frac{3}{40}\left(\frac{Z\alpha}{2}\right)^2 \sim 10^{-6}$$

Thus, if the electric dipole contribution to the lifetime is zero, lifetimes of a metastable state decaying by electric quadrupole radiation is of ~ 10^{-2}s.

1.5.4 Selection Rules

The selection rules for electric dipole, magnetic dipole and electric quadrupole transitions in both atoms and molecules are summarised in table 1.1.

Table 1.1 Selection rules for electric dipole, magnetic dipole and electric quadrupole transitions.

Selection Rule	Electric Dipole	Magnetic Dipole	Electric Quadrupole
1	$\Delta J = 0,\pm1$ $0 \nleftrightarrow 0$	$\Delta J = 0,\pm1$ $0 \nleftrightarrow 0$	$\Delta J = 0,\pm1,\pm2$ $0 \nleftrightarrow 0$ $\frac{1}{2} \nleftrightarrow \frac{1}{2}$ $0 \nleftrightarrow 1$
2	$\Delta M = 0,\pm1$	$\Delta M = 0,\pm1$	$\Delta M = 0,\pm1,\pm2$
3	Parity Change	No Parity Change	No Parity Change
4	$\Delta l = \pm1$	$\Delta l = 0$	$\Delta l = 0,\pm2$
5	$\Delta S = 0$	$\Delta S = 0$	$\Delta S = 0$
6	$\Delta L = 0,\pm1$ $0 \nleftrightarrow 0$	$\Delta L = 0$	$\Delta L = 0,\pm1,\pm2$ $0 \nleftrightarrow 0$ $0 \nleftrightarrow 1$

Selection rules (1), (2) and (3) are rigorous. Rule (1) is derived from the fact that the photon possesses intrinsic spin angular momentum, h, and, by the principle of conservation of angular momentum, the change in the total angular momentum of the atom is limited. The angular symmetry properties of the atomic wavefunction lead to rule (2). Rule (3) is derived from symmetry requirements in reflection through the origin.

The other three selection rules are not rigorous, having been derived by using hydrogenic wavefunctions. Rule (4) applies if both the initial and final states can be described by a single configuration of electrons. Rules (5) and (6) apply only in Russell-Saunders (LS) coupling. This approximation is only valid when the spin-orbit interaction is much smaller than the electrostatic force between the electrons. The transition probability for electric dipole radiation is only non-zero if those selection rules summarised above are satisfied. For example consider atomic oxygen, the ground state configuration is $2p^4$, giving the levels shown in figure 1.6.

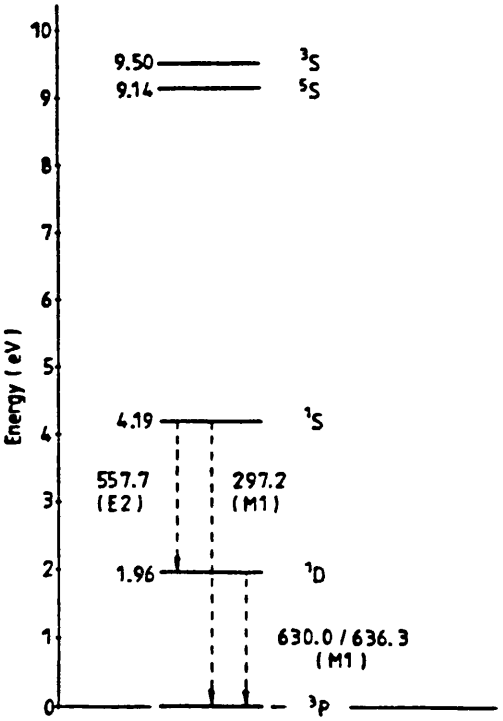

Figure 1.6 Energy levels in atomic oxygen showing transitions by magnetic dipole and electric quadrupole radiation.

Since each of these levels has even parity, by the selection rules for electric dipole transitions, decay of O($^1S_0$) or O($^1D_2$) to the ground state O($^3P_2$) by electric dipole radiation is forbidden. In the absence of collisions, these levels may only decay by magnetic dipole and electric quadrupole transitions. The transitions proceeding by electric quadrupole and magnetic dipole transitions are indicated on figure 1.6. The states O($^1S_0$) and O($^1D_2$) are metastable with lifetimes of 1s and 100s respectively.

1.6 Dissociation of Molecules

Dissociation of molecules may be divided into three categories;

1. Dissociative recombination

$$ABC^+ + e_E \rightarrow \begin{matrix} A^* + BC \\ A + BC^* \end{matrix}$$

The incident electron is captured by the target ion, the molecule is formed in an excited electronic state which subsequently dissociates giving atomic and/or molecular fragments of which one or more may be in excited states.

2. Dissociative ionisation

$$ABC + e_E \rightarrow \begin{matrix} A^+ + BC + e_I + e_{E-\delta E} \\ A + BC^+ + e_I + e_{E-\delta E} \end{matrix}$$

$$ABC + h\nu \rightarrow \begin{matrix} A^+ + BC + e_I \\ A + BC^+ + e_I \end{matrix}$$

Dissociative ionisation may be initiated both by electron and photon impact. The incident electron, or photon, has sufficient energy δE to dissociate the molecule leaving one or more of the fragments as ions.

3. Dissociative excitation

$$ABC + e_E \rightarrow \begin{matrix} A^* + BC + e_{E-\delta E} \\ A + BC^* + e_{E-\delta E} \end{matrix}$$

$$ABC + h\nu \rightarrow \begin{matrix} A^* + BC \\ A + BC^* \end{matrix}$$

The incident electron or photon provides the energy δE necessary to dissociate the molecule AB and to promote either fragment A or BC to an excited electronic state A^* or BC^*.

In each of these three processes, the fragment molecules may be electronically, vibrationally or rotationally excited. The importance of dissociation processes lies in the nature of the dissociation products. The energy released when the molecular bond is broken is carried away by the collision products as kinetic energy. The fragments are therefore fast moving or 'hot', the line widths associated with the decay of the dissociation products are highly Doppler broadened, equivalent to temperatures in excess of 30,000K (Zipf and Wells 1980).

1.6.1 Mechanism of Dissociative Excitation

As discussed in section 1.4, the electronic states of molecules may be represented by the potential energy of the molecule, V(r), as a function of the internuclear separation of the atoms, r. In this representation, one atom is considered as fixed on the $r=0$ axis while the other is allowed to oscillate along the r axis. In dissociative excitation the initial step involves the electronic excitation of the target molecule either through direct or exchange scattering by the incident projectile. The Franck-Condon principle states that transitions between electronic states take place so rapidly that the internuclear distance between the atoms does not change, therefore a transition from one electronic state to another occurs vertically on a diagram of V(r) as a function of r. Figure 1.7a shows the transition between two states of the same equilibrium internuclear separation. The transition occurs between the v=0 vibrational level to the v'=0 level in the higher lying electronic state. When there is a small difference in the internuclear separation, figure 1.7b, the transition occurs from the v=0 level to the v'=1 level in the upper state. Figure 1.7c shows two states which have a large difference in the equilibrium separation. The transition occurs from the v=0 level to the v'=3 vibrational level.

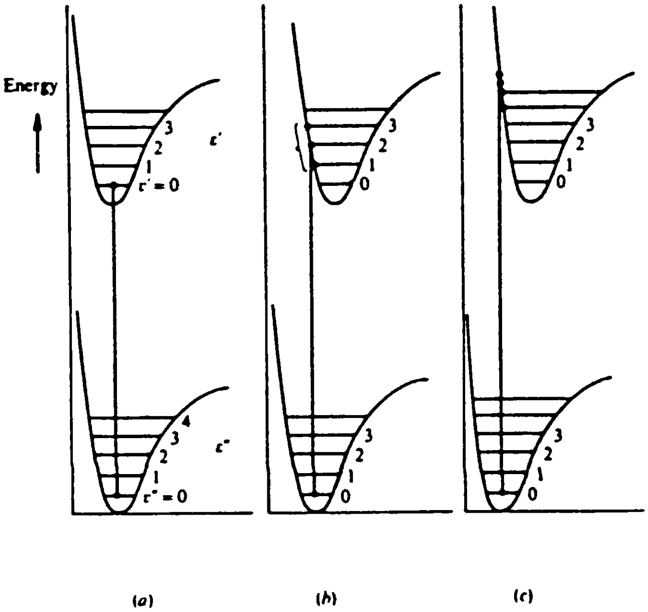

Figure 1.7 The Franck-Condon principle, a) transition between two states of the same equilibrium internuclear separation, b) transition between two states in which the upper state has a slightly larger internuclear separation and c) transition between two states in which the upper state has a much larger internuclear separation.

For dissociation to occur from such a bound state, the excitation must occur to the repulsive part of a bound potential energy curve. Dissociation will therefore be likely if the potential energy curve of the excited state has a minimum at large internuclear separation. Clearly the molecule will also dissociate if the excitation occurs to a purely repulsive state.

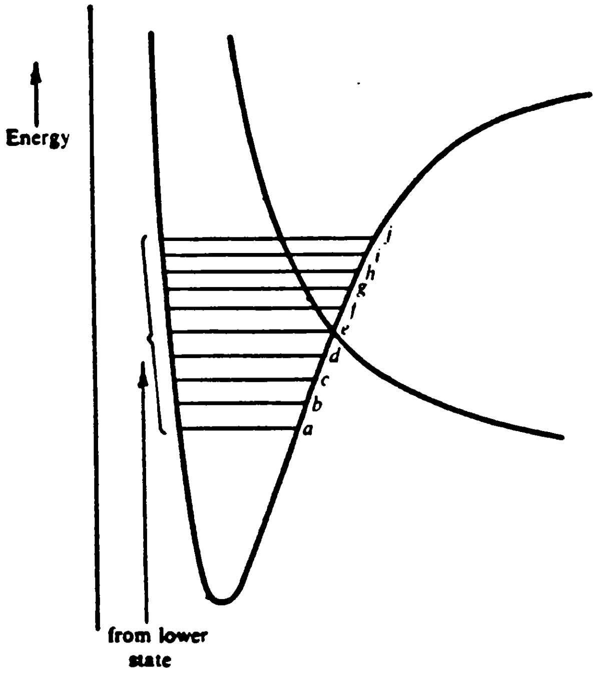

Figure 1.8 Predissociation in a molecule, excitation of the molecule occurs to vibrational levels in a higher-lying bound state which is crossed by an unbound state.

Predissociation arises when the potential energy curves of a molecule intersect, figure 1.8. Consider a transition occurring from a bound state into vibrational levels of a higher lying bound state which crosses an unbound state. If the transition occurs to vibrational levels (a), (b), (c) or (d), the molecule relaxes radiatively. If the vibrational levels (e) or (f) are populated, there is only a small probability that the molecule will cross over to the unbound state and thus dissociate. In the higher vibrational levels, (g), (h), (i) and (j), the molecule spends most of its time at the ends of its motion and therefore when the molecule is excited to one of these vibrational levels, the probability of the molecule crossing over and dissociating is large.

1.6.2 Kinetic Energy Distributions of the Metastable Products

Excitation from a bound state to both an unbound state and to the repulsive part of a bound potential energy curve is shown in figure 1.9. Each process gives rise to a characteristic kinetic energy distribution of the fragments, these are also shown in the figure.

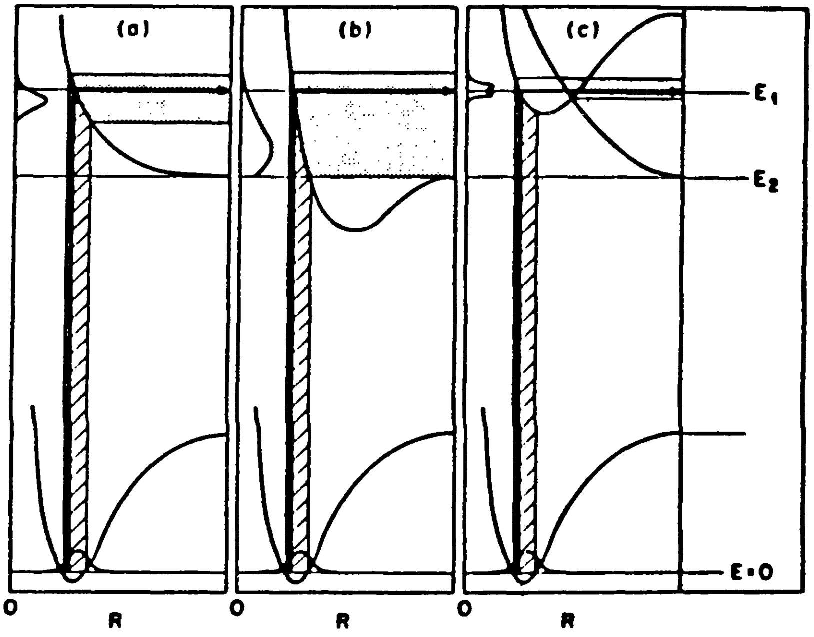

Figure 1.9 Diagram showing excitation of the molecule to dissociating states and the derivation of the characteristic kinetic energy distributions of the fragments in each case.

In excitation to the repulsive part of a bound state, the kinetic energy distribution of the fragments shows a finite probability of the fragments being produced with zero kinetic energy. In the production of $CO(a^3\pi)$ from the dissociation of carbon dioxide, the mean fragment kinetic energy is $\sim 0.2eV$, ten times thermal energies.

When the electron excites the molecule to a purely repulsive state, the excited molecule subsequently dissociates and the kinetic energy distribution of the fragments shows a minimum kinetic energy with which fragments may be produced. In the production of O(^{5}S) atoms from the dissociation of carbon monoxide, the peak kinetic energy is 4eV, equivalent to a velocity of approximately 5kms^{-1}.

1.6.3 Angular Distribution of Dissociation Products

When an electronic transition occurs to a purely repulsive state, the molecule dissociates. The time taken for the dissociation is small compared with the rotational motion of the molecule and therefore the dissociation products travel in a direction characteristic of the vibrational motion of the molecule.

If the probability of excitation of the molecule to the unstable state depends on the orientation of the molecule with respect to the incident electron beam, the products will exhibit a corresponding angular distribution.

Anisotropies were first observed in the product protons from electron impact ionisation of molecular hydrogen (Sasaki and Nakao 1935a,b, 1941). Improved measurements revealed a cos^{2}y distribution where y is the angle with respect to the incident electron beam. This agreed with their Born approximation calculation for excitation of molecular hydrogen for $H_2(^1\Sigma^+_g)$ to $H_2(^3\Sigma^+_u)$.

Dunn (1962) deduced symmetry principles for dissociative attachment in diatomic molecules and generalised these to dissociative excitation and ionisation. These give a qualitative description of the dissociation processes. Dunn states that the interaction potential is a scalar sum of Coulombic terms and therefore any symmetries existing prior to the collision will be preserved by the collision products.

Considering dissociative capture, the incident electron beam may be considered as a plane wave, exp(ik.r), which is symmetric with respect to all rotations about **k** and to reflection in planes containing **k**, figure 1.10. If the target molecule has an axis aligned along the **k** direction, it will also have symmetry with respect to rotations about **k** and reflection in planes containing **k**, figure 1.10a. For dissociation fragments to be produced along the **k** direction, the final anti-bonding orbital must have the same symmetries. A homonuclear molecule has symmetry with respect to reflection in a plane which is perpendicular to **k** and which contains the internuclear axis and has symmetry to a rotation of 180° about **k**, figure 1.10b. If dissociation products are to be produced perpendicular to **k**, the initial and final molecular states must have the same symmetry with respect to these operations. If the target molecule is heteronuclear and has an axis aligned perpendicular to **k**, the only symmetry is reflection in a plane containing both **k** and the axis of symmetry, figure 1.10c.

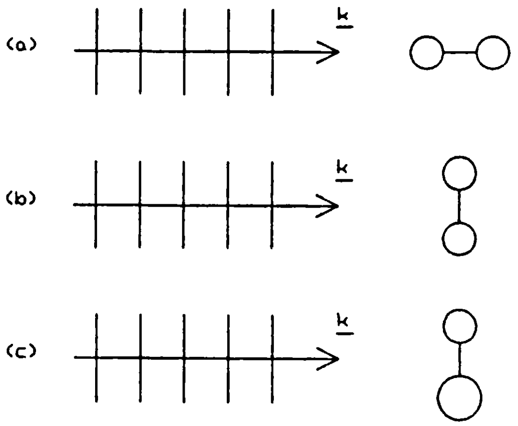

Figure 1.10 Symmetries involved in dissociation processes.

Dissociative excitation is more complicated because the scattered electron must be represented by a spherical outgoing wave and no definite symmetries are observed. However, at energies at which the Born approximation is valid the scattered electron can be described as a plane wave and the scattered and incident waves combine to give exp(i**K**.**r**), where **K** = **k** - **k'**. **K** may now be considered as the symmetry axis for the collision.

The symmetry of the dissociation products has important consequences in experimental studies. In the dissociation of molecular oxygen, for example, if the final molecular state is $O_2(^2\Pi_u)$, the transition probability for the molecule when aligned in the direction of the electron beam is zero. Therefore if the products are detected at right angles to the incident electron beam, the cross section for the process will be overestimated.

Dunn's selection rules must also be taken into account when determining the excited molecular states involved in dissociation. For example, considering again molecular oxygen dissociating to give the atomic fragments $O(^xS)$ and $O(^yP)$ which are observed at an angle of 90° to the incident electron beam. Possible dissociating molecular states are $\Sigma^+{}_{u,g}$ and $\Pi_{u,g}$. $\Sigma^+{}_u$ states may be discounted since the ground state of molecular oxygen is $^3\Sigma^-{}_g$ and the transition $- \rightarrow +$ is strictly forbidden in electron impact excitation. Π_g may be discounted since, according to Dunn's rules, the matrix element is zero for excitation from $\Sigma^-{}_g$ to Π_g at an observation angle of 90°. Dunn's rules also state that the matrix element for excitation from $\Sigma^-{}_g$ to Π_u is finite at this observation angle. The dissociating molecular state is therefore $O_2(\Pi_u)$.

1.6.4 Spectral Line Shapes

It has been known for some time that dissociative excitation of molecules causes broadening of the associated emission line profiles (Zipf and Wells 1980). Poland and Lawrence (1973) studied the Doppler broadening of dissociatively excited O(1304Å) from electron impact on molecular oxygen and carbon dioxide. Freund et al (1976) measured the broadened Balmer line shapes produced by electron impact dissociative excitation of molecular hydrogen. Both studies found the lines to be highly Doppler broadened, equivalent to environmental temperatures >20,000K.

There is a lack of detailed data describing broadening of such spectral lines and consequently such broadening has been neglected in the study of planetary atmospheres. The effective line width of the dissociation products is large compared with that expected for thermal oxygen atoms. The dissociatively excited atomic oxygen therefore behaves as if it were 'optically thin', i.e. the excited atoms do not trap photons resulting from the collision and the photons escape from the collision region.

Zipf and Wells (1980) calculated the spectral line shapes for radiation emitted by the excited atomic oxygen produced by electron impact dissociation from oxygen, carbon monoxide, carbon dioxide and nitric oxide. They used previously published time of flight spectra, P(t), (Wells and Zipf 1972, Wells et al 1978), from which they deduced the radial velocity distribution of the oxygen atoms, F(v), taking into account the in-flight decay

$$F(v) = t^2 \, P(t) \, e^{(t/\tau)}$$

where τ is the radiative lifetime of the excited state. Zipf and Wells identified the state detected as O(^{5}S) which has a radiative lifetime of 185μs (Wells and Zipf 1974, Johnson 1972).

The spectral line width is related to the radial velocity distribution (Rogers and Biondi 1964) by

$$S(\delta\tilde{\nu}) = \int \frac{F(v)}{v} \, dv$$

where S($\delta\tilde{\nu}$) is the spectral line shape and $\delta\tilde{\nu}$ is the Doppler shift in wave number,

$$\delta\tilde{\nu} = \tilde{\nu}_0 \, v_z$$

and $\tilde{\nu}_0$ is the wave number of the emission line, v_z is the line of sight velocity of the atomic oxygen and c is the speed of light.

When the spectral line widths for the dissociatively excited oxygen atoms are compared with thermal Doppler profiles, the temperature of the Doppler profile is typically in the range 20,000K to 60,000K depending on the incident electron energy and the parent molecule.

1.7 Review of Experimental and Theoretical Studies

It was the need to interpret the growing volume of airglow data collected since the beginning of space exploration about 30 years ago that rekindled interest in the experimental study of dissociation processes. In this section, an overview of investigation of dissociative excitation by electron and photon impact is given. Details of studies of carbon monoxide, carbon dioxide, carbonyl sulphide and nitrous oxide will be given in chapters six and seven.

1.7.1 Experimental Electron Impact Dissociation Studies

Time of flight techniques have been used to study those fragment atoms or molecules produced in metastable or high lying Rydberg states. These studies are limited to fragments of lifetime greater than 10^{-6}s, i.e. those which remain in excited states long enough to reach the detector. Time of flight studies give information concerning the kinetic energy distribution of the fragments from which the Doppler line widths and parent potential energy curves may be deduced. The lifetimes of the product metastable fragments may also be determined from the kinetic energy spectra (Mason 1990).

Experimental studies have been restricted mainly to dissociation of molecular nitrogen, molecular oxygen, carbon dioxide and carbon monoxide. A comprehensive list of other molecules studied has been given by Zipf (1984). A detailed review of experimental studies of the dissociation of molecular hydrogen is given by Compton and Bardsley (1984), and of molecular nitrogen by Field and Franklin (1970). Publications after 1984 include new investigations of molecular oxygen (Mason and Newell 1990a) and of nitrous oxide (Mason and Newell 1989).

Experimental results currently available are often contradictory in their results and conclusions. Particular difficulty has been found in the interpretation of the results of those experiments in which one of the fragments is produced in more than one metastable state. Individual metastable states may be selected using a laser to ionise the metastable state (Schohl et al 1991). A state selective detector may also be used which discriminates between the states either on the basis of the work function of the detector or by using a particular excimer reaction (Kiefl et al 1983, Kume et al 1986a,b). Such detection methods are described in chapter two.

Another problem concerning the detection of metastable species is the calibration of the detector. The detection efficiency to each metastable species, or to different metastable states of the same species, will not be the same. Absolute measurements of the production cross sections requires the detector to be calibrated and monitored throughout the experiment since impurities on the surface may alter the detection efficiency. The method of detection of metastable species will be described in detail in chapter two, and the design, operation and calibration of the detectors used in this work in chapter five.

The in-flight decay due to the finite lifetime of the metastable products affects the time of flight spectra and will be reflected in the kinetic energy spectra. To compensate for this, the lifetimes of the metastable states concerned must be known. Some lifetimes are well defined, for example $N_2(a^1\pi_g)$ for which population by cascade from higher lying states is negligible, while others are uncertain, for example, the lifetime of $CO(a^3\pi)$ lies between 10μs and 10ms depending on the vibrational levels populated.

1.7.2 Experimental Photon Impact Dissociation Studies

The photodissociation of a wide variety of molecules has been studied (e.g. Ashfold et al 1979) using photons of energy less than $\sim$18eV. The photon has an intrinsic spin of one unit while the spin of the electron is ½, therefore different states may be excited in collisions with photons than in collisions with electrons. Photodissociation studies therefore complement electron impact studies.

1.7.3 Theoretical Studies

Few calculations of these dissociation processes have been carried out since during the initial excitation of the molecule, the electron is promoted to a state lying in a continuum of states which are too numerous to be included in current theoretical calculations. Presently, theoretical electronic excitation cross sections for the simple diatomic molecules at low incident electron energies are being generated using new computational techniques such as the R-matrix code (Branchett and Tennyson 1990, Branchett et al 1991, Burke et al 1987). These methods are likely to be extended to describe the more complicated electron-polyatomic molecule interactions and eventually will include dissociative excitation.

At high incident electron energies, however, dissociative excitation and ionisation may be treated by the Born approximation. The only theoretical study of dissociative excitation in the relevant energy range for this work concerns the dissociation of molecular hydrogen. Chung and Lin (1978) calculated cross sections for direct excitation of molecular hydrogen using the close-coupling method and used these to make deductions concerning the dissociation of hydrogen.

1.8 Importance of Dissociative Excitation

The importance of dissociative processes arises since they are a source of kinetically energetic atoms, molecules and ions, chemically active metastable species and short-lived excited states. In industrial gaseous discharges and in laser systems pumped by a pulsed beam of high energy electrons, a high proportion of the atoms or molecules are in metastable states, produced either by direct electron impact excitation or dissociative excitation. Dissociative excitation is also relevant to a number of interdisciplinary problems such as plasma chemistry and the study of planetary atmospheres.

1.8.1 Plasma Chemistry

Measurements in the environment surrounding the Space Shuttle have indicated the presence of regions of enhanced ionisation (e.g. Raitt et al 1984). The numerical solution of rate equations for processes occurring in this environment by Lai et al (1988) demonstrated that metastable states of gases substantially contribute to the rapidity of the ionisation processes. Since the metastable states are long-lived they effectively store energy so that in subsequent collisions with low energy electrons these metastable states are rapidly ionised.

1.8.2 Planetary Atmospheres

Dissociative excitation is important in the upper atmosphere where the density is sufficiently low to make collisional de-excitation negligible. Dissociative excitation occurs both by photon and electron impact. Typical electron concentrations in the terrestrial upper atmosphere are in range 10^4 to 10^6cm^{-3}, figure 1.11, and are sufficiently high for electron impact processes to be significant.

Many spectral features in the airglow originate from transitions in electronically excited species, many of which involve emission via magnetic dipole or electric quadrupole transitions. An important example is the O(^{1}S - ^{1}D) transition in atomic oxygen which is responsible for the 557.7nm line in both the terrestrial aurora and airglow. A knowledge of dissociation processes is required if such complex systems are to be explained and modelled. Subjects of environmental concern at the moment include the changes in the terrestrial ozone layer and the prediction of energy degradation in the atmosphere after the sudden production of large fluxes of secondary electrons as in nuclear explosions and auroral substorms. The interpretation of a large volume of airglow data from other planetary atmospheres is also of interest.

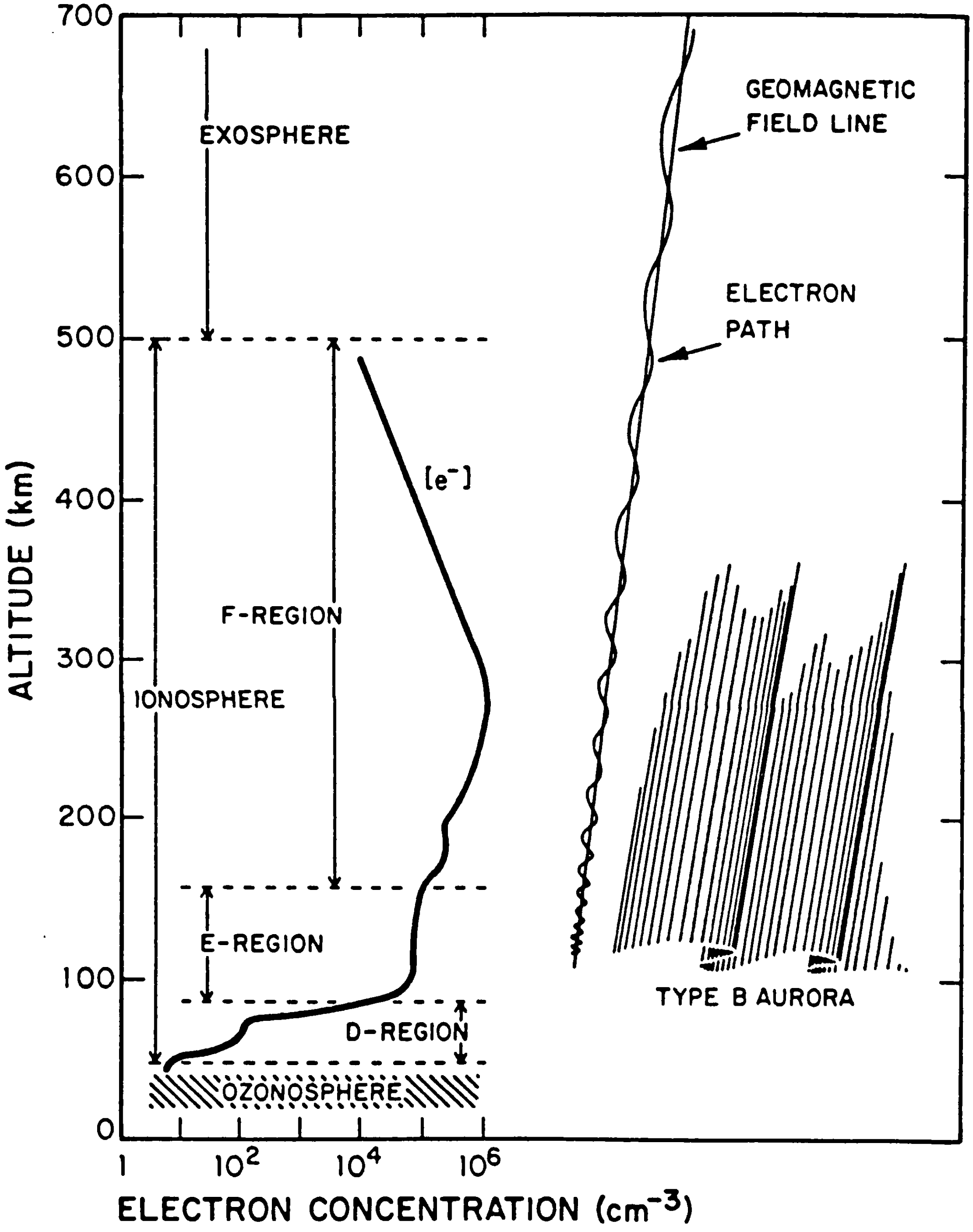

Figure 1.11 Variation of electron concentration with altitude in the terrestrial atmosphere (Csanak et al 1984).

a) Titan

Titan is the largest satellite of Saturn and is one of the two satellites in our solar system to have an atmosphere. The atmosphere is composed predominantly of nitrogen, 97%, with a variable methane content and traces of water, carbon dioxide and hydrocarbons. The airglow, figure 1.12, has been modelled by Strobel and Shemansky (1982) by considering transitions in atomic nitrogen, molecular nitrogen and nitrogen ions produced by electron impact excitation, dissociation and ionisation. This model compares well with the ultraviolet emission spectrum obtained from Voyager 1. A significant feature is the Lyman-Birge-Hopfield band of molecular nitrogen, involving the metastable $N_2(a^1\pi_g)$ state.

b) Mars

The Martian atmosphere is composed predominantly of carbon dioxide, the surface temperature and pressure are variable over time and latitude but average 217K and 5torr. The airglow spectrum was observed from Mariner 9, figure 1.13 (Barth et al 1972). The Cameron band system of carbon monoxide, the spin forbidden transition $CO(a^3\pi - X^1\Sigma^+)$ (Cameron 1926), is the dominant feature of the Martian airglow.

The possible sources of $CO(a^3\pi)$ are

(a) photodissociation of carbon dioxide,

$$CO_2 + h\nu\ (\lambda<108.2nm) \rightarrow CO(a^3\pi) + O(\Gamma)$$

(b) electron impact dissociation of carbon dioxide,

$$CO_2 + e^-(E>11.5eV) \rightarrow CO(a^3\pi) + O(\Gamma) + e^-$$

(c) electron impact excitation of carbon monoxide,

$$CO + e^- \rightarrow CO(a^3\pi) + e^-$$

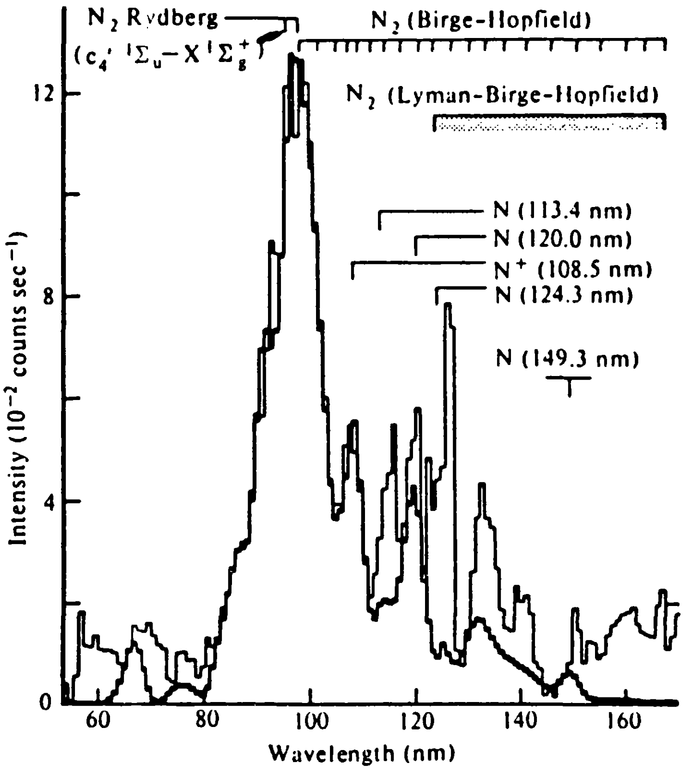

Figure 1.12 Emission spectrum of Titan showing the Lyman-Birge-Hopfield lines, $N_2(a^1\pi_g - X^1\Sigma^+{}_g)$. The overplotted spectrum is the model calculated assuming that the emission features are the result of electron impact excitation, dissociation and ionisation (Strobel and Shemansky 1982).

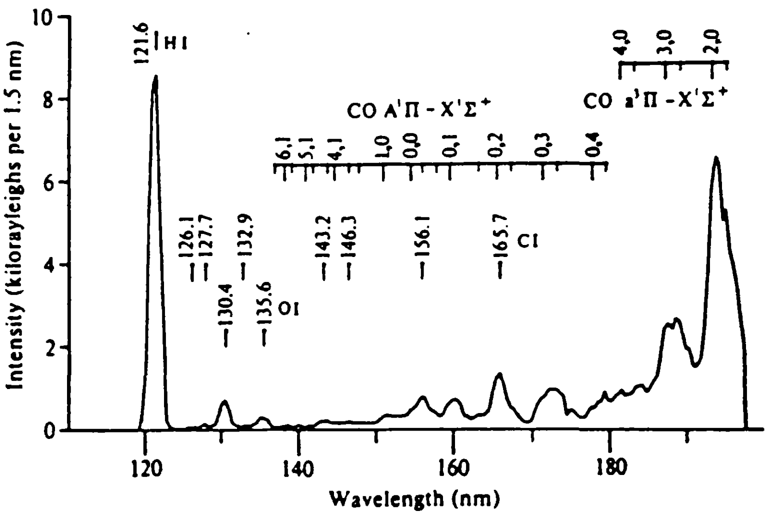

Figure 1.13 Emission spectrum of Mars showing the Cameron bands, $CO(a^3\pi - X^1\Sigma^+)$, and the Fourth Positive bands, $CO(A^1\Pi \rightarrow X^1\Sigma^+)$, (Barth et al 1972),

(d) dissociative recombination of CO_2^+,

$$CO_2^+ + e^- \rightarrow CO(a^3\pi) + O(\Gamma)$$

(e) photo-excitation of carbon monoxide,

$$CO + h\nu\,(\lambda<203.0nm) \rightarrow CO(a^3\pi)$$

Fox and Dalgarno (1979) calculated the importance of each of these sources to the production of CO($a^3\pi$) in the Martian atmosphere. Production of CO($a^3\pi$) by process (e) is negligible since the concentration of carbon monoxide in the atmosphere is negligible and scattering of sunlight is optically forbidden. Table 1.2 compares the production rates of four Martian airglow features for each production process at an altitude of 100km.

Table 1.2 Contributions of different collision processes to the Martian airglow (Fox and Dalgarno 1979).

Band System	Source					Total
	(a)	(b)	(c)	(d)	(e)	
Cameron CO($a^3\pi \rightarrow X^1\Sigma^+$)	1830	2350	90	650		4920
Fourth Positive CO($A^1\Pi \rightarrow X^1\Sigma^+$)	75	65	21	73		231
Fox-Duffendack-Barker $CO_2^+(A^2\Pi \rightarrow X^2\Pi_g)$	2035	400			840	3275
Ultraviolet Doublet $CO_2^+(B^2\Sigma^+_u \rightarrow X^2\Pi_g)$	925	240			45	1210

Fox and Dalgarno also calculated the altitude profiles of the major sources of the Cameron bands, figure 1.14, and showed that the main source of emission below 135km is electron impact dissociation of carbon dioxide, while the main source above 135km is photodissociation.

The Fourth Positive band system arising from the transition $CO(A^1\Pi - X^1\Sigma^+)$ is also an important feature in the Martian airglow (Barth 1969). $CO(A^1\Pi)$ lies at 8.02eV and is populated via the same mechanisms that populate the $CO(a^3\pi)$ state. Fox and Dalgarno (1979) calculated the altitude profiles for the Fourth Positive bands, figure 1.15, and showed that the dominant production process are dissociative recombination and dissociative excitation by electron impact and photons.

1.8.3 Lasers

Modelling of complex systems such as gas lasers requires data on a wide range of collision processes including dissociation processes. Formation of metastable species by direct and dissociative excitation influences energy transfer processes occurring in the cavity. Little and Browne (e.g. 1987,1988,1989) have modelled the processes occurring in carbon monoxide and carbon dioxide lasers and have investigated the radiation induced and laser oscillation induced perturbations in the system. Little and Browne (1989) observed the intensity of the Swan bands, $C_2(d^3\pi_g - a^3\pi_u)$, in a CO-He-Xe laser and related increases in the intensity of these bands to an increase in the dissociation of carbon monoxide. They showed that the dominant dissociation process involves collisions between metastable $CO(a^3\pi)$ molecules and ground state molecules.

$$CO(a^3\pi) + CO(X^1\Sigma^+) \rightarrow CO_2 + C$$

Dissociation by electron impact is also important

$$CO + e^- \rightarrow C + O + e^-$$

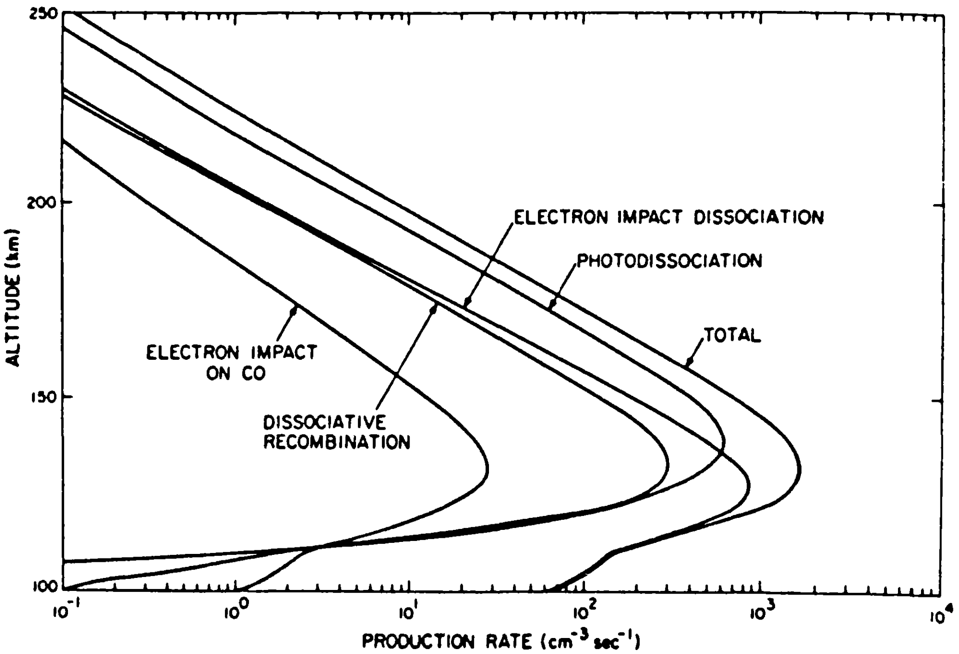

Figure 1.14 Altitude profiles for the production of the Cameron bands in carbon monoxide (Fox and Dalgarno 1979).

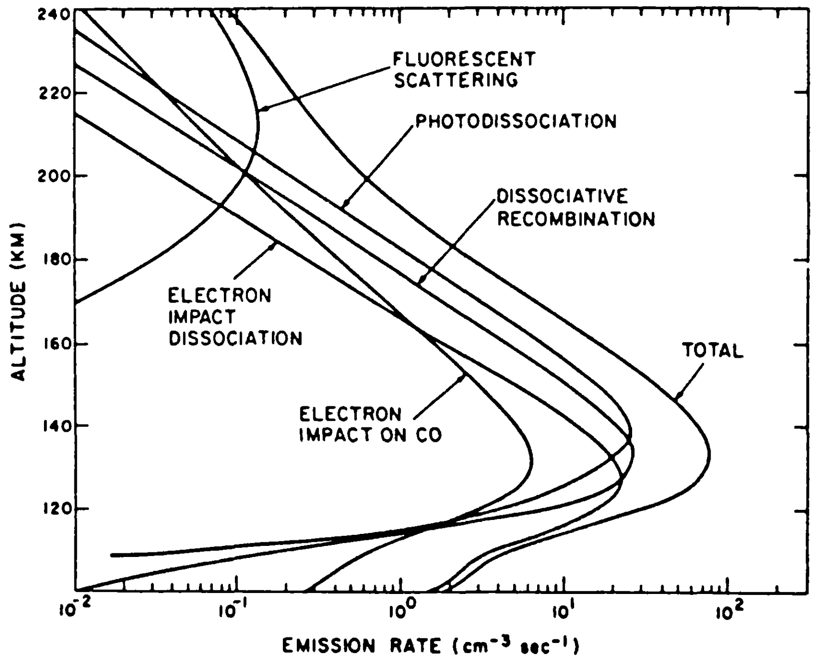

Figure 1.15 Altitude profiles for the production of the Fourth Positive bands in carbon monoxide (Fox and Dalgarno 1979).

Recombination of the atomic carbon produced in these dissociation processes leads to the radiation observed in the Swan bands.

1.9 Summary

In this chapter, classification of molecular states, molecular bonding and the concept of metastable species have been reviewed as a background to the discussion of dissociation of molecules. A brief guide to the previous experimental studies of electron impact and photon impact dissociation and the problems associated with such experiments has been given. The studies most closely related to this work are reviewed fully in the results chapters, six and seven. A theoretical treatment of dissociation is complicated and at present only simple molecules such as hydrogen have been studied. The importance of dissociation processes has been illustrated by examples from planetary atmospheres, plasmas and lasers.

Chapter Two

Review of Methods of Detection of Metastable Species

The bearing of this observation lies in the application of it.
Charles Dickens (*Dombey and Son)*

2.1 Introduction

Electron impact excitation of atoms and molecules has been widely studied both experimentally and theoretically since the 1920s. Such collision processes have traditionally been studied experimentally by observing the residual energy and angular dependence of the electrons scattered out of the interaction region. This technique has been successfully applied to many excitation processes, but is not as useful in the study of near threshold excitation, dissociation or ionisation processes. These collision processes may, however, be monitored by observing directly the metastable products of the collision (e.g. Freund 1971a, Borst and Zipf 1971a, Brunt et al 1976).

In this chapter, several methods for the detection of the metastable collision products are outlined and examples of each discussed. Particular attention is given to the detection of metastable species by secondary electron emission from a metal surface since this technique has been used in this study of electron impact dissociative excitation.

2.2 Detection by Penning Ionisation

2.2.1 Introduction

In a collision between a metastable atom (or molecule), A^*, and a ground state target atom (or molecule), B, energy may be transferred from the metastable atom to the target by a resonant process,

$$A^* + B \rightarrow A + B^*$$

If the excitation energy of the metastable atom is greater than the ionisation potential of the target, Penning ionisation of the target occurs,

$$A^* + B \rightarrow A + B^+ + e^-$$

Penning ionisation was first used as a means of identifying the metastable products of electron impact on atoms and molecules by Cermak (1966) and has since been refined as a detection technique by Hotop and Niehaus (1970) and Weissmann et al (1984).

The apparatus used by Cermak consisted of a vacuum chamber in which the metastable beam was produced by electron impact on a target gas beam, and a gas cell filled with a 'detector' gas, figure 2.1. Several detector gases were chosen so that they formed a series of increasing ionisation potentials, table 2.1. By filling the gas cell with each detector gas in turn and observing the formation of ions as the metastable beam passed through the gas cell, Cermak was able to determine the excitation energy of the metastable species.

Table 2.1 summarises Cermak's results for metastable species of molecular hydrogen, nitrogen and carbon monoxide produced by electron impact, a '✓' indicates the detection of ions.

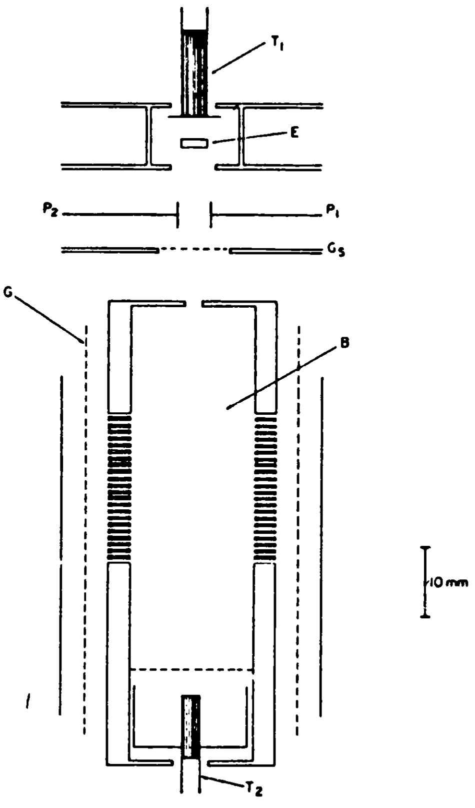

Figure 2.1 Schematic diagram of the experimental arrangement used by Cermak (1966). T_1 is the beam of unknown metastable molecules, E the incident electron beam and T_2 the beam of detector molecules. B is the collision chamber. Grids P_1, P_2 and G_s remove charged particles and scattered electrons from the molecular beam while positive ions are collected on grid G.

Table 2.1 Penning ionisation of selected detector gases by unknown metastable species Cermak (1966). Ionisation potentials (eV) are given in brackets.

Detector Gas Metastable Species	NO (9.2)	cyclo C_3H_6 (10.2)	C_2H_4 (10.5)	CH_3OH (10.8)	C_2H_2 (11.4)	C_2H_8 (11.6)
H_2	✓	✓	✓	✓	✓	x
N_2	✓	✓	✓	✓	✓	x
CO	✓	✓	?	x	x	x

From these results, Cermak was able to conclude that the excitation energies of the metastable species produced in the experiment were in the following ranges,

H_2^*	11.4 - 11.6
N_2^*	11.4 - 11.6
CO^*	10.2 - 10.8

Since more than one metastable state may be produced during electron impact excitation of these molecules, this excitation energy must be that of the highest lying metastable state excited. For example, in electron impact excitation of molecular nitrogen, three metastable states may be excited, $N_2(A^3\Sigma^+_u)$, $N_2(a^1\pi_g)$ and $N_2(E^3\Sigma^+_g)$ of excitation energies 6.17eV, 8.55eV and 11.79eV respectively. Therefore this information alone is not sufficient to identify the metastable fragments produced.

Cermak therefore also measured the ion flux as a function of the incident electron energy used to excite the metastable beam. The threshold and shape of these excitation functions were then used in the determination of the metastable state produced.

2.2.2 Identification of $N_2(E^3\Sigma^+_g)$

To illustrate the use of Penning ionisation as a method of detecting metastable species, the identification by Cermak of the $N_2(E^3\Sigma^+_g)$ metastable state will be described.

The excitation functions for the detector gases NO, C_3H_6 and C_2H_2 all revealed a sharp peak at 12.6eV, figure 2.2. Cermak attributed this peak to a new higher lying metastable state capable of ionising all three detector gases. This metastable state must therefore have an excitation energy of between 10eV and 12eV. The excited states of molecular nitrogen in this energy range are $N_2(C^3\Pi_u)$, $N_2(E^3\Sigma^+_g)$ and $N_2(^5\Pi)$ together with vibrational levels of the states $N_2(a^1\pi_g)$ and $N_2(a'^1\Sigma^-_u)$.

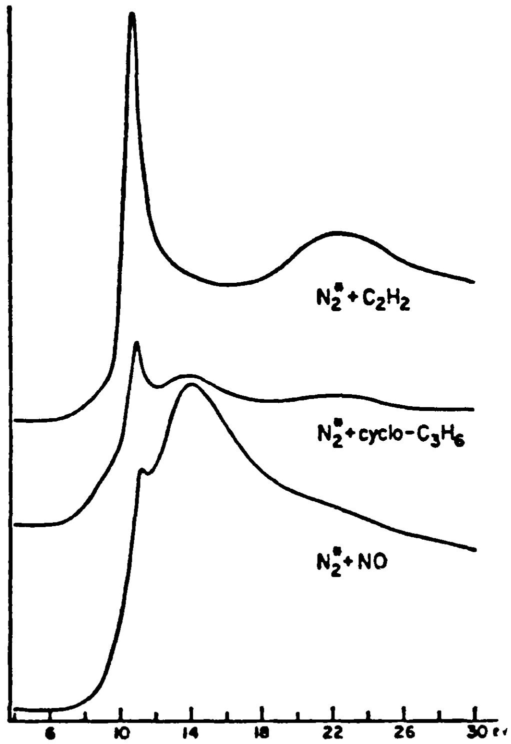

Figure 2.2 Excitation functions for the Penning ionisation of NO, C_3H_6 and C_2H_2 molecules by metastable molecular nitrogen.

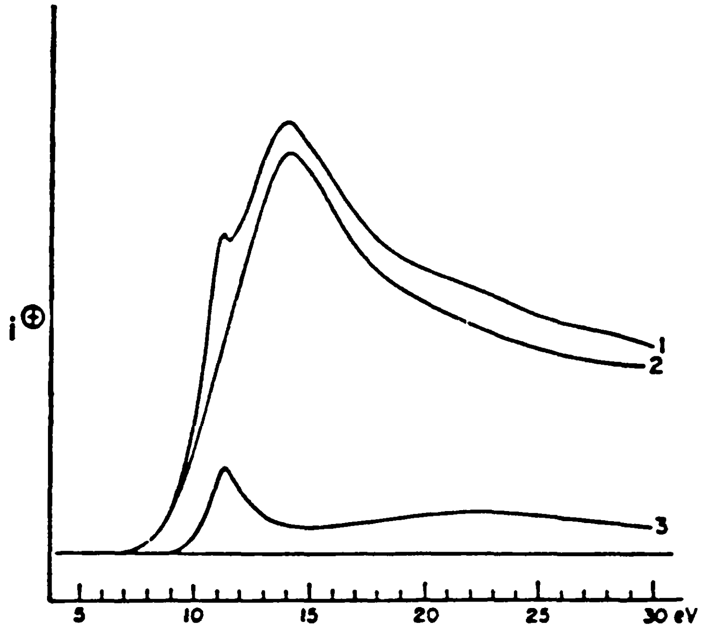

Figure 2.3 Efficiency curves for the excitation of metastable states of nitrogen (Cermak 1966).

The efficiency curve corresponding to the peak at 12.6eV is sharply peaked, figure 2.3. This sharpness was explained by Cermak as being due to the resonance capture of the exciting electron by the target nitrogen molecule and the subsequent decomposition of the unstable negative ion formed

$$N_2(^1\Sigma_g^+) + e^- \rightarrow (N_2^-)^* \rightarrow N_2^*(?) + e^-$$

The efficiency curve for this 12.6eV feature therefore does not have any similarities with the efficiency curves derived for the lower lying $N_2(a^1\pi_g)$ and $N_2(a'^1\Sigma_u^-)$ states and therefore cannot be due to these vibrational levels which contribute to these curves.

The excited state produced must be long lived if it is to reach the gas chamber. Cermak stated that the $N_2(C^3\Pi_u)$ state is not metastable and decays to the $N_2(B^3\Pi_g)$ state and cannot therefore be this new state.

The excited state must have odd multiplicity. The ionisation of C_2H_2 detector molecules may be represented by

$$N_2^*(?) + C_2H_2(^1\Gamma) \rightarrow N_2(^1\Sigma_g^+) + C_2H_2^+(^2\Gamma) + e^-$$

The state cannot be a quintet, since a quintet state could not ionise the C_2H_2 detector molecule without violation of spin conservation (Wigner 1927). It must therefore be singlet or triplet.

From this, Cermak concluded that the excited state of nitrogen produced was the $N_2(E^3\Sigma^+{}_g)$ state. Later work (e.g. Borst 1972, Brunger et al 1988) has shown that the $N_2(E^3\Sigma^+{}_g)$ state is indeed metastable with a lifetime of 190μs and could therefore be the state of nitrogen produced. Moreover, the efficiency curve derived by Cermak for production of the higher lying state agrees well with the cross section for production of the $N_2(E^3\Sigma^+{}_g)$ state deduced by Borst 1972 (see chapter five). Both show a resonance-like feature which occurs between 10eV and 13eV although while the cross section of Borst falls to zero above 13eV, the curve derived by Cermak, rises slowly giving a shallow bump. Such a feature could be due to the incomplete separation of the metastable states produced in Cermak's work.

Penning ionisation is a useful method of detection of metastable species, since it is potentially also a method of selecting one of the metastable products of electron impact excitation. However identification of the states is not straight forward and ions may be produced by processes other than Penning ionisation such as associative ionisation,

$$A^* + BC \rightarrow ABC^+ + e^-$$

Other disadvantages are the bulkiness of the apparatus and the low signal intensities due to the use of a secondary collision process. It is also not possible to determine the kinetic energy distributions of the metastable collision products by this method.

2.3 Detection by Secondary Electron Emission

2.3.1 Introduction

The technique most widely used in the detection of metastable species is by collision with a metal surface. If the internal energy of the metastable species is greater than the work function of the surface, it is capable of causing the emission of secondary electrons from the surface. The secondary electrons may then be detected by a channel electron multiplier.

The emission of secondary electrons from a metal surface by the action of metastable species was first observed by Webb (1924) in a discharge of mercury vapour. Webb used a pulsed electron beam to excite mercury vapour in the discharge tube and studied the duration of the resultant radiation in the discharge. The detector used was a four electrode tube connected to an electrometer. His results did not compare well with his calculations based on the successive absorption and re-emission of radiation through the discharge as proposed by Compton (1922), but were in good agreement with the hypothesis that the persistence of radiation was due to the formation of metastable states of the vapour (Kannerstine 1924) and that it was these metastable atoms which produced the observed photoelectric current at the electrodes.

Couliette (1928) repeated Webb's work using the same apparatus and confirmed that metastable atoms did cause secondary electron emission at a metal surface, in this case a nickel surface. He also determined that the velocity distribution in the metastable gas beam is the same as that in the target gas beam by measuring the diffusion rate for both ground state and metastable atoms across the gas cell.

Messenger (1926) placed a quartz window between a source of metastable mercury atoms and a nickel detector, thus allowing photons to reach the detector while blocking the metastable atoms. In this experiment she demonstrated that the secondary electron current was predominantly due to the incidence of metastable atoms, with only a few percent of the current due to photons.

2.3.2 Mechanism of Secondary Electron Emission

These early studies led to an interest in the mechanism of secondary electron emission from the metal surface. Oliphant and Moon (1930) were the first to propose a mechanism for the production of secondary electrons when a metastable atom is incident on a metal surface. They postulated that as the metastable atom approaches the surface, a three body reaction occurs between the metastable atom, a lattice atom and a lattice electron. The result of this reaction is the emission of an electron.

Shekhter (1937) modelled the neutralisation of positive hydrogen ions at a metal surface. His theory assumed an Auger type process in which two electrons from the metal lattice undergo simultaneous transitions, one to the ground state of the atom and the other to the continuum of the metal surface, appearing as a secondary electron. Varnerin (1953) extended Shekhter's theory to include de-excitation of metastable species at a surface, postulating that as the metastable atom approaches the surface it captures an electron into its ground state and ejects the outer electron. Both these theories have been incorporated in more recent theories (e.g. Sesselmann et al 1987).

Hagstrum (1954, 1978) made extensive studies of the behaviour of ions at a metal surface and measured the secondary electron emission coefficient. In Hagstrum's semi-quantative theory, a metastable atom of excitation energy E_m is ionised as it approaches the surface if the effective ionisation potential, E_i, is greater than the work function of the surface, ϕ. In ionisation of the metastable atom, the outermost electron tunnels into the metal lattice. The ion is then neutralised by one electron from the metal lattice, while a second lattice electron escapes from the surface.

More recent theories of the mechanism of secondary electron emission are refinements of Hagstrum's theory. Sesselmann et al (1987) describe two routes by which de-excitation of metastable species at a surface may occur, (a) resonance ionisation followed by Auger neutralisation and (b) Auger de-excitation.

a) Resonance Ionisation and Auger Neutralisation

Resonance ionisation followed by Auger neutralisation occurs when the excited level in the metastable atom, E_m, corresponds to a vacant level in the metal band structure, figure 2.4. As the metastable atom approaches the surface, there is a high probability of a resonance transition between the excited level in the metastable atom and the vacant level in the lattice. The electron in the excited metastable level tunnels into the empty lattice level, leaving a positive ion which is neutralised as the hole in the ground state level of the metastable ion is filled by an electron transition from the surface. The energy released in this process causes a second valence electron to be ejected from the surface.

The rate of resonance ionisation is much faster than that of Auger de-excitation, therefore resonance ionisation followed by Auger neutralisation dominates when the

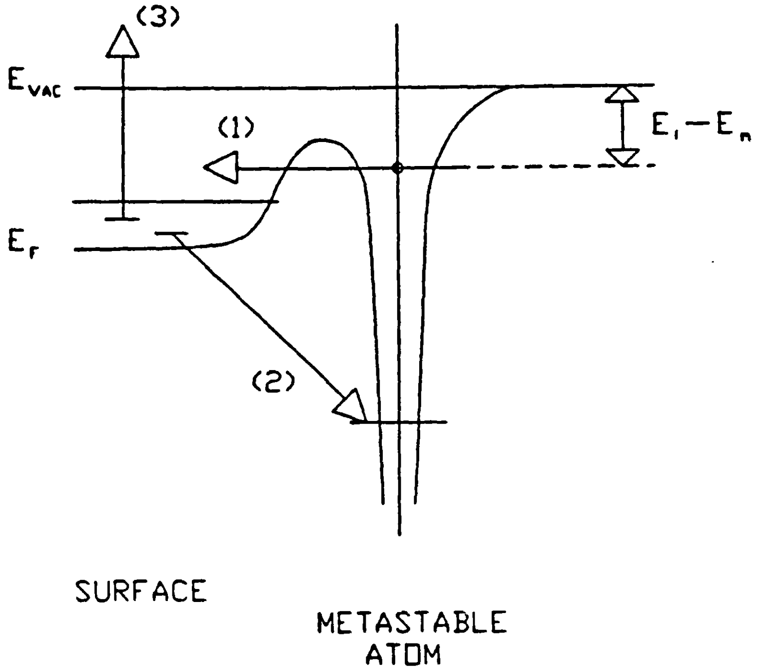

Figure 2.4 Mechanism of resonance ionisation followed by Auger neutralisation. The metal surface has a continuum of unoccupied states between the Fermi level, E_F, and the continuum, E_{vac}.

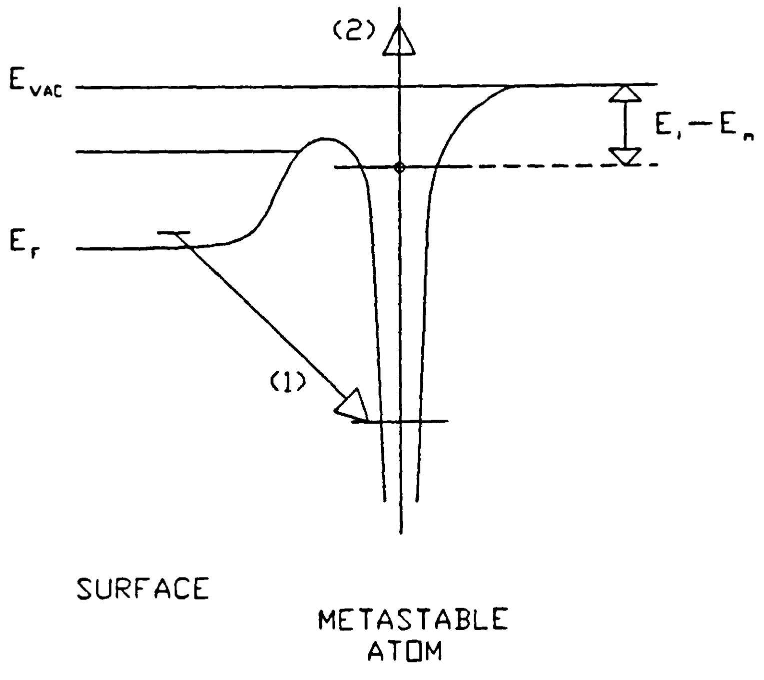

Figure 2.5 Mechanism of Auger de-excitation. The metal surface has a continuum of unoccupied states between the Fermi level, E_F, and the continuum, E_{vac}.

electron of the excited metastable state may tunnel into the surface, i.e. when the local work function of the surface exceeds the effective ionisation potential of the excited level in front of the surface,

$$E_i - E_m < \phi$$

where E_i is the effective ionisation potential of the atom, E_m is the excitation energy of the metastable state and ϕ is the work function of the surface. Note that the effective ionisation potential is lower in the vicinity of a surface than in a free gas because of the polarisation effects due to the surface.

b) Auger De-excitation

Auger de-excitation occurs when there is no vacant level in the lattice corresponding to the excited level of the incident metastable atom, and consequently resonance ionisation cannot occur, figure 2.5. An exchange interaction takes place by which a lattice electron tunnels to the unoccupied ground state of the incident metastable atom while the electron in the excited level is ejected.

Auger de-excitation dominates if the effective ionisation potential is greater than the local work function,

$$E_i - E_m > \phi$$

If the excited level is in the band gap of a semi-conductor or insulator or if tunnelling of the excited electron is suppressed by the presence of a dense layer of molecular adsorbate, resonance ionisation cannot occur and Auger de-excitation dominates.

c) Ions Incident on a Metal Surface

When resonance ionisation followed by Auger neutralisation is the dominant process, metastable species interact with the surface as ions. In Auger de-excitation, ions approaching the surface are resonance neutralised to excited neutrals before impact and therefore both metastable species and ions interact with the surface as excited neutrals. It is expected therefore that ions and metastable species of the same atom would cause similar secondary electron yields and that these electrons would have the same angular distribution.

Hagstrum (1954, 1956) measured the secondary electron yield for ions on metal surfaces. The values obtained by Hagstrum for helium, neon and argon ions on a chemically clean tungsten surface are included in table 2.3 for comparison with the determinations of the secondary electron yield for the corresponding metastable species incident on the same surface. The secondary electron yields for both ions and metastable atoms appear to be similar. Delchar et al (1969) measured the energy distributions of the secondary electrons produced by incident metastable atoms and incident ions in the same apparatus and showed them to be identical within experimental error.

The energy distribution of the ejected electrons is determined by the overlap between the wavefunctions of the surface and the unoccupied ground state level of the incident metastable atom. If electron emission occurs through Auger de-excitation, one electron from the target is involved whereas if emission occurs through resonance ionisation followed by Auger neutralisation two electrons participate. The resultant energy distribution of the ejected electrons will therefore be different for the two processes. In Auger de-excitation the maximum kinetic energy of the emitted electron is $(E_m - \phi)$ while in resonance ionisation and Auger neutralisation the maximum kinetic energy is $(E_i - 2\phi)$.

Analysis of the energy distribution of ejected electrons from a surface following ion impact is the basis of ion neutralisation spectroscopy (Hagstrum 1979). The high kinetic energy of ions, however, causes other effects which complicate the spectra. The use of neutral metastable atoms of thermal kinetic energies has none of these disadvantages. Metastable de-excitation spectroscopy has been developed over the last fifteen years (e.g. Munakata et al 1978, Johnson and Delchar 1978, Conrad et al 1979, Boiziau et al 1980, Bozso et al 1983) and is a sensitive method of investigating surface structure.

d) Effect of Adsorbates

In experiments performed at pressures $>10^{-8}$ torr, the detector surface will be covered with a layer of adsorbates. Delchar et al (1969) proposed that a covalent bond exists between the adsorbate and the surface, perturbing the ground state of the adsorbate and providing an intermediate energy level between the conduction band of the surface and the ground state of the incident metastable atom.

This intermediate energy level increases the probability that there will be a vacant energy level in the lattice corresponding to the energy level of the excited electron in the incident metastable atom. Therefore the dominant process occurring at the surface is resonance ionisation followed by Auger de-excitation.

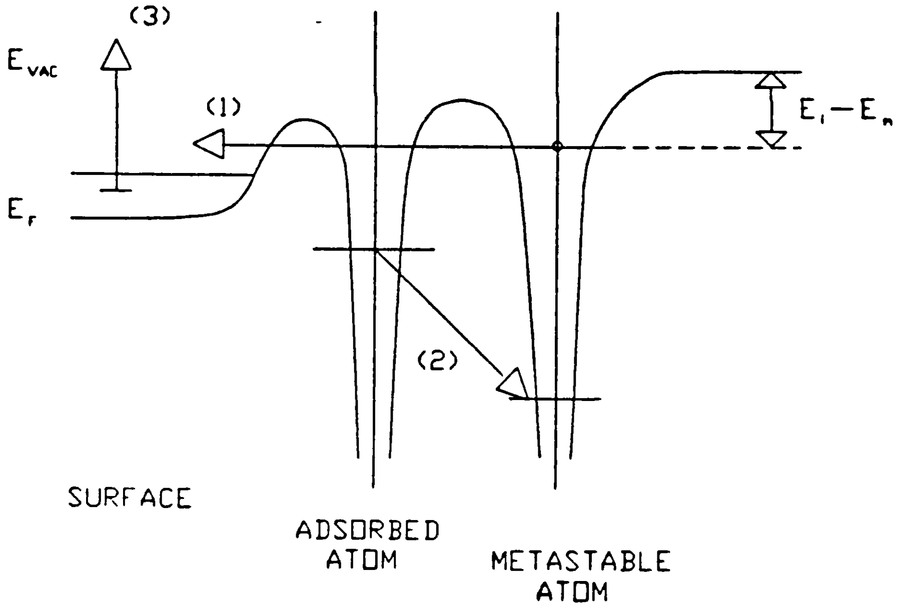

Figure 2.6 Mechanism of secondary electron emission from an adsorbate covered surface.

The metastable atom is first resonance ionised and the resulting ion neutralised by the transition of an electron from the adsorbate to the ion, figure 2.6. A lattice electron is ejected to balance the energy.

Dunning et al (1971) measured the secondary electron yield for metastable helium atoms incident on a chemically clean stainless steel surface to be >1.0, implying the emission of more than one electron per incident metastable atom. They proposed that adsorbates on the surface having an ionisation potential less than the excitation energy of the incident metastable atom were Penning ionised, resulting in the emission of two electrons, one from the ionisation of the adsorbate and one from the surface.

2.3.3 Effect of Surface Impurities

The first study of the effect of surface impurities was that of Sonkin (1933) who investigated the action of metastable $Hg(6^3P_0)$ atoms of energy 4.68eV on tungsten, nickel, platinum, iron, molybdenum and tantalum surfaces located in a side arm of a discharge tube. To ensure that the secondary electron current was due entirely to the incident metastable atoms, he used a quartz window to stop the metastable atoms reaching the surface and confirmed Messenger's result that only a few percent of the secondary electron current was due to the photoelectric effect. He also found that the response of each of the detectors to the metastable mercury atoms was not correlated to the response to photons of the same energy, 265nm.

Sonkin also established in experiments using the tungsten surface that the efficiency of secondary electron emission was increased when the surface was outgassed. However, following 'flashing', heating to $\sim$2000K, there was a sudden decrease in the sensitivity of the surface before a slow recovery. The rate of recovery increased when the vapour pressure of mercury in the discharge was decreased and when the tungsten was maintained at a temperature of $\sim$1300K.

To explain these results, Sonkin proposed that flashing drives off oxides, leaving an atomically clean tungsten surface of reduced sensitivity to metastable mercury atoms and as mercury atoms cover the tungsten surface, the sensitivity drops further. He associated the recovery with the deposition of oxygen on top of this mercury surface which facilitated the more rapid deposition of further mercury atoms. It is not clear why this should cause a recovery in the sensitivity. In the light of more recent experiments it seems that the drop in sensitivity is due to impurities being driven off the surface, an atomically clean surface not being the most efficient detecting surface. The recovery in sensitivity is most probably due to the deposition of more impurities onto the surface.

Impurities adsorbed onto the surface will not all be removed by flashing the surface since the removal of some would require heating to temperatures above the melting point of the surface (Rundel and Stebbings 1972). It has also been noticed in many experiments that there are always carbon impurities in a tungsten surface (Stern 1964, Taylor 1964, Estrup and Anderson 1968). The carbon is not removed from the surface by heating since carbon diffuses out from the body of the sample. The carbon can be oxidised and removed, however, by heating in oxygen. Vance (1967) confirmed this by studying the impact of helium and neon metastable atoms on a tungsten surface which was cleaned by flashing at 2300K for 15s before heating at 1700K for thirty minutes in an oxygen atmosphere of 10^{-4} torr. The sensitivity increased after heating in oxygen, indicating the reduction of carbon at the surface.

Varney (1968) compared three surfaces, atomically clean tungsten, oxidised tungsten, and tungsten coated with barium carbonate which was then reduced to barium oxide by heating. He found the work functions of pure tungsten and oxidised tungsten to be 4.3eV and 6.6eV respectively and proposed that the effect of impurities on the surface is to increase the work function. He also demonstrated that the barium oxide surface had a low work function, 1.6eV.

The effect of contamination of the surface with contaminants other than air has also been studied. These results are summarised in table 2.2

Table 2.2 Effect of surface impurities on the secondary electron yield from the detector surface.

Surface	Adsorbates	Species Detected	Effect on Electron Yield	Reference
Tungsten	H_2, N_2, CO	He^+, Ne^+, Xe^+	decrease	Hagstrum (1956)
		He^*, Ne^*	decrease	MacLennan (1966)
	air	He^*	increase	Dunning et al (1971)
Tungsten (110,111)	N_2	He^*	no change	Delchar et al (1969)
Tungsten (100)	N_2	He^*	decrease	Delchar et al (1969)
Molybdenum (110)	O_2, CO	He^*, Ne^*, Ar^*	decrease	Boiziau et al (1976)
Nickel (100)	O_2, S	He^*	increase	Johnson and Delchar (1978)

2.3.4 Determination of Secondary Emission Coefficient

Following such investigations of the effect of surface impurities on the sensitivity of the metal surface, it became necessary to quantify the response by measuring the secondary emission coefficient, or electron yield, which is defined as the number of secondary electrons emitted for each incident metastable atom or molecule. It is unique for a given metastable state incident on a particular surface, but depends on the degree of contamination of the surface. Table 2.3 gives a summary of the secondary emission coefficients for metastable states of the noble gases incident upon a range of detector surfaces and demonstrates that secondary electron yield varies considerably in different experiments.

Table 2.3 Secondary electron emission coefficients for metastable rare gas atoms on atomically clean and adsorbate covered surfaces.

Detector Surface	He(2^3S)	He(2^1S)	He(2^1S) + He(2^3S)	Ne($^3P_{0.2}$)	Ar($^3P_{0.2}$)
Platinum, chemically clean	0.26 ± 0.03[7] 0.24 ± 0.04[1]				
Platinum, gas covered	0.26 ± 0.03[7]	0.48 ± 0.08[1]		0.12 ± 0.02[1]	
Tungsten, atomically clean	0.32 ± 0.03[9] 0.14 ± 0.02[8]		0.31 ± 0.03[9] 0.28 ± 0.06[3]	0.22 ± 0.02[9] 0.20 ± 0.04[3]	0.08 ± 0.02[9]
Tungsten, chemically clean			0.30 ± 0.06[4] (He$^+$ 0.29[6])	0.21 ± 0.04[4] (Ne$^+$ 0.213[6])	0.09 ± 0.02[4] (Ar$^+$ 0.095[6])
Tungsten, gas covered	0.17 ± 0.02[7]				
Molybdenum, chemically clean	0.11 ± 0.02[7]				
Molybdenum, gas covered	0.19 ± 0.02[7]				
Gold, chemically clean	0.29 ± 0.03[10] 0.63 ± 0.07[3] 0.67 ± 0.10[2]	0.46 ± 0.09[3] 0.49 ± 0.09[2]	0.56 ± 0.06[3] 0.57 ± 0.06[3]	0.52 ± 0.06[3]	0.66 ± 0.10[3]
St. steel, chemically clean	0.67 ± 0.08[5] 0.70 ± 0.08[5] 0.70 ± 0.11[5]	0.52 ± 0.07[5] 0.57 ± 0.07[5] 0.51 ± 0.08[5]	0.92 ± 0.11[3] 0.98 ± 0.10[4]	0.92 ± 0.11[3] 0.65 ± 0.08[5] 0.56 ± 0.06[5] 0.63 ± 0.10[5]	0.97 ± 0.15[3] 1.00 ± 0.12[4]
Copper, chemically clean			0.93 ± 0.11[3]		0.85 ± 0.11[3]
Copper-Beryllium	0.63[5]	0.51[5]		0.44[5]	
Cadmium	0.40 ± 0.06[4]	0.39 ± 0.06[4]	0.40 ± 0.06[4] 0.35 ± 0.06[4] 0.36 ± 0.07[3]	0.22 ± 0.06[4]	0.32 ± 0.03[4] 0.32 ± 0.04[4] 0.33 ± 0.05[4] 0.33 ± 0.05[3]
Sodium					0.14 ± 0.06[4]

References for table 2.3

1. Dorrestein (1942)
2. Dunning and Smith (1970b)
3. Dunning and Smith (1971)
4. Dunning et al (1971)
5. Dunning et al (1975a)
6. Hagstrum (1954,1956)
7. Hasted (1959)
8. Hasted and Mahadevan (1959)
9. MacLennan (1966)
10. Stebbings (1957)

Two methods have been used in the determination of secondary electron coefficients, (a) depletion of the metastable beam by Penning ionisation and (b) by photoionisation.

a) Metastable Flux determined by Penning Ionisation

Stebbings (1957) measured the secondary electron yield from a gold surface. The apparatus used by Stebbings is shown schematically in figure 2.7. A metastable atomic beam, He^*, originating from the source, S, was directed through chamber C before impinging on the surface detector, W. The current due to the secondary electrons from the surface was measured.

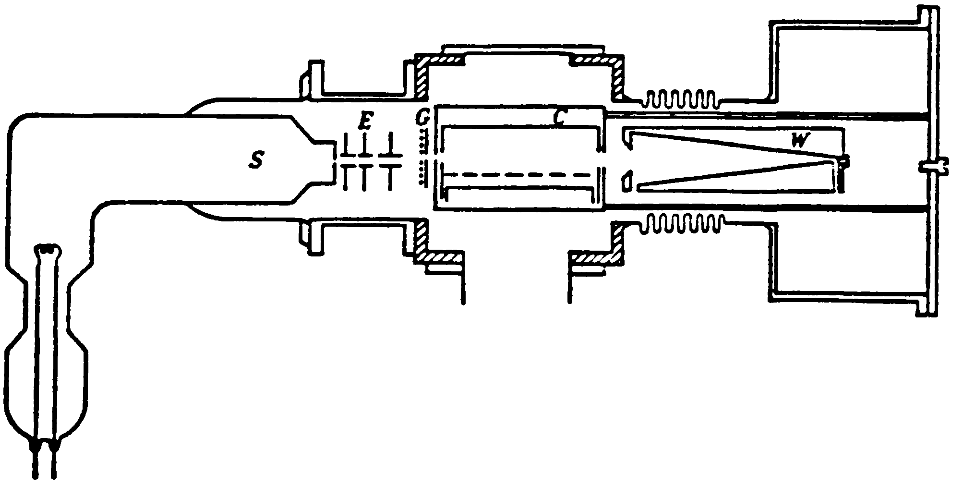

Figure 2.7 Schematic diagram of the experimental arrangement used by Stebbings (1957) to determine the secondary electron yield from a gold surface. S is the source of metastable atoms, the electrodes, E, and a grid, G, prevent unwanted charged particles reaching the collision chamber, C. The surface detector is W.

When the collision chamber was evacuated, the metastable helium beam was allowed to impinge on the detector. This resulted in a current, I_1, due to N_1 metastable atoms incident on the surface per second. Thus the current is given by

$$I_1 = \gamma\, e\, N_1$$

where γ is the secondary electron yield, and e the charge on an electron.

Stebbings then let argon into the chamber C. Argon was chosen since the ionisation potential of argon is less than the excitation energy of metastable states of helium. The argon atoms are therefore Penning ionised by the metastable helium atoms,

$$He^{*} + Ar \rightarrow He + Ar^{+} + e^{-}$$

The effect is to remove metastable helium atoms from the beam, reducing the number incident on the gold surface and the current from the surface. The new current is given by

$$I_2 = \gamma\, e\, N_2$$

where N_2 is the new metastable flux.

The argon ions produced by Penning ionisation were collected, the current due to these ions, I_3, is given by

$$I_3 = e\,(N_1 - N_2)$$

Combining these expressions for the three measured currents gives the secondary electron yield,

$$\gamma = \frac{(I_1 - I_2)}{I_3}$$

The assumption made in this analysis is that the reduction in metastable flux is due entirely to Penning ionisation. Elastic scattering of the metastable helium atoms by the argon atoms must also be taken into account. For example, Dunning and Smith (1970a) used a similar method to Stebbings' and made measurements of the electron yield for helium metastable atoms incident on a gold surface but including elastic scattering in the analysis. The secondary electron yields measured by Dunning and Smith were higher than those of Stebbings.

The result of Stebbings was used extensively as a standard in other experiments (e.g. Schultz and Fox 1956, Hasted 1959 and Sholette and Muschlitz 1962). However such a use of this result is not strictly valid since the sensitivity of the surface depends on its cleanliness and the impurities adsorbed onto the surface which are different for each experimental arrangement and may change during the course of an experiment.

These studies were extended using both a gas cell (Dunning and Smith 1970b, 1971) and crossed beams (Dunning et al 1971) to the determination of electron yields from chemically clean stainless steel and copper and for atomically clean cadmium and tungsten. The cadmium surface was formed by the continuous deposition of cadmium from an oven onto a rotating wheel (Dunning 1972) thus producing an uncontaminated surface.

Hasted (1959) measured the secondary electron yield for atomically clean tungsten, molybdenum and platinum surfaces. Although the surface was cleaned by flashing, the vacuum conditions were not good enough to maintain a chemically clean surface. Hasted assumed that gas was adsorbed onto the surface to form a monolayer and extrapolated his results to zero time after flashing to obtain results for an atomically clean surface. This procedure is not valid since the formation of a monolayer is not correct (MacLennan 1966) and Hasted normalised his results by reference to Stebbings' result for a chemically clean gold surface. Hasted's results have therefore been included in table 2.3 as gas covered surfaces.

MacLennan (1966) also used Penning ionisation to determine the absolute metastable flux. He studied the action of helium and neon metastable atoms on a tungsten surface. Unlike the gold surface used by Stebbings, MacLennan maintained a high state of cleanliness of the tungsten surface by frequent flashing. MacLennan's results for secondary electron yields for metastable helium and neon atoms incident on a tungsten surface agree well with those of Dunning and Smith (1971).

The method used by Dunning and Smith (1970a) was extended by Dunning et al (1975a) to determine secondary electron coefficients for metastable helium and neon atoms incident on a stainless steel surface. The apparatus is shown schematically in figure 2.8. The determination of the metastable flux and hence the secondary electron emission coefficient is in principle the same as in the work of Stebbings.

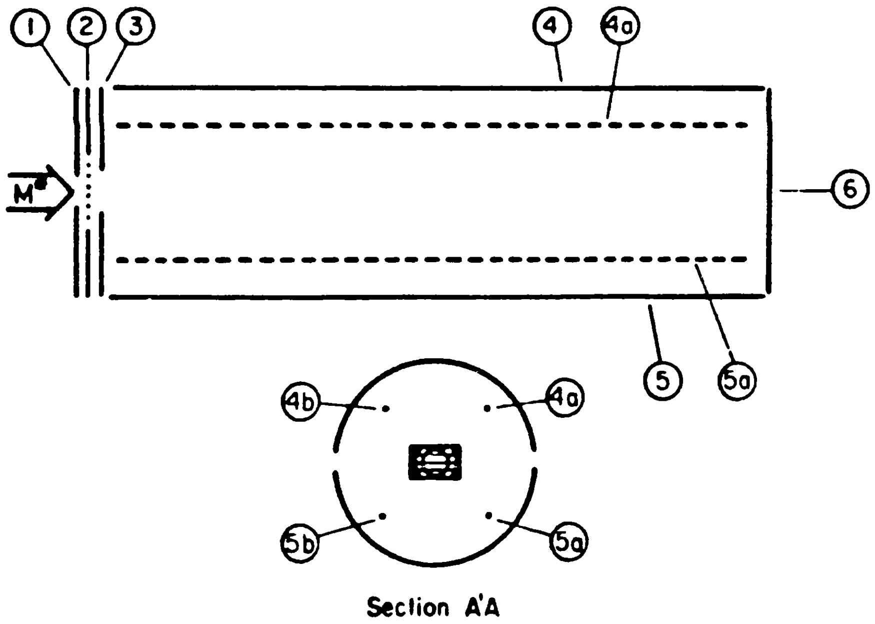

Figure 2.8 Schematic diagram of the experimental arrangement used by Dunning et al (1975a) for depletion of the metastable beam by Penning ionisation. The metastable beam passes through a collimating plate, (1), a monitor grid (2) and the front plate (3). (4) and (5) are half cylinders on which ions are collected following Penning ionisation. Ions are also collected on the grid wires (4a), (4b), (5a) and (5b).

Dunning et al (1975a) showed that the secondary electron coefficient determined by Penning ionisation depends also on the gas used in the cell. The secondary electron coefficients in table 2.3 were obtained using argon in the gas cell. Table 2.4 shows the range of values of the electron yield for different gases in the cell.

Table 2.4 Dependence of the measured secondary electron coefficient on the target gas used in Penning ionisation (Dunning et al 1975a).

Target	He(2^1S)	He(2^3S)	Ne($^3P_{0.2}$)	Ar($^3P_{0,2}$)
Ar	0.57	0.70	0.56	
Kr	0.55	0.65		
NO	0.55	0.60	0.67	0.79
CO_2	0.57	0.59		
O_2	0.67	0.75		
N_2	0.57	0.70		
H_2	0.51	0.57		
CO	0.65	0.76		
C_2H_2	0.65	0.61	0.37	
C_2H_6			0.99	
NH_3			0.51	
H_2S			0.56	
C_4H_6			0.77	1.4
NO_2				1.4

The secondary electron yields for metastable helium atoms lie within a range of 20%, while those for metastable neon, argon and krypton atoms show a much larger range. Dunning et al attributed this large range to processes other than Penning ionisation contributing to the reduction in metastable flux. Gases are adsorbed onto the detector surface by the formation of a covalent bond in which electrons are shared between the adsorbate and the atoms in the metal lattice (Delchar et al 1969). Some of these adsorbates are Penning ionised by incident metastable states. Metastable helium atoms of excitation energy 19.6eV are capable of Penning ionising essentially all the adsorbates while metastable neon, argon and krypton atoms of excitation energies 16.6eV, 11.6eV and 10eV respectively ionise fewer of the adsorbates.

b) Determination of Metastable Flux by Photoionisation

Dunning et al (1975a) proposed an alternative method of depleting the metastable flux by use of a laser. The experimental arrangement is shown in figure 2.9. The metastable beam is directed onto a metal surface and causes secondary electron emission from that surface, the secondary electrons produced are accelerated and detected at a particle multiplier. When a laser beam intersects the metastable beam, a fraction of the metastable atoms are photoionised and the photoions are accelerated and detected at another particle multiplier. The determination of the metastable flux is in principle the same as Stebbings'.

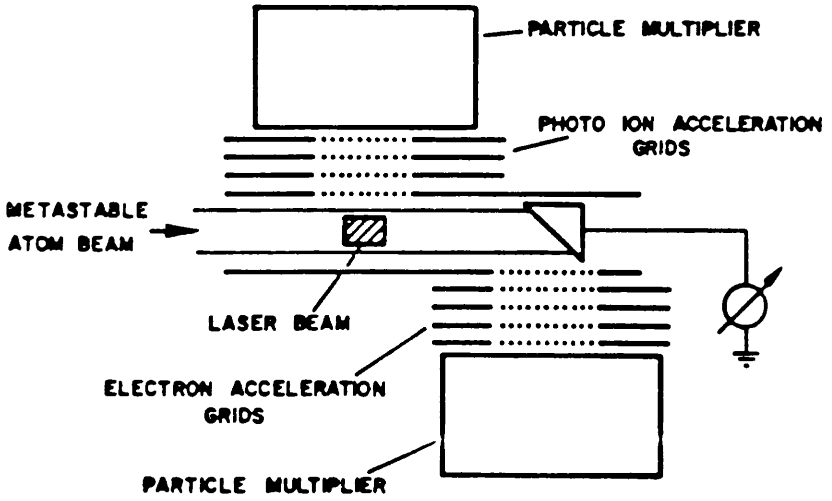

Figure 2.9 Schematic diagram of the experimental arrangement used by Dunning et al (1975a) for depletion of the metastable beam by photoionisation.

The results obtained by Dunning et al by this method were for helium and xenon metastable atoms incident on a gas covered stainless steel surface,

He (2^3S)	$y = 0.6 \pm 0.3$
Xe ($^3P_0$)	$y = 0.02 \pm 0.01$

The large error is due to a combination of low photoionisation cross sections and the difficulty in obtaining a laser of sufficient power. The cw lasers available were not of sufficient intensity to ionise sufficient metastable atoms to give a measurable change in current. Dunning et al therefore used a pulsed laser of 4ns pulse length and 100kW peak power which necessitated gating the measurement of the currents. This resulted in 10% ionisation and an error of 50% in the measurement of the difference in electron current measured with and without the laser.

Dunning et al also investigated the variation of the secondary emission coefficient with gas contamination of the surface by positioning other surfaces in the metastable beam and using the original surface as a reference. They found that while the emission coefficient varied by $<15\%$ for metastable helium atoms, variations of $\sim 300\%$ were found for metastable xenon atoms.

In a second experiment, Dunning et al (1975b) used a tunable dye laser to deplete the chosen metastable state. The wavelength of the laser was chosen so as to excite either the $^3P_0$ or the $^3P_2$ state of the rare gas atoms to a more highly excited state which decays by electric dipole radiation to a state other than the original metastable state. Thus the selected metastable state in the beam is depopulated, resulting in a reduction of the current due to secondary electron emission at the surface. By this method, Dunning et al determined the composition of the metastable beam for a range of incident electron energies, and found that the secondary electron yield for Ne($^3P_2$) was equal to that for Ne($^3P_0$).

Depletion of the metastable flux by photoionisation has been used recently in the experiments by Schohl et al (1991) to determine the secondary electron yield for metastable states of the rare gases on several metal surfaces. The experimental arrangement is shown in figure 2.10. The method is similar to the crossed beam method of Dunning et al (1971). Photoionisation of the metastable atoms causes a reduction in the current at the metastable detector, ΔI_s. The photoelectron current, ΔI_p, is also measured. The secondary electron emission is given by

$$\gamma = \frac{\Delta I_s}{\Delta I_p}$$

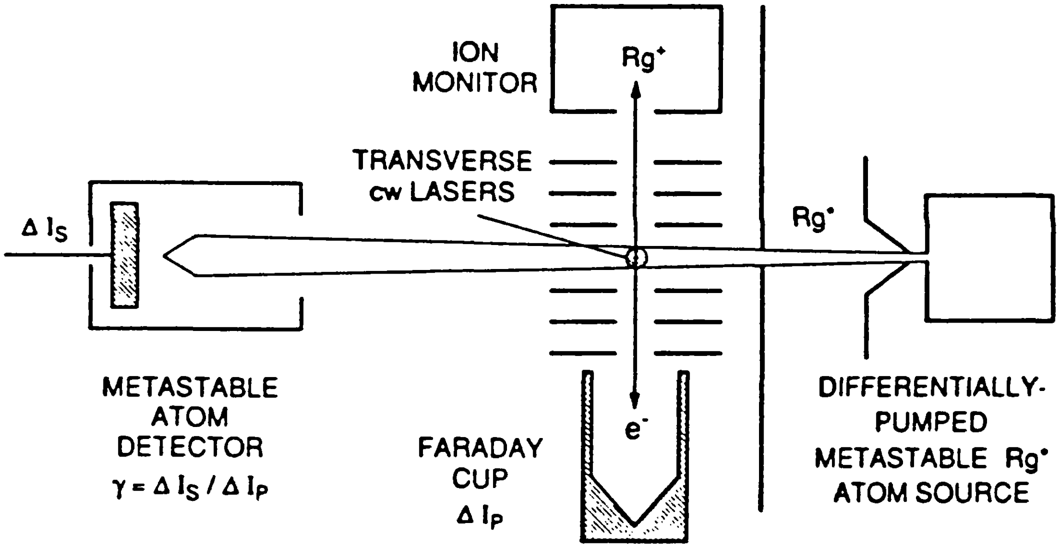

Figure 2.10 Schematic diagram of the experimental arrangement used by Schohl et al (1991) for depletion of the metastable beam by photoionisation.

The ionisation was achieved in a two step process. The metastable beam consists of two species, $^3P_0$ and $^3P_2$, the laser is tuned to excite the $^3P_2$ state to the higher lying $^3D_3$ state.

Laser excitation results in approximately 50% of the atoms present populating each state. The $^3D_3$ state is then photoionised. Since the only route by which the $^3D_3$ state may decay is by radiative decay back to the $^3P_2$ state, the only mechanism for depletion of the $^3P_2$ state is by this two step photoionisation. The photoelectron current therefore represents the number of $^3P_2$ metastable atoms ionised and the reduction in current at the metastable detector represents the number of secondary electrons which would have been ejected had these metastable atoms survived to reach the detector.

The main advantage of the experiment of Schohl et al over that of Dunning et al is that a cw laser was used, eliminating the need to make time resolved measurements. The cw laser used was capable of causing 15% photoionisation. The currents measured by Schohl et al were measured in Faraday cups with 100% efficiency while the particle multipliers used by Dunning et al were difficult to calibrate accurately. The results obtained by Schohl et al are summarised in table 2.5.

Table 2.5 Secondary electron emission coefficients for metastable rare gas atoms on metal surfaces (Schohl et al 1991).

Surface	Ne($^3P_2$)	Ar($^3P_2$)	Xe($^3P_2$)
Polished stainless steel	0.30	0.04 - 0.22	0.01 - 0.05
Polished Cu-Be alloy	0.40	0.06 - 0.25	
Graphite sprayed onto stainless steel	0.35	0.10 - 0.22	0.01 - 0.10
Gold deposited onto stainless steel		0.007 - 0.044	0.003 - 0.008
Molybdenum deposited onto stainless steel		0.02	0.006

In addition, Schohl et al studied the time dependence of the secondary electron yield and found that, in general, there was a decrease in efficiency with time. The exception was the gold surface which showed a slight increase in sensitivity over time. The coefficients determined for the surface at 300K and at 360K showed that heating increased the secondary electron yield and reduced the dependence on the surface material.

2.3.5 Borst's Universal Curve

Borst (1971) proposed a universal curve which related the excitation energy of the metastable species incident on the surface to the secondary electron emission from the surface, figure 2.11 and table 2.6. The points plotted by Borst on this curve were derived from two sources, his own time of flight measurements for $CO(a^3\pi)$, $N_2(A^3\Sigma^+{}_u)$, $N_2(a^1\pi_g)$ and $He(2^3S)$ incident on a Cu-Be-O dynode and the results of Hagstrum (1956) for neon, argon, krypton and xenon ions incident on a tungsten surface.

Borst related the count rate at the detector to several experimental parameters; the electron beam current, the number density in the gas source and the angle subtended by the detector. The count rate is also related to the secondary emission coefficient and the cross section for direct electron impact excitation. From known cross sections, Borst was therefore able to determine the secondary electron yield from the detector.

The secondary electron yields for metastable neon, argon, krypton and xenon atoms were deduced from Hagstrum's results by extrapolating to thermal kinetic energies and equating the secondary electron yield for ions with that of metastable species. This assumes that the electron yield from a Cu-Be-O surface is the same as that from a tungsten surface and that the electron yield for ions is the same as that for metastable states of the same species.

Table 2.6 Secondary electron coefficients determined by Borst (1971).

Metastable Species	Excitation Energy /eV	Electron Yield
$CO(a^3\pi)$	6.2	6.0×10^{-5} (v=1)
$N_2(A^3\Sigma^+_u)$	7.5	1.2×10^{-5} (v=8)
$N_2(a^1\pi_g)$	9.15	9.0×10^{-3} (v=3)
$He(2^3S)$	19.86	0.15
Ne^*	16.5	0.12
Ar^*	11.4	3.5×10^{-2}
Kr^*	10.0	2.0×10^{-2}
Xe^*	8.4	5.0×10^{-3}

Borst's justification of this method was that the yield for $He(2^3S)$ atoms incident on Cu-Be-O was found to be 0.15, in agreement with the value of 0.17 obtained by MacLennan (1966) for $He(2^3S)$ incident on a nitrogen covered tungsten surface. It also agreed with the electron yield measured by Hagstrum (1956) for helium ions incident on a nitrogen covered tungsten surface. Plotting these results Borst found that the electron yield is independent of the gas species and depends only on the excitation energy.

However, Borst has been over simplistic in his analysis. As discussed above, equating of the secondary electron yields for ions and metastable atoms is valid only for an atomically clean surface since adsorbates on the surface modify the emission mechanism and ions and metastable species no longer behave in the same way

(Delchar et al 1969). The secondary electron yield for carbon monoxide may be inaccurate since Borst used the cross section of Ajello (1970) which has subsequently been shown to be in error (Wells et al 1972).

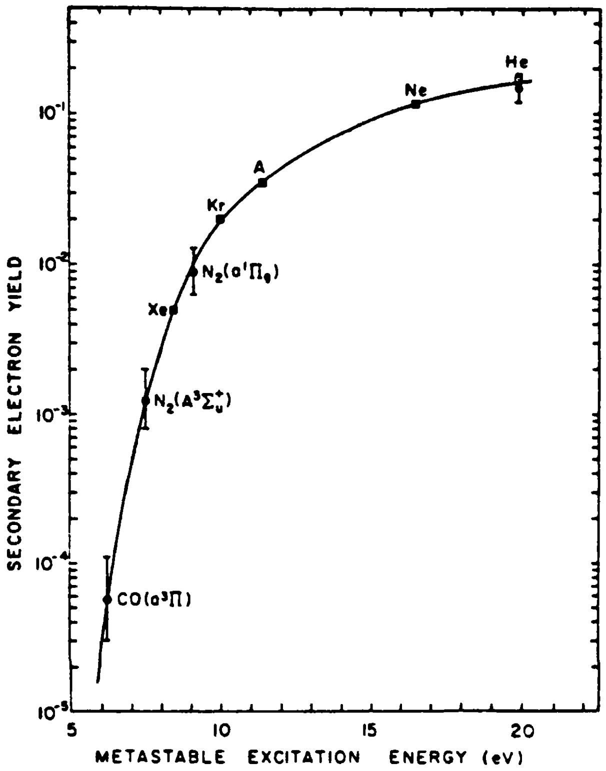

Figure 2.11 Borst's Universal Curve relating secondary electron coefficient to the excitation energy of the metastable state or ion incident on a particular surface.

However, although this a curve should not be used as a means of calibration of a surface, the trend of increasing secondary electron yield with increasing excitation energy is certainly valid and has been clearly demonstrated by the results of Dunning and Smith (1970b, 1971), Dunning et al (1971, 1975a) and Schohl et al (1991).

2.3.6 Energy Distribution of the Secondary Electrons

Oliphant (1929) investigated the energy distribution of the electrons emitted from a molybdenum target as metastable helium atoms were incident upon it by varying the retarding potential between the target and the electron collector. He determined that the maximum energy with which an electron is ejected corresponds to the incident metastable atom losing all its potential energy to that electron. The electron is emitted with a kinetic energy e_{kin},

$$e_{kin} = E_{pe} - \phi$$

where E_{pe} is the potential energy of the metastable atom and ϕ is the work function of the surface.

Allison et al (1972) investigated the energy distribution and the angular distribution of the emitted electrons. The energy distribution agreed qualitatively with that of Oliphant. The angular distribution was found to be strongly forward peaked. This was explained in terms of the roughness of the surface; if the surface is considered to be composed of small spheres, and the possible direction of emission of the electron is summed, the most probable direction is that normal to the surface. The angular distribution of the emitted electrons was also found to be independent of the angle of incidence of the metastable atoms.

2.3.7 Summary

Ever more sophisticated methods of determination of the secondary electron yield from surfaces are being developed. However it should be remembered that there can be no universal standards for such quantities. The only truly reproducible surface is an atomically clean surface, but such a surface is neither readily achievable or desirable. It has been shown that even heating to just below the melting point will not remove some impurities such as carbon which diffuse out of the bulk of the material (Rundel and Stebbings 1972). An atomically clean surface is not necessarily the most efficient at detecting metastable species as the impurities on the surface can enhance the secondary electron yield, possibly by Penning ionisation of the impuri ties by the incident metastable atom (Dunning et al 1971). Heating the surface generally results in an increase of the sensitivity (Schohl et al 1991, chapter five).

Any accurate determination of the electron yield needs an accurate determination of the metastable flux incident on the surface and an absolute measurement of the electron yield from the surface. The method using Penning ionisation to deplete the metastable beam (Dunning and Smith 1970) is a reliable method of determining the metastable flux when the metastable atoms used are helium or neon atoms. Argon, xenon and krypton atoms produce ions by associative ionisation in addition to Penning ionisation. The secondary electron yield will be different depending on the gas used in the gas cell since these molecules will form part of the adsorbate layer on the surface. Those methods which use lasers to deplete the metastable beam are advantageous as they selectively deplete one of the components in the beam.

Even when the secondary electron yield has been accurately determined, it remains applicable only to that surface, contaminated with those particular adsorbates and for the specific metastable species incident upon it.

Nevertheless, secondary electron emission has been widely used as an efficient method of metastable detection when absolute measurements are not required and has been used in this work to detect the metastable products of electron impact dissociative excitation (chapters six and seven).

2.4 State Selective Detection Techniques

2.4.1 Introduction

In this section the detection of metastable species by photoionisation, photoexcitation and by specific excimer reactions will be reviewed. The advantage of these methods over those discussed above is that each method may be used to detect a specific metastable state of an atom or molecule.

Weissmann et al (1984) developed a method of state selection of a particular metastable state from a mixed metastable beam by intracavity excitation of the required metastable state in a cw laser. The components of the metastable beam were investigated by observing the Penning ionisation of a suitable gas. They were able to demonstrate that this method was capable of producing a state selected beam and to determine the proportion of each state in the beam.

Metastable species may also be detected by photoexcitation and ionisation. The wavelength of a dye laser is tuned to that required to depopulate one of the metastable states in the beam, either by photoionising the atom or molecule or by exciting it to a higher lying, short lived state. The fluorescence produced as this state relaxes is then detected.

It is also possible to detect metastable species by fluorescence from a surface. This relies on an excimer reaction occurring between the metastable atom or molecule and the surface upon which it is incident. Such reactions have been observed for metastable benzene on anthracene (Ohshima et al 1985), $N_2(A^3\Sigma^+{}_u)$ on biacetyl (Kume et al 1986a), $N_2(a^1\pi_g)$ on anthracene (Kume et al 1986b) and $O(^1S)$ on solid xenon (Kiefl et al 1983).

2.4.2 Detection by Laser Pumping

Phillips et al (1985) measured the production cross sections for the electron impact excitation of the metastable Ne($^3P_{0,2}$) states. The metastable neon atoms were irradiated by a dye laser tuned to the wavelength required to promote one of the components to a higher lying state, Ne($^3D_3$). The fluorescence emitted as this state decayed was detected by a cooled photomultiplier. If atoms in the higher lying state decayed back to the original metastable state they were pumped back up to the higher state. The intensity and bandwidth of the laser were sufficient to promote all metastable atoms to this higher lying state.

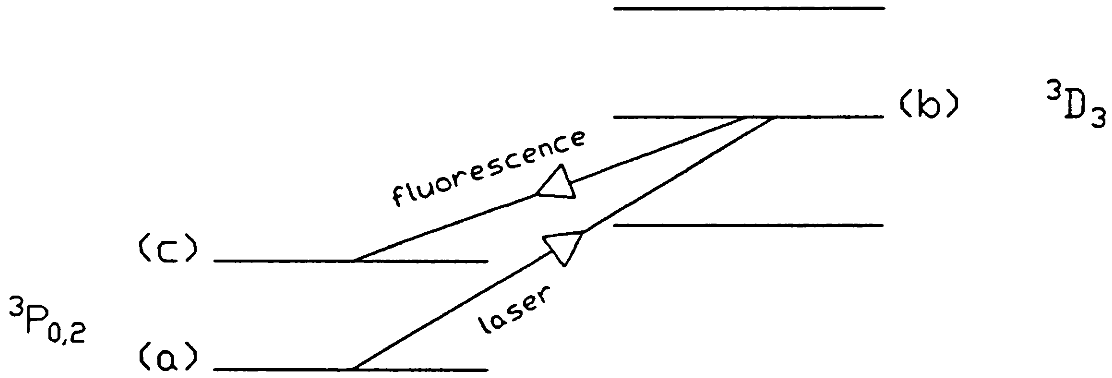

Figure 2.12 Diagram of the transitions in neon involved in the work of Phillips et al (1985).

Let the original metastable state be state (a), the higher lying level be state (b) and the level into which state (b) decays be state (c), figure 2.12. The metastable neon atoms are produced by electron impact at a rate which is related to the cross section for electron impact excitation. The laser promotes all the required metastable atoms to state (b) if the transition (a → b) is much faster than the metastable decay rate. Then the rate of production of metastable atoms is equal to the rate of population of state (b) by photoabsorption and so must be proportional to the rate of fluorescence of the (b → c) transition.

Phillips et al then set up rate equations for the rate of population of state (a) by electron impact and state (b) by laser action and solved these to determine the production cross section of state (a). The total cross sections for production of metastable neon atoms determined by Phillips et al (1981a,b) are compared with those of Teubner et al (1985) and Mason and Newell (1987), figure 2.13.

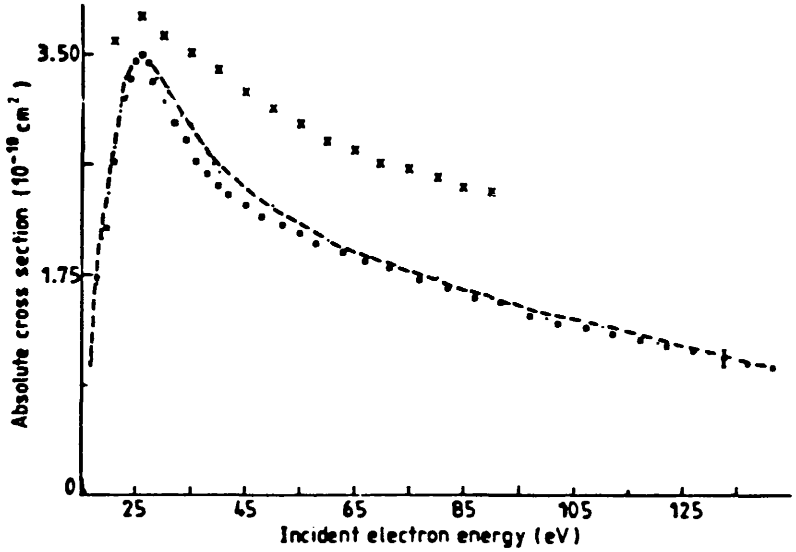

Figure 2.13 Total cross sections for electron impact excitation of metastable states of neon, x x x Phillips et al (1981a,b), - - - Teubner et al (1985) and ▪ ▪ ▪ Mason and Newell (1987).

Teubner et al determined the relative cross sections for production of metastable neon atoms by translational spectroscopy. These were then normalised by comparison with the relative cross section for excitation of helium since the absolute cross section for helium is well established (Bransden and McDowell 1978, de Heer and Jansen 1977). They assumed that the secondary electron yield from the detector surface was that determined by Dunning et al (1975a). Mason and Newell (1987) also used translational spectroscopy to determine the cross section detected metastable atoms with a channel electron multiplier. They normalised their data to that of Teubner et al (1985) at an incident electron energy of 26eV. The cross sections determined by Teubner et al and by Mason and Newell by translational spectroscopy agree well in the position of the peak with the cross section determined by Phillips et al. The magnitude of the cross sections determined by Teubner et al is also in good agreement but falls off more rapidly than that of Phillips et al.

2.4.3 Detection by Excimer Reaction

Detection of metastable species by the observation of fluorescence as the metastable species forms an excimer with the surface is limited by the number of metastable states of interest which form such excimers. Kume et al (1986a) detected $N_2(A^3\Sigma^+{}_u)$ on a biacetyl surface cooled to 77K. It had been noticed that in a mixture of $N_2(A^3\Sigma^+{}_u)$ and gaseous biacetyl the energy of the $N_2(A^3\Sigma^+{}_u)$ state was transferred to the biacetyl and phosphorescence was observed (Stedman et al 1968). Thus it was expected that phosphorescence would occur in the reaction between gaseous $N_2(A^3\Sigma^+{}_u)$ and solid biacetyl.

The beam of ground state nitrogen molecules was produced in a supersonic gas source before being excited by electron impact. The biacetyl surface was prepared by allowing biacetyl to effuse through a multichannel slit onto a copper block cooled to 77K.

The emission of wavelength 500nm to 600nm from the biacetyl surface produced by collision of the metastable nitrogen molecule was detected by a photomultiplier. No emission was observed when the incident electron energy was below 6eV, i.e. below the production threshold for $N_2(A^3\Sigma^+{}_u)$.

When the $N_2(A^3\Sigma^+{}_u)$ molecules collide with the biacetyl surface, the energy of the $N_2(A^3\Sigma^+{}_u)$ molecule is transferred to one of the biacetyl molecules on the surface. The emission spectrum observed by Kume et al consists only of phosphorescence bands in the region 500 - 600nm. The fluorescence band at ≤460nm was not observed when metastable $N_2(A^3\Sigma^+{}_u)$ was allowed to impinge on the surface, but was observed when the surface was irradiated by the laser. From this fact, Kume et al deduced that the biacetyl molecule is excited directly to a triplet state in the collision with $N_2(A^3\Sigma^+{}_u)$. The triplet state to which the biacetyl is excited was proposed as a vibrational level of the $N_2(B^3\Pi_u)$ state which cascades to the $N_2(A^3\Sigma^+{}_u)$ state with the emission of the phosphorescence observed.

Another triplet state of molecular nitrogen capable of producing such phosphorescence is $N_2(E^3\Sigma^+{}_g)$, but lifetime and cross section determinations indicate that the concentration of this state at the surface would be 10^{-3} that of the $N_2(A^3\Sigma^+{}_u)$ state. $N_2(a^1\pi_g)$ was also estimated to be a minor part of the metastable beam, 10^{-2} the concentration of the $N_2(A^3\Sigma^+{}_u)$ state, but its contribution to phosphorescence will be negligible since energy transfer from a singlet to a triplet state is spin forbidden.

The efficiency of phosphorescence detection, γ_D, is the ratio of the number of $N_2(A^3\Sigma^+{}_u)$ molecules incident on the surface to the number of photons emitted from the surface.

The count rate of phosphorescence, I_P, is given by

$$I_P = \gamma_D \, N_A \, \frac{\Omega_1}{4\pi}$$

where N_A is the number of metastable molecules colliding with the surface per unit time and Ω_1 is the solid angle subtended by the biacetyl surface.

The biacetyl surface was removed and the transition $N_2(C^3\Pi_u)$ - $N_2(B^3\Pi_g)$ was observed by measuring the fluorescence as the $N_2(C^3\Pi_u)$ molecules cascade promptly to the $N_2(B^3\Pi_g)$ state (Lofthus and Krupenie 1977). Then, the number of $N_2(C^3\Pi_u)$ molecules produced in the excitation region per unit time, N_C, is given by

$$N_C = I_C \, \frac{4\pi}{\Omega_2} \qquad 2.1$$

where Ω_2 is the solid angle subtended by the excitation region and I_C is the intensity of the $N_2(C^3\Pi_u$ - $B^3\Pi_g)$ emission.

The phosphorescence intensities, I_P and I_C, were corrected for the different spectral response of the monochromator and the photomultiplier.

N_A and N_C are related by

$$\frac{N_A}{N_C} = \frac{\sigma_A}{\sigma_C} \qquad 2.2$$

where σ_A and σ_C are the excitation cross sections for the $N_2(A^3\Sigma^+_u)$ and $N_2(C^3\Pi_u)$ states respectively.

Combining 2.1 and 2.2 gives

$$\gamma_D = \frac{I_P\, \sigma_C\, \Omega_2}{I_C\, \sigma_A\, \Omega_1}$$

Ω_1 and Ω_2 were calculated from the known geometry of the electron impact region. σ_A was taken as the sum of the cross sections for the direct excitation to each of the five lowest triplet states, $N_2(A^3\Sigma^+_u)$, $N_2(B^3\Pi_g)$, $N_2(W^3\Delta_u)$, $N_2(B'^3\Sigma^-_u)$ and $N_2(C^3\Pi_u)$, the last four of which cascade to the $N_2(A^3\Sigma^+_u)$ state.

Kume et al estimated γ_D to be 1 x 10^{-3} at an incident electron energy of 12eV, comparable to the secondary electron yield from a typical Cu-Be-O surface as estimated by Borst (1971).

Kume et al (1986b) have also studied the fluorescence from an anthracene surface at 77K on collision of $N_2(a^1\pi_g)$ molecules. In this case, energy transfer from the singlet state of molecular nitrogen excited a singlet state of anthracene which decays to the lowest lying singlet state. No fluorescence from the anthracene surface was observed for incident electron energies less than 8.5eV, indicating that $N_2(A^3\Sigma^+_u)$ does not contribute to the fluorescence. $N_2(a'^1\Sigma^-_u)$ also contributes to the excitation of the anthracene to a singlet state. The ratio of the $N_2(a^1\pi_g)$ molecules to the $N_2(a'^1\Sigma^-_u)$ molecules in the work of Kume et al was 3:7.

Species other than molecular nitrogen have been detected by their reactions with the surface. Kiefl et al (1983) used the formation of an excimer between rare gas atoms and highly electronegative atoms to detect O(^{1}S) metastable atoms produced in the dissociation of molecular oxygen. The xenon surface was prepared by directing a continuous flow of xenon onto a liquid nitrogen cooled copper block (chapter five).

Kiefl et al observed emission from the xenon surface due to the formation of an XeO excimer on the surface,

$$O(^5S) + Xe + B \rightarrow XeO^* \rightarrow Xe + O + B + h\nu(500\text{-}600nm)$$

In this reaction, B is the third body necessary to stabilise the excimer. The fast O(^{1}S) atoms lose their energy in several elastic collisions close to the surface and form an excimer in a three body collision with loosely bound xenon atoms. The excitation energy of the O(^{1}S) atoms is transferred to the XeO molecules thus formed. These molecules are incorporated into the xenon lattice before dissociating to a xenon and an oxygen atom with the associated emission of light.

2.4.4 Detection by Analysis of Secondary Electrons from a Surface

If there is more than one metastable constituent in a beam incident on a metal surface, each will contribute to the secondary electron flux observed. It is expected that different metastable states give rise to ejected electrons of different energy distributions (Zubek 1986) and therefore electrons due to unwanted metastable states may be prevented from reaching the detector by applying electrostatic fields between the metal surface and the secondary electron detector.

This was the principle used by Zubek (1986) in the development of a state selective detector. The detector, figure 2.14, consisted of a detection surface, a retarding grid and an accelerating electrode. The detecting surfaces used were tungsten and molybdenum. The retarding grid and the accelerating electrode were made of high transmission molybdenum mesh to reduce secondary electron emission from these surfaces due to impinging metastable atoms and electrons. The secondary electrons were focused into a channel electron multiplier.

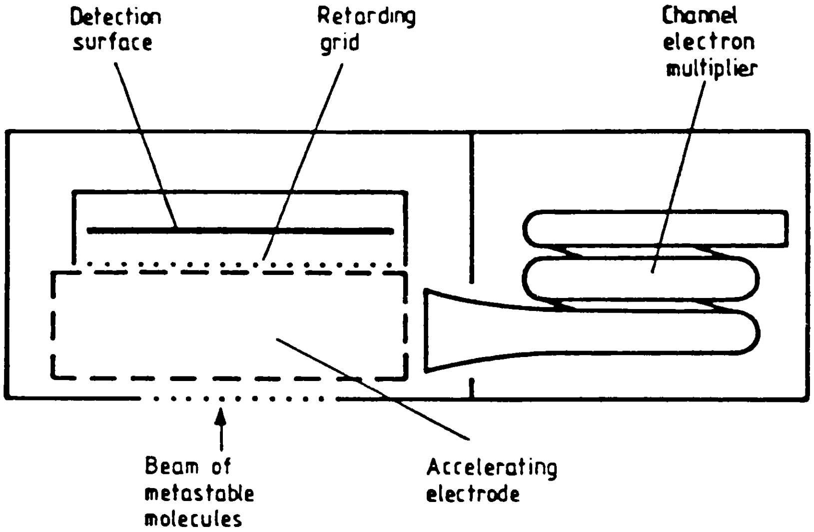

Figure 2.14 Schematic diagram of the state selective detector used by Zubek (1986).

Zubek and King (1987) used this system to detect selectively the new metastable state of mercury first proposed by Newman et al (1985). The detector surface used in this experiment was lead silicate glass heated in an atmosphere of hydrogen, as used in commercial channel electron multipliers. The work function of this surface was estimated to be 7eV. The potential applied to the retarding grid was adjusted to allow only the highest energy electrons emitted from the surface to reach the channel electron multiplier.

The background due to metastable atoms incident on the retarding grid was estimated by recording an excitation function with the detector surface biased positive with respect to the retarding grid so that no secondary electrons from the surface reach the grid. Two excitation functions were recorded to isolate the unknown metastable state of mercury. The first, with no energy analysis, was due to all metastable states of mercury with excitation energy >7eV. The second used energy analysis to allow only the highest energy electrons to reach the channel electron multiplier.

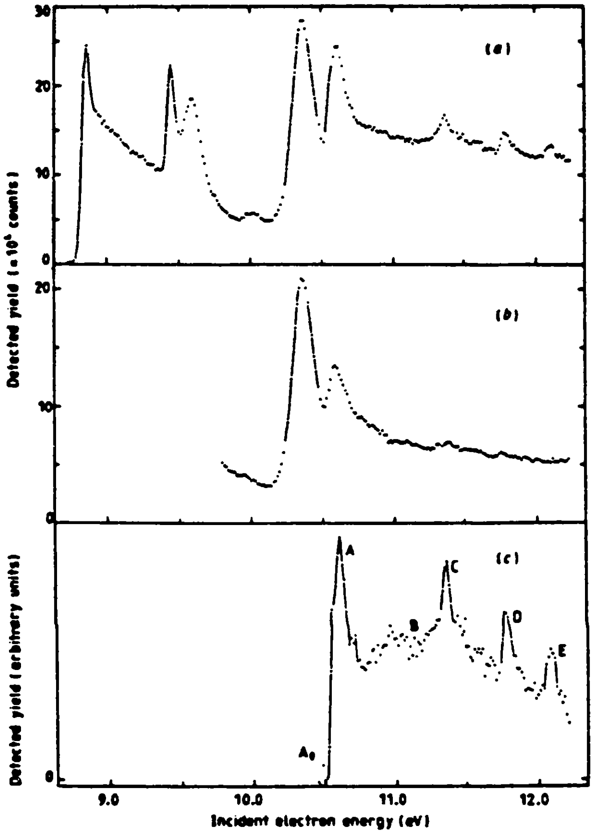

Figure 2.15 Excitation function of a new metastable state of mercury detected at a lead silicate glass surface detector (Zubek and King 1987), a) metastable excitation function with no energy analysis of the electrons ejected from the detector surface, b) metastable excitation function for Hg($^3D_3$) obtained by energy analysis of the ejected electrons and c) excitation function for the new metastable state obtained by subtracting (b) from (a).

The state corresponding to these highest energy electrons was found to be the Hg($^3D_3$) state of excitation energy 8.80eV. Subtracting the second excitation function from the first revealed the excitation function for the new state of mercury, figure

2.15. The excitation energy of this state was found to be 10.53eV. The energy of the emitted electrons is not, therefore, related simply to the excitation energy of the metastable state.

There are two mechanisms by which secondary electrons may be ejected, by Auger de-excitation and by resonance ionisation and Auger neutralisation (section 2.3.2). In the first mechanism, the maximum energy of the emitted electron was $(E_m - \phi)$ where E_m is the excitation energy of the metastable state and ϕ is the work function of the surface. In resonance ionisation and Auger neutralisation, the maximum energy of the secondary electron is $(E_i - 2\phi)$ where E_i is the ionisation potential of the metastable state. In the experiment of Zubek and King the secondary electrons due to the $Hg(^3D_3)$ state must be produced by Auger de-excitation, and those due to the new state by resonance ionisation and Auger neutralisation.

2.5 Summary

In this chapter, several methods of detection of metastable species have been discussed. Particular emphasis has been placed on the detection of metastable species by secondary electron emission from a metal surface since this method was used in the present study of dissociative excitation, chapters six and seven. Detection of metastable species by secondary electron emission from a metal surface may be applied to most metastable species, unlike the methods of selective detection described, the limitation being the development of stable detectors of sufficiently low work function. Absolute measurements cannot be made by this method since the secondary electron yield for a particular metastable state on a specific metal depends not only on the state and the metal but also on adsorbates on the surface and the vacuum conditions. However methods have been developed (Schohl et al 1991, Dunning et al 1975a) by which the secondary electron yield may be determined in situ.

Chapter Three

The Vacuum System and Electron Gun

We have three principal means: observation of nature, reflection, and experiment. Observation gathers the facts, reflection combines them, experiment verifies the result of the combination.

Denis Diderot (1753)

3.1 Introduction

In this work, the electron impact dissociation of polyatomic molecules has been investigated by studying the product metastable fragments. An electron beam was produced in an electron gun consisting of three three-element electrostatic lenses. Chromatic aberration in the central lens was used to produce a quasi-monoenergetic beam. This electron beam was crossed with the target gas beam and the collision products detected.

In this chapter, the design and operation of the electron gun are described. The vacuum systems used to evacuate the experimental chamber and the target gas line are described. To complete the description of the apparatus, the gas sources used are described in chapter four and the detectors in chapter five.

3.2 The Vacuum System

The vacuum system for these experiments is shown schematically in figure 3.1. The electron gun, gas source and detection system were mounted in an experimental stainless steel vacuum chamber. The chamber was evacuated by a single pumping stack bolted directly beneath the chamber and isolated from it by a butterfly valve.

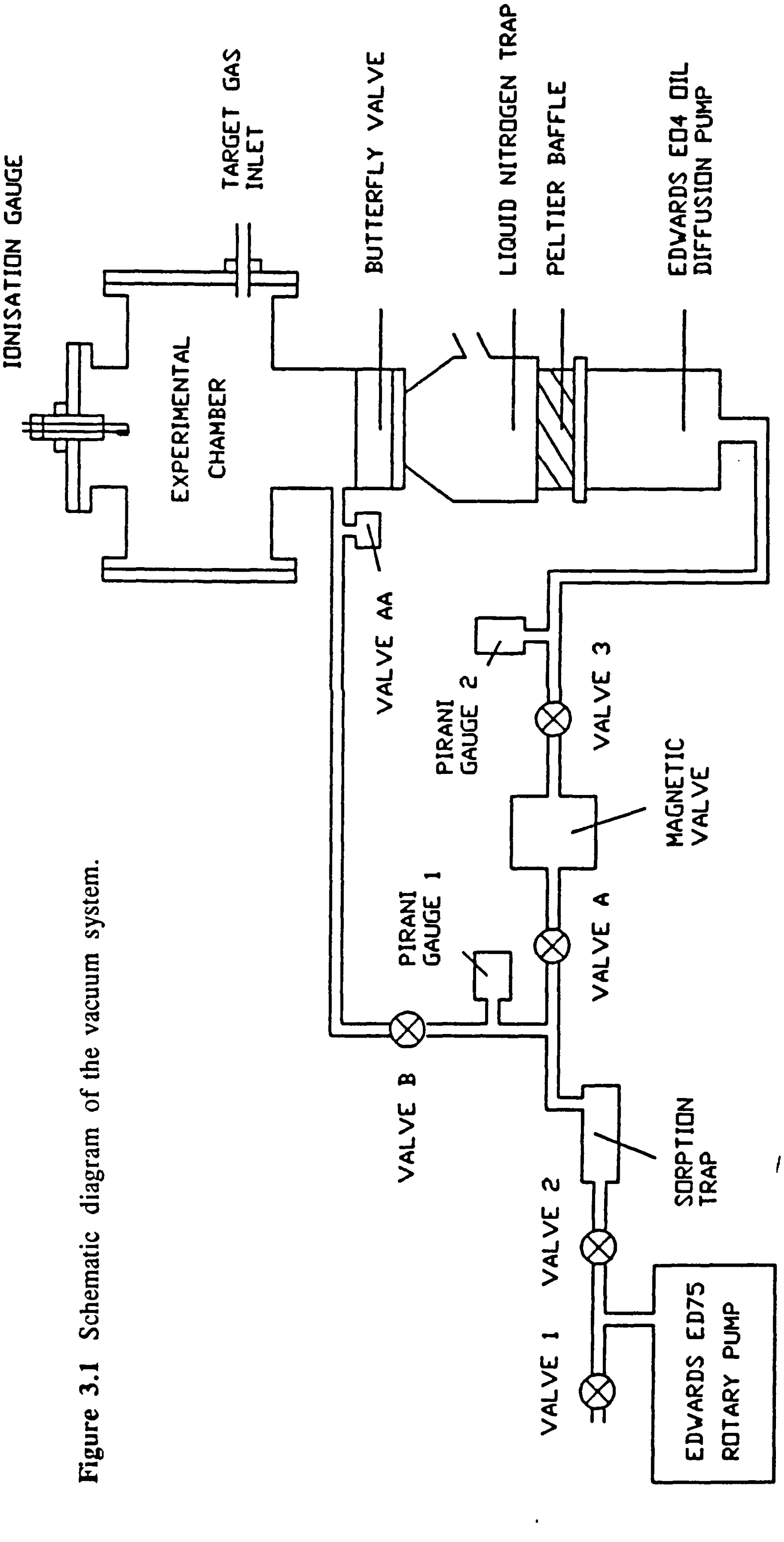

Figure 3.1 Schematic diagram of the vacuum system.

The pumping stack consisted of an Edwards EO4 water-cooled oil diffusion pump, a Peltier-cooled chevron baffle, and a liquid nitrogen trap. The baffle and liquid nitrogen trap were included to prevent uncondensed oil vapour entering the experimental chamber and degrading the electron optics.

The diffusion pump was backed by an Edwards ED75 rotary pump through a magnetic valve and a sorption trap. The sorption trap contained activated alumina to prevent rotary pump oil entering the high vacuum part of the system. The pressure in the backing line was monitored at two positions, one each side of the magnetic valve, using two Edwards 6A Pirani gauges. Typical pressures achieved in the backing line were ~0.02 torr.

The experimental chamber was evacuated initially by the rotary pump via valve B and by-passing the diffusion pump. An air admittance valve, valve AA, in the line allowed the chamber to be vented by either the introduction of air or, more usually, an inert gas.

An Edwards type IG3 ionisation gauge mounted on the top port flange of the experimental chamber was used to make high vacuum pressure measurements within the chamber. Typical base pressures obtained after one or two days pumping were 6×10^{-8}torr. A projector bulb mounted inside the chamber was used to heat the apparatus to a temperature of approximately 330K. This maintained the cleanliness of the electron optics by expelling residual gases adsorbed onto the electrostatic lenses.

The experimental apparatus was protected by a series of electrical trips. A trip incorporated into the meter of the ionisation gauge caused the gauge and all the electronics to switch off if a pressure surge in the experimental chamber resulted in a reading >1.5 times the full scale deflection. When the pressure in the backing line, monitored by the Pirani gauge on the high vacuum side of the magnetic valve, increased to >0.1 torr, a trip on this Pirani gauge then operated, causing the diffusion pump and Peltier baffle to switch off and the magnetic valve to close. The trips on the ionisation gauge, 'high vacuum', and on the backing line, 'low vacuum', could be overridden to allow the experimental chamber, pumping stack and backing line to be evacuated from atmospheric pressure. If the water supply failed, a trip in the flow meter caused the ionisation gauge, diffusion pump, Peltier baffle and the high voltage, detector and filament supplies to switch off. The magnetic valve closed simultaneously to isolate the rotary pump from the diffusion pump.

When the diffusion pump was in operation the liquid nitrogen trap was filled normally in the morning and evening. The use of some gases, which condensed onto the walls of the trap, e.g carbon dioxide, nitrous oxide and especially carbonyl sulphide, necessitated more frequent filling. In such cases, and for overnight operation, an automatic filler was used. A reservoir of liquid nitrogen was connected to the nitrogen trap through a pump and a copper pipe. Two germanium diode sensors were positioned on this pipe, one at the bottom of the trap and the other just inside the trap. When the liquid nitrogen in the trap fell below the level of the bottom sensor, the automatic filling system was activated. The filling system was deactivated when the liquid nitrogen covered the top sensor.

3.3 The Target Gas Inlet System

The target gas line is shown schematically in figure 3.2. The gas line is evacuated by an Edwards rotary pump, type ES75. The valve GV1 allows the gas line to be isolated from the rotary pump when it is necessary to purge the pump. The valve GV2 allows the rotary pump to be closed off while the gas is let into the experimental chamber during normal operation. The gases used were spectroscopic grade of ≥99.9% purity and were contained in standard lecture bottles with a gas regulator valve to control the pressure of the gas entering the gas line. The needle valve N1 allows a controlled flow of gas into the main gas line while the needle valve N2 controls the flow of gas into the experimental chamber. Since the gas line must be disconnected at N2 when the experimental chamber is opened, a diaphragm controlled on-off valve, GV3, is incorporated in the gas line to prevent the whole gas line from venting when disconnected.

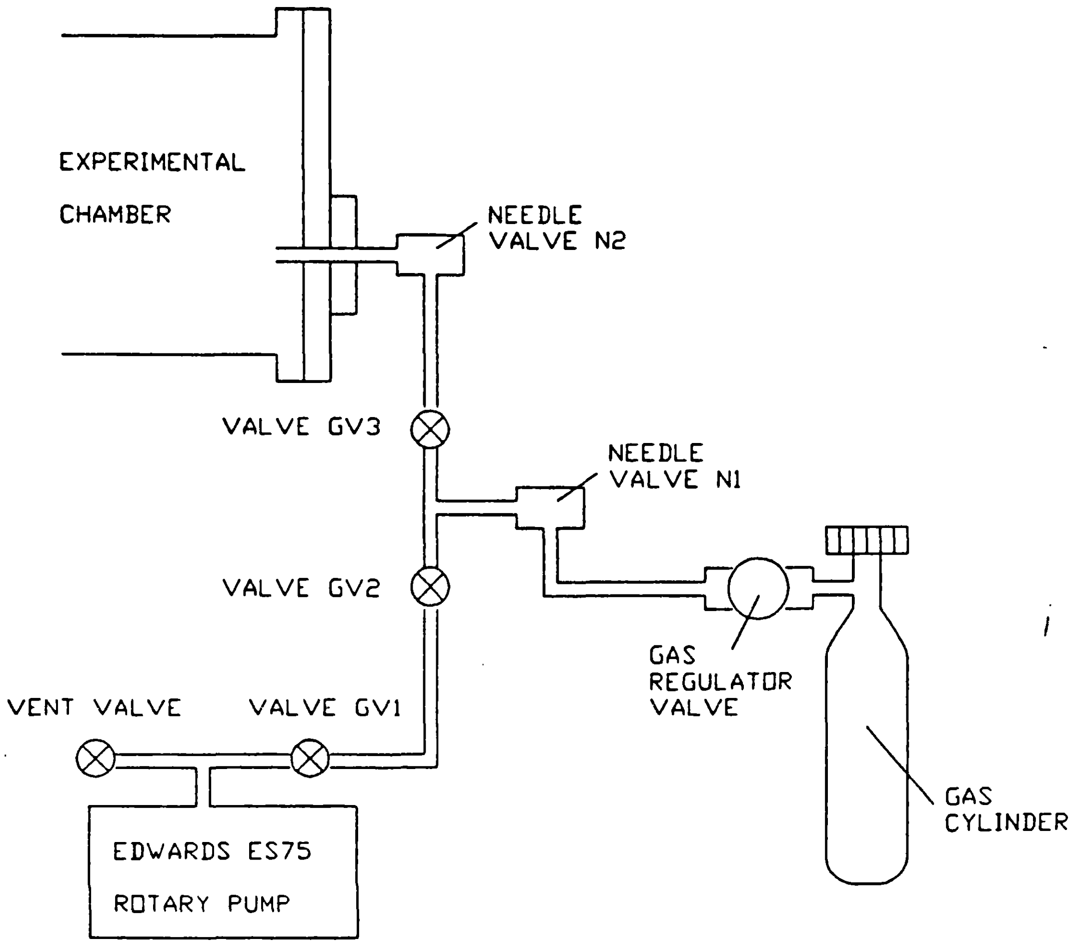

Figure 3.2 Schematic diagram of the gas inlet system.

The time of flight technique used in this work may be used as an internal leak detector. The cross section for the excitation of nitrogen to metastable states is large, $> 10^{-17}$ cm^2, relative to the cross sections for those dissociation processes studied in this work, $\sim 10^{-20}$ cm^2 and the detection systems used are particularly sensitive to the $N_2(a^1\pi_g)$ metastable state of nitrogen. In the time of flight spectra obtained, even the residual nitrogen in a gas line evacuated to a pressure ≤ 0.05 torr was sufficient to produce a distinct peak. To check the gas line for small leaks, a time of flight spectrum of the metastable products of dissociation of carbon dioxide was recorded. The dissociative peaks due to $CO(a^3\pi)$ and $O(^5S)$ metastable fragments appear at much shorter flight times than the nitrogen metastable molecules making the nitrogen peak clearer.

3.4 The Electron Gun

The electron gun used in the present work was designed to produce a beam of electrons of the required energy in the range of 5 - 100V (Mason and Newell 1986). The resolution of the electron beam was not considered to be as important as a high electron beam current, $\sim 1\mu A$, in these studies since the collision cross sections for electron impact dissociative excitation are very small, $\sim 10^{-20}$ cm^2.

Electrons produced from a heated metal cathode filament leave the filament with a range of energies, typically of FWHM ~ 0.5eV. This energy spread can be reduced in the electron gun by using a mirror lens, (section 3.4.3) but inevitably any reduction in the energy spread reduces the usable current produced by the electron gun.

3.4.1 Electron Sources

Heated cathode filaments provide the highest electron currents, are cheap and are simple to use. There are three basic types of heated cathode filaments; pure metal filaments, doped metal filaments and metal oxide coated filaments. Examples of these filaments and their typical properties are given in table 3.1.

The most commonly used pure metal filament is a tungsten filament since these are durable, having a lifetime of thousands of hours in non-oxidising atmospheres. The thoriated metal filaments consist of the pure metal wire doped with a few percent of thorium oxide. They must be activated before use by flashing at a higher temperature than the normal emission temperature. This flashing drives the thorium oxide to the surface. Further heating at a lower temperature reduces the thorium oxide to metallic thorium. The filament may then be operated for many hundreds of hours at a lower temperature than pure tungsten and will give an electron beam of a lower energy spread. Over time the thorium evaporates but the filament may be reflashed to drive more thoria to the surface. Eventually, when all the thorium has evaporated the filament behaves as a pure tungsten filament and can be operated as such.

Table 3.1 Properties of filament materials (Mason and Newell 1990b).

Filament Type	Example	Work Function /eV	Emission Temp. /K	Energy spread /eV
Pure metal	Tungsten	4.54	2900	0.64
	Thoriated tungsten	2.96	2100	0.46
Doped Metal	Thoriated iridium	2.6	1700	0.38
Metal oxide coated	Barium, strontium, magnesium oxide	1.6	1100	0.15

Metal oxide coated filaments are the most sensitive to the environment in which they operate. The base metal, usually nickel, is coated with a carbonate solution consisting of equal quantities of barium and strontium carbonates possibly with a small amount of calcium carbonate. The filament must also be activated by heating strongly to convert the carbonates to oxides. Because of the low work function of the filament surface it can be operated at a much lower temperature than metallic filaments. The surface, however, is not robust, being easily poisoned by water, hydrocarbons and target gases, subject to evaporation and damaged by positive ion bombardment. The surface must therefore be renewed each time the vacuum system is let up to atmosphere.

Three types of filament were used in the course of this work: tungsten, thoriated tungsten and thoriated iridium. The filaments used were all in the form of a hairpin held between two pins on a ceramic plate, figure 3.3.

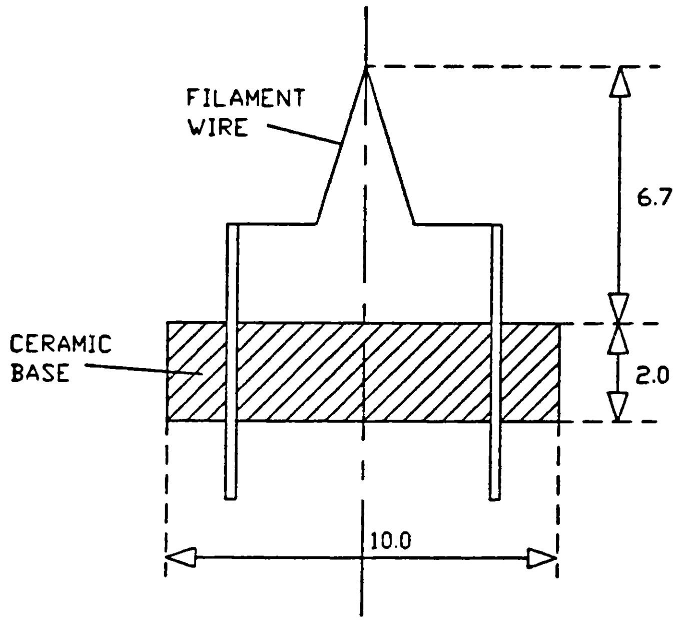

Figure 3.3 Schematic diagram of a hairpin filament mounted on a ceramic plate.

3.4.2 Electron Optics

Electrostatic lenses are analogous to thick lenses in light optics, but additional aberrations result from the charge on the electrons and the finite spread in the energies of the electrons in the beam. Design of electrostatic lens systems to produce an electron beam of the desired energy and size has been greatly aided by the publication of data tables by Harting and Read (1976) and the availability of the Simion programs. In this section the principles of electron optics and aberrations in electrostatic lenses are described and related to the electron gun used in this work.

a) Electron Lenses

Electron lenses may take the form of either apertures or cylinders. In this work three-element cylindrical lenses were used, figure 3.4. In such lenses the focusing is determined by the voltage ratios

$$\frac{V_2}{V_1}\ ,\ \frac{V_3}{V_1}$$

and the geometric ratios

$$\frac{G}{D}\ ,\ \frac{A}{D}$$

where V_i are the voltages applied to each of the three lens elements, G is gap size between adjacent elements, A is the distance between the midpoints of each gap and D is the internal diameter of the lenses.

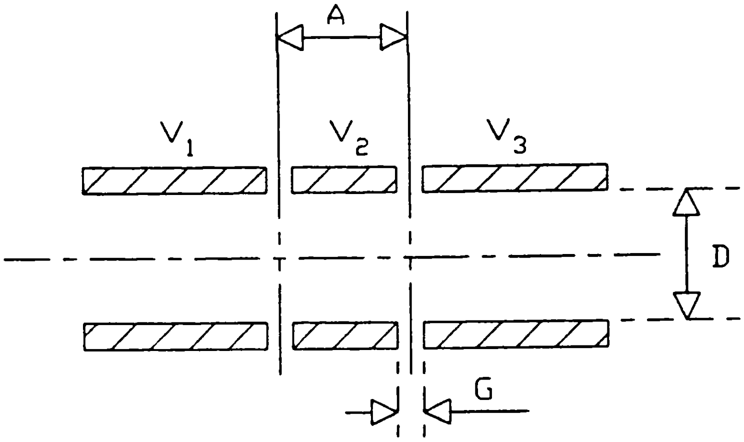

Figure 3.4 Diagram showing the dimensions A, G and D of a three element lens.

b) Pupils, Windows, Beam Angles and Pencil Angles

The angular divergence of the electron beam is defined in terms of the beam and pencil angles and the positions of the pupils and windows in the lenses.

All rays emitted from the same point on the object are called pencils and meet again at the corresponding point on the image. The angle formed by the centre and the extreme rays of a pencil is known as the pencil angle. This angle is associated with the emission process. It therefore depends on the temperature of the filament and the subsequent accelerating potential, V_A, and is given by

$$\alpha_p = \sqrt{\frac{V_K}{V_K + V_A}}$$

where

$$V_K = \frac{T}{11600}$$

and T is the filament temperature in kelvin.

The pencil angle may therefore be reduced by using a low work function emitting surface or a high anode potential but it will always be finite. As the electron beam passes through a series of electrostatic lenses the new pencil angle can be calculated by the Helmholtz-Lagrange law, figure 3.5,

$$r_1^2 \, V_1 \sin^2\theta_1 = r_2^2 \, V_2 \sin^2\theta_2$$

or, for paraxial rays, θ is small and $\sin \theta \approx \theta$,

$$r_1^2 \, V_1 \, \theta_1^2 = r_2^2 \, V_2 \, \theta_2^2$$

The angles θ_1 and θ_2 are the initial and final pencil angles respectively, r_1 is the object size and r_2 the image size, V_1 and V_2 are the lens voltages. For a decelerating lens of unit magnification the pencil angle will therefore increase.

Unlike the pencil angle which is a consequence of the emission process at the electron source, the beam angle is a purely geometric quantity set by the size of the window and the pupil-to-window separation. The pupil limits the size of an object which can be imaged by a lens while the window is the aperture in front of the object. The beam angle may be reduced to zero by placing the window at the first focal plane of a lens since this results in the image of the window being projected to infinity.

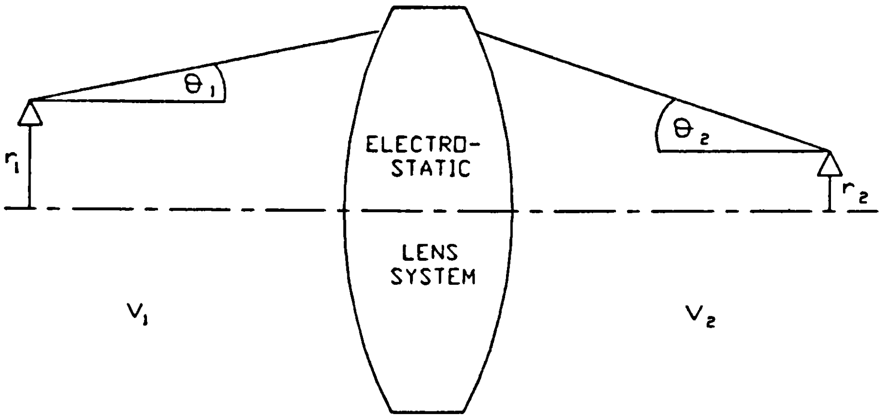

Figure 3.5 Definition of the symbols in the Helmholtz-Lagrange law (Harting and Read 1976).

c) Aberrations

Electrons of equal energy starting from points in the object plane are focused onto corresponding points in the Gaussian image plane if their paths are paraxial, both parallel and close to the axis of the lens. Non-paraxial rays are not focused at the same point as the paraxial rays.

There are two types of aberration common in lenses, geometrical aberration which arises from the shape of the lenses and chromatic aberration which arises from the energy spread of the electrons. Geometrical aberrations may be divided into three types: spherical aberration, coma astigmatism and field curvature. Chromatic and spherical aberrations are the most important in electrostatic lenses.

i) Spherical Aberration

The principle of spherical aberration is shown in figure 3.6. Consider rays in three regions of the lens; axial rays which are close to and almost parallel with the axis, zonal rays which follow a path further from the axis, and marginal rays which are close to the electrodes. In a lens with spherical aberration, axial rays are focused at F_a while zonal and marginal rays are focused at F_z and F_m respectively. Rays from each region therefore have a different focal point and the diameter of the electron beam forming the image is not narrowest at the image plane but at some point between the centre of the lens and the image plane. This minimum diameter is the 'disc of least confusion' and is the closest approximation to a 'sharp' image.

If the lens is operated close to the mirror condition, i.e. $V_2 \approx -V_1$, electrons are slowed down and there is an increase in space charge. This produces a negative spherical aberration for zonal rays and the focus for zonal rays, F_z, tends towards that for axial rays, F_a.

The degree of aberration depends on the geometry of the lens elements. For three-element lenses the aberration decreases as

1. the element diameter increases,
2. the image distance increases,
3. the focal length decreases.

The aberration is a minimum for elements of equal diameter. Therefore all the lenses used have elements of large diameter, 10mm, and short focal lengths.

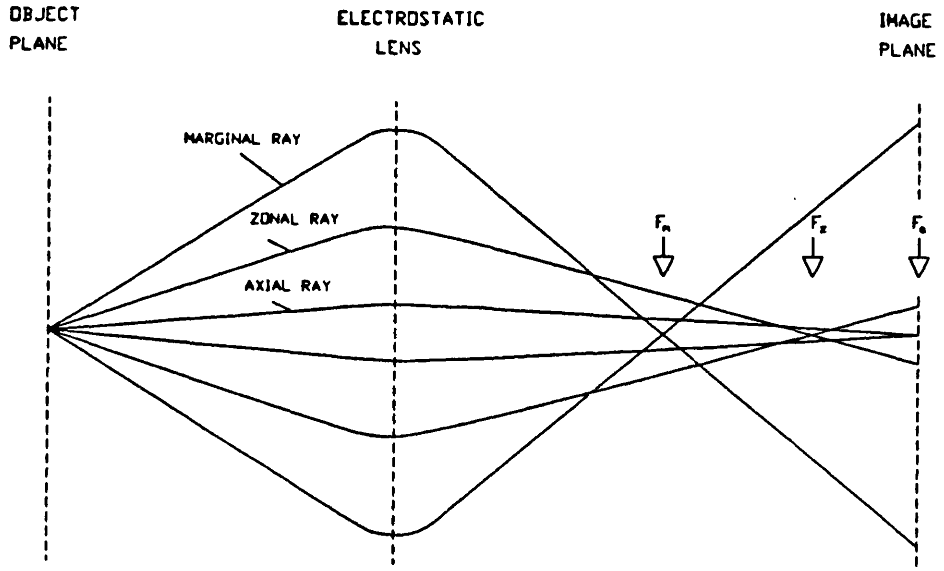

Figure 3.6 Diagram showing the principle of spherical aberration. Axial rays are focused at F_a while zonal and marginal rays are focused at F_z and F_m respectively (Harting and Read 1976).

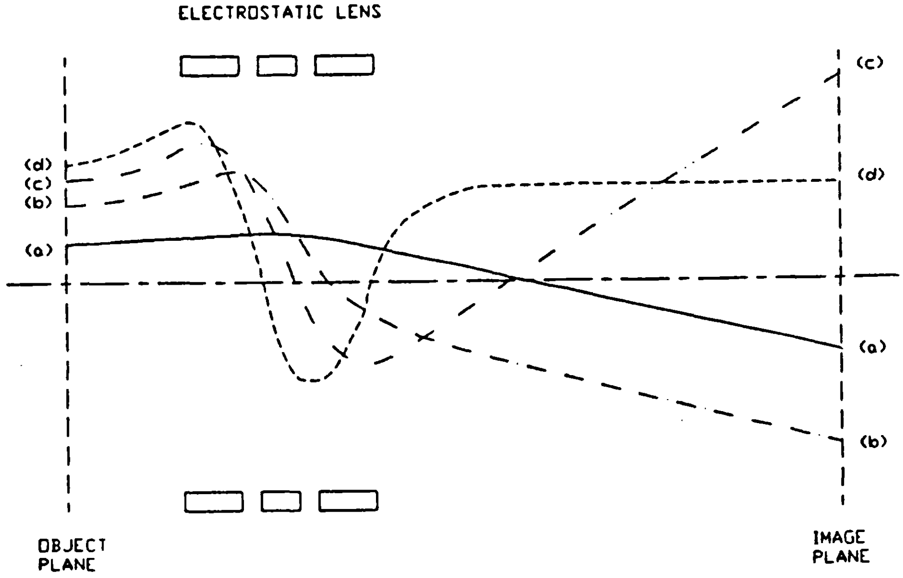

Figure 3.7 Diagram showing the principle of chromatic aberration.

ii) Chromatic Aberrations

The electron beam has a velocity distribution due to

1. the emission mechanism of the cathode,
2. space charge effects within the lenses,
3. fluctuations in the accelerating or retarding potentials applied.

Electrons of different initial velocities will therefore be refracted in the lens field by different amounts. Slower electrons experience greater deviations than faster electrons. The slower electrons consequently pass through a focus closer to the lens centre than the faster electrons. Chromatic aberration therefore produces a series of foci along the axis, figure 3.7. The longitudinal spread resulting is of length δf where

$$\delta f = C_{CR} \frac{\delta v}{v}$$

where C_{CR} is the chromatic aberration coefficient of the lens and δv is the spread in velocities in the electron beam.

Chromatic aberration may be used to velocity select the electron beam by mechanically selecting a region of the chromatic focus or by filtering the electron beam in the central element of the lens (Metherell and Cook 1971). In the electron gun used in this work a quasi-monoenergetic electron beam is produced by utilising chromatic aberrations in the central lens, allowing only electrons with velocities in the high energy tail of the distribution to pass through to the interaction region (Mason and Newell 1986).

d) Electron Optics in the Gun

A schematic diagram, figure 3.8, shows the electron lenses with the positions of the pupils and windows indicated.

i) Extraction System

The purpose of the extraction system is to achieve the maximum available current density from the filament surface. If the extraction field at the emitting surface varies, the emission density available from each point depends on the field strength at that point. The average emission density over the surface may therefore be substantially below its maximum. Pierce (1940) found that if the filament was placed at the centre of an aperture in an electrode whose surface was cut at an angle of 67.5° to the central axis, the field at the filament would be homogenous.

The tip of the hairpin filament is therefore located at the centre of a Pierce electrode extraction system, the cathode housing, KH. The aperture in the cathode housing is 2.0mm. The pupil, P1, of the hairpin filament is located at the tip of the hairpin and the size of the pupil is taken to be twice the effective radius of the hairpin tip (Kuyatt 1979, Klemperer 1974). The window W1 is a 0.5mm diameter aperture in the anode AN. The anode and the aperture are at a potential, V_A, of 75V. In the electron gun used, the distance between the pupil P1 and the window W1, d, is 6.63mm. This gives a pencil angle, when using the tungsten filament, of 4.38°. The thoriated filaments operate at a lower temperature (Mason and Newell 1990b) and therefore give beams of slightly lower pencil angle.

i) First Zoom Lens

The electron gun consists of three three-element cylindrical lenses. The first zoom lens (AN-L1-L2) focuses the pupil P1 onto P2. P2 is a 0.7mm diameter aperture in the lens element L2. The window W1 is focused onto W2 which lies on the principal plane of the einzel lens (L2-L3-L4).

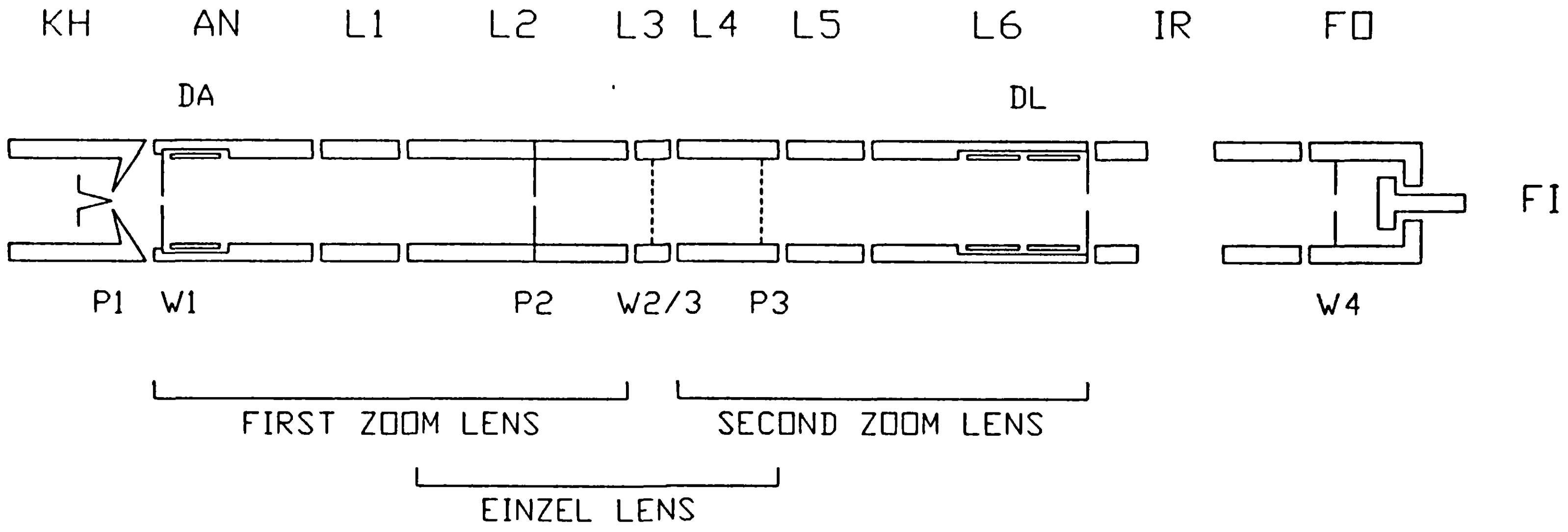

Figure 3.8 Schematic diagram of the electron gun, interaction region and Faraday cup. The positions of the windows and pupils are indicated. DA represents two sets of orthogonal deflector plates in the anode and DL four sets in the lens element L6.

iii) Einzel Lens

An einzel lens is a three element lens in which the outer two lens elements are at the same voltage and only the central element potential is variable. Since the voltages on both sides of the lens are equal, the focal lengths are equal and the two nodal points and the principal planes are almost coincident. The focal length depends on the length of the central element. In the gun used in this work, the central lens element is short, 4mm, and the lens therefore has a short focal length.

The einzel lens focuses P2 onto P3 in the focal plane of second zoom lens (L4-L5-L6) and focuses the window W2 onto W3 from the first principal plane to the second principal plane with unit magnification. Due to the properties of the einzel lens, the principal planes of the lens are almost coincident at the centre of the lens, therefore W2 and W3 effectively coincide at the centre.

iv) Second Zoom Lens

The second zoom lens was designed to focus P3 to infinity and form a real image of the window W3 at W4 where W4 is an aperture of diameter 2.0mm in the Faraday cup.

3.4.3 The Filter Lens

The einzel lens in the centre of the electron gun fulfils two functions

1. To reduce the beam angle to zero by focusing P2 onto P3 placed at the focal plane of the second zoom lens while maintaining the window W2 in the centre of the einzel lens,
2. To filter the electron beam, reducing the energy spread in the incident electron beam.

The einzel lens is operated with the element L3 at a negative potential. Electrons which do not enter the lens along the axis, marginal electrons, experience a stronger field than axial electrons as shown in figure 3.9. As the negative potential on the central lens element is increased, the marginal electrons will be the first to be reflected back towards the filament. The axial electrons continue through the lens. The einzel lens therefore spatially filters the electron beam.

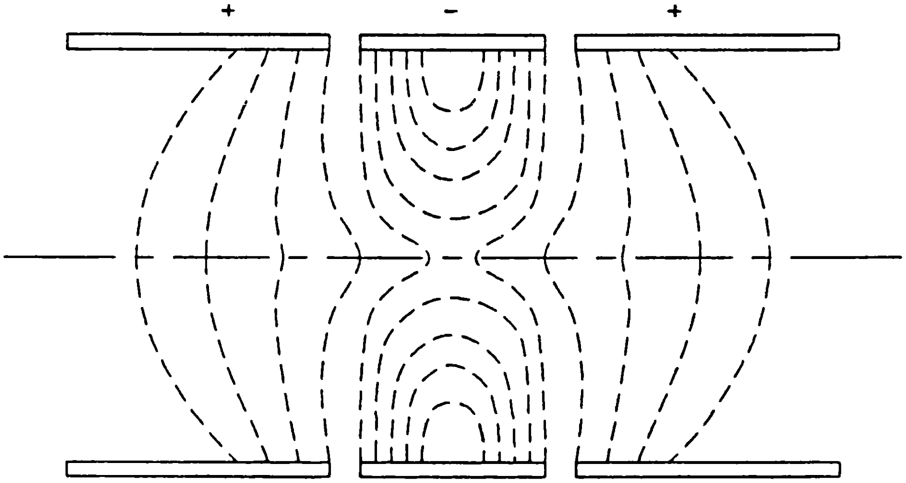

Figure 3.9 Diagram of the electrostatic field inside the filter lens.

If the central lens element is made still more negative, the axial electrons oscillate about the symmetry axis. Those in the high energy tail of the velocity distribution of the electron beam will pass through the lens while those with lower energies will be reflected as shown in figure 3.10. Thus the einzel lens may be used to select electrons in a narrow velocity range.

When the central element is made sufficiently negative, all electrons in the incident beam are reflected back onto the real aperture P2 and the mirror condition is achieved. This condition is used to pulse the electron gun. The potential on the central lens element is set to satisfy the mirror condition and a small positive square wave is then applied to the lens element. This periodically raises the potential on the lens element to allow electrons to pass through the einzel lens and reach the interaction region.

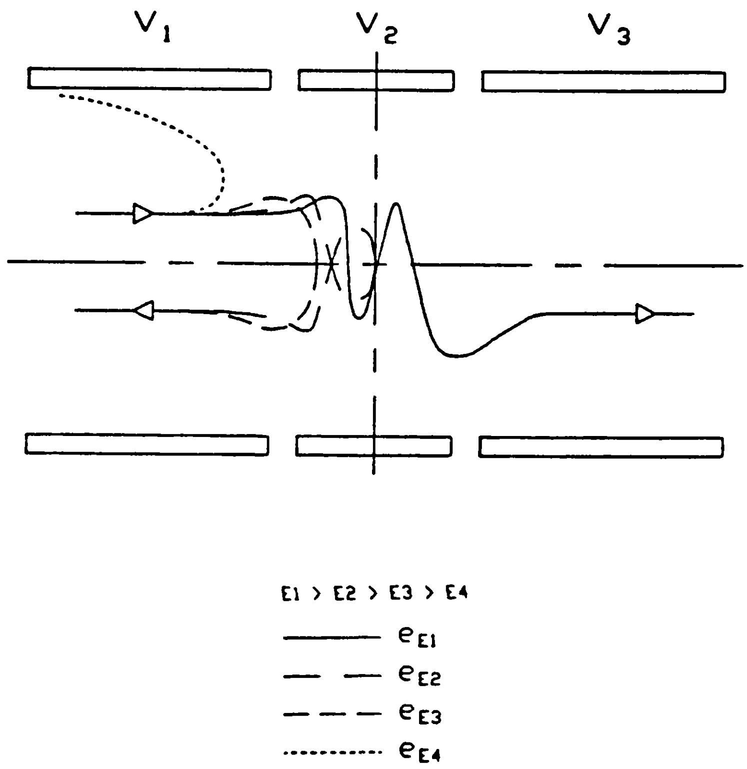

Figure 3.10 Diagram showing electrons in the high energy tail passing through the lens while the lower energy electrons oscillate abut the symmetry axis and are reflected.

3.4.4 Electron Gun Operation

Electron beam energies from 6eV to 70eV were used in the present work. The beam energy was set by the potential applied to lens element L6, the interaction region, IR, and the outer Faraday cup, FO, figure 3.8. The potential applied to the anode AN was 75V while L2 and L4 were maintained at 30V. These potentials were fixed, irrespective of the final electron beam energy. The intensity and size of the electron beam was monitored along the electron gun by measuring the current on the apertures in AN, L2 and L6. A set of deflector plates consisting of two orthogonal pairs was incorporated in the anode and two sets in the lens element L6 to adjust for geometric misalignments. The single set in the anode compensated for any tilt in the extraction system, for example, for the filament sagging. The two sets in the lens element L6 allowed the electron beam to be steered across the interaction region and maximised in the Faraday Cup. The interaction chamber is shown in figure 3.8 and was a titanium electrode of internal diameter 10mm and external diameter 15mm with two holes in the wall. The gas beam was introduced through the 8mm hole by a demagnetised stainless steel hypodermic needle. The products pass through a 10mm hole to enter the flight tube.

The Faraday cup consisted of an outer electrode, FO, containing a 1.0mm diameter aperture, and an inner electrode, FI, electrically isolated from each other by PTFE. The ratio of currents observed on the inner and outer cup allows the size of the beam at the Faraday cup to be determined and from this the size of the beam at the centre of the interaction region may be deduced. The beam size decreases with increasing beam energy but was typically 1-2mm diameter. The gas beam was greater than 3mm in diameter and therefore any change in the overlap geometry due to variations in day-to-day focusing of the gun was insignificant.

To maximise the current observed at the Faraday cup lens elements L1, L3 and L5 are iteratively adjusted. The potential applied to L3 was constrained by its use in maintaining the beam angle at zero in the interaction region and also by its importance in pulsing the gun for time of flight spectroscopy. The potential applied to the cathode housing, KH, was varied to maximise the current from the filament. The potential required depended on the type of filament used but was usually ~-2V. The thoriated iridium filament, however, was found to require a positive potential, ~+0.4V, for optimum performance.

Table 3.2 shows the design parameters of the lenses in the electron gun. Table 3.3 gives the typical voltages on the lens elements and the currents measured on the apertures in the electron gun for an incident electron energies of 15eV and 50eV.

Table 3.2 Design parameters of the electrostatic lenses in the electron gun.

Internal diameter of lens elements	10.00mm
Gap size between lens elements	1.00mm
Gap size between KH and AN	0.45mm

Lens AN-L1-L2		Lens L2-L3-L4		Lens L4-L5-L6	
V_{AN}/V_{L2}	2.5	V_{L2}/V_{L4}	1.0	V_{L4}/V_{L6}	5.0
V_{L1}/V_{L2}	8.0	V_{L3}/V_{L4}	2.5	V_{L5}/V_{L6}	10.0

3.4.5 Assembly

The electron lens elements were cylinders of titanium with an internal diameter of 10mm and an external diameter of 15mm. Titanium was used since it is a non-magnetic material and has a low electron reflection coefficient therefore requiring no surface coating unlike copper and aluminium which must be coated with colloidal graphite or soot. The apertures were manufactured from a 0.05mm molybdenum sheet. To reduce electron reflection the apertures were coated with DAG50, a colloidal solution of graphite.

The electron lens elements had to be clean and free from grease to avoid the build up of charge on the surfaces of the lens elements and thus instabilities in the electron beam. The lens elements, together with the optical bench, studding, nuts, washers and ceramic spacers used in assembly, were cleaned in a bath of acetone placed in an ultrasonic cleaner. The components were left in the ultrasonic cleaner for several hours and the acetone bath replaced as necessary. The components were then kept under methylated spirits until required when they were once again rinsed in acetone before final assembly.

Table 3.3 Typical potentials applied to the lens elements in the electron gun to produce electron beams of energy 15eV and 50eV.

	Electron Energy 15eV		Electron Energy 50eV	
Lens Element	Potential /V	Current /μA	Potential /V	Current /μA
KH	-1.7		-1.5	
AN	75.0	2.0	75.0	2.0
DA1	73.1		72.5	
DA2	76.9		77.5	
DA3	74.7		74.6	
DA4	75.3		75.4	
L1	257.3		233.8	
L2	30.0	0.36	30.0	0.54
L3	-11.0		-13.2	
L4	30.0		30.0	
L5	122.1		195.0	
L6	15.0	0.11	50.0	0.14
DL1	14.8		47.8	
DL2	15.2		52.2	
DL3	14.2		45.8	
DL4	15.8		54.2	
DL5	14.4		46.5	
DL6	15.6		53.5	
DL7	13.9		45.0	
DL8	16.1		55.0	
IR	15.0		50.0	
FO	15.0	0.20	50.0	0.31
FI	18.0	0.10	53.0	0.19

The studding, nuts and washers used to attach the electron lenses to the optical bench were made of stainless steel. These needed to be demagnetised periodically. This was achieved by heating them strongly in the flame of an oxy-acetylene torch until they were red hot. The components were then transferred, while still glowing, to a mu-metal can of residual magnetic field <100 mG. They were then allowed to cool isolated from the Earth's magnetic field. The components were checked periodically using a Bell Instruments type 120 Gaussmeter.

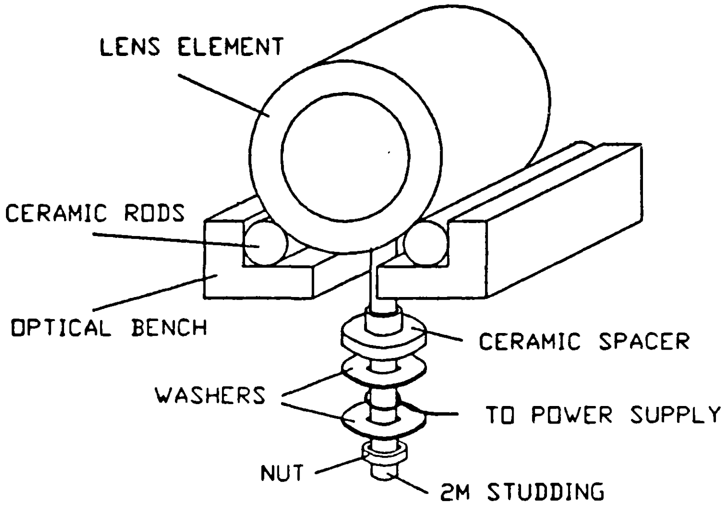

Figure 3.11 Schematic diagram of the assembly of electron lens elements on the optical bench.

The electron lenses were assembled on an optical bench as shown in figure 3.11. The lens elements rested upon a pair of ceramic rods and were secured to the optical bench by electrically isolated studding, a washer and a nut. The lenses are thus electrically isolated from the optical bench. The potential was applied to the lens by a colour coded, vacuum compatible PTFE coated silver-plated copper wire sandwiched between two washers. The deflector plates in the anode and in lens element L6 are also made of titanium and were separated from the lenses by a 1mm sheet of PTFE and secured by isolated screws.

It was necessary to shield the experiment from the Earth's magnetic field for the electron optics to operate as designed. Therefore the whole apparatus was enclosed within a single mu-metal can to reduce the magnetic field to <5mG. Additional mu-metal sleeves surrounded those openings needed for efficient pumping and for electrical feedthroughs to reduce field penetration through these apertures.

3.4.6 Electronics

The filament supply used was a Coutant type LB1000.2 and the connections to the filament inside the chamber were made by glass screened copper wire.

The power supplies for all the electron lenses, except L3, were built in the laboratory and driven by a split Kingshill supply providing 280V and 140V. These have less than 2meV peak to peak ripple voltage and have proved capable of providing stable voltages for the long periods necessary. The power supplies are shown in figure 3.12 and the circuit diagrams are given in figure 3.13. The lens element L3 was driven directly from a Kingshill 15AOIC 0-150V supply connected to provide a negative potential with respect to the bias potential modulated using a Farnell PG102 square wave generator. The output from the supplies was taken on multicore screened cable to the multiple feedthroughs on the front flange of the experimental chamber.

The supply to each of the lenses was controlled by an 100kΩ potentiometer. Jack sockets were included to allow the voltage and current to be sampled for each lens. A Keithley 168 autoranging voltmeter was used to measure the voltage and a Keithley 602 solid state electrometer to measure the electron beam currents.

The 'bias' potential was applied to the centre point of the filament by a Kingshill 15AOIC 0-150V supply and, as the zero energy of the system, was used as the common reference for all electron lens element supplies. The deflector plates are referenced from their associated lens element.

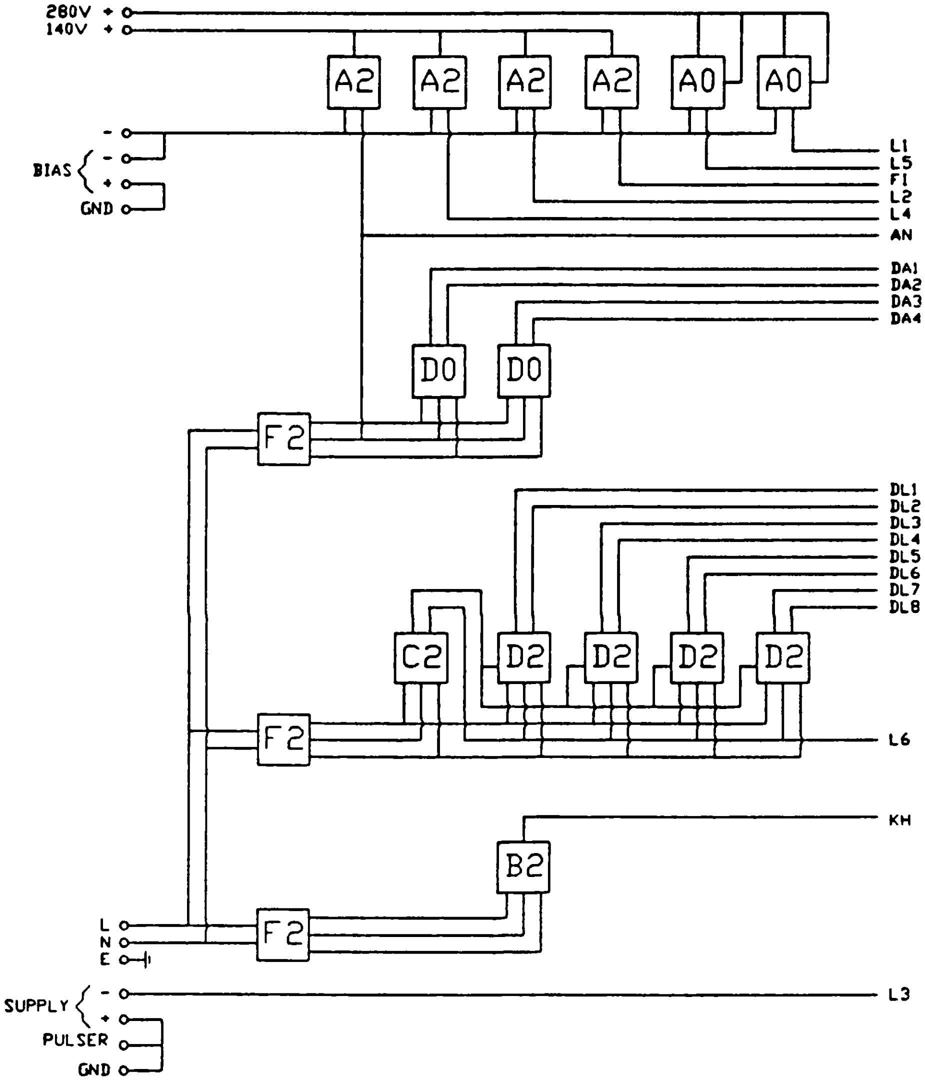

Figure 3.12 Schematic diagram of the power supplies providing the voltages to the lens elements in the electron gun.

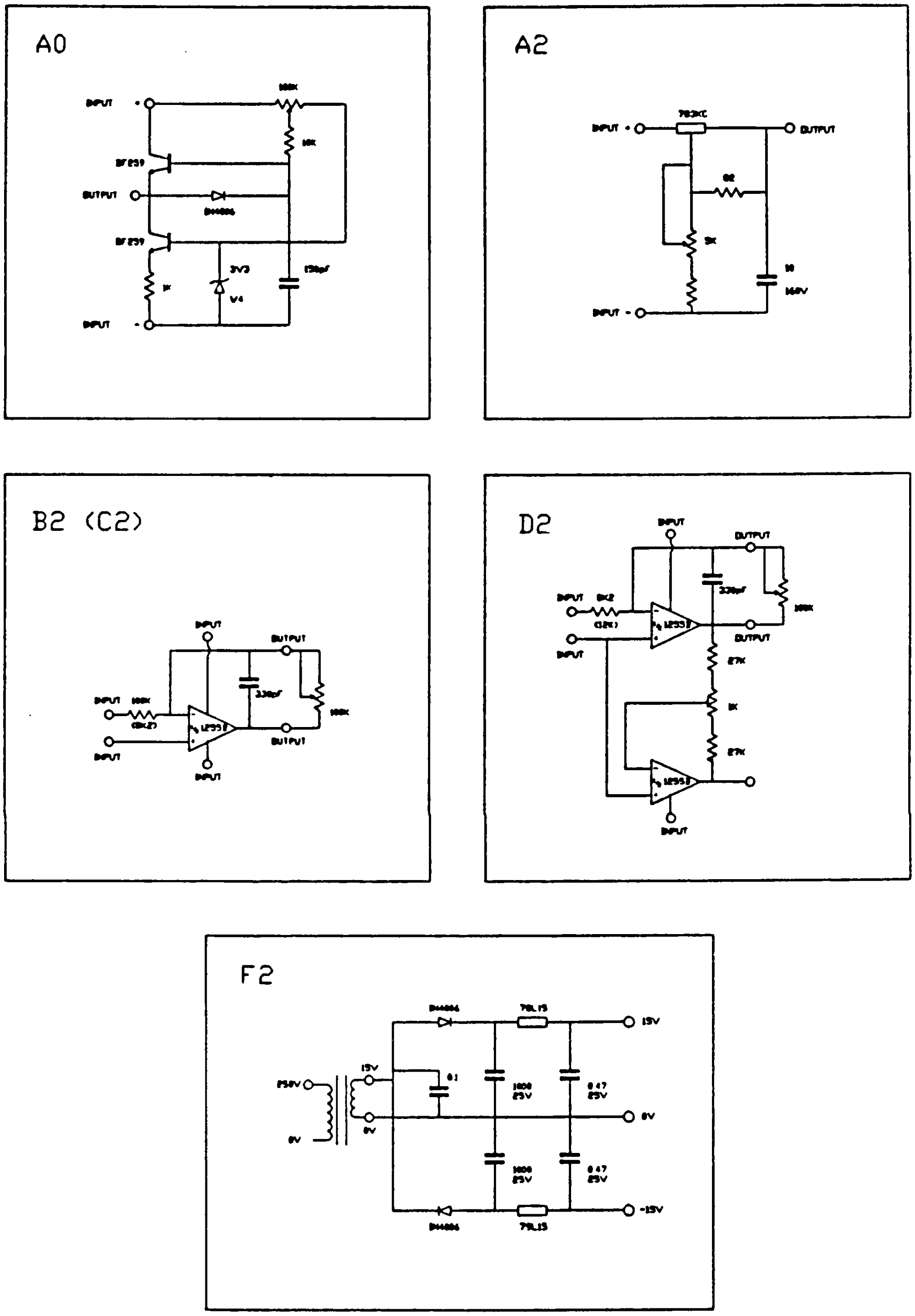

Figure 3.13 Circuit diagrams of the power supplies providing the voltages to the electron gun lens elements.

All the electronics were disconnected from the mains earth and connected to the laboratory earth which consisted of copper strips connected to the substation earth. This eliminated unwanted electrical noise from the mains earth.

3.5 Summary

In this chapter, the vacuum system and gas inlet system have been described. The electron gun used in this work has been discussed in detail with emphasis on the central einzel electrostatic lens which made use of chromatic aberrations in the lens to velocity select the electron beam. To complete the description of the apparatus, the gas sources used will be described in the next chapter while the detection systems used will be discussed in chapter five. The energy of the electron beam was determined by the potential applied to the final lens element, L6. Contact potentials arising from charging on the electrostatic lenses were estimated by observing the direct electron impact excitation of molecular nitrogen. The resolution of the electron beam was $\sim$0.5eV.

Chapter Four

The Technique of Translational Spectroscopy

"Why," said the Dodo, "The best way to explain it is to do it."

Lewis Carroll *(Alice in Wonderland)*

4.1 Introduction

In this chapter the technique of translational spectroscopy, the dynamics of the parent gas beam and the effects of momentum transfer during the collision will be discussed.

The electron beam collides with the target gas beam in a field free region, the interaction region, which is defined as the intersection of electron and target gas beams in the field of view of the detector. Unscattered electrons are collected at the Faraday cup while the collision products leave the interaction region through an aperture in the interaction chamber and enter the flight tube. The collision products include photons, ions and electrons in addition to atoms or molecules which may be in the ground state, in short-lived excited states and in metastable states.

Direct electron impact excitation of atoms or molecules may be investigated by studying the scattered electrons, the product atoms and molecules themselves or the photons produced on decay of excited states. Differential cross sections may be determined by studying those electrons which have lost energy during excitation of the target, the electron flux being measured at different angles with respect to the incident electron beam. Total cross sections may then be obtained by extrapolating the differential cross sections and integrating them between 0° and 180°. For incident electron energies close to the excitation threshold of any process the scattered electrons will have very small residual velocities and thus will be easily deflected in any stray electric and magnetic fields. Consequently the measurement of cross sections and resonance structure close to threshold will be difficult to determine. However, if the excited atoms are in metastable states, i.e. excited states of lifetime in excess of $50\mu s$, these will reach the detector and may be studied directly. A convenient way of investigating the excitation process close to threshold is therefore to study the metastable atoms or molecules produced (e.g. Brunt et al 1976, 1978).

In electron-molecule collisions additional scattering channels are available such as electron impact dissociative excitation in which the fragment atoms and molecules carry away the energy released in breaking the chemical bond. The fragments produced may be in the ground state or in excited, possibly metastable, states. The study of the metastable fragments produced therefore gives information concerning the strength of the chemical bond and the potential energy state of the parent molecule (Zipf 1982).

In this chapter the technique of translational spectroscopy will be described. To analyse the spectra obtained by this method it is important to understand the dynamics of the target gas source and the effect of the collision itself on the velocity distributions of the product metastable species observed at the detector.

In direct electron impact excitation the speed distribution of the metastable atomic or molecular beam is the same as that of the parent target gas beam, although momentum transfer may modify the velocity distribution as seen at the detector. In the collision, momentum is transferred from the electron to the target atom or molecule and results in an additional velocity component being imposed on the metastable product.

In electron impact dissociative excitation, momentum transfer does not play such an important part. The energy released on breaking the molecular bond is shared between the fragments. This energy is far in excess of the thermal energies of the molecules in the target gas beam and consequently the velocity distribution of the fragments dominates over the thermal distribution of the parent molecules.

4.2 The Technique of Translational Spectroscopy

In the technique of translational spectroscopy the time taken for the metastable atoms or molecules to travel from the interaction region to the detector is measured and their velocity distribution determined. Unwanted ions and scattered electrons are deflected away from the detector by electrostatic fields applied to the lenses in the flight tube. Ground state atoms reach the detector but do not have the internal energy required to produce secondary electrons at a surface and are not detected. Therefore only photons and metastable atoms or molecules are detected. The translational spectroscopic method distinguishes signal due to the photons produced in decay of short lived excited states from that due to metastable atoms or molecules.

To allow the measurement of the travel time of the collision products it is necessary to pulse the electron beam. In the present apparatus, to pulse the electron beam, the central element of the einzel lens, L3, is set at 15V below the potential required to allow the electrons to pass through the lens. A square wave of 15V amplitude and 20ns rise time is applied to this lens element. The pulser used is a Farnell PG102 and has two output channels. The period of the pulsing for both output channels is set by a single period control, but a delay may be introduced between the pulse trains from each channel. The widths and amplitudes of the pulses from each channel may be set independently. The second channel of the pulser is used to provide a start pulse to the timing electronics.

The timing electronics are shown schematically in figure 4.1. The pulse from the second channel of the pulser is used as the start pulse to the EG&G Ortec 467 time to pulse height converter (TPHC). The stop pulse for the TPHC is provided by the signal from the detector.

The signal from the detector is of the order of 10-20mV and is first amplified by a preamplifier and then an EG&G Ortec 574 timing amplifier to ~100mV before passing through an EG&G Ortec 473A constant fraction discriminator which rejects pulses <50mV. The positive output from the TPHC is directed to an EG&G Ortec

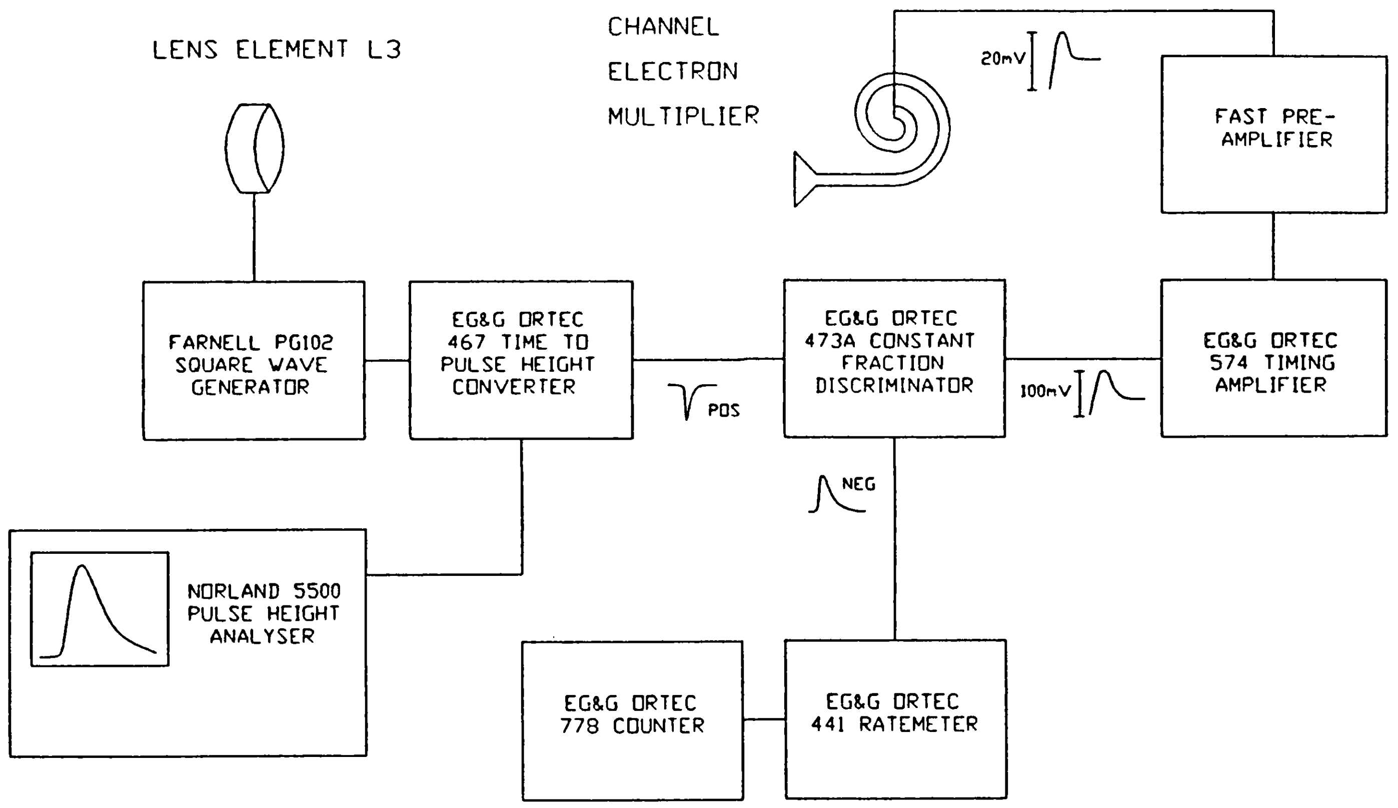

Figure 4.1 Schematic diagram of the timing electronics used in translational spectroscopy.

441 ratemeter, while the negative output is directed to the TPHC which provides a pulse of between 0 and 10V and which is proportional to the time between start and stop pulses. This pulse is directed to a Norland 5500 pulse height analyser, PHA. This effectively displays the number of events per time interval. The display is divided into 1024 channels giving a resolution of typically between 0.1μs and 1μs per channel.

Use of a TPHC and pulse height analyser means that only one event per period will be detected. If more than one metastable atom or molecule produced in the interaction region reaches the detector, only the first to reach the detector will be registered. After that event the detection system is effectively 'dead' until the next start pulse from the pulser resets the TPHC and pulse height analyser. In the present work, the count rates in direct excitation were typically 400 counts per second and the pulsing frequency 1250Hz. Therefore one event is expected every three periods and the probability of two events occurring in one period is small. In dissociative excitation the count rates observed were typically less than 20 counts per second, one event in each 250 periods and the probability of detecting more than one event per period is consequently negligible. The effect of multiple events occurring in each period can be demonstrated by observing the electron signal. If the electron intensity is increased so that sufficient electrons are produced for more than one electron per period to reach the detector, only the first event in the period is registered by the TPHC, all others in the same period are ignored and the electron pulse is trapezial rather than a square wave, figure 4.2.

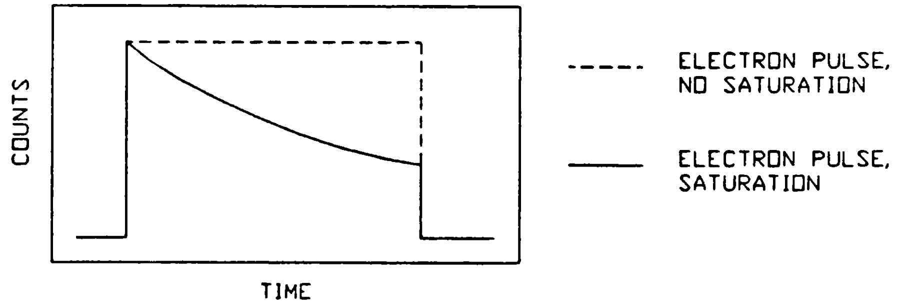

Figure 4.2 Diagram of the initial electron pulse showing the effect of saturation of the electronics.

The delay between the two output channels of the pulser could be used to discriminate between the events due to prompt photons and those due to metastable atoms and molecules if required. The delay was set before a data collection run to give a clear photon peak at the start of the display. This enabled the screen to be calibrated for that TPHC setting and pulsing period and the zero time position on the screen to be accurately established. The photons may be considered as arriving at the detector instantaneously. For an electron pulse of finite width the zero time was taken at the centre of the pulse.

The number of photons or electrons contributing to the prompt pulse are included in the overall count rate. This can cause the count rate to reach the level at which the probability of two events being produced in one period is no longer negligible. Since the event in the prompt pulse, being the first to arrive, will always be recorded in preference to the later metastable signal, distortion of the time of flight spectrum occurs. In such a case it is necessary to adjust the delay to exclude the prompt pulse.

4.2.1 Data Analysis

The data was analysed on the college Unix system. The program was written in Fortran 77 and extensive use was made of the Gino and Ginograf libraries for plotting the data. The data and results could be printed on the computer centre Apple Laserwriter.

The program was written in the form of a main program with a number of subroutines each performing a single calculation or plotting routine. It has the following functions:

1. To read in data from a named file,
2. To plot the raw data,

3. To process the data:
    a. To fit a theoretical distribution to the data,
    b. To convert a distribution in time to one in energy,
4. To plot the results.

4.2.2 Period of Pulsing

The period of pulsing is defined as the time interval between the onset of successive pulses. The pulsing period selected depends on the flight time of the metastable species from the interaction region to the detector. Table 4.1 shows the periods and on-times typically used in the excitation and dissociative excitation of the gases studied in the present work.

Table 4.1 Pulsing period and pulse duration typically used for direct and dissociative excitation in this work.

Direct Excitation			Dissociative Excitation		
Gas	Period /μs	On-Time /μs	Gas	Period /μs	On-Time /μs
He	100	1.0	N_2O	200	4.0
Ar	500	5.0	CO_2	200	4.0
N_2	800	8.0	OCS	200	6.0
CO	800	8.0			

4.3 Time of Flight Spectra

Examples of the time of flight spectra for direct electron impact excitation and for electron impact dissociation are shown in figure 4.3.

4.3.1 Excitation

In direct electron impact excitation, the metastable beam emanating from the interaction region has the same speed distribution as the parent target gas beam. This distribution may be described by the modified Maxwellian distribution (Freund and Klemperer 1967) as will be described in detail in section 4.4.1,

$$N(v)\,dv = C\,v^{G}\,e^{-v^2/\alpha^2}\,dv \qquad 4.1$$

where G is a constant, $2 \leq G \leq 3$, depending on the gas beam dynamics and

$$\alpha^2 = \frac{2kT}{m}$$

where m is the mass of the atom or molecule, k is Boltzmann's constant and T is the temperature of the gas in kelvin.

This is more usefully expressed in terms of time when performing time of flight spectroscopy. Substituting $v=L/t$ where L is the distance between the interaction region and the detector, gives

$$P(t) = \frac{A}{t^{g}}\,e^{-L^2/\alpha^2 t^2} \qquad 4.2$$

where A is a normalising constant, g is a constant such that $g = G+2$.

The significance of the constant 'g' and its experimental determination will be discussed in detail in section 4.4.1. It is sufficient in this discussion to take $g=5$.

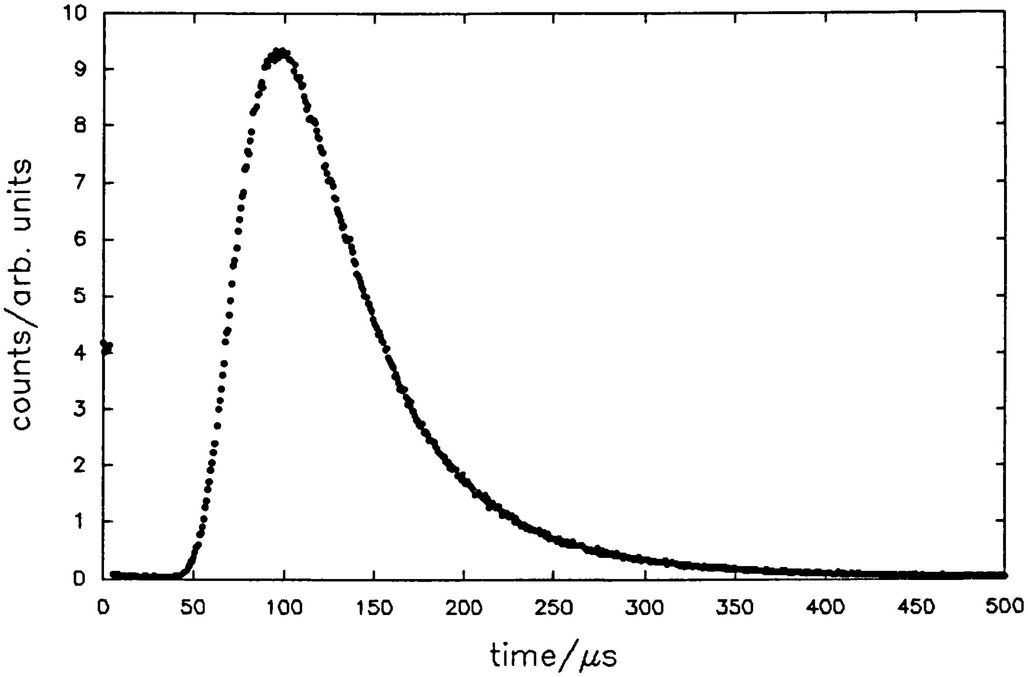

Figure 4.3a Typical time of flight spectrum for direct electron impact excitation of molecular nitrogen at an incident electron energy of 21eV.

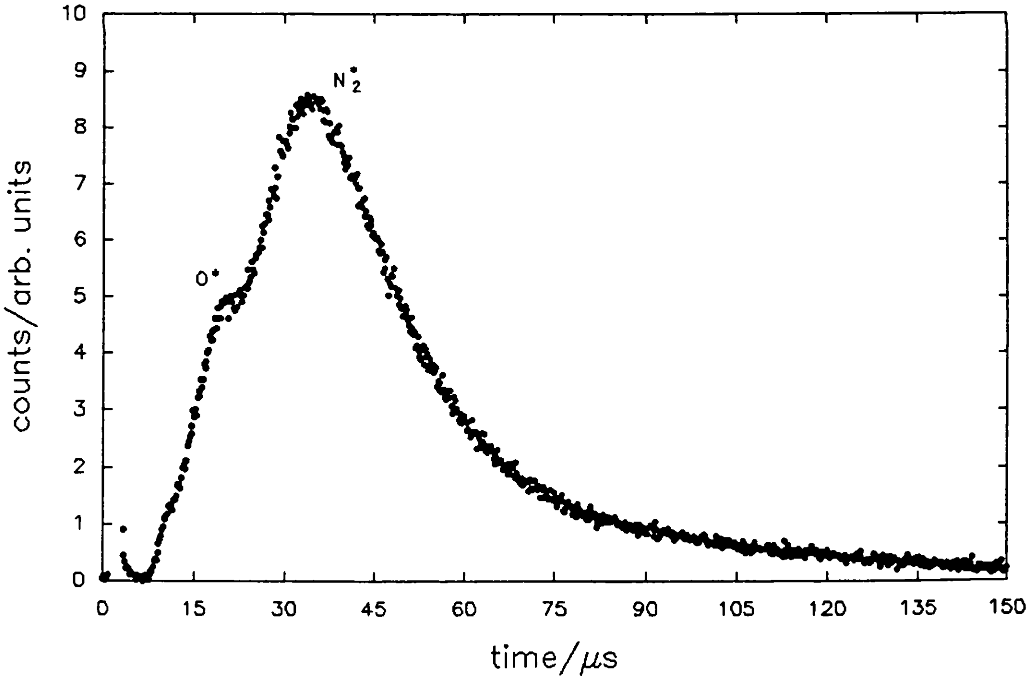

Figure 4.3b Typical time of flight spectrum for electron impact dissociation of nitrous oxide at an incident electron energy of 30eV.

It can be seen that the shape of the time of flight spectrum will be affected by the mass of the atoms or molecules, m, the temperature of the gas beam, T, and the path length, L.

Heating the gas before it enters the interaction region increases the mean velocity of the atoms or molecules in the gas beam. The time of flight spectra calculated at two different temperatures are shown in figure 4.4. Differences in temperature of between 200K and 400K were not distinguishable in the experimental time of flight spectra. In figure 4.4 the temperatures used to generate these curves were 300K and 800K. In the present sources the temperature is taken to be the room temperature, 300K.

Molecules of different masses have different arrival times at the detector. If a mixture of gases is used, the resulting time of flight spectrum will have two peaks, one corresponding to each gas. Figure 4.5 shows the experimental time of flight spectrum for a mixture of helium and argon. The first peak is due to helium, mass 4, and the second to argon, mass 40 amu. The components of a gas mixture are therefore separable, this is of some practical use in the detection of nitrogen leaks.

Impurities in the gas beam can be identified using translational spectroscopy. An impure gas sample will contain traces of several gases and the metastable states of these impurities will be observed as small peaks or shoulders in the time of flight spectrum. The position of the peak in the time of flight spectrum for direct electron impact excitation for a particular atom or molecule is obtained from equation 4.2. At the peak, time t = t_m, and

$$\frac{d}{dt}\left(\frac{C}{t^5}\,e^{-L^2/\alpha^2 t^2}\right) = 0$$

$$\Rightarrow \; t_m = \frac{L}{\sqrt{5}}\sqrt{\frac{m}{kT}}$$

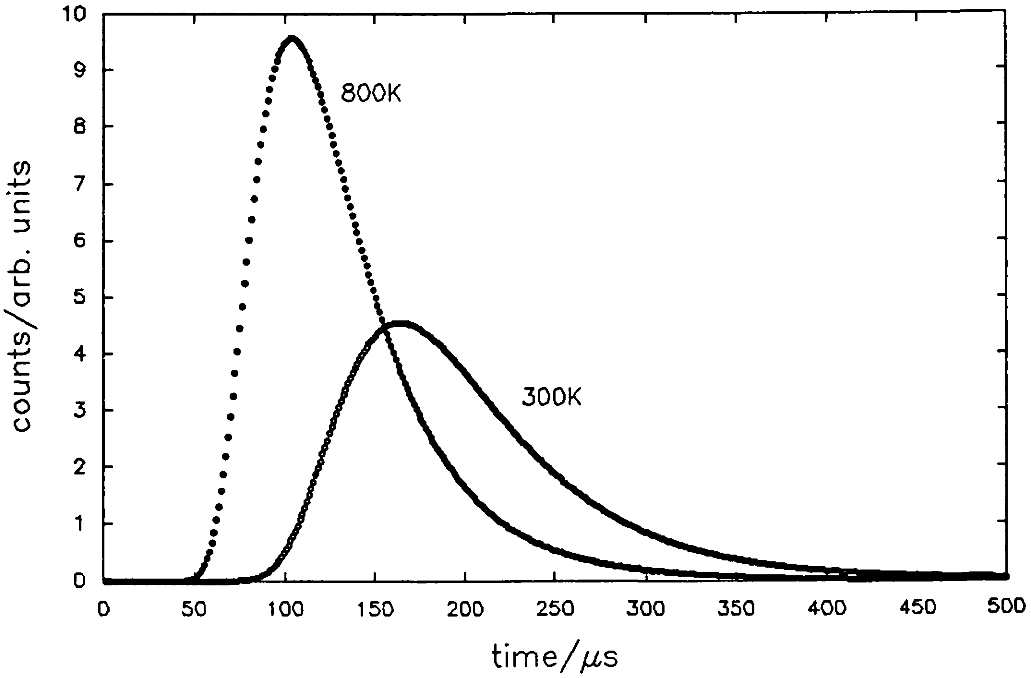

Figure 4.4 Computed time of flight spectra showing the effect of the temperature of the target gas beam.

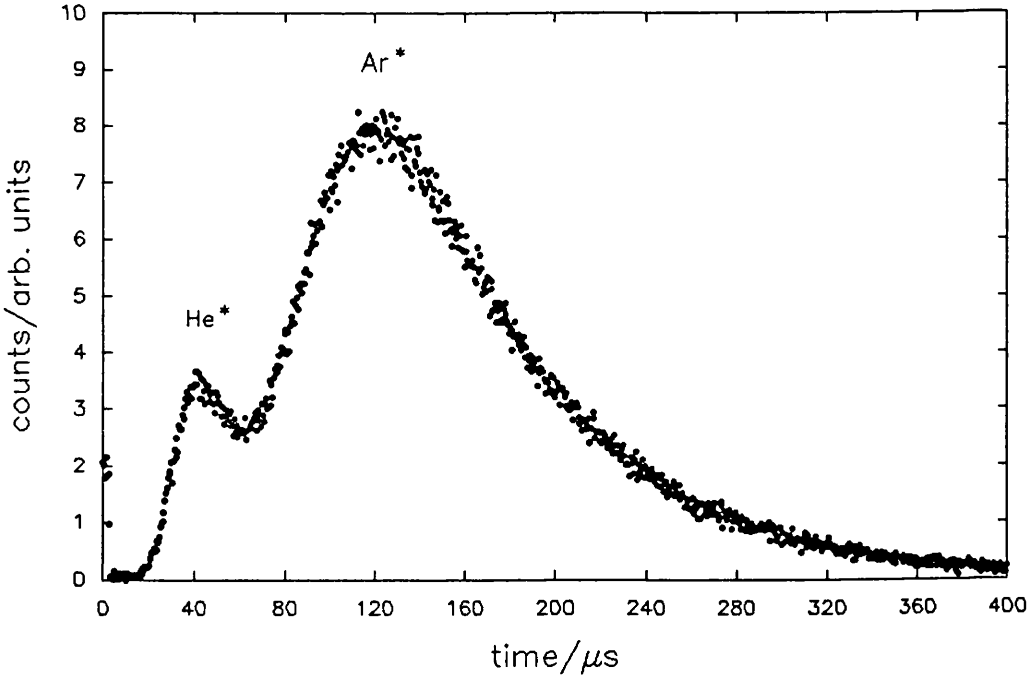

Figure 4.5 Experimental time of flight spectrum for a mixture of helium and argon showing the effect of the mass of the target atom or molecule.

Therefore, from measurement of the mean arrival time, t_m, the mass of the atom or molecule responsible may be determined. This has a special use in leak detection since the channel electron multiplier is particularly sensitive to the $N_2(a^1\pi_g)$ metastable state. Knowing the mass of molecular nitrogen, the mean arrival time of these metastable molecules can be calculated. Observation of a peak at this arrival time clearly indicates a leak in the target gas line.

The lifetime of the metastable state will also affect the time of flight distribution. If the lifetime is much shorter than the travel time between the interaction region and the detector, most of the metastable atoms or molecules will decay to the ground state before reaching the detector. If the lifetime is much larger than the travel time, there will be no effect on the time of flight spectrum since the probability of in flight decay is small. If the lifetime is comparable to the travel time, the time of flight spectrum will be depleted in the low energy tail. The slower atoms or molecules from the interaction region take longer to reach the detector and therefore are more likely to decay in flight than the faster metastable species, figure 4.6. Equation 4.2 may be modified to account for the lifetime of the metastable states by the introduction of a second exponential term:

$$P(t) = \frac{A}{t^8} e^{-mL^2/2kTt^2} e^{-t/\tau} \qquad 4.3$$

where τ is the lifetime of the metastable state.

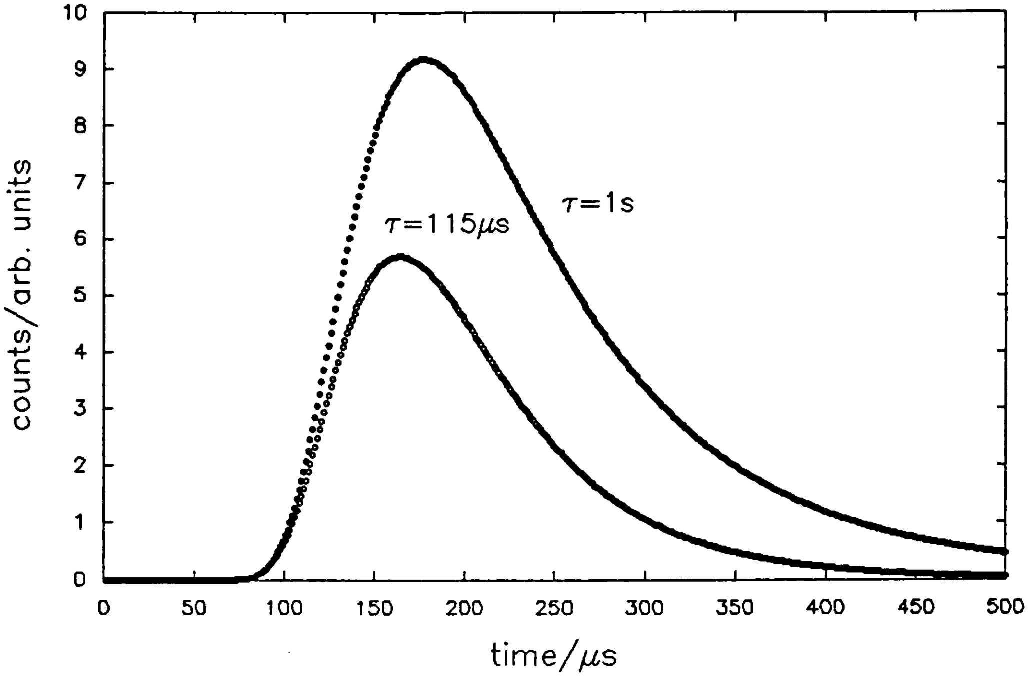

Figure 4.6 Computed time of flight spectra showing the artificial depletion of low energy metastable species due to their finite lifetime.

If more than one metastable state contributes to the time of flight spectrum, the lifetime of each state must be included. The lifetime term in equation 4.3 is then replaced by

$$K_T\, e^{-t/\tau} = \sum_i K_i\, e^{-t/\tau_i}$$

where K_T is a constant depending on the total cross section and the detection efficiency of the detector to each state and K_i are constants depending on the individual cross section for excitation of each state and detection efficiency to each state.

The ratio of metastable states present in the metastable beam depends solely on the cross section for the excitation of each metastable state. However, the time of flight spectra do not accurately reflect this ratio since the efficiency of the detector to each metastable state may be different. The ratio of metastable states in the time of flight spectrum therefore depends not only on the cross section for the production of each state but also on the efficiency of the detector to each state.

4.3.2 Dissociation

In dissociative excitation, the energy of the fragments is far in excess of the thermal velocities of the target molecules. The position of the time of flight peaks due to each atomic or molecular species cannot be predicted by their mass, the environmental temperature and a knowledge of the path length alone. There is no equation which can be universally applied to the time of flight spectra of the dissociation products since the shape depends on the bonding in the parent molecule, the mass of the fragments and the energy of the metastable fragments produced at that incident electron energy.

It is more useful to replot such time of flight spectra as kinetic energy distributions, from which deductions may be made concerning the potential energy state of the parent molecule (chapters six and seven).

The kinetic energy of the metastable molecule arriving at the detector at time t is given by

$$\varepsilon = \frac{1}{2} m \left(\frac{L}{t}\right)^2 \tag{4.4}$$

Let T(t) be the number of counts in each time channel of width dt in the time of flight spectrum and D(ϵ) be the number of counts in each energy channel of width dϵ in the kinetic energy spectrum. The area under each distribution must be the same since both the spectra contain the same number of events. Therefore

$$\int D(\varepsilon)\, d\varepsilon = \int T(t)\, dt \tag{4.5}$$

From 4.4,

$$d\epsilon = m\,L^2\,t^{-3}\,dt$$

Substituting in 4.5,

$$\int D(\epsilon)\,dt = \int \frac{1}{m}\,L^{-2}\,t^3\,T(t)\,dt$$

giving,

$$D(\epsilon) \propto t^3\,T(t) \tag{4.6}$$

The time of flight spectrum may be converted to a kinetic energy spectrum point by point. Statistical fluctuations, especially in the tail of the time of flight spectrum, are amplified in the kinetic energy spectrum because of the t^3 dependence. Therefore, if the statistics in the long flight time (low kinetic energy) part of the time of flight spectrum were poor and the peak in kinetic energy lies in this region of the spectrum, the error in the location of the peak would be large.

4.3.3 Accuracy

In direct excitation, to ensure accurate fitting of the observed time of flight spectrum to the theoretical distribution, the statistics in the observed spectrum at flight times greater than approximately twice the mean arrival time must be good. In dissociative excitation, the peak in kinetic energy distribution corresponds to a position in the tail of the time of flight spectrum. The time of flight spectrum must therefore be complete, the tail must not 'wrap around' and be included at the beginning of the spectrum.

In translational spectroscopy the accuracy depends on three factors;

1. statistical fluctuations in the counts per channel,
2. the signal to noise ratio,
3. the on-time of the electron beam.

The error due to statistical fluctuations is proportional to the square root of the number of counts in the channel and may be reduced by long data collection periods. The time for data collection depends on both the cross section of the process being studied and the accuracy required. The cross sections for dissociative processes are very small, typically 10^{-20} cm^2, and for reliable analysis of the spectra good accuracy is essential. Therefore spectra for electron impact dissociative excitation processes were recorded for periods between 50 and 120 hours.

The observed time of flight spectrum, s(t), will always be a convolution of the pulse modulation function which represents the shape of the electron pulse, m(t), and the true time of flight spectrum, z(t). The ideal electron beam pulse length would therefore be one of vanishingly small width, finite pulse widths will always cause broadening in the observed time of flight spectrum. The on-time of the electron beam was typically <3% of the pulsing period and this was considered to cause insignificant broadening compared to the statistical fluctuations. No broadening was observed when time of flight spectra with on-times of 1% and 5% were compared.

To improve the accuracy in the location of the peak in the kinetic energy distributions of the fragments produced by dissociative excitation, an attempt was made to fit the observed time of flight spectrum to a mathematical curve. This mathematical function was then used to generate a data set and the kinetic energy distribution was derived from this set. In their work on electron impact dissociative excitation Freund and Klemperer (1967) chose as the mathematical function the sum of two Lorentzians, although it is unclear whether they used true Lorentzians or a modified expression. In the present work the time of flight spectrum was compared with the sum of two true Lorentzians. This fitting was found to be unsatisfactory since the sum of the two Lorentzians seldom gave a smooth function, any small changes in the fitted curve gave rise to false peaks in the kinetic energy distribution when converted. Consequently the method of point by point conversion of the unprocessed time of flight spectrum was continued. To reduce errors in the kinetic energy spectra, the data collection periods were extended to give good statistics in the tail of the time of flight spectra.

4.4 Gas Beam Dynamics and Collision Effects

The velocity distribution in the target gas beam depends on the geometry of the gas source. The geometric configuration used may provide a gas beam of a Maxwellian distribution while others may give distributions deficient in either high or low energy atoms or molecules compared to the ideal Maxwellian distribution. In an electron-atom or electron-molecule collision, momentum is transferred from the electron to the atom or molecule. This distorts the velocity distribution observed at the detector which will accept only part of the beam.

As stated previously, in dissociation of molecules the energies of the fragments are far in excess of the thermal energies in the parent gas beam, 0.2-6.0eV compared with thermal energies of 0.02eV. The velocity distribution of the parent molecules is therefore dominated by this new distribution. Any momentum transfer effects are insignificant when compared to the new, fast, velocity distribution. The discussion below therefore applies only to direct electron impact excitation.

4.4.1 Gas Beam Dynamics

The behaviour of gas molecules flowing through an aperture depends on the aperture diameter, D, compared with the mean free path, λ, of molecules in gas. If $D << \lambda$ only molecules which would strike the aperture pass through. This type of flow is known as effusive or molecular flow. If $D >> \lambda$, the molecules suffer frequent collisions with each other in the vicinity of the aperture. As some molecules travel towards the aperture and pass through it, the next layer of molecules experience a net force which results in a drift velocity in the direction of the aperture. The force arises because of the collisions between gas molecules on one side of this layer and the absence of molecules on the other side of the layer. This type of flow is known as hydrodynamic or viscous flow.

The mean free path is defined by

$$\lambda = \frac{1}{\sqrt{2}n\pi a^2}$$

where a is the collisional cross section of the molecule, n is the number density of molecules and is proportional to the gas pressure. Typical values at room temperature and pressure are $a \approx 5\text{x}10^{-15}$ cm^2, $n \approx 3\text{x}10^{-19}$ cm^{-3}, giving $\lambda \approx 7\text{x}10^{-6}$ cm.

The flux entering a solid angle dΩ normal to the aperture assuming effusive flow is

$$N(v)\, dv = C\, \frac{d\Omega}{\pi}\, v^3\, e^{-v^2/\alpha^2}\, dv \qquad 4.7$$

where

$$\alpha^2 = \frac{2kT}{m}$$

and N(v) dv is the number of molecules in the beam with velocities between v and v+dv, dΩ is the solid angle subtended by the detector, m is the mass of the molecule, k is Boltzmann's constant and T is the absolute temperature of the gas.

The total intensity I_0 is given by

$$\begin{aligned} I_0 &= \int I(v)\,dv \\ &= C\,\frac{d\Omega}{\pi}\int v^3\,e^{-v^2/\alpha^2}\,dv \\ &= C\,\frac{d\Omega}{\pi}\,\frac{\alpha^4}{2} \end{aligned}$$

Substituting for C in 4.7,

$$N(v)\,dv = \frac{2I_0}{\alpha^4}\,v^3\,e^{-v^2/\alpha^2}\,dv \qquad 4.8$$

At very low pressures, <0.1 torr, flow is effusive. Only molecules which would strike the aperture leave the source. This results in the preferential selection of molecules having velocities in the direction required to pass through the aperture. To compensate for this, the Maxwellian distribution must be multiplied by v to give 4.7 and 4.8 and resulting in t^{-5} in the time expression.

At higher pressures, >0.5 torr, molecules will collide more frequently in the vicinity of the aperture. Slower molecules may then be scattered out of the beam and the depletion of these low energy molecules must be compensated for by the multiplication of the Maxwellian distribution by a velocity term v^h where $0 \leq h \leq 1$.

At intermediate pressures collisions between gas molecules in the vicinity of the aperture result in a 'diffuse' gas beam emanating from the aperture. This can be represented by the Maxwellian distribution. This is represented by $h=0$.

A long-lived metastable state of a heavy target such as the $(3p^5 4s)^3P_{0,2}$ states in argon may be used to determine the initial velocity distribution of the target gas (French and Locke 1967). The time of flight spectrum observed for the direct electron impact excitation of these states shows no lifetime effects and no recoil effects (see section 4.4.2). Comparison of this experimental velocity distribution with the theoretical distribution described by equation 4.8 enables an accurate determination of the path length between the interaction region and the detector to be made. However, during this work it became apparent that the Maxwellian distribution did not describe adequately the observed velocity distribution. The experimental velocity distribution appeared to have fewer molecules in the low velocity tail of the spectrum.

Mason and Newell (e.g. 1988) follow Borst and Zipf (1971a) in using the Maxwellian distribution with the parameter $h=0$. This is only valid if the gas source produces a purely diffuse beam. Freund and Klemperer (1967) used the modified Maxwellian distribution of Lichten (1957) and generalised it by including the velocity term v^G. The introduction of the multiplying velocity term accounts for the depletion in the low energy tail. 'G' is an adjustable parameter such that $2 \leq G \leq 3$. The value of 'G' depends on the dimensions of the source and the bulk properties of the gas.

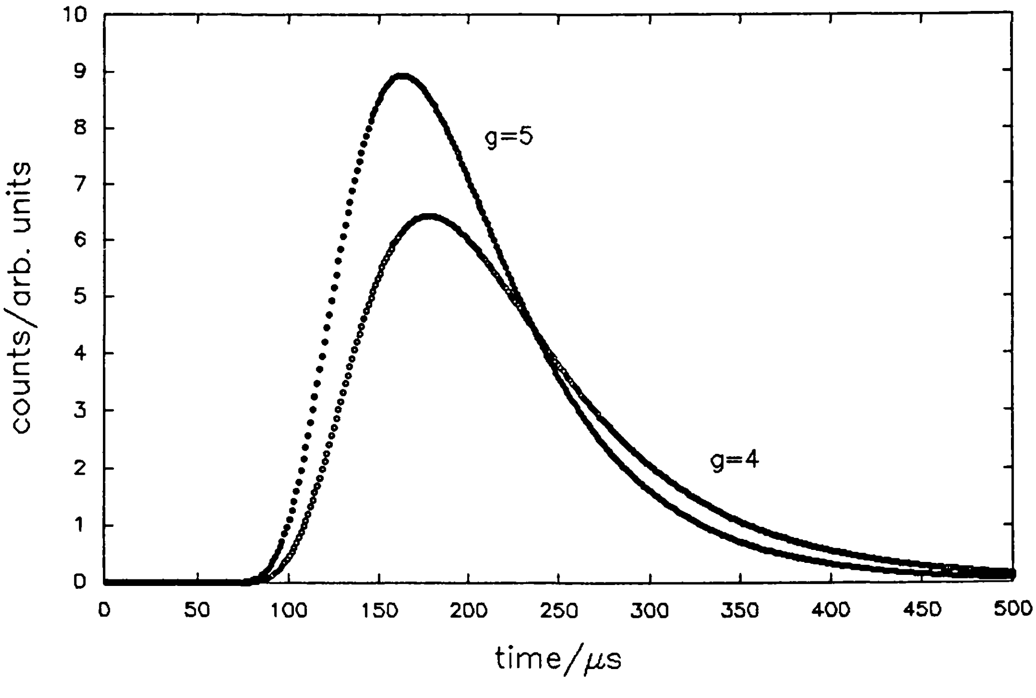

Figure 4.7 Computed time of flight spectra for distributions described by $g=4$ and $g=5$ for temperature $T=300K$.

In the present work, the source was calibrated by assigning a value of 'g' to the observed time of flight spectrum, where g = G+2. The effect of 'g' on the distribution is illustrated in figure 4.7. The value of g will depend on the gas used and the pressure in the gas line, therefore for each gas used the relevant value of g was determined by selecting an incident electron energy at which only one metastable state of known lifetime was detected.

The parameters 'g' and 'L' were varied iteratively until a best fit of the experimental data with the theoretical distribution was found. A value of the path length L was determined by direct measurement of the appropriate distance inside the experimental chamber, this was then used to impose limits on the acceptable values of the path length determined in a least squares fitting process. Consequently a reliable value of 'g' was deduced. Table 4.2 lists the experimentally determined values of 'g' for the gases used in this work.

Table 4.2 Experimentally determined values of 'g' for the gases used in this work.

Gas	Mass /amu	'g'
Ar	40	4.46 ± 0.03
N_2	28	4.95 ± 0.03
CO	28	4.94 ± 0.03

4.4.2 Momentum Transfer

In direct electron impact excitation of atoms or molecules, the momentum transferred from the incident electron to the target gas beam results in an additional velocity component being imposed on the target.

The maximum recoil occurs at the threshold for excitation of a metastable state. At threshold all the energy and momentum of the electron is transferred to the target atom, the electron is therefore scattered with zero energy. The momentum transfer vector, K, can be shown to be antiparallel to the incident electron beam, figure 4.8a.

By conservation of momentum in the direction of the incident electron beam,

$$m_e u_e = m_e v_e + m_a v_a \sin\theta_a$$

where m_a and m_e are the masses of the atom and electron respectively, u_e is the velocity of the electron before the collision, v_e is the final velocity of the electron beam, v_a is the velocity of the target after the collision and θ_{max} is the maximum value of θ_a, the angle of recoil.

Since the velocity of the electron after the collision, v_e, is zero, the maximum recoil angle is given by

$$\theta_{max} = \sin^{-1}\left(\frac{m_e u_e}{m_a v_a}\right)$$

For incident electron energy just sufficient to excite the atom or molecule to a state of energy, E

$$u_e^2 = \frac{2E}{m_e}\left(1-\frac{m_e}{m_a}\right)$$

Assuming the target atom to have thermal energy, the magnitude of the velocity of the scattered atom, v_a, may be approximated by

$$v_a \approx \frac{2222}{\sqrt{A}} \qquad 4.9$$

where A is the atomic weight in atomic mass units.

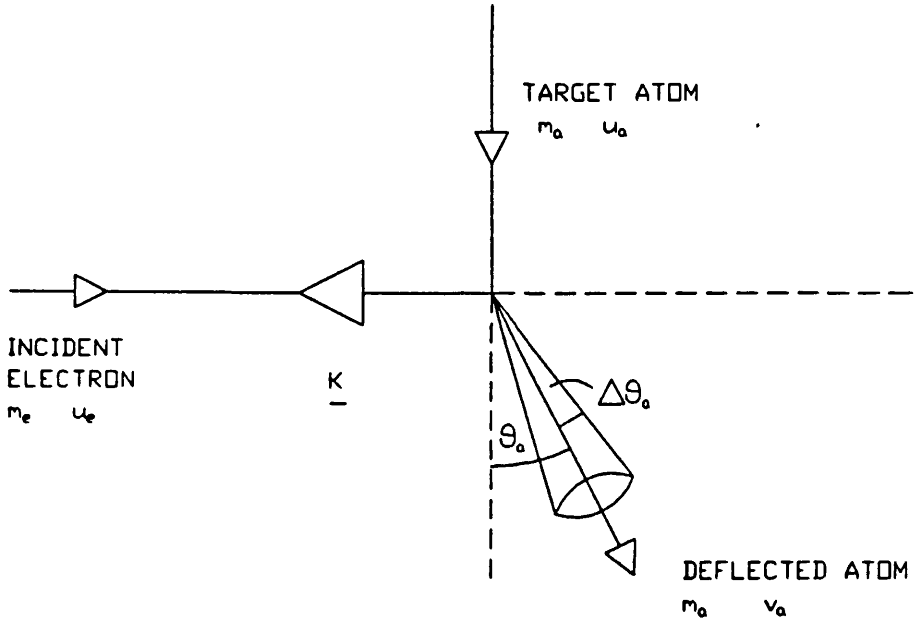

Figure 4.8a Diagram of the electron beam direction, gas beam direction, momentum transfer vector **K**, and recoil angle at threshold.

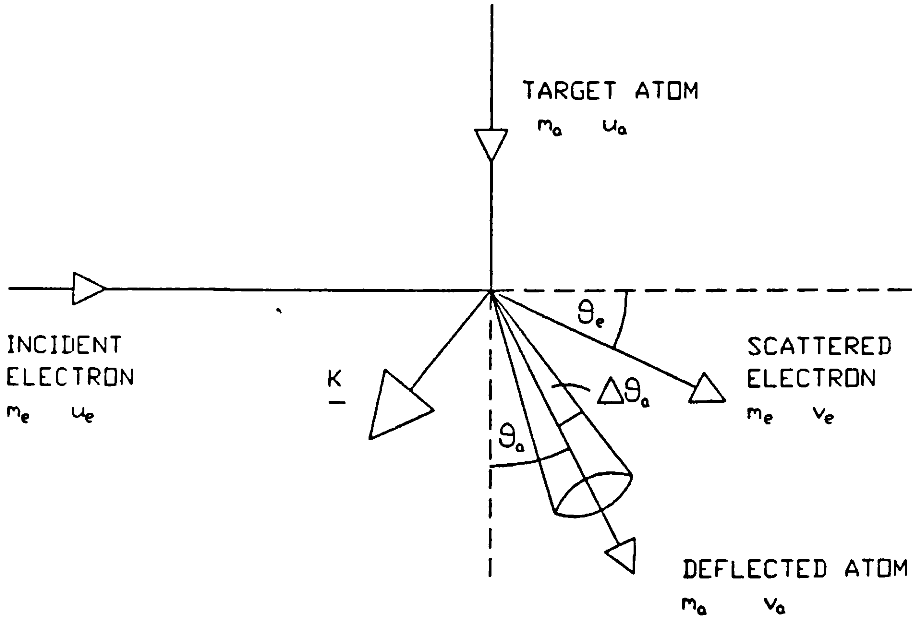

Figure 4.8b Diagram of the electron beam direction, gas beam direction, momentum transfer vector **K**, and recoil angle at energies above threshold.

The maximum recoil angles for the metastable states of the gases used in the present work are given in table 4.3.

Table 4.3 Maximum recoil angles for the metastable states studied in this work. The velocity of the target atom is given by equation 4.9.

Metastable State	Energy /eV	Recoil angle θ_{max}	Metastable State	Energy /eV	Recoil Angle θ_{max}
He($2^1S,2^3S$)	19.6	18.9°	$N_2(a^1\pi_g)$	8.55	4.6°
Ar($^3P_{0,2}$)	8.4	4.5°	CO($a^3\pi$)	6.01	3.85°
$N_2(A^3\Sigma^+_u)$	6.17	3.88°	CO(10eV)	8.45	4.85°

As the incident electron energy increases the momentum transfer vector tends towards the direction perpendicular to the incident electron beam energy, figure 4.8b, and the angle of recoil is reduced.

Since the atoms or molecules of the target beam have a range of velocities, there will be a range of recoil angles. No recoil phenomena are observed if the acceptance angle of the detector is greater than the sum of the mean recoil angle, Θ_a, and the angular divergence of the gas beam, $\delta\Theta_a$. The acceptance angles of the detectors used in this work are given in table 4.4.

The plane angle calculated is the angle between the edge of the view cone of the detector and the normal to the detector surface. The solid angle, Ω, subtended by the detector at the interaction region is given by

$$\Omega = \frac{\delta A}{L^2}$$

where δA is the surface area of the detector and L is the distance of the detector from the interaction region.

Table 4.4 Acceptance angles of the detectors used in this work.

Detector	Plane Angle	Solid Angle /sr
Channel electron multiplier	4.1°	0.016
Ceramic channel electron multiplier	3.6°	0.012
Tantalum Surface Detector	6.5°	0.046

If the view cone of the detector is greater than the recoil angle of the metastable atoms or molecules studied no recoil effects are observed. The recoil angles in the excitation of molecular nitrogen, carbon monoxide and argon are less than the acceptance angles of all three detectors used in the present work, therefore it was not expected that any recoil effects would be observed. The recoil angle in helium, however, is greater than the acceptance angles of these detectors and recoil would be observed. Therefore, when calibration of the apparatus was necessary, argon was used instead of helium.

If recoil effects are to be studied, a collimated gas source is required since in a diffuse source the angle of recoil of atoms or molecules from different regions of the beam lie within the angular spread of the beam and no effects will be observed.

The momentum transfer from the electron to the scattered atom, or molecule, at threshold has been described above. At energies above threshold, figure 4.8b, the electrons are scattered with an angular distribution and have finite kinetic energies. The momentum transferred to the target is slightly different in each scattering event. This is reflected in the motion of the scattered atoms, the velocity of each atom and thus the arrival time at the detector being slightly different.

The effect of recoil on the time of flight spectrum has been studied by Donnelly et al (1971), figure 4.9. In s-wave scattering in helium, electrons scattered in two different directions, one forward scattered and one backward scattered, cause the corresponding atoms to be scattered through the same angle, θ_a, but because the final momenta of the electrons are different, the magnitude of the velocities of the scattered atoms must be different. This results in two peaks in the time of flight spectrum. The first peak at the shorter flight time is due to the atoms corresponding to the backward scattered electrons. The second peak is due to the slower atoms corresponding to the forward scattered electrons. The relative size of these peaks depends on the incident electron energy. At energies close to threshold backward scattering dominates while at higher energies the forward scattering peak becomes dominant.

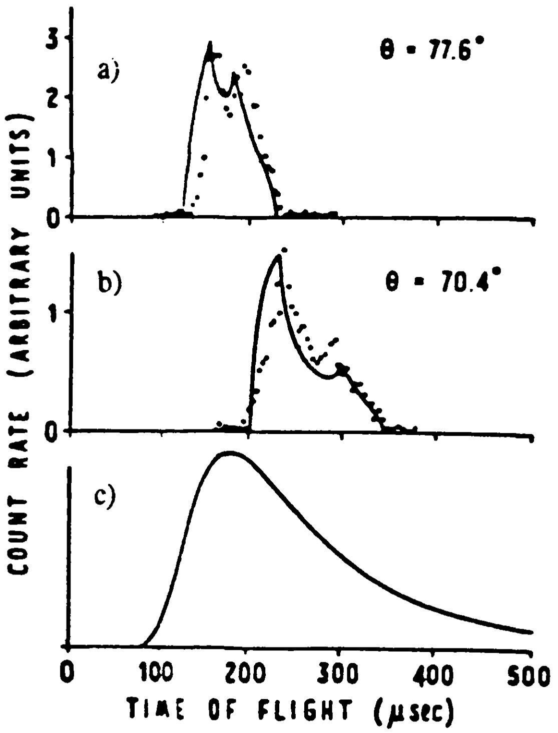

Figure 4.9 Effects of collimation of the gas beam on the time of flight spectrum, a) 3% collimation, observation angle 77.6°, b) 3% collimation, observation angle 70.4° and c) no collimation (Donnelly et al 1971).

To observe recoil effects in the time of flight spectrum it is necessary to have a collimated gas beam, a monochromatic electron beam and a detector of small acceptance angle. A finite energy spread in the electron beam or a large detector acceptance angle will smooth out the recoil features in the spectrum in the same way as a diffuse gas beam. In this work, a gas source was designed to produce a collimated beam to investigate recoil effects (section 4.5).

4.5 Experimental Gas Sources

Four different gas sources were investigated by observing the experimental velocity distributions obtained for direct electron impact excitation of helium.

a) A glass discharge tube of 8mm internal diameter,
b) A short, 5mm, hypodermic needle, internal diameter 1mm, mounted in a copper tube,
c) A long, 30mm, hypodermic needle, internal diameter 1mm, mounted in a copper tube,
d) A short, 5mm, hypodermic needle, internal diameter 1mm, mounted perpendicularly to the gas line.

The design of each of these sources is shown in figure 4.10. A time of flight spectrum for the metastable states He(2^1S) and He(2^3S) was recorded for each source at an incident electron energy of 22eV, 2.5eV above threshold.

The time of flight spectra showed some collimation of the gas beam produced by sources (b) and (c). The peak in the time of flight spectrum was at a shorter flight time than expected and there was a distinct shoulder in the high velocity tail of the spectrum, figure 4.11a. Although the time of flight spectrum observed when using source (a) showed only a single peak, a comparison of the experimental data with the theoretical Maxwellian distribution did not show good agreement. This suggests that there is some degree of collimation in the gas beam produced by this source.

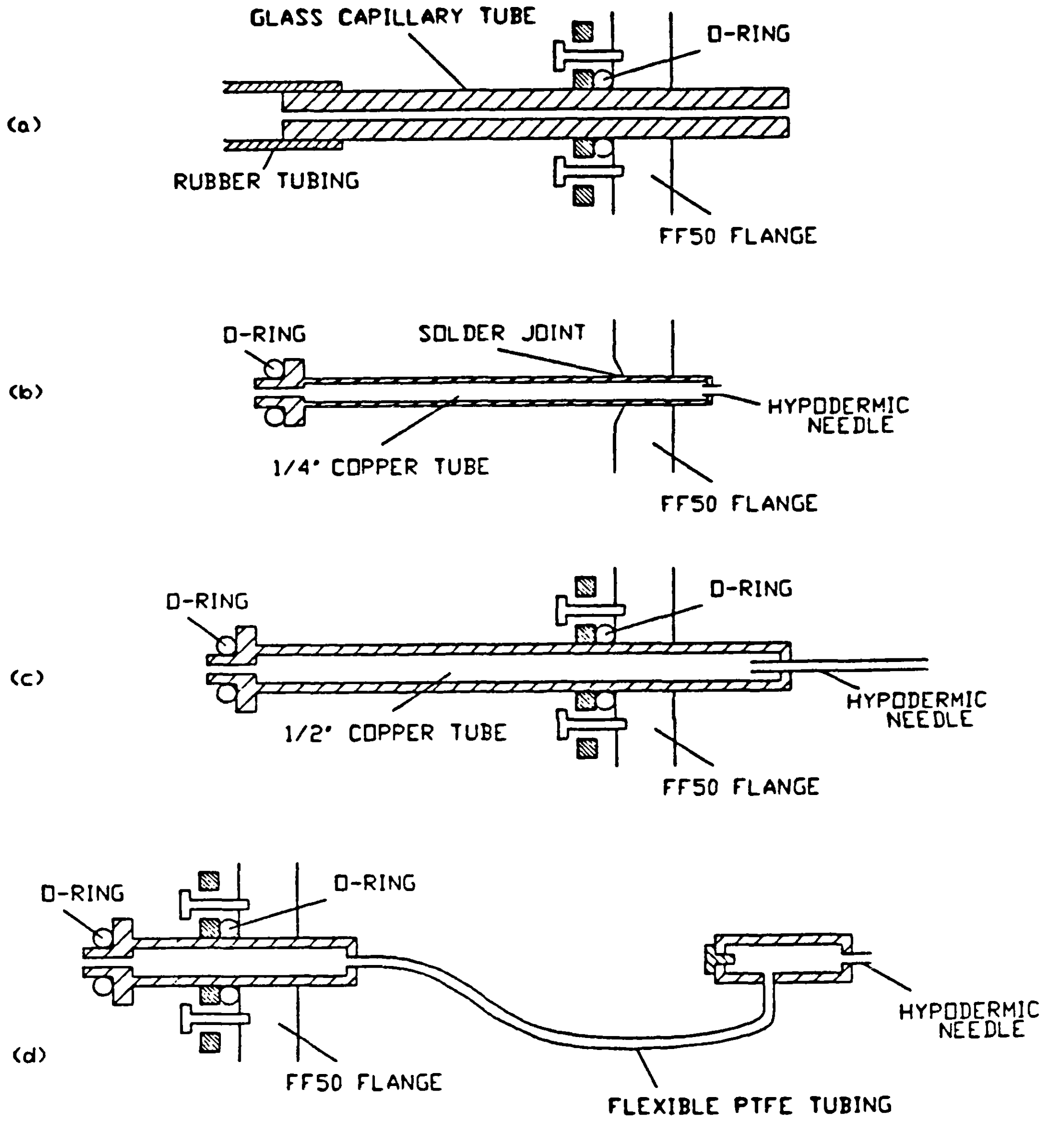

Figure 4.10 Diagrams of the gas sources tested, a) glass discharge tube, b) 5mm hypodermic needle, c) 30mm hypodermic needle and d) 5mm hypodermic needle mounted perpendicular to the gas inlet.

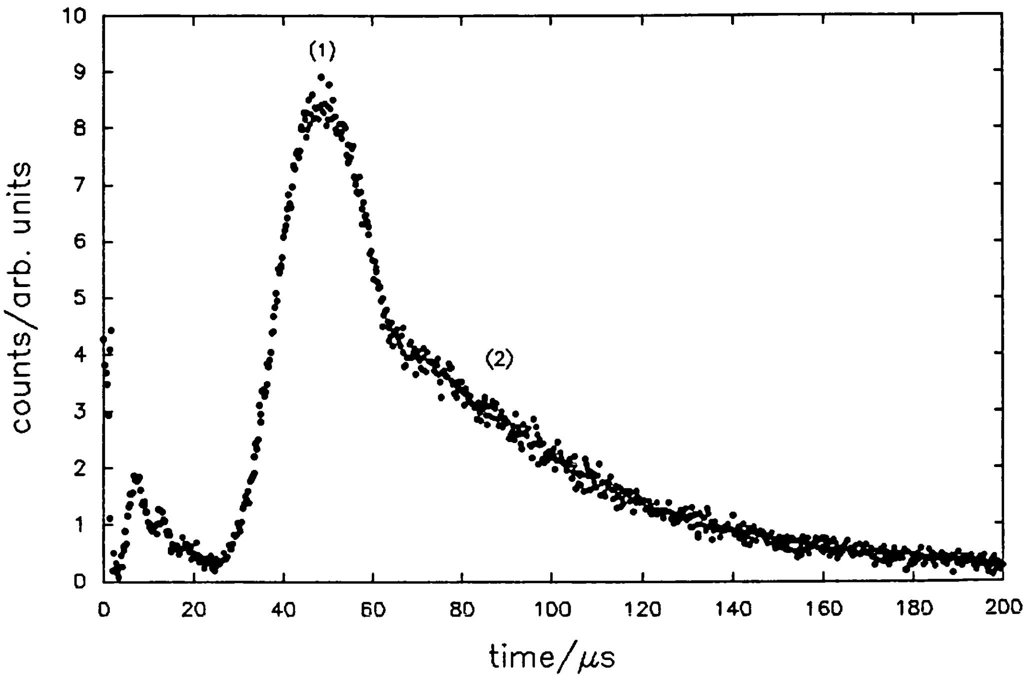

Figure 4.11a Time of flight spectrum of metastable helium atoms for an incident electron energy of 21eV using the 30mm hypodermic needle.

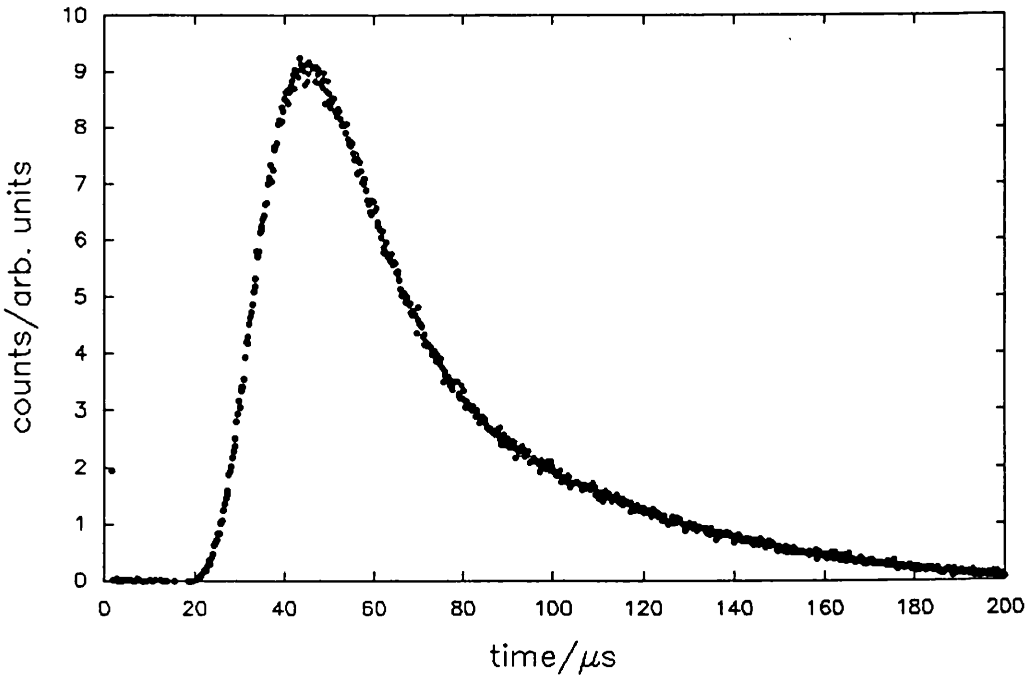

Figure 4.11b Time of flight spectrum of metastable helium atoms for an incident electron energy of 20eV using the 5mm hypodermic needle mounted perpendicularly.

Source (d) was designed to produce a diffuse gas beam. The gas entered the vacuum chamber through a needle valve mounted in a flange. In the experimental chamber a PTFE tube connected the needle valve to the source. This PTFE tube was not straight and to prevent it from bending and closing a thick copper wire was threaded inside it throughout the whole length. The hypodermic needle itself was mounted at 90° to the incoming gas beam to ensure that there was no collimation. Tests of this source with helium revealed no noticeable collimation, figure 4.11b. This source was used in all subsequent experiments.

4.6 Summary

The technique of translational spectroscopy has been described in this chapter and the information gained from the time of flight spectra discussed. In electron impact excitation, the metastable species produced in the interaction region retain the speed distribution of the parent target gas beam. The finite lifetime of the metastable species may cause distortions of this speed distribution as observed in the time of flight spectra. Consequently the lifetime of the metastable beam emanating from the interaction region may be deduced from the time of flight spectra. This was used in the calibration of the detectors used in this work, described in the next chapter. To determine the lifetime accurately, the speed distribution of the parent target gas beam must be known and this will depend on the gas source used. In dissociative excitation, the energy imparted to the fragments on the dissociation of the molecule is greatly in excess of the thermal energies of the parent gas beam. The speed distribution of the fragments may be deduced from the time of flight spectra and the parent potential energy state from which the fragments originate may be identified.

Chapter Five

Calibration of Detectors

> *The generals, the institution, can select a strategy, lay it all out, but what happens on the battlefield is quite different.*
>
> Leo Tolstoi (1898)

5.1 Introduction

Two systems for the detection of metastable species were used in the course of this work, a commercial Mullard type B419BL channel electron multiplier and a specifically designed tantalum surface detector. Two other detection systems, a Murata EMW6081B ceramic channel electron multiplier and a xenon surface detector were also investigated.

The channel electron multiplier is a convenient method of detecting metastable species since it has a detection threshold of ~8eV and is simple to install and operate. In this work, the channel electron multiplier was used to detect selectively those metastable states of excitation energy greater than 8eV such as the $O(^5S)$ atoms produced in the dissociation of carbon monoxide, carbon dioxide and carbonyl sulphide. Studies of metastable species of excitation energy <8eV required a detector of detection threshold less than 8eV to be developed. A tantalum surface detector was therefore designed and constructed and its work function established by a series of calibration tests.

A simple method of detecting selectively one of the several possible metastable products of electron impact collisions is by choosing a detector of high enough work function to discriminate against the lower lying states. However such a detector cannot be used to isolate a lower lying state from higher lying states since all states of excitation energy greater than the work function of the surface will be detected. For example, to study metastable $O(^1S)$ atoms of excitation energy ~4eV in a beam containing $O(^5S)$ atoms of excitation energy ~9eV an alternative method of detection is required. One such method of detection of $O(^1S)$ atoms using a condensed xenon surface was investigated.

5.2 The Channel Electron Multiplier

Channel electron multipliers have been used extensively as a means of detecting metastable species (e.g. Brunt et al 1978, Mason and Newell 1987). The detection threshold of the channel electron multiplier depends on the material used and the manufacturing process. The detection threshold and efficiency are also influenced by the environment in which the channel electron multiplier has been kept and its age.

It is therefore desirable to determine the detection threshold of the channel electron multiplier in situ. This may be determined conveniently by establishing which metastable species are detected. Mason and Newell (1987) studied the direct electron impact excitation of molecular nitrogen using a Mullard B419BL channel electron multiplier. They established that the channel electron multiplier used was efficient in detecting metastable $N_2(a^1\pi_g)$ molecules of excitation energy 8.55eV, but did not detect metastable $N_2(A^3\Sigma^+{}_u)$ molecules of excitation energy 6.17eV. Brunt et al (1978) state that the detection efficiency of the channel electron multiplier used in their studies drops below 8eV and falls to zero at ~7eV. However they do not state the type of channel electron multiplier used.

5.2.1 Description of the Channel Electron Multiplier

The Mullard B419BL electron multiplier is a coiled, hollow glass tube of internal diameter 2.2mm. The tube is closed at one end with a conical opening of diameter 10mm, the mouth, at the other. Fine nickel wires allow a potential to be applied between the ends of the tube. The inside wall of the channel electron multiplier is coated with a resistive material of high secondary electron emission coefficient. When the potential is applied across the multiplier, this forms a continuous dynode and an accelerating field is established. The minimum operating potential of the B419BL multiplier is 2.5kV and the maximum 3.5kV. In this work, the mouth was operated at the bias potential and a potential of +3kV applied to the other end.

Channel electron multipliers are sensitive to electrons, excited neutral species, ions, short wave ultraviolet radiation and soft x-rays. When such a particle enters the mouth of the channel electron multiplier it will impinge upon the wall of the tube causing secondary electron emission. These secondary electrons are accelerated along the tube and collide again with the wall producing tertiary electrons. Thus an avalanche of electrons is produced at the high voltage end of the tube and up to 10^8 electrons contribute to the output pulse of 12ns FWHM with a rise time 5ns. The nominal background pulse rate from the channel electron multiplier is $0.25s^{-1}$ (Petley 1971).

The channel electron multiplier was mounted on an optical bench perpendicular to the electron gun bench. The channel electron multiplier was mounted in a PTFE sleeve inside a copper cylinder. This cylinder was of the same diameter as the lenses of the flight tube so that the centre of the channel electron multiplier mouth was aligned with the centre of the interaction region. The channel electron multiplier was covered with a copper shield maintained at bias potential. The inside of the shield was coated with DAG50 to reduce electron reflection.

The path length from the interaction region to the channel electron multiplier was 7.0cm. A flight tube consisting of three lens elements, L7, L8 and L9, was placed between the interaction region and the channel electron multiplier, figure 5.1. The lens elements of the flight tube were similar to those used in the electron gun being made of titanium and having internal diameter 10mm and external diameter 15mm. Potentials were applied to each lens element by a Kingshill 1500 0-150V supply connected to provide a negative potential with respect to the bias potential. The potential at each of the lens elements was varied by a potentiometer.

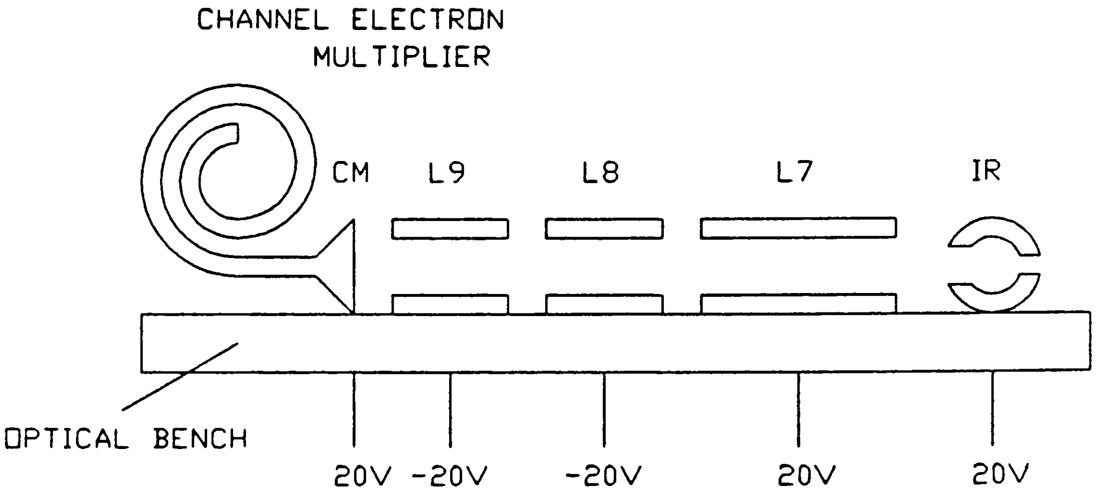

Figure 5.1 Schematic diagram of the Mullard B419BL channel electron multiplier positioned on an optical bench. Typical voltages on the lens elements of the flight tube are indicated.

The first of these lens elements, L7, is at the same potential as the outer Faraday cup and the interaction chamber to prevent electrostatic field penetration from the flight tube into the interaction region. The second and third lens elements, L8 and L9, were operated at a negative potential, -bias, to deflect electrons scattered out of the interaction region away from the channel electron multiplier.

5.2.2 Determination of the Detection Threshold

Direct electron impact excitation of the metastable states of several gases was investigated to determine in situ the detection threshold of the Mullard B419BL channel electron multiplier used in this work.

The channel electron multiplier was found to be very efficient in detecting the He(2^1S) and He(2^3S) metastable states of excitation energies of 20.61 and 19.82eV respectively, figure 5.2a, and the Ar($^3P_{0,2}$) metastable states of excitation energies 11.72 and 11.55eV, figure 5.2b.

There are two metastable states of carbon monoxide, the CO($a^3\pi$) state of excitation energy 6.01eV and an as yet unclassified state of excitation energy >9.5eV (Mason and Newell 1988). In this work, no signal was observed in the direct excitation of carbon monoxide at incident electron energies <10eV indicating that the channel electron multiplier did not detect CO($a^3\pi$) and therefore had a detection threshold >6.01eV. This was confirmed in later studies of the dissociation of carbon dioxide and carbonyl sulphide in which no metastable states of carbon monoxide were observed in time of flight spectra recorded by the channel electron multiplier (chapter seven).

The most conclusive results for the determination of the detection threshold followed from a study of electron impact excitation of molecular nitrogen. There are three metastable states of nitrogen, $N_2(A^3\Sigma^+_u)$, $N_2(a^1\pi_g)$ and $N_2(E^3\Sigma^+_g)$ with excitation energies 6.17eV, 8.55eV and 11.87eV respectively.

At incident electron energies less than 8eV, no signal was observed from the channel electron multiplier indicating that no $N_2(A^3\Sigma^+_u)$ metastable molecules were detected. Metastable $N_2(a^1\pi_g)$ molecules were observed at incident electron energies of >9eV. A typical time of flight spectrum is shown in figure 5.2c.

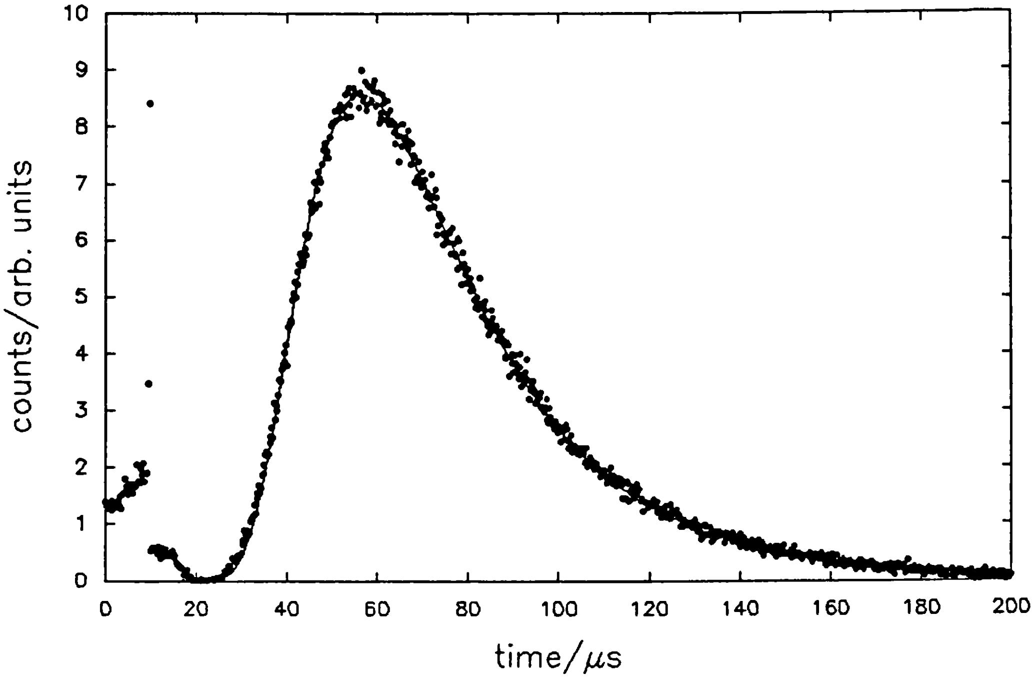

Figure 5.2a Time of flight spectra recorded using the channel electron multiplier for direct excitation of helium at an incident electron energy of 21eV. The fit assume a lifetime of 0.06s, giving g=4.98.

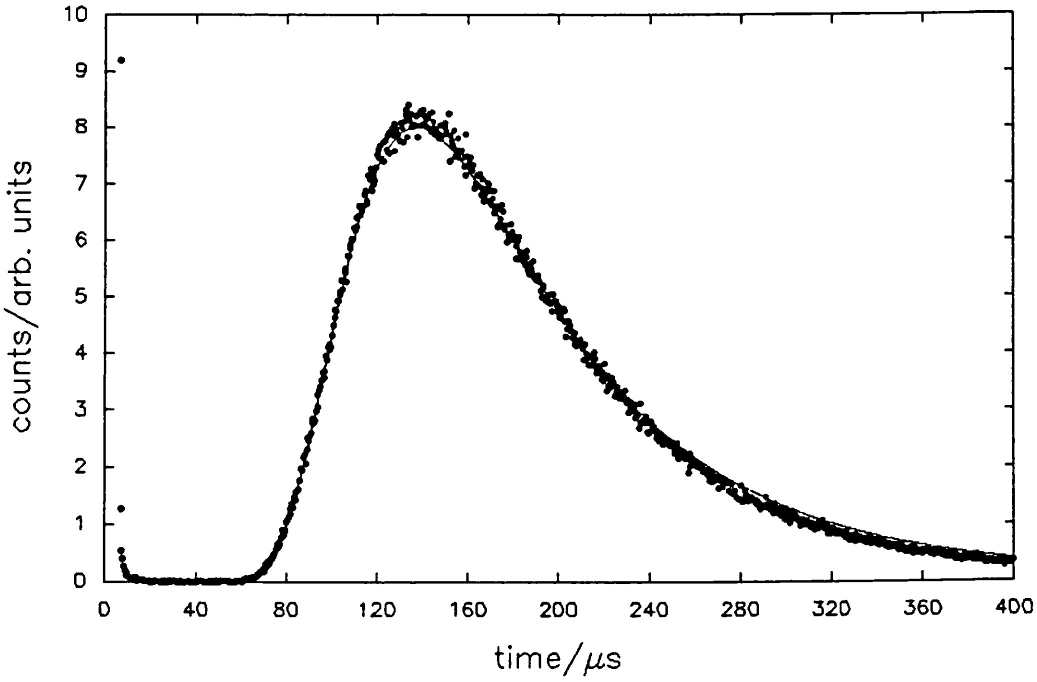

Figure 5.2b Time of flight spectra recorded using the channel electron multiplier for direct excitation of argon at an incident electron energy of 23eV. The fit assumes a lifetime of 3s, giving g=4.46.

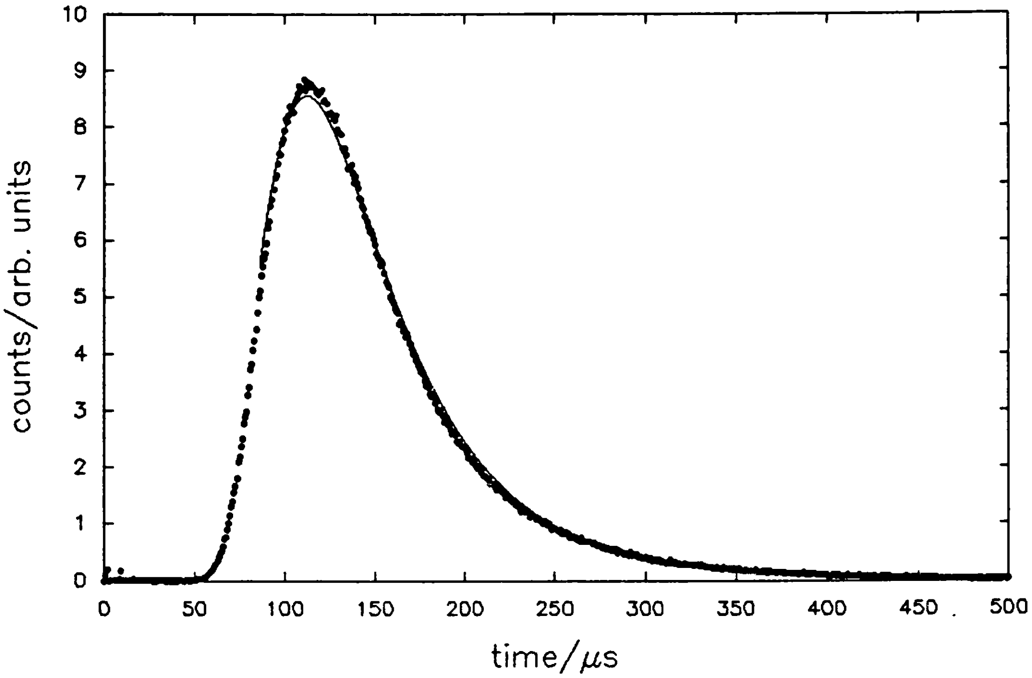

Figure 5.2c Time of flight spectra recorded using the channel electron multiplier for direct excitation of nitrogen at an incident electron energy of 12eV. The fit assumes a velocity distribution of the parent gas beam described by g=4.94 determined from the time of flight spectrum for $N_2(A^3\Sigma^+_u)$ metastable molecules detected by the tantalum surface detector. Using this value of g, the lifetime of the metastable beam was found to be 120μs, indicating that only $N_2(a^1\pi_g)$ metastable molecules contribute to the beam.

5.2.3 Conclusions

These studies show that the channel electron multiplier has a detection threshold of between 6.17eV and 8.55eV and is therefore a good method of discriminating against lower lying states such as $CO(a^3\pi)$. The channel electron multiplier was therefore used in this work to isolate the $O(^5S)$ fragment of excitation energy 9.14eV produced in the dissociation of carbon monoxide, carbon dioxide and carbonyl sulphide from the lower lying $CO(a^3\pi)$ and $S(^5S)$ fragments (chapter seven).

5.3 The Tantalum Surface Detector

Detection of metastable species at a metal surface is possible if the excitation energy of the metastable state is greater than the work function of the surface. Transition metals are both simple to work with and have work functions in the range 3eV to 6eV and are therefore useful in the detection of low lying metastable species. The secondary electrons emitted as metastable species impinge on the surface may be conveniently detected at a channel electron multiplier.

5.3.1 Description of Tantalum Surface Detector

The low work function detector used in this work was based on that of Zubek and King (1982) who developed a tantalum surface detector with detection threshold ~4eV to study excitation of low lying metastable states such as $Hg(^3P_{0,2})$. In this work, tantalum ribbons were used since heated tantalum has been shown to be sensitive to $CO(a^3\pi)$ and $N_2(A^3\Sigma^+{}_u)$ metastable states (Freund 1971b, Newman et al 1983). The secondary electrons from the surface were detected by the Mullard B419BL channel electron multiplier.

The tantalum surface detector used in this work is shown in figure 5.3. Seven tantalum strips of 23 x 3mm cut from a tantalum sheet of thickness 0.025mm were mounted at 45° in slits cut into a hollow ceramic block of external dimensions 23 x 18 x 7mm and internal dimensions 17 x 10 x 7mm. Constantan heating wires of 0.5mm diameter were spot welded along the back of each tantalum strip and were spot welded together so that currents passing through successive ribbons were antiparallel. The heating wires were connected to a Coutant LB1000.2 supply which provided a stable current through the constantan wires. The tantalum surface detector was mounted on two 25mm lengths of M2.5 studding on a modified optical bench and the channel electron multiplier placed behind the tantalum surface. The path length from the interaction region to the tantalum surface was 7cm.

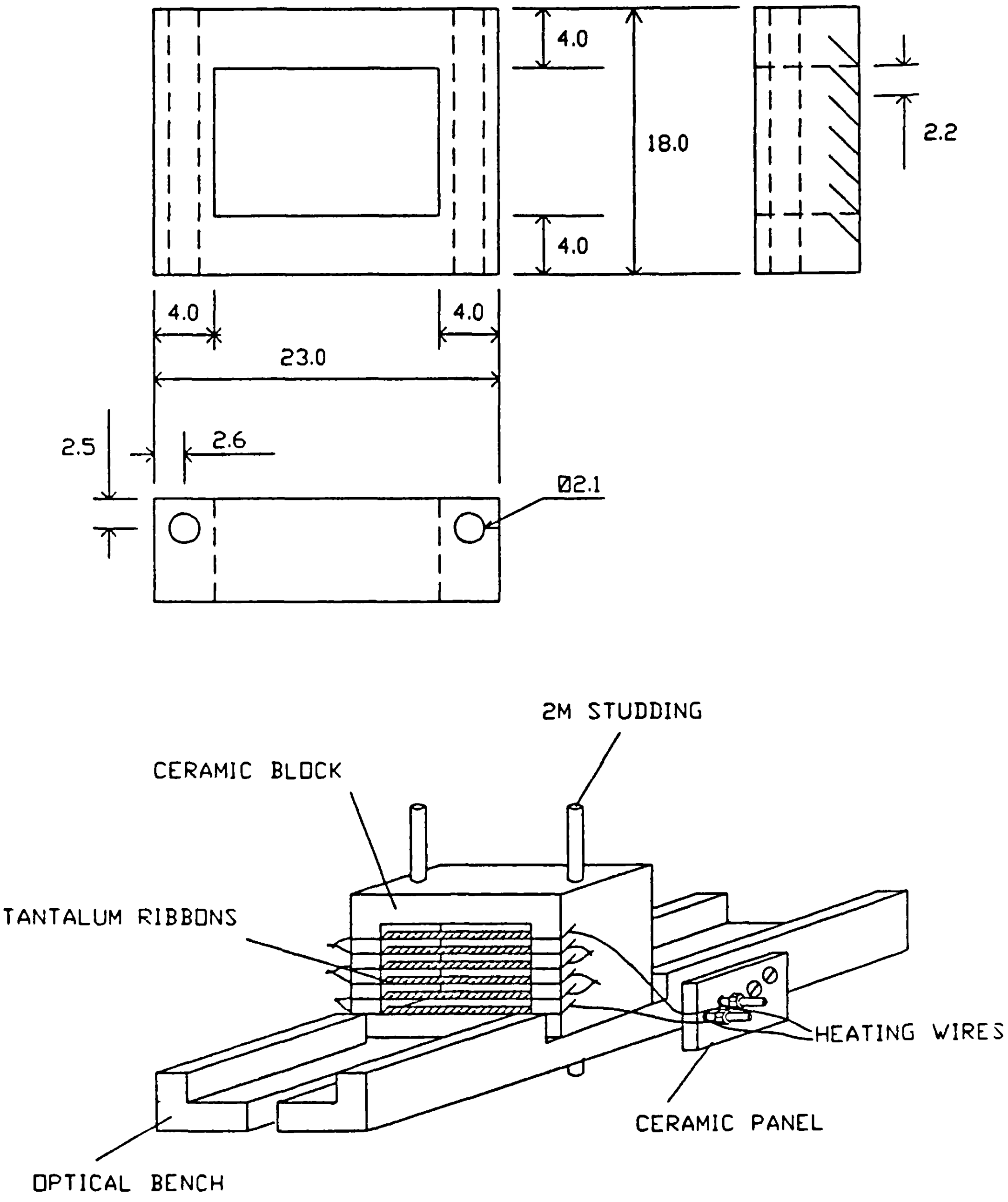

Figure 5.3 Schematic diagram of the tantalum surface detector used in this work.

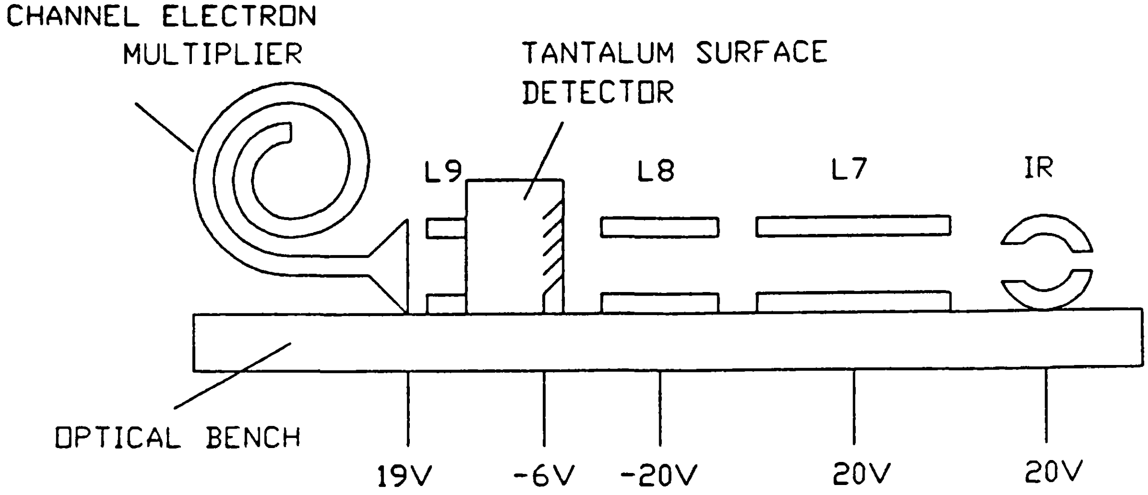

Figure 5.4 Electrostatic lens elements of the flight tube used with the tantalum surface detector. Typical potentials are indicated.

The electrostatic lens elements of the flight tube were arranged as shown in figure 5.4. A small cylindrical electrode, L9, was placed between the tantalum surface detector and the channel electron multiplier to focus the secondary electrons from the tantalum into the multiplier. A negative lens element, L8, was placed immediately in front of the tantalum surface to direct the secondary electrons emitted in the forward direction into the channel electron multiplier. The lens element adjacent to the interaction region, L7, was again maintained at bias potential to prevent electrostatic fields penetrating into the interaction region. The lens element L8 was also used to prevent electrons scattered out of the interaction region striking the tantalum surface, therefore the potential on this lens element was varied depending on the incident electron energy. The potentials applied to the lens elements L8 and L9 and to the tantalum ribbons were determined experimentally to optimise the count rate at the channel electron multiplier.

In the studies of electron impact excitation of molecular nitrogen and carbon monoxide it was found that heating the tantalum ribbons increased the detection efficiency considerably. The effect of surface impurities on the detection efficiency of a metal surface was discussed in chapter two. Some authors (e.g. Dunning et al 1971) concluded that impurities increase the secondary electron yield since the impurities are Penning ionised by the incident metastable species. The low lying metastable states detected in this work are unlikely to cause Penning ionisation of all the surface impurities since one of the major adsorbates is expected to be molecules of the target gas itself. Heating is also expected to result in a decrease in the work function of the metal by $\sim 10^{-4}$eV K^{-1} (Hughes and DuBridge 1932). Thus in this work it is reasonable that the detection efficiency of the surface increases as adsorbates are removed by heating. It was determined experimentally that a heating current of 3A through the constantan wires was sufficient to cause thermionic emission from the wires resulting in an unwanted signal at the channel electron multiplier. This placed an upper limit on the operating temperature of the tantalum ribbons and the constantan wires were only heated by passing 3A through the wires when it was necessary to clean the tantalum and no data was being recorded. Currents of between 1 and 2A were used to heat the tantalum gently during data collection. The resulting temperature is estimated to be between ~ 40 and $\sim 70\,^\circ$C, much lower than the operating temperatures of 450°C to 550°C used by Zubek and King.

The tantalum ribbons were heated by a current of 2A in these studies of excitation of molecular nitrogen and carbon monoxide to maximise the sensitivity of the surface to the $CO(a^3\pi)$ and $N_2(A^3\Sigma^+{}_u)$ metastable states. However in studies of dissociation of carbon monoxide, carbon dioxide, carbonyl sulphide and nitrous oxide it was found that heating the tantalum ribbons caused a decrease in the detection efficiency. The most dramatic effect occurred when carbon dioxide was introduced into the system, the count rate rapidly falling to zero. The tantalum was not heated when studying the dissociation of carbon dioxide and was heated gently by a current of 1A when studying dissociation of the other gases. In electron impact dissociation of all of these molecules atomic oxygen is produced. Undissociated target molecules reaching the hot tantalum may also dissociate on the hot surface to produce atomic oxygen. It is suggested that these oxygen atoms adsorbed onto the surface reduced the detection efficiency of the tantalum.

5.3.2 Determination of the Detection Threshold

The detection threshold was determined experimentally by studying the direct electron impact excitation of molecular nitrogen and carbon monoxide. For each of these molecules time of flight spectra were recorded for several incident electron energies from threshold to $\sim$30eV. These experimental spectra were compared with the modified Maxwellian distribution (chapter four) to determine the lifetime of the metastable beam.

The metastable beam detected at the tantalum surface contains more than one metastable state and consequently the lifetime of the beam depends on the lifetime of each of the components of the beam, their production cross sections and the detection efficiency of the tantalum surface to each state. Comparison with the modified Maxwellian distribution to determine the lifetime of the metastable beam requires knowledge of the path length, L, between the interaction region and the detector, the temperature of the target molecules, T, and the parameter 'g' which describes the velocity distribution of the gas molecules.

The path length L measured directly in the apparatus was 7.2cm. This was confirmed by recording a time of flight spectrum for the direct electron impact excitation of $Ar(^3P_{0,2})$ metastable atoms. The lifetime of these states have been reported as $>$3s (Small-Warren and Chui 1975, van Dyck et al 1972). This experimental spectrum was then compared with the modified Maxwellian distribution by an iterative fitting procedure varying both L and g. The values found for L and g by this method were 7.1 ± 0.2cm and 4.46 ± 0.03 respectively.

Changes in the time of flight spectra due to temperature differencies of ±50K were not observable above the statistical fluctuations in the spectra. Therefore any cooling of the gas beam on admittance to the chamber was considered to have little effect and the temperature of the gas beam was assumed to be 300K. In the excitation of molecular nitrogen and carbon monoxide, the value of 'g' appropriate to the specific target gas had to be determined. This was achieved by choosing an incident electron energy at which only one metastable state of target gas is excited. If the lifetime of this metastable state is known, the experimental spectrum may be compared with the theoretical distribution to determine the value of 'g'.

a) Excitation of Molecular Nitrogen

Electron impact excitation of molecular nitrogen has been widely studied and only a brief summary will be given here, a full review has been published by Lofthus and Krupenie (1977) and Trajmar and Cartwright (1984). The tantalum surface was expected to be capable of detecting all three metastable states of nitrogen, $N_2(A^3\Sigma^+_u)$, $N_2(a^1\pi_g)$ and $N_2(E^3\Sigma^+_g)$ of excitation energies 6.17eV, 8.55eV and 11.87eV respectively.

Time of flight spectra were recorded for a range of incident electron energies from threshold to 21eV. A typical time of flight spectrum is shown in figure 5.5.

i) Lifetimes of the Metastable States of Molecular Nitrogen

The lifetime of the metastable state or states detected must be known for the experimental time of flight spectra to be compared with the modified Maxwellian distribution. Experimental and theoretical determinations of the lifetime of each of the metastable states of molecular nitrogen are summarised in tables 5.1, 5.2 and 5.3.

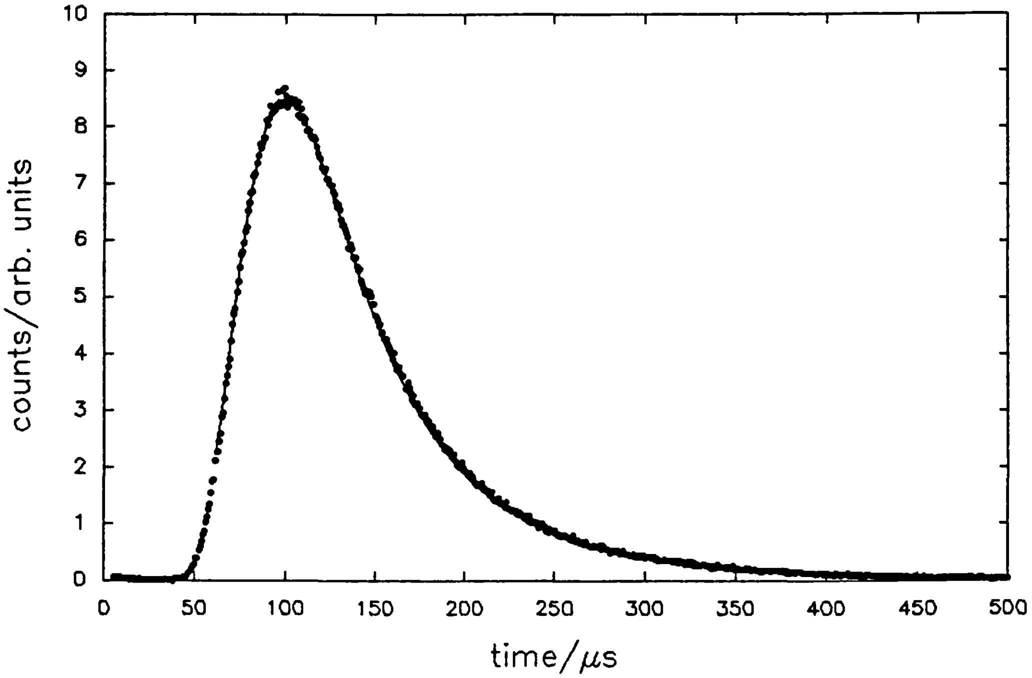

Figure 5.5 Typical time of flight spectrum for direct excitation of metastable molecular nitrogen at an incident electron energy of 15eV and detected at a tantalum surface detector. The fit assumes g=4.94, giving the lifetime of the metastable beam as 456μs.

Table 5.1 Experimental and theoretical determinations of the lifetime of the $N_2(a^1 \pi_g)$ metastable state.

Lifetime /μs	Vib. Level	Reference	Method
170 ± 0.30	all	Lichten 1957	Molecular beam time of flight and detection of metastable products
120 ± 0.50	all	Olmsted et al 1965	Molecular beam time of flight and detection of metastable products
115 ± 20	all	Borst and Zipf 1971a	Molecular beam time of flight and detection of metastable products
115 ± 10	all	Mason and Newell 1987	Molecular beam time of flight and detection of metastable products

Table 5.1 continued

Lifetime /μs	Vib. Level	Reference	Method
120 ± 20	all	Mason 1990	Measured kinetic energy distribution of molecular nitrogen fragments from dissociation of nitrous oxide
46	all	Garstang 1961	Measured generalised oscillator strengths
150	all	Skerbele and Lessettre 1970	Measured generalised oscillator strengths
144 ± 43	v=0	Shemansky 1969	Measured oscillator strengths
146 ± 44	v=1		
148 ± 44	v=2		
150 ± 45	v=3		
152 ± 46	v=4		
80	all	Holland 1969	Measured radiation from the transition $N_2(a^1\pi_g - X^1\Sigma^+{}_g)$
120 ± 20	v=1	Curtis and Erman 1977	Measured radiation from the transition $N_2(a^1\pi_g - X^1\Sigma^+{}_g)$
56 ± 4	v≤2	Marinelli et al 1989	Used two photon excitation of specific vibrational levels and observed emission from the transition $N_2(a^1\pi_g - X^1\Sigma^+{}_g)$
30	all	Ching et al 1967	Calculated oscillator strengths
76 ± 10	v=1	Pilling et al 1971	Calculated oscillator strengths
90 ± 8	v=2		
92 ± 8	v=3		
59	v=0	Dahl and Oddershede 1986	Calculated the rate of the $N_2(a^1\pi_g - X^1\Sigma^+{}_g)$ transition
59	v=1		
60	v=2		
62	v=3		
68	v=4		

Table 5.2 Experimental and theoretical determinations of the lifetime of the $N_2(A^3\Sigma^+_u)$ metastable state.

Lifetime /s	Reference	Method
0.01	Lichten 1957	Molecular beam time of flight and detection of metastable products
0.9	Zipf 1963	Molecular beam time of flight and detection of metastable products
2.0	Carleton and Oldenberg 1961	Measured radiation from the transition $N_2(A^3\Sigma^+_u - X^1\Sigma^+_g)$
1.4	Shemansky and Carleton 1969	Reanalysis of the results of Carleton and Oldenberg (1961)
<3.5	Meyer et al 1971	Measured radiation from the transition $N_2(A^3\Sigma^+_u - X^1\Sigma^+_g)$

Table 5.3 Experimental and theoretical determinations of the lifetime of the $N_2(E^3\Sigma^+_g)$ metastable state.

Lifetime /µs	Reference	Method
190	Borst and Zipf 1971a	Molecular beam time of flight and detection of metastable products
270 ± 100	Freund 1969	Molecular beam time of flight and detection of metastable products
210 ± 100	Freund 1969	Reanalysis of Freund's results by Borst and Zipf (1971a)
225 ± 20	Mason (unpublished)	Molecular beam time of flight and detection of metastable products

At incident electron energies <8.55eV, the only metastable state of molecular nitrogen excited is $N_2(A^3\Sigma^+_u)$. The lifetime of this state is long with respect to the average flight time in this work, 500μs, and therefore decay effects in the time of flight spectrum will be negligible. The time of flight spectrum recorded for an incident electron energy of 8.0eV was therefore compared with the modified Maxwellian distribution to determine the value of 'g'. The value of 'g' determined by the fitting procedure was 4.94.

This value of 'g' was then used to fit all the other direct electron impact excitation spectra to determine the apparent lifetime of the metastable beam at each excitation energy by comparison with the modified Maxwellian distribution. Lifetime determinations are shown in table 5.4.

Table 5.4 Lifetime of the metastable nitrogen beam at incident electron energies between 10 and 21eV.

Incident Electron Energy /eV	Apparent Beam Lifetime /μs	Incident Electron Energy /eV	Apparent Beam Lifetime /μs
10	1000	15	456
12	175	17	479
13	376	21	288

The variation of the lifetime of the metastable beam with incident electron energy can be explained qualitatively by reference to the production cross section of each metastable state.

ii) Cross Sections for Production of the Metastable States

A summary of the methods used to determine the cross sections for production of metastable states of nitrogen by direct electron impact excitation is given in table 5.5. Cascade contributions to the $N_2(a^1\pi_g)$ state are negligible (Mason and Newell 1987b) and consequently the cross sections determined both experimentally and theoretically are in good agreement in the general shape and the position of the peak at between 15eV and 18eV.

Table 5.5 Experimental and theoretical determinations of the cross sections for excitation of metastable states of molecular nitrogen.

Reference	Metastable States	Method
Borst 1972 Borst et al 1972	$N_2(A^3\Sigma^+_u)$ $N_2(E^3\Sigma^+_g)$ $N_2(a^1\pi_g)$	Total cross section measured by molecular beam time of flight and detection of metastable products
Mason and Newell 1987b	$N_2(a^1\pi_g)$	Total cross section measured by molecular beam time of flight and detection of metastable products
Brunger et al 1988	$N_2(E^3\Sigma^+_g)$	Total cross section measured by molecular beam time of flight and detection of metastable products
Brinkman and Trajmar 1970	$N_2(a^1\pi_g)$	Integral cross section determined from measured electron energy loss differential cross sections
Cartwright et al 1977	$N_2(a^1\pi_g)$	Integral cross section determined from measured electron energy loss differential cross sections
Finn and Doering 1976	$N_2(a^1\pi_g)$	Integral cross section determined from measured electron energy loss differential cross sections
Mazeau et al 1973	$N_2(E^3\Sigma^+_g)$	Integral cross section determined from measured electron energy loss differential cross sections

Table 5.5 continued

Reference	Metastable States	Method
Aarts and de Heer 1971	$N_2(a^1\pi_g)$	Measured radiation from the $N_2(a^1\pi_g$ - $X^1\Sigma^+{}_g)$ transition
Holland 1969	$N_2(a^1\pi_g)$	Measured radiation from the $N_2(a^1\pi_g$ - $X^1\Sigma^+{}_g)$ transition
Ajello 1970	$N_2(a^1\pi_g)$	Measured radiation from the $N_2(a^1\pi_g$ - $X^1\Sigma^+{}_g)$ transition
Kurzweg et al 1973	$N_2(E^3\Sigma^+{}_g)$	Measured radiation from the transition $N_2(C^3\Pi_u$ - $B^3\Pi_g)$ due to collisional energy transfer from $N_2(E^3\Sigma^+{}_g)$
Golden et al 1974	$N_2(E^3\Sigma^+{}_g)$	Measured radiation from the transition $N_2(C^3\Pi_u$ - $B^3\Pi_g)$ due to collisional energy transfer from $N_2(E^3\Sigma^+{}_g)$
Ajello and Shemansky 1985	$N_2(a^1\pi_g)$	Repeated the experiment of Ajello (1970)
Chung and Lin 1972	$N_2(a^1\pi_g)$ $N_2(E^3\Sigma^+{}_g)$	Calculated by Born approximation
Roznyyai et al 1967	$N_2(a^1\pi_g)$	Calculated by Born approximation
Rescigno et al 1976	$N_2(a^1\pi_g)$	Calculated by Distorted Wave method
Fliflet et al 1979	$N_2(E^3\Sigma^+{}_g)$	Calculated by Distorted Wave method
Holley et al 1981	$N_2(a^1\pi_g)$	Calculated by Close Coupling method
Cartwright 1970, 1972	$N_2(E^3\Sigma^+{}_g)$	Calculated by Ockhur-Rudge approximation

In the discussion of the present results the cross sections determined by Borst (1972) and by Borst et al (1972) are used. These cross sections were determined in electron impact studies over a similar incident electron energy range and with a similar energy resolution as those used in this work. Borst (1972) studied the production of $N_2(A^3\Sigma^+{}_u)$ and $N_2(a^1\pi_g)$ in direct electron impact excitation of molecular nitrogen using a Cu-Be-O surface detector of ~4eV. In later work, Borst et al (1972)

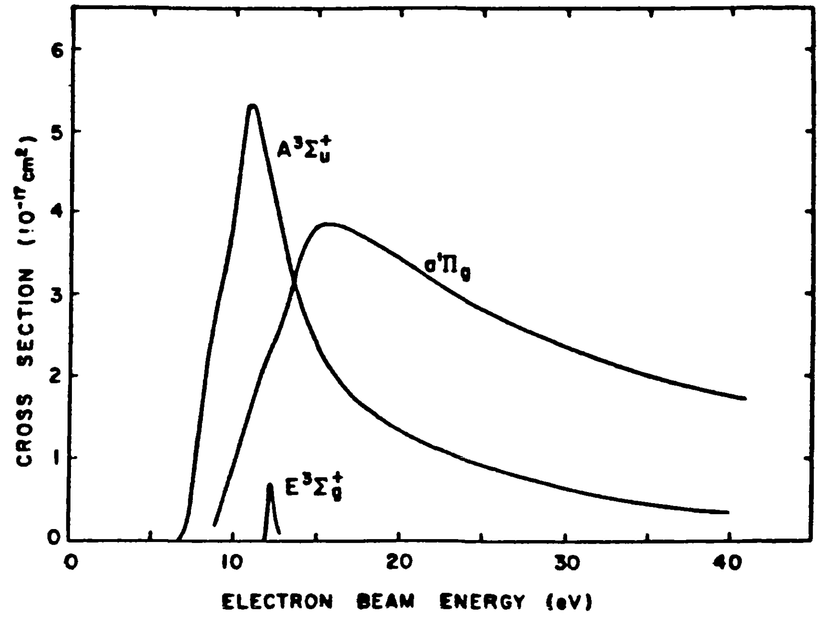

Figure 5.6a Cross sections for the production of metastable states of molecular nitrogen (Borst 1972, Borst and Zipf 1972).

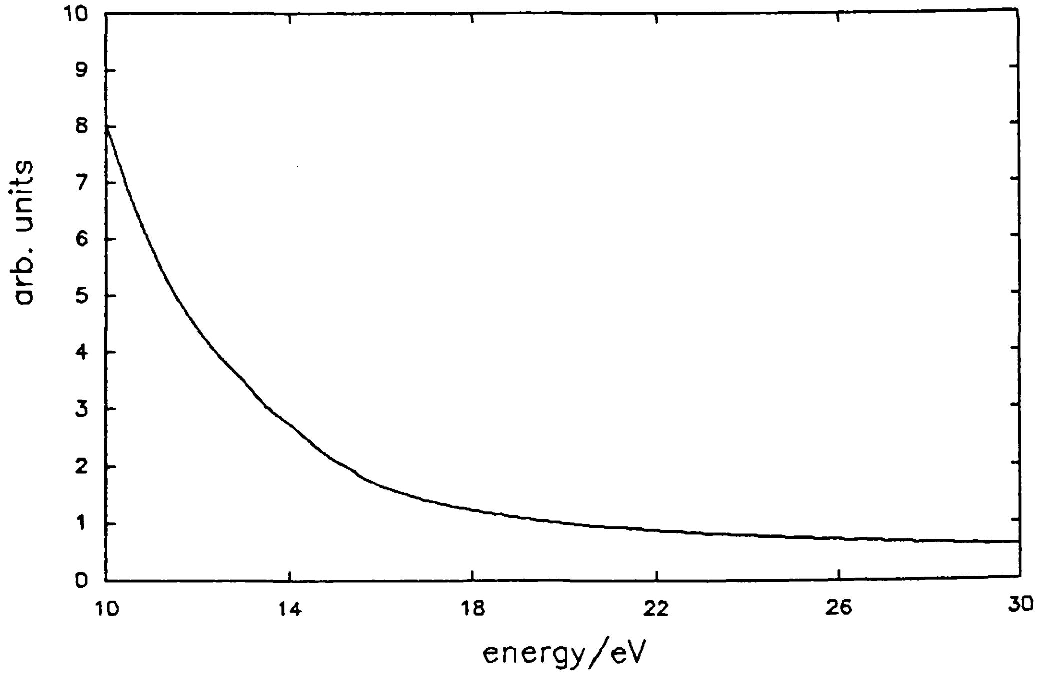

Figure 5.6b Ratio of the cross sections for production of $N_2(A^3\Sigma^+{}_u)$ and $N_2(a^1\pi_g)$ states (Borst 1972).

measured the cross section for direct excitation of $N_2(E^3\Sigma^+{}_g)$ and found it to be resonance-like, peaking at 12.2eV. Borst's cross sections are shown in figure 5.6a.

The ratio of the cross sections for the production of the $N_2(A^3\Sigma^+{}_u)$ and $N_2(a^1\pi_g)$ states obtained from this data is shown in figure 5.6b. The apparent lifetimes determined for each incident electron energy in the present work, table 5.4, can be qualitatively explained using these cross sections. At incident electron energies below 8.55eV only the $N_2(A^3\Sigma^+{}_u)$ metastable state is present in the beam, and the apparent lifetime of the metastable beam will be the same as the lifetime of the $N_2(A^3\Sigma^+{}_u)$ state, 1.4s. As the incident electron energy passes through the threshold for $N_2(a^1\pi_g)$ production, 8.55eV, the apparent lifetime of the metastable beam is reduced since the lifetime of the $N_2(a^1\pi_g)$ state is 115μs. The cross section of the $N_2(a^1\pi_g)$ state rises very slowly close to its threshold and this is reflected in the gradual reduction of the apparent lifetime of the metastable nitrogen beam. At incident electron energies greater than $\sim$16eV the ratio of the $N_2(A^3\Sigma^+{}_u)$ state to the $N_2(a^1\pi_g)$ state in the beam decreases slowly and steadily and so the apparent lifetime of the beam is expected also to decrease slowly. The short lifetime observed at 12eV can be explained by the production of $N_2(E^3\Sigma^+{}_g)$ which has a lifetime of 190μs. The presence of this third state in the metastable beam will therefore reduce the apparent lifetime over a small energy range around 12eV.

The ratio of the $N_2(A^3\Sigma^+{}_u)$ and $N_2(a^1\pi_g)$ states in the time of flight spectra depends both on the production cross section of each state and the detection efficiency of the tantalum surface to each state. Therefore the ratio of the $N_2(A^3\Sigma^+{}_u)$ and $N_2(a^1\pi_g)$ states measured by Borst cannot be applied to the experimental spectra obtained in this work. However, the apparent lifetimes measured in this study follow the trends that would be expected from the cross sections of Borst.

iii) Conclusion

This study of direct electron impact excitation of molecular nitrogen demonstrates that the tantalum detector can detect both the $N_2(A^3\Sigma^+{}_u)$ and $N_2(a^1\pi_g)$ states.

b) Excitation of Carbon Monoxide

The excitation of carbon monoxide was also studied in order to determine the detection threshold of the tantalum surface detector. There are two metastable states of carbon monoxide, CO($a^3\pi$) of excitation energy 6.17eV and an unclassified state, denoted by CO^m, with an excitation threshold of ~10eV. This higher lying state may in fact be two separate metastable states of excitation energies 9.5eV and 10.5eV since there is a distinct change of gradient in the measured excitation function (Mason and Newell 1988).

i) Lifetimes of the Metastable States of Carbon Monoxide

The experimental and theoretical determinations of the lifetimes of the metastable states of carbon monoxide are summarised in tables 5.6 and 5.7.

The lifetime of the CO($a^3\pi$) metastable state is strongly dependent on the vibrational levels populated. Different vibrational levels may be excited in different experiments, for example, vibrational levels excited by direct electron impact may not be the same as those excited by dissociative excitation of carbon dioxide (Johnson 1970).

Borst and Zipf (1971) determined the lifetime of CO($a^3\pi$) by time of flight spectroscopy. The metastable lifetime was inferred from the shape of the recorded time of flight spectrum, S(t), compared with that expected if there were no decay, F(t). These two spectra are related by

$$S(t) = F(t)\, e^{-t/\tau}$$

where τ is the lifetime of the metastable state.

They note that they were not able to investigate the dependence of the lifetime on the vibrational and rotational levels populated and consequently the lifetime obtained is an average over all such levels populated in the experiment.

Table 5.6 Experimental and theoretical determinations of the lifetime of the CO($a^3\pi$) metastable state.

Lifetime /ms	Reference	Method
1.0 ± 1.04	Borst and Zipf 1971a	Molecular beam time of flight and detection of metastable products
10-60	Johnson and van Dyck 1972	Molecular beam time of flight and detection of metastable products
6.5 ± 0.7 - 9.6 ± 0.5	Johnson 1970	Measured from time of flight spectra of CO($a^3\pi$) produced in dissociation of carbon dioxide
0.01	Hansche 1940	Measured radiation from the transition CO($a^3\pi$ - $X^1\Sigma^+$)
0.06	Papaliolios 1965	Measured radiation from the transition CO($a^3\pi$ - $X^1\Sigma^+$)
7.5 ± 1.0	Lawrence 1971	Measured radiation from the transition CO($a^3\pi$ - $X^1\Sigma^+$)
4.4 ± 1.1	Slangar and Black 1971	Measured quenching rate constants
8.7 ± 0.5	Nicholls and Hussan 1971	Measured absorption band strength
9.4 ± 1.0	Fairbairn 1970	Measured absorption band strength
12	Donovan and Husain 1967	Measured absorption band strength
8.75 (2.9 - 451)	James 1971	Calculated oscillator strengths and determined the dependence of lifetime on the rotational sublevel

Table 5.7 Experimental and theoretical determinations of the lifetime of the CO(10eV) metastable state.

Lifetime /μs	Reference	Method
100	Olmsted et al 1965	Molecular beam time of flight and detection of metastable products
100	Borst and Zipf 1971a	Molecular beam time of flight and detection of metastable products
97 ± 15	Wells et al 1973	Molecular beam time of flight and detection of metastable products
80 ± 10	Mason and Newell 1988	Molecular beam time of flight and detection of metastable products

Borst and Zipf (1972) used this lifetime in their analysis of the production of CO($a^3\pi$) by electron impact dissociation of carbon dioxide. However Wells et al (1973) in their study of the excitation of the higher lying metastable state, CO^m, used a lifetime of 7ms to unfold the contribution to the time of flight spectrum from CO($a^3\pi$). This value was stated by Wells et al to be the mean lifetime for CO($a^3\pi$) and based on the measurements of Lawrence (1971), James (1971) and Johnson and van Dyck (1972). No explanation of this is offered in the publication but it must be assumed that Wells et al had good reason to discount the value of 1ms measured in their own laboratory and that 7ms is the more reliable value.

Due to the discrepancies in the determinations of the lifetime of the CO($a^3\pi$) state, a treatment of the excitation of carbon monoxide similar to that of molecular nitrogen was not possible. However time of flight spectra were recorded over a range of incident electron energies, 8eV - 60eV.

The time of flight spectrum recorded at an incident electron energy of 8eV, figure 5.7, indicates that the tantalum surface detector was efficient in detecting the CO($a^3\pi$) state since this is the only metastable state expected to be produced at this excitation energy.

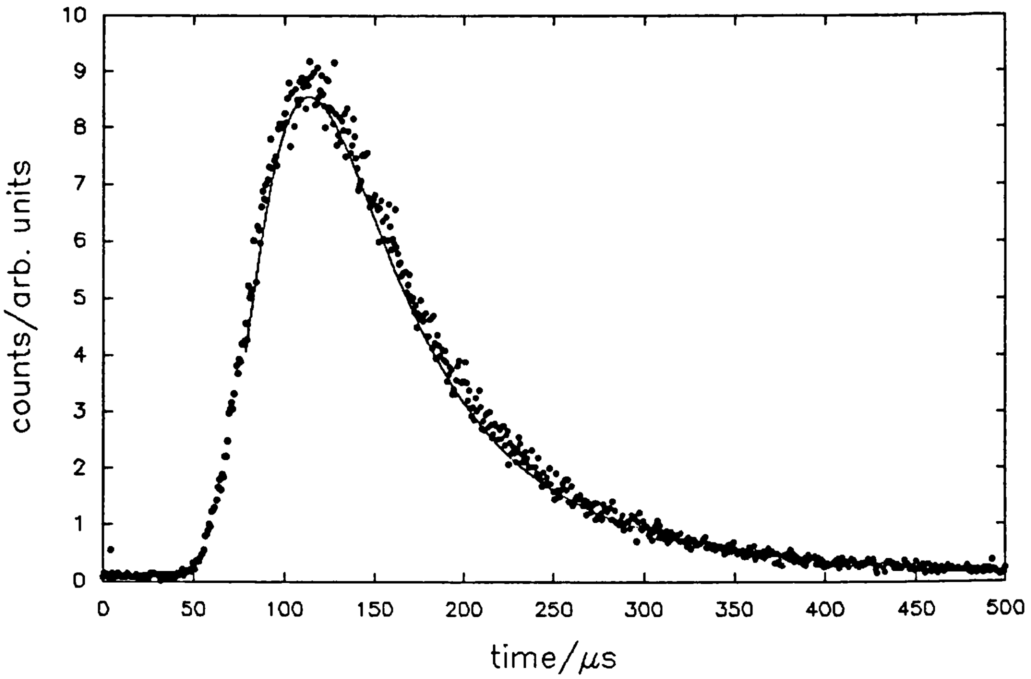

Figure 5.7 Time of flight spectrum of metastable carbon monoxide molecules at an incident electron energy of 8eV. The fit assumes a lifetime of 7ms, giving g=4.45.

This time of flight spectrum was used to determine a value for the parameter 'g' describing the distribution of the parent gas beam, however, in determining 'g' a choice of lifetime for the CO($a^3\pi$) state must be made. Two lifetimes were used, 1ms (Borst and Zipf 1971) and 7ms (Wells et al 1973), giving two possible values of 'g', 4.28 and 4.45 respectively.

The mass of carbon monoxide is the same as that of molecular nitrogen, it may be assumed that both gases will behave in a similar manner in the gas source and the value of 'g' will be the same for each gas. This assumption is simplistic since the behaviour of the gas at the hypodermic needle depends on its viscosity as well as its mass. The value of 'g' determined for molecular nitrogen (section 5.3) was 4.94, suggesting that the value of 4.45, obtained using a lifetime of 7ms, is more likely to be correct.

The lifetime of the metastable beam as observed at the detector was then determined for the full range of incident electron energies assuming a distribution of 4.28 and 4.45, table 5.8. It should be noted that the lifetime given is the lower limit.

Table 5.8 Lifetime of the metastable carbon monoxide beam at incident electron energies between 10 and 60eV.

'g' = 4.28		'g' = 4.45	
Incident Electron Energy /eV	Lifetime /ms	Incident Electron Energy /eV	Lifetime /ms
10	0.77	10	1.98
15	0.53	15	0.94
20	0.61	20	1.12
25	0.42	25	0.66
35	0.41	35	0.59
40	0.41	40	0.59
45	0.45	45	0.61
50	0.50	50	0.80
60	0.50	60	0.68

ii) Cross Sections for the Production of Metastable States of Carbon Monoxide

There have been several determinations of the production cross sections by electron impact excitation of both CO($a^3\pi$) and CO^m, table 5.9.

Table 5.9 Experimental and theoretical determinations of the cross sections for electron impact excitation of metastable states of carbon monoxide

Reference	Metastable States	Method
Borst and Zipf 1971a	CO($a^3\pi$) CO^m	Total cross section determined from molecular beam time of flight and detection of metastable products
Brunt et al 1978	CO($a^3\pi$)	Total cross section determined using high resolution electron beam and detection of metastable products
Newman et al 1983	CO($a^3\pi$)	Total cross section determined using high resolution electron beam and detection of metastable products
Wells et al 1973	CO^m	Total cross section determined from molecular beam time of flight and detection of metastable products
Mason and Newell 1988	CO^m	Total cross section determined from molecular beam time of flight and detection of metastable products

Wells et al (1973) deduced the cross sections for CO($a^3\pi$) and CO^m from time of flight spectra recorded over a range of incident electron energies from threshold to 50eV. The excitation function for the metastable beam was determined for two time of flight windows, 50-70μs and 200-350μs. The first window is expected to contain contributions of both CO($a^3\pi$) and CO^m while at the longer flight time only CO($a^3\pi$) was expected to contribute to the signal since essentially all of the CO^m decays in-flight. The difference is then expected to be the production cross section of CO^m, figure 5.8.

The lifetime determinations in table 5.8 show that the lifetime of the observed metastable beam decreases for incident electron energies >10eV, that is above the threshold for production of the CO^m state, and remains approximately constant for incident electron energies between 25eV and 45eV. This may be understood qualitatively from the cross sections of Wells et al. At incident electron energies >25eV the ratio of cross section for production of $CO(a^3\pi)$ to that of CO^m is approximately constant. The lifetime of the metastable beam containing contributions from both of these states will therefore be approximately constant.

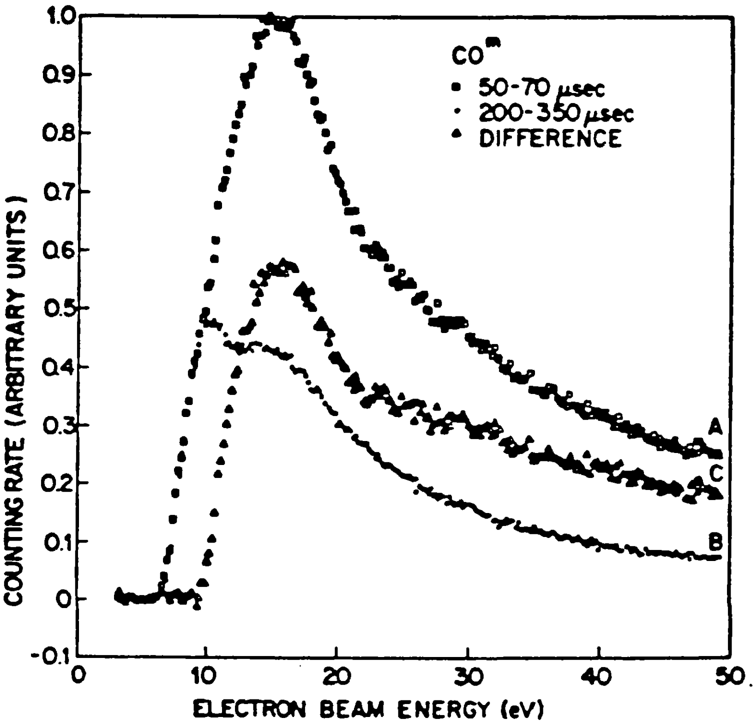

Figure 5.8 Cross sections for the production of the metastable states of carbon monoxide (Wells et al 1973).

The lifetime determined using the value for 'g' of 4.45 rises for the 50eV spectrum while no such rise is observed when using the value for 'g' of 4.28. Different values of 'g' serve only to scale the value of the lifetime obtained and should not result in a difference in the trend of the lifetime with incident electron energy. Thus the rise is spurious and should be neglected. The spectra for incident electron energies >40μs are less reliable since the dissociation of carbon monoxide results in a distinct $O(^5S)$ contribution to the spectrum, figure 5.9, and a reduction in the metastable carbon monoxide molecules reaching the detector.

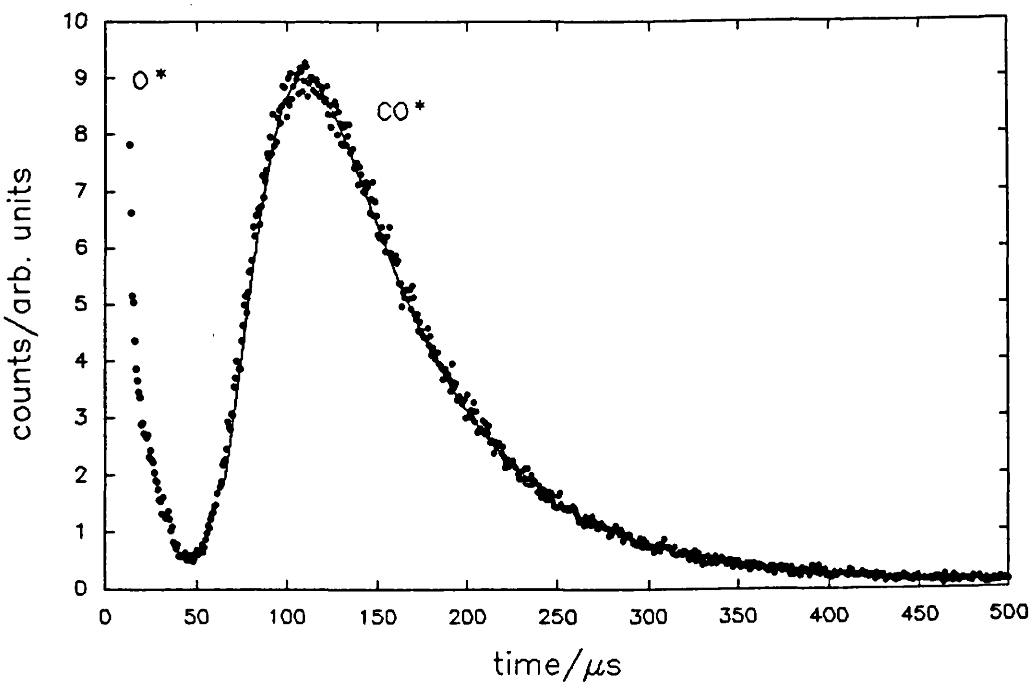

Figure 5.9 Time of flight spectrum of metastable carbon monoxide at an incident electron energy of 50eV.

iii) Conclusion

Although the proportion of each metastable state in the beam could not be determined, this study established that the tantalum surface detector was efficient in detecting both CO($a^3\pi$) of excitation energy 6.01eV and CO^m of excitation energy ~ 10eV.

c) Excitation of Nitric Oxide

A metastable state of nitric oxide, NO($a^4\pi$) of excitation energy 4.7eV and lifetime 0.16s has been reported (Nicholls 1964). This is a convenient metastable state to test the detection threshold of the tantalum surface detector. The tantalum surface has a nominal work function of 4.1eV, however adsorbates on the surface are expected to result in a detection efficiency higher than this. No signal was observed at incident electron energies of 6eV, 8eV, 10eV or 25eV. The detection threshold of the tantalum surface detector must therefore be >4.7eV.

5.3.3 Summary

Direct electron impact excitation studies have established that the tantalum surface detector has a detection threshold of between 4.7eV and 6.0eV. The surface is efficient in detecting both the low lying $N_2(A^3\Sigma^+_u)$ and $CO(a^3\pi)$ metastable states. The tantalum surface was therefore a suitable detector for the study of dissociative excitation of $N_2(A^3\Sigma^+_u)$ from nitrous oxide, chapter six, and $CO(a^3\pi)$ from both carbonyl sulphide and carbon dioxide, chapter seven.

5.4 The Ceramic Channel Electron Multiplier

As discussed in chapter two, the detection threshold of a detector depends largely on the material from which it is constructed. The glass channel electron multiplier has a detection threshold of between 6.17eV and 8.55eV (section 5.2). Ceramic channel electron multipliers are now also commercially available. Since the detection threshold and efficiency of these to metastable species have not been determined, a ceramic channel electron multiplier was installed in the apparatus. It was hoped that this channel electron multiplier would have a detection threshold such that it could be used to isolate the $N_2(E^3\Sigma^+_u)$ metastable state of excitation energy 11.87eV from the $N_2(A^3\Sigma^+_g)$ and $N_2(a^1\pi_g)$ states.

5.4.1 Description of the Ceramic Channel Electron Multiplier

The Murata EMW6081B ceramic channel electron multiplier was an open ended hollow ceramic tube with a conical mouth of 10mm diameter. The multiplier was mounted on a ceramic sheet of dimensions 100 x 25mm and was therefore easily mounted directly onto a modified optical bench.

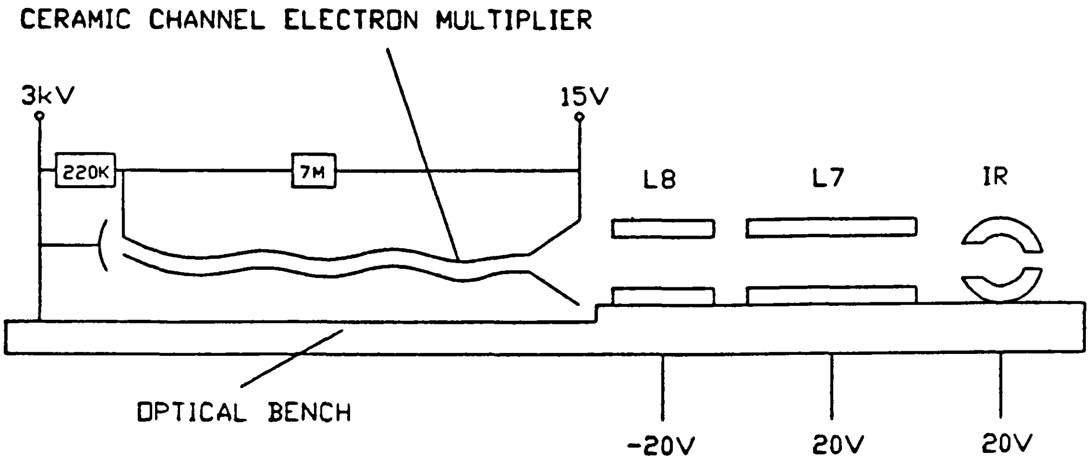

Figure 5.10 Schematic diagram of the ceramic channel electron multiplier mounted on an optical bench. Potentials applied to each of the connections of the multiplier are shown and typical potentials applied to the lens elements of the flight tube are indicated.

The multiplier had three connections, the mouth, the tail and the collector. A 3kV supply was connected across the mouth and the collector. The resistance of the ceramic channel electron multiplier was considered to be comparable to that of the glass multiplier, $\sim 10^9\Omega$. Therefore a 220kΩ resistor was connected between the collector and the tail and a chain of total resistance 7000kΩ between the tail and the mouth to divide the 3kV giving a 100V potential difference between the collector and tail and 2900V between the tail and mouth, figure 5.10.

The flight tube consisted of two lens elements. The lens element L7, was maintained at bias potential to prevent electrostatic field penetration. The lens element L8 was operated at a negative potential to prevent scattered electrons from the interaction region reaching the detector. The path length from the interaction region to the detector was 8.0cm.

5.4.2 Determination of the Detection Threshold

The detection threshold of the ceramic channel electron multiplier was determined by observing the direct electron impact excitation of metastable states of several gases; helium, nitrogen and carbon monoxide.

a) Helium

A helium spectrum was recorded to confirm that the ceramic channel electron multiplier detected metastable species with an efficiency comparable to the glass channel electron multiplier.

The time of flight spectrum recorded at an incident electron energy of 25eV is shown in figure 5.11a. At this incident energy, the proportions of $He(2^1S)$ and $He(2^3S)$ in the metastable beam are 43% and 57% respectively (Berrington et al 1985). The lifetime of the $He(2^1S)$ state >0.02s (Pearl 1970, Drake et al 1969, van Dyck et al 1970) while the $He(2^3S)$ state lives for many thousands of seconds (e.g. Griem 1969). The lifetime of the metastable beam will therefore be much longer than the flight time in this work, $50\mu s$. In flight decay is consequently negligible.

b) Molecular Nitrogen

No signal was observed for direct electron impact excitation of molecular nitrogen at incident electron energies <8eV. This indicated that the ceramic channel electron multiplier was not capable of detecting $N_2(A^3\Sigma^+{}_u)$ molecules of excitation energy 6.17eV.

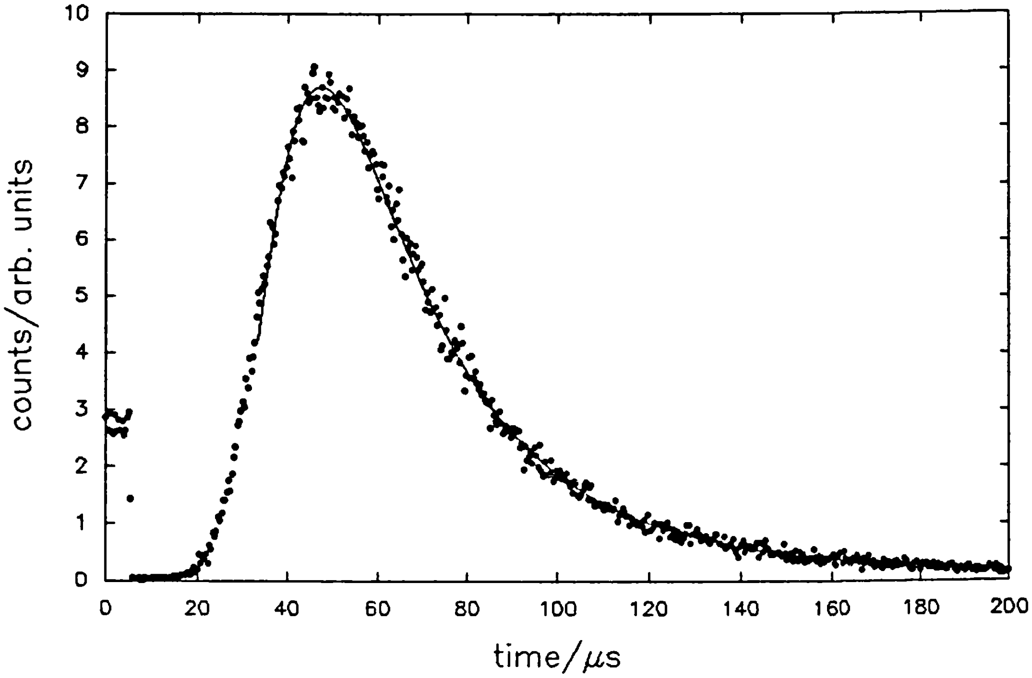

Figure 5.11a Time of flight spectrum for metastable helium at an incident electron energy of 25eV using the ceramic electron multiplier. The fit assumes a lifetime of 0.06s, giving g=4.98.

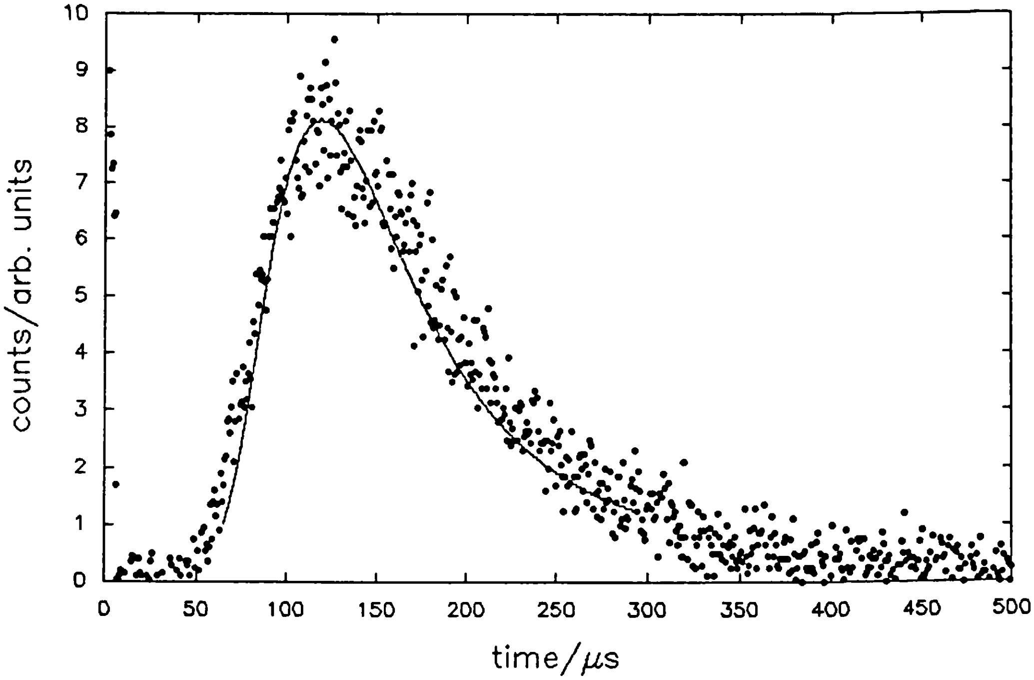

Figure 5.11b Time of flight spectrum for metastable nitrogen at an incident electron energy of 10eV using the ceramic electron multiplier. The fit shown is for g=4.8 and lifetime 840μs.

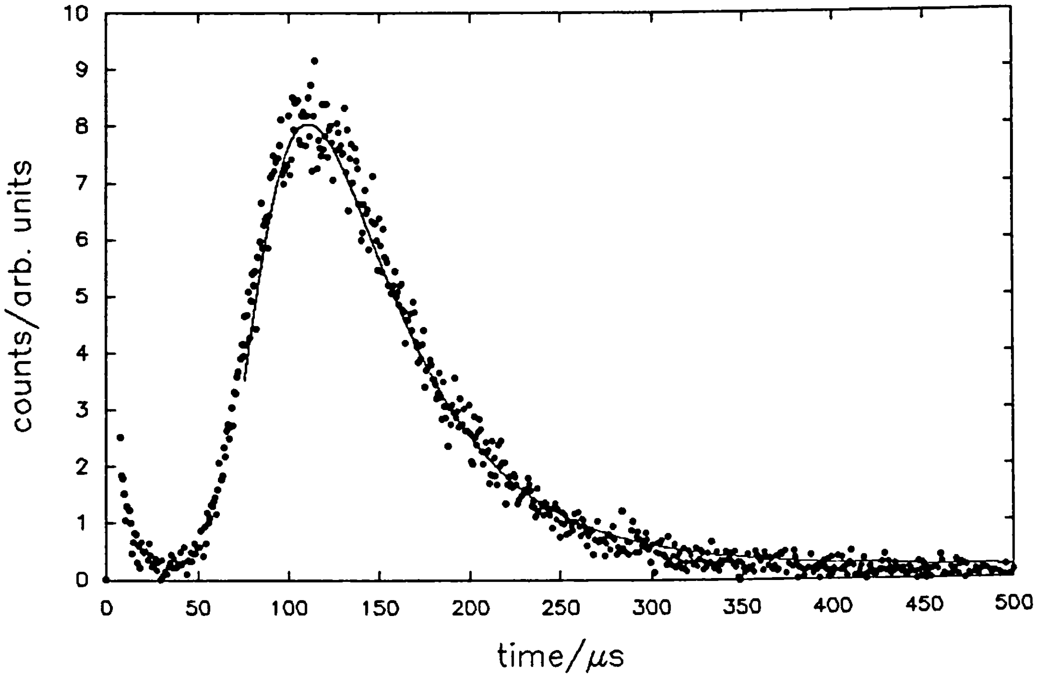

Figure 5.11c Time of flight spectrum for metastable carbon monoxide at an incident electron energy of 15eV using the ceramic electron multiplier. The fit shown is for g=4.8 and lifetime 106μs.

A time of flight spectrum was recorded for molecular nitrogen at an incident electron energy of 10eV, figure 5.11b. The statistics in this spectrum are poor since the count rate was very low. The spectrum was nevertheless compared with the modified Maxwellian distribution. The best fit obtained by varying both the parameter 'g' and the lifetime of the metastable beam gave a value of 'g' of 4.8 and a lifetime of 840μs. This value of 'g' is reasonable since a value of 4.94 was determined for 'g' during the calibration of the tantalum surface detector, section 5.3. The lifetime is longer than expected for a metastable beam consisting only of $N_2(a^1\pi_g)$ molecules of lifetime 115μs. Since the lifetime of the $N_2(A^3\Sigma^+{}_u)$ state is 1.4s, it is suggested that the metastable beam contains a contribution from higher lying vibrational levels of the $N_2(A^3\Sigma^+{}_u)$ state. That such vibrational levels were not observed at incident electron energies <8eV may be due to a lower production cross section for these levels by direct excitation than by cascade from higher lying states such as $N_2(B^3\Pi_g)$ and $N_2(C^3\Pi_u)$.

A time of flight spectrum was also recorded at an incident electron energy of 25eV. The best fit to this spectrum also resulted in a value of 'g' of 4.8 and a lifetime of 164μs. This is consistent with predominantly the $N_2(a^1\pi_g)$ state being detected.

c) Carbon Monoxide

No signal was observed in the direct electron impact excitation of carbon monoxide at incident electron energies $<$10eV. A time of flight spectrum was recorded at an incident electron energy of 15eV, figure 5.11c. The signal was very low suggesting that only the 10eV state was detected. The best fit to this spectrum gave a lifetime of 106μs and a value of 'g' of 4.8. Since the lifetime of the CO^m state is reported to be 0.1ms while that of the $CO(a^3\pi)$ state is $>$1ms, it may be concluded that the only state detected is CO^m.

5.4.3 Conclusions

The ceramic channel electron multiplier detected metastable helium atoms with an efficiency comparable to that of the glass channel electron multiplier. It was also capable of detecting $N_2(a^1\pi_g)$ and CO^m metastable species and was possibly able to detect higher lying vibrational states of the $N_2(A^3\Sigma^+{}_u)$ state, but not with a high efficiency. The multiplier did not detect $CO(a^3\pi)$ metastable states of excitation energy 6.01eV. The detection threshold of the ceramic channel electron multiplier therefore lies in the range 7 - 8eV.

5.5 A Xenon Detector

All the detectors described previously will detect all species incident on the detector which have an excitation energy greater than the detection threshold of the surface. When only one of the metastable species produced in the interaction region has an excitation energy greater than the detection threshold, the detector may be operated as a selective detector as in the detection of $O(^5S)$ from carbon monoxide, carbon dioxide and carbonyl sulphide (chapter seven).

Selection of a specific metastable state may be achieved using the formation of an excimer on a surface (chapter two, section 2.4). Such a detection mechanism was of interest since $O(^1S)$ fragments are produced in addition to $O(^5S)$ fragments in the dissociation of the molecules studied in this work. Metastable $O(^1S)$ atoms of excitation energy 4.17eV are not detectable by Auger processes at transition metal surfaces. They may be detected, however, by Auger emission from a metal oxide surface of work function less than 4eV, but $O(^5S)$ atoms and other collision products would also be detected. A method of detecting such metastable species selectively using XeO^* formation was therefore investigated.

5.5.1 Review of Detection of $O(^1S)$ at a Xenon Surface

Kiefl et al (1983) have reported the use of a xenon surface to detect $O(^1S)$ atoms. The $O(^1S)$ atoms undergo elastic collisions with loosely bound xenon atoms as they approach the surface, losing their excitation energy to the XeO molecule formed. The excimer fluoresces with the emission of radiation of wavelength between 500nm and 600nm.

The $O(^1S)$ atomic beam was prepared by electron impact dissociation of a beam of molecular oxygen in a differentially pumped system. To allow time of flight spectroscopy of the products the electron beam was pulsed. Unwanted collision products such as ions were removed from the beam by the application of high potential quenching fields. The excited atomic oxygen beam, which contained a mixture of metastable species and Rydberg atoms, was then allowed to impinge on the xenon surface.

The xenon surface was prepared on a liquid nitrogen cooled cold finger. Xenon was allowed to effuse from a multichannel slit and condensed onto this cold finger. The pressure of xenon at the surface was determined by Kiefl et al to be 3 x 10^{-4}mb (2.3 x 10^{-4}torr). Since the sublimation pressure of xenon is 3.8 x 10^{-4}torr at a temperature of 70.1K (Leming and Pollack 1970), in the experiment of Kiefl et al, a temperature <70K was required for the xenon to condense onto the surface. Therefore the liquid nitrogen in the trap was pumped to a reduced pressure of 250-300mb (190-230torr) to lower the temperature of the cold finger to below the condensation temperature of nitrogen (77K).

The emission from the surface was filtered by a cyan and a yellow edge filter before being detected by a photomultiplier. The signal from the photomultiplier was monitored by a multichannel analyser to obtain a time of flight spectrum for the metastable species.

The time of flight spectrum obtained for metastable O(^{1}S) atoms, figure 5.12a, shows a fast peak, arrival time ~35μs, and a slow peak, arrival time ~53μs. The mean kinetic energy of these fragments was measured as 3.1eV, and ranged between 1.6eV and 12eV. The kinetic energy distribution indicates that the O(^{1}S) fragments are produced from a purely repulsive potential energy curve (chapter one, section 1.6).

Kiefl et al state that no other species can be responsible for the observed spectrum. Excited oxygen molecules will have thermal kinetic energies, far below the mean 3.1eV kinetic energy determined for the fragments. Metastable O(^{1}D) atoms lie at 1.96eV above the ground state and would be expected to produce photons in the region of >600nm. Light of this wavelength was prevented form reaching the detector by the edge filters in front of the photomultiplier. Metastable O(^{5}S) atoms were detected simultaneously by collecting the in-flight decay light (Nowak et al 1978). The time of flight spectra for O(^{1}S) and O(^{5}S) atoms were found to be

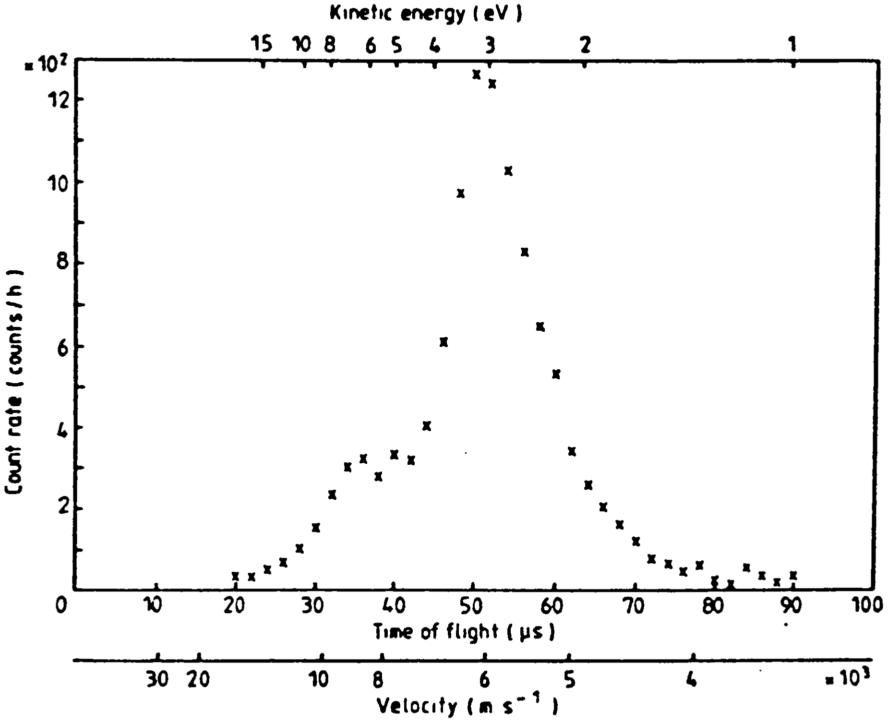

Figure 5.12a Time of flight spectrum of O(^{1}S) metastable atoms produced in electron impact dissociation of molecular oxygen (Kiefl et al 1983).

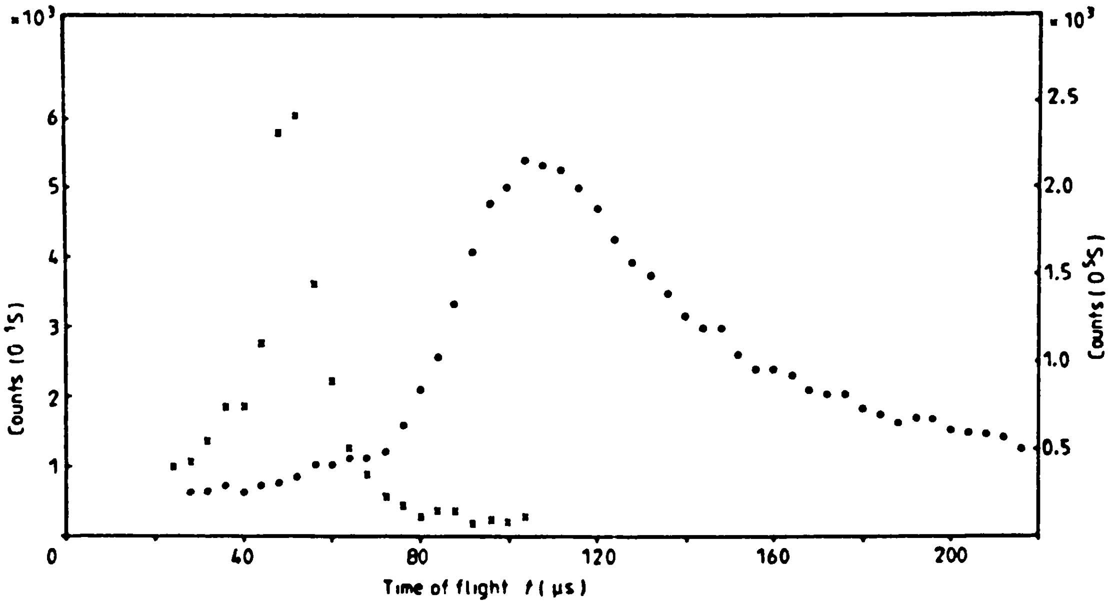

Figure 5.12b Time of flight spectrum of O(^{1}S) and O(^{5}S) metastable atoms produced in electron impact dissociation of molecular oxygen (Kiefl et al 1983).

separated in time, figure 5.12b, and therefore O(^{5}S) atoms could not contribute to the original time of flight spectrum. By varying the electrostatic quenching fields, Kiefl et al established that <5% of the observed signal was due to Rydberg atoms.

5.5.2 Description and Testing of the Xenon Detector

The liquid nitrogen cold finger used in this work was a solid copper cylinder of 25mm diameter cut at one end to provide a smooth flat surface of area 25 x 30mm, figure 5.13a. The cold finger was bolted onto a copper flange soldered onto the base of a stainless steel liquid nitrogen trap. Good thermal contact between the cold finger and the copper flange was ensured by sandwiching an indium disc between them.

The gas to be condensed onto the surface was introduced into the vacuum chamber by a second gas inlet system. Outside the vacuum chamber this gas line was identical to that used for the target gas beam (chapter three, section 3.2). Inside the vacuum chamber a copper tube of ¼" outer diameter directed the gas onto the detecting surface of the cold finger. The gas line was isolated from the cold finger and the liquid nitrogen trap by PTFE spacers. The end of the copper tube was bent and cut at an angle to direct the gas onto the surface.

a) Carbon Dioxide

The cold finger was tested initially by condensing carbon dioxide onto the surface. Carbon dioxide has a sublimation temperature of 195K at atmospheric pressure. Since this temperature is well above the boiling point of nitrogen 77K it was expected that carbon dioxide would condense onto the cold finger even under reduced pressure in the vacuum chamber.

A layer of solid carbon dioxide rapidly formed on the surface. Eventually sufficient carbon dioxide condensed to form a continuous layer between the cold finger and the end of the gas line.

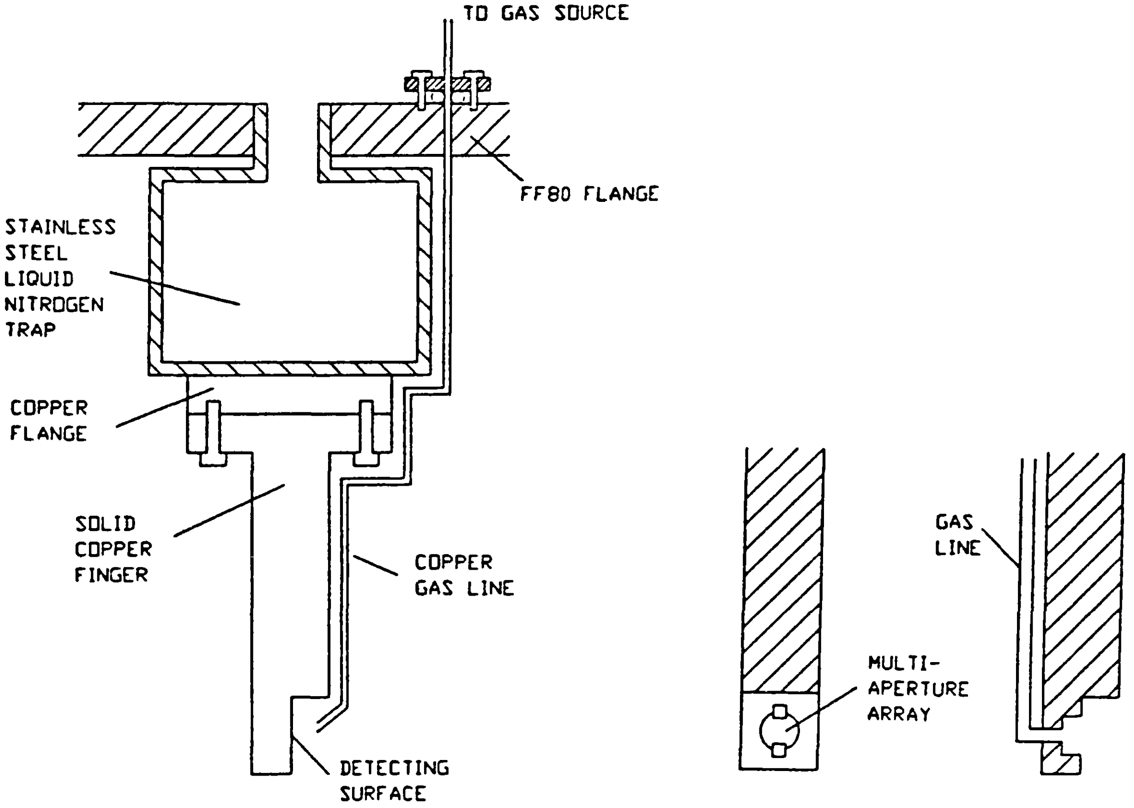

(a)

(b)

Figure 5.13 Cold finger used in this work, a) schematic diagram and b) incorporation of the multiaperture array.

b) Xenon

When xenon was directed onto the cold finger no condensation was observed. The pressure of the xenon at the surface of the cold finger was calculated to be 6 x 10^{-5}torr, the temperature necessary for condensation at this pressure would be <70K (Leming and Pollack 1970).

To increase the pressure of xenon at the surface the cold finger was adapted to include a multiaperture array, figure 5.13b. Although good thermal contact between the cold finger and the array was sought by including an indium seal between them, the array did not cool to the same temperature as the cold finger.

5.6 Summary

Two metastable detectors were used in this work, a channel electron multiplier was used to detect selectively metastable species of excitation energy >8eV while a tantalum surface detector was developed to detect lower-lying species. Calibration of the tantalum surface detector by studies of direct electron impact excitation of molecular nitrogen and carbon monoxide showed that the detection threshold was <6.0eV. The good detection efficiency to the metastable species $CO(a^3\pi)$ and $N_2(A^3\Sigma^+{}_u)$ suggests that the detection threshold may be as low as ~5eV.

A ceramic channel electron multiplier was installed and the detection threshold estimated to be ~7eV. A state selective detector designed to detect $O(^1S)$ metastable atoms was investigated. The detection mechanism used was the detection of fluorescence from the XeO excimer formed when $O(^1S)$ atoms were incident on a solid xenon surface. The development of the xenon surface detector ceased due to the problems encountered in producing a layer of solid xenon on the cold finger.

Chapter Six

Dissociative Excitation of $N_2(A^3\Sigma^+_u)$ and $N_2(a^1\pi_g)$ from Nitrous Oxide

I pass with relief from the tossing sea of Cause and Theory to
the firm ground of Result and Fact.
W S Churchill *(The Story of the Malakand Field Force)*

6.1 Introduction

Nitrous oxide is present in the upper atmosphere in significant quantities (Prinn et al 1983) and is one of the greenhouse gases responsible for radiation trapping in the atmosphere. Tropospheric nitrous oxide is the principal source of the family of stratospheric nitrogen oxides, NO_x. The reaction between nitrous oxide and ground state atomic oxygen, $O(^3P)$, is endothermic but the reaction with atomic oxygen in the metastable state, $O(^1D)$, is exothermic and proceeds rapidly. This reaction is the major source of nitric oxide,

$$O(^1D) + N_2O \rightarrow 2NO$$

The nitric oxide is subsequently oxidised to one of the nitrogen oxides NO_x which are responsible for destruction of much of the atmospheric ozone.

The major natural source of nitrous oxide is the oxidation of ammonia produced by denitrifying bacteria in the oceans and in the soil. In addition to these, the combustion of fossil fuels and the use of fertilisers are increasingly important sources (Cox and Derwent 1981). Nitrous oxide is also formed in collisions between metastable nitrogen molecules and molecular oxygen,

$$N_2(A^3\Sigma^+_u) + O_2 \rightarrow N_2O + O$$

Again, this reaction is endothermic for molecular nitrogen in the ground state, $N_2(X^1\Sigma^+_g)$, and proceeds very slowly, while for metastable $N_2(A^3\Sigma^+_u)$ the reaction is exothermic and occurs rapidly.

In addition to these processes, the reactions of nitrous oxide are significant in lasers such as the nitrous oxide laser (Fox and Reid 1985), an important radiation source in medical applications. The presence of long lived excited species, N_2^* and O^*, in the electron induced nitrous oxide discharge must be included in theoretical models developed to describe such systems, as has been the case for the more well known carbon monoxide and carbon dioxide lasers (Little and Browne 1988, 1989).

In electron impact dissociation of nitrous oxide, several atomic or molecular metastable species may be excited, depending on the energy of the incident electron, E. For example;

$$e_E + N_2O \rightarrow \begin{array}{l} e_{E-\delta E1} + \underline{N_2(A^3\Sigma^+_u)} + O(^3P) \\ e_{E-\delta E2} + \underline{N_2(a^1\pi_g)} + O(^3P) \\ e_{E-\delta E3} + N_2(X^1\Sigma^+_g) + O(^1D) \\ e_{E-\delta E4} + N_2(X^1\Sigma^+_g) + O(^1S) \\ e_{E-\delta E5} + N_2(X^1\Sigma^+_g) + \underline{O(^5S)} \end{array}$$

In each case the metastable state detected in this work is underlined. Table 6.1 lists the low lying excited states of molecular nitrogen discussed in this chapter together with the excitation energy of each state. The lifetimes of the metastable states of molecular nitrogen were discussed in chapter five. The potential energy levels in molecular nitrogen are shown in figure 6.1.

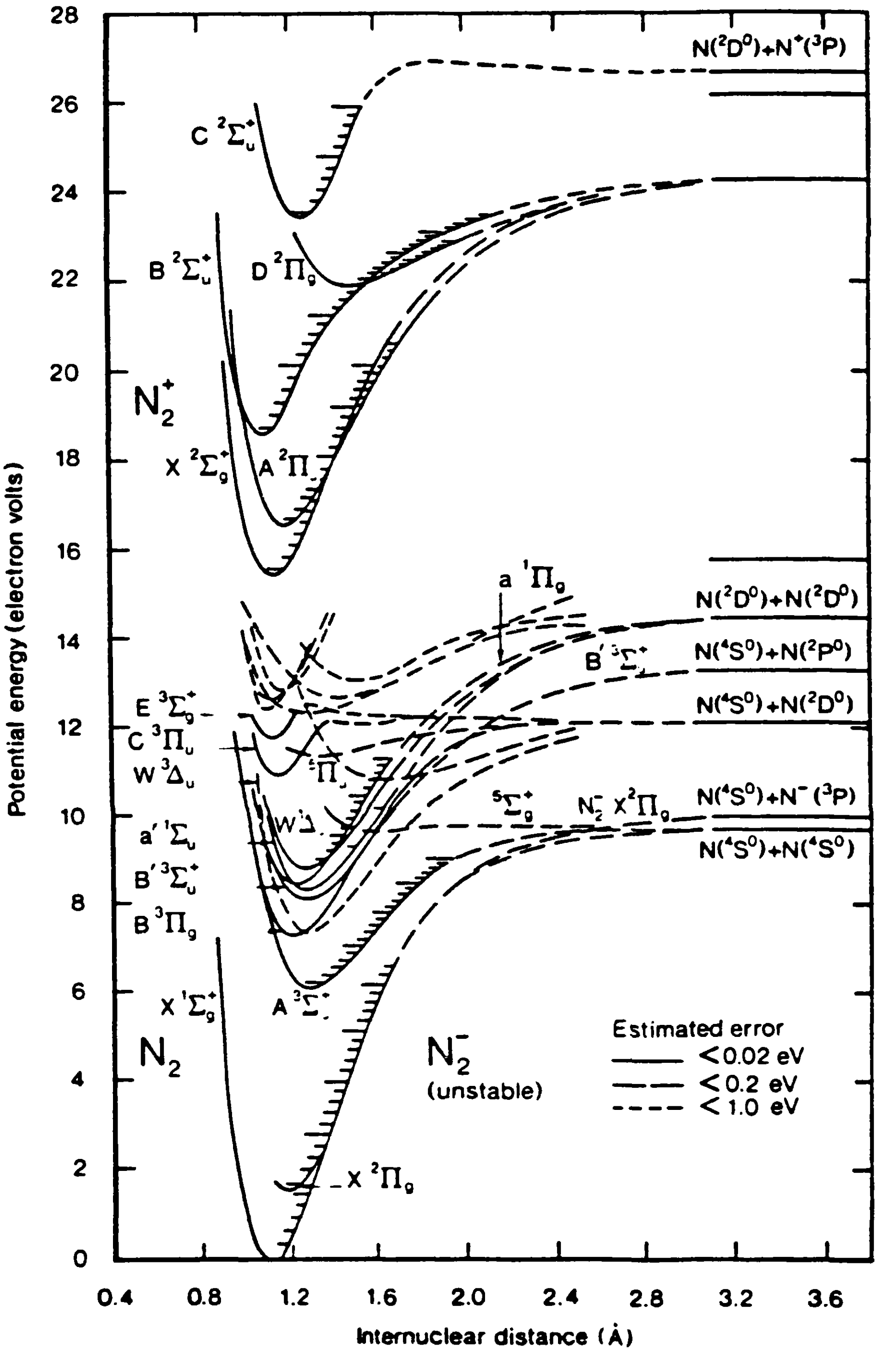

Figure 6.1 Potential energy levels of molecular nitrogen (Gilmore 1961).

Table 6.1 Low lying excited states of molecular nitrogen

Metastable State	Energy /eV	Metastable State	Energy /eV
$N_2(X^1\Sigma^+_g)$	ground state	$N_2(B'^3\Sigma^-_u)$	8.2
$N_2(A^3\Sigma^+_u)$	6.17	$N_2(a^1\pi_g)$	8.55
$N_2(W^3\Delta_u)$	7.2	$N_2(C^3\Pi_u)$	11.0
$N_2(B^3\Pi_g)$	7.3	$N_2(E^3\Sigma^+_g)$	12.2

6.2 Review of Dissociation of Nitrous Oxide

6.2.1 Introduction

Previous work on the dissociation of nitrous oxide has been reported by Freund and Klemperer (1967), Clampitt and Newton (1969), Gilpin and Welge (1971), McEwan et al (1974), Allcock and McConkey (1978) and Mason and Newell (1989). These experiments have concentrated on a determination of the kinetic energy distribution of the fragments produced and yet in some cases have failed to determine the precise nature of the fragments. A consequence of this failure is that the corrections necessary to compensate for the radiative lifetimes cannot be made (Mason 1990).

The effect of the finite lifetime of the metastable fragments is to reduce artificially the number of low kinetic energy fragments reaching the detector, thus distorting the time of flight spectrum. The lifetime of the product metastable beam as observed at the detector and recorded in the time of flight spectrum depends on the lifetime of each state, the production cross section of each and the detection efficiency to each. These effects (chapter four) must be taken into account if the time of flight spectra are to be correctly interpreted.

6.2.2 Electron Impact Dissociative Excitation

Allcock and McConkey used the time of flight method to study several of the electron impact dissociation channels of nitrous oxide. The detector used was a Cu-Be photomultiplier tube with the glass envelope removed. This detector had a work function less than 6eV and would therefore have been efficient in detecting the $N_2(A^3\Sigma^+{}_u)$ metastable state which lies at 6.17eV above the ground state.

The path length between the interaction region and the detector was 0.431m resulting in a mean arrival time of $\sim 200\mu s$. Consequently Allcock and McConkey would have detected very little of the $N_2(a^1\pi_g)$ state since the lifetime of this state is $115\mu s$ and more than 80% would be expected to decay before reaching the detector (Corr et al 1987). Allcock and McConkey have agreed with this proposal and suggested that the long tail observed in the photon flux from the electron pulse was due to the in-flight decay of $N_2(a^1\pi_g)$. The kinetic energy distribution would not be expected to be distorted due to the decay of the $N_2(A^3\Sigma^+{}_u)$ state since the lifetime is 1.4s. The peak fragment kinetic energy of the N_2^* metastable fragments deduced from the time of flight spectra was 0.27eV.

Thresholds for the production of the metastable states of interest and of other excited states are summarised in table 6.2. Processes involving the production of Rydberg states and ions are not included. The thresholds were calculated from the excitation energies of the product states (Gilmore 1965, Herzberg 1966) and the dissociation energy of the ground state of nitrous oxide, 1.73eV. Possible symmetries and multiplicities of the parent molecular state for each dissociation channel are included in the table.

Table 6.2 Thresholds for the production of metastable fragments in the dissociation of nitrous oxide (Allcock and McConkey 1978).

Dissociation Channel	Calculated Threshold /eV	Measured Threshold /eV	Possible Parent Symmetry	Possible Parent Multiplicity
$N_2(A^3\Sigma^+_u) + O(^3P)$	7.88	7.9	Π	1, 3
$N_2(B^3\Pi_g) + O(^3P)$	8.98	8.9	Π, Σ^+	1, 3
$N_2(A^3\Sigma^+_u) + O(^1D)$	9.84		Π, Σ^+	3
$N_2(B'^3\Sigma^-_u) + O(^3P)$	9.88	9.8	Π, Σ^+	1, 3
$N_2(a^1\pi_g) + O(^3P)$	10.28		Π, Σ^+	3
$N_2(C^3\Pi_u) + O(^1S)$	16.83	16.6	Π	3

Allcock and McConkey note that the $N_2(B^3\Pi_g)$ state is not metastable and quickly radiates into the $N_2(A^3\Sigma^+_u)$ metastable state (McEwan et al 1974). Similarly the $N_2(B'^3\Sigma^-_u)$ and $N_2(C^3\Pi_u)$ states cascade into the $N_2(B^3\Pi_g)$ state and hence to the $N_2(A^3\Sigma^+_u)$ state.

Mason and Newell also studied the dissociation of nitrous oxide by recording several time of flight spectra over the incident electron energy range 11eV to 50eV. The detector used was a bare channel electron multiplier of work function ~8eV which was capable of detecting the $N_2(a^1\pi_g)$ state which lies at 8.55eV above the ground state, but which would not have detected the $N_2(A^3\Sigma^+_u)$ state lying at 6.17eV.

They measured the threshold for the production of metastable $N_2(a^1\pi_g)$ to be 10.3eV, and the threshold for production of $O(^5S)$ metastable atoms to be ~29eV. This threshold is high since the process responsible for the formation of the $O(^5S)$ state also results in the formation of the $N_2^+(B^2\Sigma^+_u)$ ion. Allcock and McConkey predicted that the parent molecular state involved is a $^4\Sigma^-$ state and measured the threshold to be 29.1 ± 1eV compared to the calculated value of 29.52eV.

Mason and Newell converted the time of flight spectra to kinetic energy spectra for both the $N_2(a^1\pi_g)$ and $O(^5S)$ metastable fragments. The kinetic energy distribution of the nitrogen fragments peaked at 0.125eV when using a flight path of 14.5cm and at 0.114eV when using a flight path of 5.5cm. The difference is due to the in-flight decay of the metastable nitrogen fragments. The slower fragments produced in the interaction region are more likely to decay in-flight than the faster fragments, resulting in the depletion of the low energy tail of the time of flight spectrum, and hence an increase in the peak kinetic energy. If the lifetime of the metastable state is known, the time of flight spectrum may be corrected for such in-flight decay.

The kinetic energy spectrum for the atomic oxygen fragments was found to peak at 4.5eV and did not vary with the path length used. The kinetic energy distributions showed that the $N_2(a^1\pi_g)$ fragments were produced from the repulsive part of a bound potential energy curve while the $O(^5S)$ fragments were produced from a purely repulsive potential energy state (chapter one).

Freund and Klemperer observed the production of N_2^* metastable fragments from the dissociation of nitrous oxide by translational spectroscopy using a warm tantalum surface detector, work function ~5eV. Since the flight path was 72cm, most of the product $N_2(a^1\pi_g)$ metastable fragments produced decayed before being detected. The time of flight spectra were replotted by Freund and Klemperer as velocity distributions. In this work, these have been converted to kinetic energy distributions and the mean fragment kinetic energy found to be 0.15eV.

Clampitt and Newton studied the metastable products of dissociative excitation by time of flight spectroscopy and detected the fragments by Auger ejection from a bare photomultiplier tube. The threshold for production of metastable molecules was measured as 10.5 ± 0.3eV, suggesting the production of $N_2(a^1\pi_g)$ and $O(^3P)$. They converted the time of flight spectra to kinetic energy distributions and found the mean kinetic energy of the nitrogen fragments to be 0.20 ± 0.03eV. They also concluded that the $N_2(A^3\Sigma^+_u)$ state was populated by cascade from the $N_2(B'^3\Sigma^-_u)$ state, although their measured threshold for the production of metastable products suggests that they did not detect $N_2(A^3\Sigma^+_u)$.

6.2.3 Photodissociation

There have been several studies of the photodissociation of nitrous oxide (e.g. Young et al 1968, 1969, Gilpin and Welge 1971). In the experiment of Gilpin and Welge, the $N_2(A^3\Sigma^+{}_u)$ state was detected at a caesium surface. They observed that the $N_2(a^1\pi_g)$ state was not produced in significant quantities by the flash lamp since the wavelength range of the lamp, 105-144nm, was not low enough. However since the detector was located 46cm from the interaction region, resulting in a flight time of 250μs for the metastable nitrogen molecules, little of any $N_2(a^1\pi_g)$ produced would be expected to reach the detector.

McEwan et al (1974) used photon absorption at wavelengths <125.6nm (>9.87eV) to study the photodissociation of nitrous oxide. The production of $N_2(B^3\Pi_g)$ and $O(^3P)$ was studied by monitoring the radiative decay of the $N_2(B^3\Pi_g)$ state to the $N_2(A^3\Sigma^+{}_u)$ state. The measured dissociation threshold for this channel was in agreement with the calculated value of 8.98eV.

6.3 Present Results

6.3.1 Introduction

In the present work, the tantalum surface detector was calibrated by studying the production of metastable states of molecular nitrogen by direct electron impact excitation (see chapter five). These studies demonstrated that the tantalum surface detector detected both the $N_2(A^3\Sigma^+{}_u)$ and $N_2(a^1\pi_g)$ states with good efficiency.

The tantalum surface detector was then used to investigate the electron impact dissociation of nitrous oxide. The purpose of this study was to observe simultaneously both the $N_2(A^3\Sigma^+{}_u)$ and $N_2(a^1\pi_g)$ states produced in dissociative excitation, and thereby determine the relative cross sections for the production of each state in the dissociation process.

Time of flight spectra of the metastable dissociation products were recorded for incident electron energies in the range 13eV to 60eV. From these, kinetic energy distributions for the metastable nitrogen molecules were determined. The nature of the parent molecular potential energy state was then deduced from the kinetic energy distribution.

6.3.2 Time of Flight Spectra

The time of flight spectra for the dissociation products from nitrous oxide are shown in figure 6.2. At incident electron energies of 13eV and 20eV there is a single peak, peak (1), having a mean arrival time $\sim 36\mu s$. There is a distinct peak, peak (2), on the short flight time side of peak (1) at an incident electron energy of 30eV. This signal emerges as a peak of mean arrival time $\sim 12\mu s$ at an incident electron energy of 40eV. At incident energies above 40eV, peak (2) dominates the spectrum. The fast peak is due to metastable $O(^5S)$ atoms and the second, slower. peak is due to the metastable states of molecular nitrogen.

Long data collection periods, typically 50 hours, gave good statistics in the peaks, but because of the t^3 dependence (chapter four) small statistical fluctuations at long flight times give rise to large variations in the low kinetic energy part of the energy distribution. To reduce the error due to the statistical fluctuations in the tail of the metastable peak, a constant background was deduced from the long flight time part of the time of flight spectrum where no metastable molecules reach the detector and this constant background subtracted from the data. The uncertainty in the position of the kinetic energy peak of typically 10%.

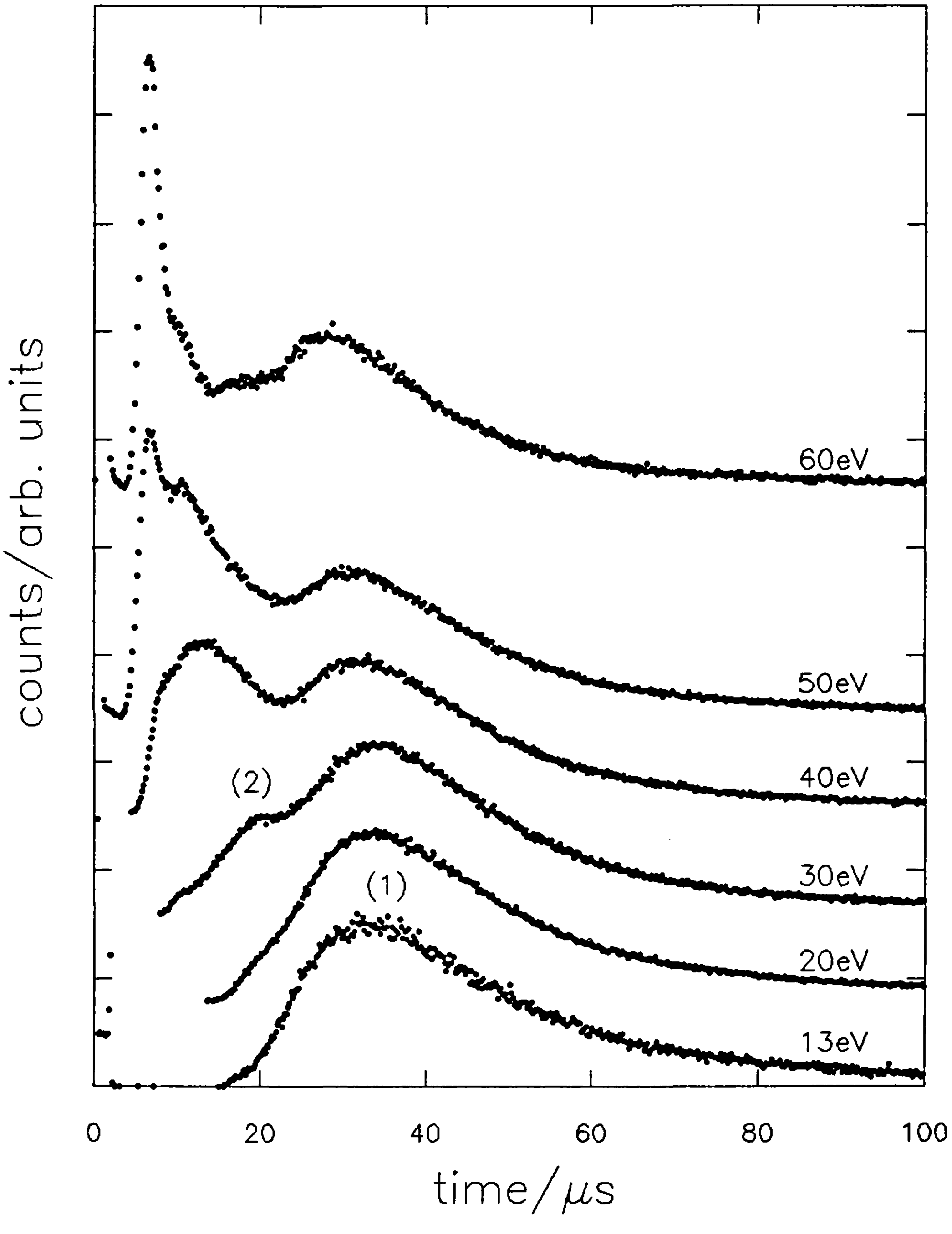

Figure 6.2 Time of flight spectra of fragments from the dissociation of nitrous oxide for incident electron energies of 13eV to 60eV.

6.3.3 Kinetic Energy Distributions

A point by point conversion of the time of flight to a kinetic energy distribution was made for the region of the time of flight spectrum in which only metastable nitrogen molecules contributed to the signal.

The kinetic energy distributions obtained for the nitrogen peak are shown in figure 6.3. The energy at which each distribution peaks and the half height energy are given in table 6.3.

Table 6.3 Positions and half heights of the peaks in the kinetic energy distributions of the metastable nitrogen fragments produced in dissociation of nitrous oxide.

Incident Electron Energy /eV	Peak Kinetic Energy /eV ± 0.016	Half Height Energy /eV ± 0.016
13	0.130	0.649
15	0.146	0.698
20	0.162	0.682
25	0.195	0.746
30	0.244	0.731
40	0.292	0.779
50	0.292	0.747
60	0.292	1.039

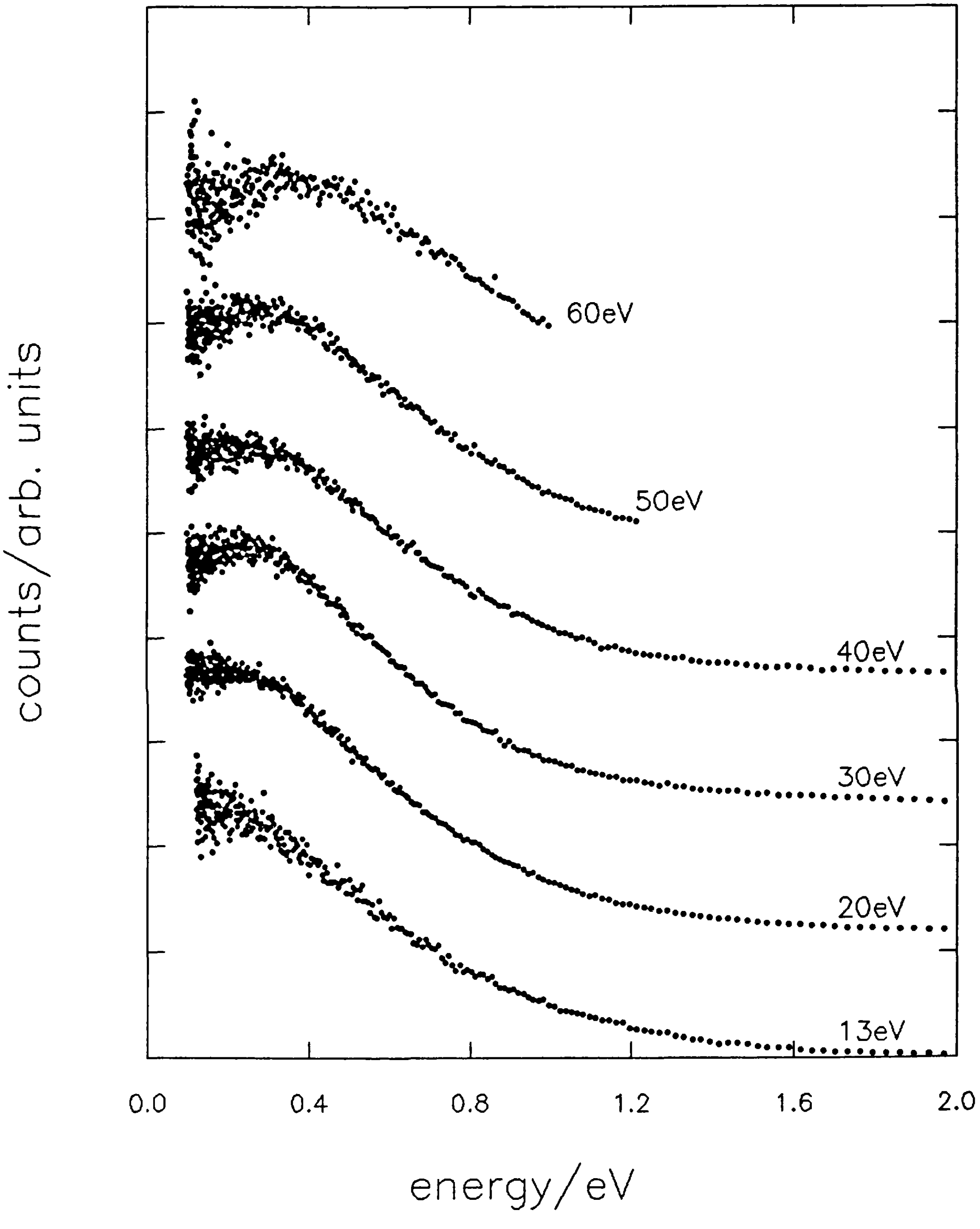

Figure 6.3 Kinetic energy distributions for the metastable nitrogen fragments deduced from the time of flight spectra shown in figure 6.2.

As the incident electron energy increases, the mean fragment kinetic energy increases and the distribution broadens. The increase of the mean kinetic energy in the first five eV above threshold occurs as the Franck-Condon overlap region is exceeded. The broadening at higher energies is due to an increased number of dissociation processes contributing to the metastable nitrogen flux by cascade from higher lying excited states.

Previous work on the dissociation of nitrous oxide by electron impact was reviewed in section 6.2.2. Freund and Klemperer detected mainly the $N_2(A^3\Sigma^+{}_u)$ state since ~95% of the $N_2(a^1\pi_g)$ state produced in the collision would have decayed before reaching the detector which was placed 72cm from the interaction region. Clampitt and Newton measured a threshold of 10.5eV for the production of metastable nitrogen molecules indicating the state detected was the $N_2(a^1\pi_g)$ state. Mason and Newell observed only the $N_2(a^1\pi_g)$ state since they used a bare channel electron multiplier, work function ~8eV. Allcock and McConkey used a photomultiplier tube as a metastable detector placed 41cm from the interaction region. Since most of the $N_2(a^1\pi_g)$ state would have decayed before reaching the detector, their observed kinetic energy spectrum was due to the $N_2(A^3\Sigma^+{}_u)$ state only.

The 12eV and 75eV spectra of Allcock and McConkey are reproduced in figure 6.4a. This data agrees well with the kinetic energy distributions from this work, the present 60eV kinetic energy spectrum peaks at 0.292 ± 0.016eV whereas the 75eV spectrum of Allcock and McConkey peaks at 0.27eV but is not as broad. Such a difference could be due the presence of the $N_2(a^1\pi_g)$ state in the present work but which was absent in the work of Allcock and McConkey. The 12eV and 13eV spectra are, however, in excellent agreement.

Figure 6.4b shows the kinetic energy spectra for an incident electron energy of 20eV from the work of Mason and Newell. The peak in this distribution occurs at 0.125 ± 0.009eV compared with a peak of 0.162 ± 0.016eV in the present work. This substantial difference is due to the different processes being observed. Mason and Newell selectively detected only the $N_2(a^1\pi_g)$ metastable state while in this work a mixture of both the $N_2(A^3\Sigma^+{}_u)$ and the $N_2(a^1\pi_g)$ states was detected.

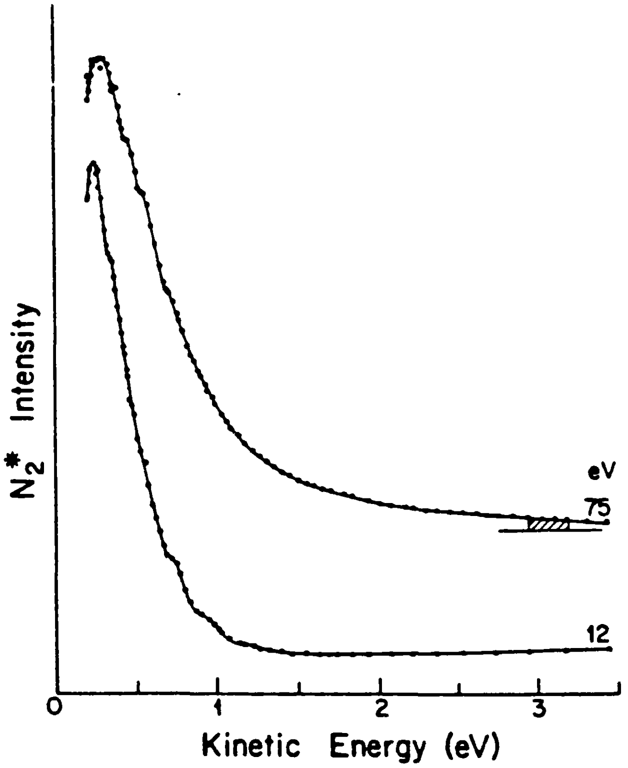

Figure 6.4a Kinetic energy distributions of the metastable nitrogen fragments determined by Allcock and McConkey at incident electron energies of 12eV and 75eV.

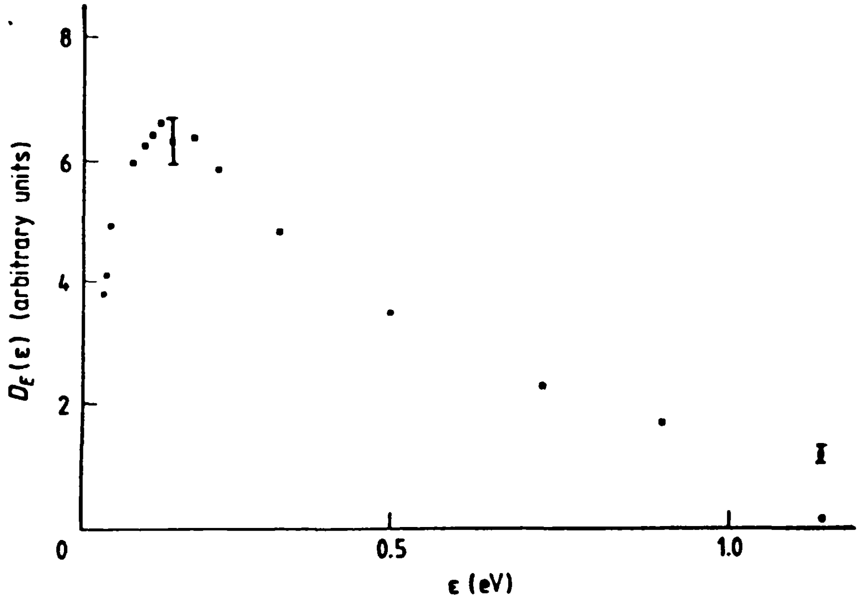

Figure 6.4b Kinetic energy distribution of the metastable nitrogen fragments determined by Mason and Newell at an incident electron energy of 20eV.

The good agreement between the results presented here and those of Allcock and McConkey provides evidence that the dissociative excitation cross section for production of $N_2(A^3\Sigma^+{}_u)$ from N_2O is greater than that for the production of $N_2(a^1\pi_g)$ from N_2O. This was supported by the study of direct electron impact excitation of molecular nitrogen (chapter five) which demonstrated that the tantalum surface detector was preferentially sensitive to the $N_2(a^1\pi_g)$ metastable state.

The steady broadening of the kinetic energy distribution between threshold and 60eV indicates additional processes contributing to the observed metastable molecular nitrogen flux. It has previously been confirmed that cascade contributions to the $N_2(a^1\pi_g)$ state are small (Mason and Newell 1987b, 1989). Therefore in this case the broadening must be due to cascade to the $N_2(A^3\Sigma^+{}_u)$ state. It has been demonstrated by studies of photodissociation of nitrous oxide (McEwan et al 1974) that substantial cascade occurs from both the $N_2(B^3\Pi_g)$ and $N_2(C^3\Pi_u)$ states. It is therefore necessary to consider the following processes in dissociative excitation:

$$
\begin{array}{lll}
 & N_2(A^3\Sigma_u^+) + O(^3P) & \\
e^- + N_2O \rightarrow & N_2(B^3\Pi_g) + O(^3P) & \rightarrow N_2(A^3\Sigma_u^+) + O(^3P) \\
 & N_2(C^3\Pi_u) + O(^3P) & \rightarrow N_2(A^3\Sigma_u^+) + O(^3P)
\end{array}
$$

Such two step processes are not unusual in dissociative excitation as recent studies of dissociative excitation in molecular oxygen have revealed that the $O(^5S)$ metastable fragment is produced predominantly by cascade from $O(^5P)$ (Mason and Newell 1990a).

6.3.4 Potential Energy Curves

Partial potential energy curves for the repulsive part of the bound state cannot be constructed from the kinetic energy spectra determined in the present work because of this significant cascade contribution. Such partial potential energy curves have been deduced for fragments from diatomic molecules such as O_2 (Borst and Zipf 1971b, Freund 1971a) in which the potential of the ground state is well established. To apply the same technique to a triatomic molecule requires knowledge of the ground state potential surface and extension of two dimensional arguments to a three dimensional problem. However, earlier calculations of the potential energy levels of the lowest excited electronic states of nitrous oxide may be reconsidered in the light of the present results.

Semi-empirical calculation of potential energy curves for the lower lying states of nitrous oxide are reproduced in figure 6.5 (Chutjian and Segal 1972). Chutjian and Segal predict that excitation to three different molecular states results in the production of $N_2(A^3\Sigma^+{}_u)$;

1. The bound $N_2O(^1\Sigma^-)$ state,
2. The unbound $N_2O(2^1\Pi)$ state,
3. The unbound $N_2O(2^3\Pi)$ state.

The results of this work indicate that the excited molecular nitrogen fragments originate from the repulsive part of a bound potential energy state since a finite number of metastable fragments are produced with zero kinetic energy, Therefore the production cross section of $N_2(A^3\Sigma^+{}_u)$ via the unbound curves, $N_2O(2^1\Pi)$ and $N_2O(2^3\Pi)$, must be low.

The prediction of the parent molecular state $N_2O(^1\Sigma^-)$ being responsible for the production of the $N_2(A^3\Sigma^+{}_u)$ state does not agree with the deduction of Allcock and McConkey that the possible symmetries of the parent molecular state are Π or Σ^+, while the potential energy states of Chutjian and Segal do not show any bound Π or

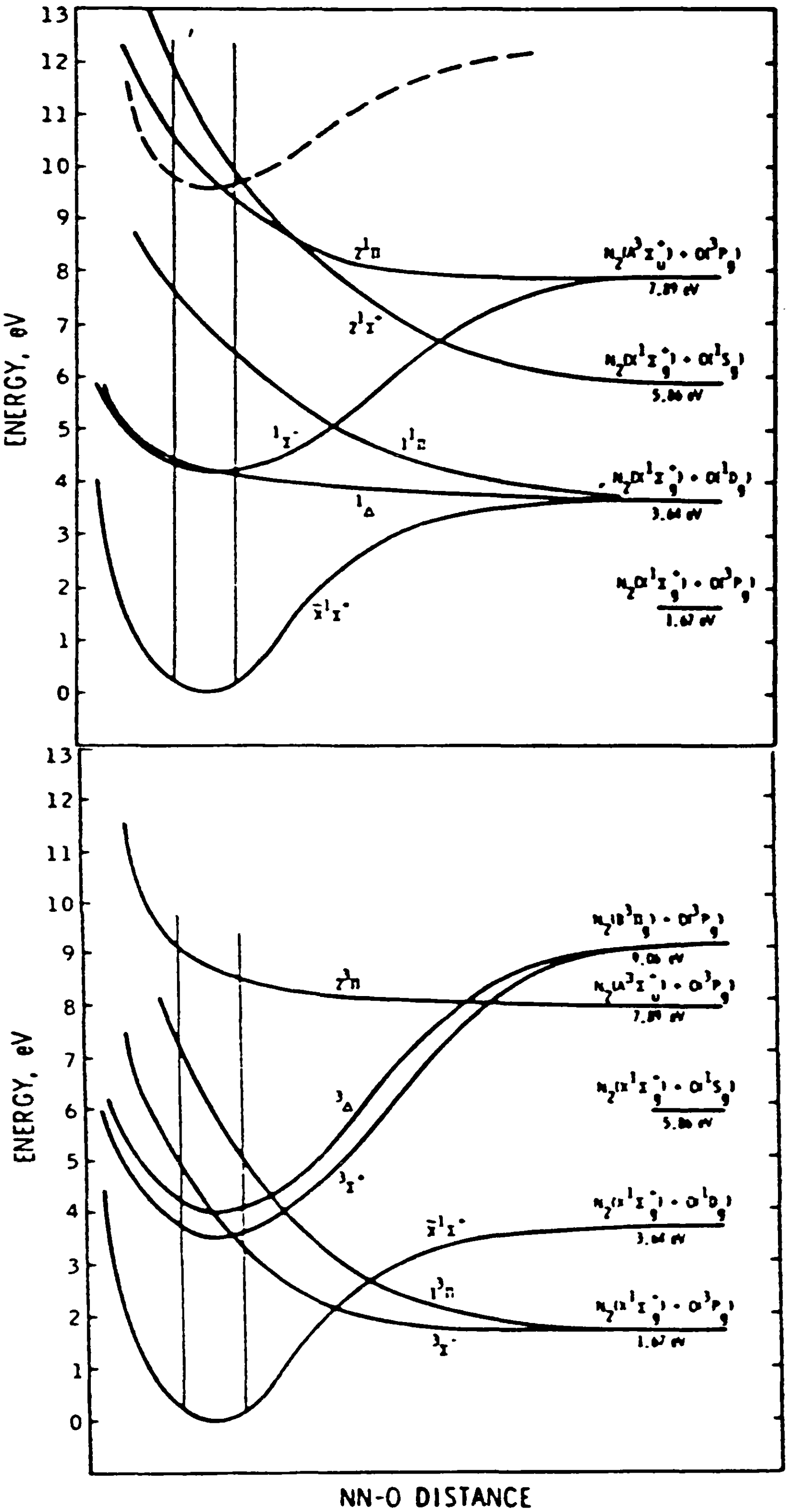

Figure 6.5 Potential energy curves for low lying states of nitrous oxide calculated using a semi-empirical technique (Chutjian and Segal 1972).

Σ^+ states of nitrous oxide which would dissociate producing $N_2(A^3\Sigma^+{}_u)$. However $N_2(B^3\Pi_g)$ is said to be produced from the parent molecular states $N_2O(^3\Delta)$ and $N_2O(^3\Sigma^+)$ and it is well known that $N_2(B^3\Pi_g)$ decays radiatively to $N_2(A^3\Sigma^+{}_u)$ (McEwan et al 1974). Such a process would have a threshold of 9.06eV, higher than that of 7.9eV measured by Allcock and McConkey, however the bound potential energy curves $N_2O(^3\Delta)$ and $N_2O(^3\Sigma^+)$ intersect the unbound curve $N_2O(2^3\Pi)$, allowing predissociation. The kinetic energy distributions of the fragments obtained in the present work are not characteristic of fragments produced by predissociation (chapter one). It is therefore more probable that the $N_2(A^3\Sigma^+{}_u)$ fragments originate from $N_2O(^3\Delta)$ or $N_2O(^3\Sigma^+)$ and are produced predominantly by cascade from the $N_2(B^3\Pi_g)$ state. No calculations of the electronic state of N_2O yielding $N_2(C^3\Pi_u)$, $O(^3P)$ or $O(^5S)$ fragments are available.

6.4 Summary

Knowledge of the properties of the tantalum surface detector allowed a new investigation of the electron impact dissociation of N_2O to be performed in which both the $N_2(A^3\Sigma^+{}_u)$ and $N_2(a^1\pi_g)$ states were observed simultaneously. Comparison of the results obtained in the present work with previous experiments leads to the conclusion that the production of the $N_2(A^3\Sigma^+{}_u)$ state dominates in the dissociation process. The metastable nitrogen fragments are produced from the repulsive part of a bound molecular potential energy curve. There are three possible parent states, $N_2O(^1\Sigma^-)$, $N_2O(^3\Sigma^+)$ or $N_2O(^3\Delta)$. There is also evidence that several competing dissociative channels populate the $N_2(A^3\Sigma^+{}_u)$ state by cascade at the higher energies.

Chapter Seven

Dissociative Excitation of CO($a^3\pi$) and O(^5S) from Carbonyl Sulphide, Carbon Dioxide and Carbon Monoxide

> *Not wrung from speculation and subtleties but from common sense and observation*
>
> Thomas Browne *(Religio Medici)* 1643

7.1 Introduction

In this chapter, the electron impact dissociation of carbonyl sulphide is discussed and compared with the dissociation of carbon dioxide and carbon monoxide. Carbonyl sulphide, carbon dioxide and carbon monoxide are all important molecules in planetary atmospheres.

7.1.1 Carbonyl Sulphide

Carbonyl sulphide is one of the most abundant sulphur bearing compounds in the terrestrial atmosphere and is found in the greatest concentrations in the troposphere (Crutzen 1976) and in the stratosphere (Inn et al 1979). The dissociation of carbonyl sulphide is an initial step in the formation of stratospheric sulphate aerosol particles (Crutzen 1976) which affect the earth's radiation balance and climate. Like carbon dioxide, carbonyl sulphide contributes to the 'greenhouse effect' in which far infrared radiation from the earth's surface is trapped, resulting in heating of the atmosphere. Carbonyl sulphide is also present in significant quantities in the interstellar medium (Hollis and Ulich 1977) and transitions in carbonyl sulphide have been observed in the interstellar clouds Sgr B2 (OH) and W51 (Hollis and Ulich 1977).

The carbonyl sulphide concentration in the stratosphere is maintained by diffusion of carbonyl sulphide from the troposphere (Turco et al 1981 and references therein). The main source of tropospheric carbonyl sulphide is the reaction of carbon disulphide with hydroxyl radicals,

$$CS_2 + OH \rightarrow OCS + SH$$

Sources of tropospheric carbon disulphide include anaerobic fermentation, emissions from the oceans and marshes and industrial processes such as manufacture of viscose rayon, brick making and fish meal processing.

Other sources of tropospheric carbonyl sulphide are fuel combustion, organic decomposition, agricultural burning, forest fires and emissions from blast furnaces, coke ovens and mills (Cox and Derwent 1981). As much as 50% of the atmospheric carbonyl sulphide may be due to anthropogenic processes (Turco et al 1980). A small contribution comes from volcanic activity.

The carbonyl sulphide produced during combustion of fossil fuels may be as much as 0.1% by volume of the gases produced (Turco et al 1980). Cleaning of gases before emission reduces this significantly. Catalytic converters in cars may occasionally produce large quantities of carbonyl sulphide and hydrogen sulphide. All the sulphur in petrol, although only ~0.05% by weight, is released to the atmosphere.

The major atmospheric sink of carbonyl sulphide is its reaction with hydroxyl radicals,

$$OCS + OH \rightarrow CO_2 + SH$$

in which the main greenhouse gas, carbon dioxide, is produced. Ultraviolet photodissociation of carbonyl sulphide above 20km is both a sink for carbonyl sulphide and a source of sulphur for stratospheric aerosols.

7.1.2 Carbon Dioxide and Carbon Monoxide

In the terrestrial atmosphere, carbon dioxide is the major greenhouse gas. The sources of atmospheric carbon dioxide are processes occurring in the terrestrial biosphere such as combustion of fossil fuels, limestone burning, destruction of forests, plant respiration and oxidation of carbon monoxide. A small proportion of the terrestrial carbon dioxide also comes from metamorphism and volcanism (Cox and Derwent 1981). Sources of carbon monoxide are the oxidation of naturally occurring methane and natural and man-made hydrocarbons, industrial processes involving the incomplete combustion of wood, gas, coal and oil, forest fires and emissions from the oceans.

Carbon monoxide makes up ~20% of the gases in cometary tails while carbon dioxide is a major constituent of the Martian and Venusian atmospheres. The Martian airglow spectrum recorded by Mariner 9 (Barth et al 1972) is dominated by the Cameron band system, $CO(a^3\pi - X^1\Sigma^+)$. Calculations by Fox and Dalgarno (1979) indicate that the upper state of this system is populated predominantly by dissociation of carbon dioxide by photons and photoelectrons. Another important feature of the Martian airglow is the Fourth Positive band system, $CO(A^1\Pi - X^1\Sigma^+)$ (Barth 1969). The calculations of Fox and Dalgarno show that the upper state of this band system is populated through photon and electron impact dissociation and by dissociative recombination. The calculated altitude profiles have already been presented in chapter one.

7.2 Review of Dissociation of Carbonyl Sulphide

In the dissociation of carbonyl sulphide several atomic or molecular metastable species may be excited, depending on the energy, E, of the incident electron. Some of these dissociative modes are described by the equations:

$$e_E + OCS \rightarrow \begin{array}{l} \underline{CO(a^3\pi)} + S(^3P) + e_{E-\delta E1} \\ CS(X^1\Sigma) + \underline{O(^5S)} + e_{E-\delta E2} \\ CO(X^1\Sigma) + \underline{S(^5S)} + e_{E-\delta E3} \end{array}$$

in which the metastable fragment produced in each case is underlined.

7.2.1 Photodissociation

Previous work on the photodissociation of carbonyl sulphide is summarised in table 7.1.

Table 7.1 Experimental and theoretical studies of photodissociation of carbonyl sulphide.

Reference	Wavelength Range /nm	Method
Ashfold et al 1979		Review of photodissociation up to 1978
Black et al 1975	111-170	Experimental study of the quantum yield of S(^{1}S) by observation of fluorescence
Lee and Judge 1975	68.6-123.9	Experimental study of the CS yield by observation of fluorescence
Lee and Chiang 1982	106-124	Experimental determinations of the cross sections for production of excited states
Strauss et al 1989	157	Experimental identification of the electronic states of the S and CO
Ondrey et al 1983	157	Experimental time of flight analysis of atomic sulphur fragments
Klemm et al 1975	>105	Experimental comparison of the yield of (CO + S) with that of (CS + O)
Rudolph and Inn 1981	200-300	Experimental determination of the quantum yield of CO
Turco et al 1981	>270	Calculation of dissociation rates

7.2.2 Electron Impact Dissociation

There have been several studies of the electron scattering cross sections for electron impact on carbonyl sulphide. These are summarised in table 7.2.

Table 7.2 Experimental determinations of the cross sections for electron scattering from carbonyl sulphide.

Reference	Energy Range /nm	Method
Lynch et al 1979	0-100	Calculation of the integral elastic scattering cross section
Szmytkowski and Zubek 1978	0-8	Experimental determination of absolute total cross sections
Szmytkowski 1983	0.4-30	Experimental determination of absolute total cross sections
Szmytkowski et al 1984	0-22	Experimental determination of absolute total cross sections
Szmytkowski et al 1989	40-100	Experimental determination of absolute total cross sections
Leclerc et al 1981	5-17	Experimental determination of energy and angular dependence of scattered molecules
Sohn et al 1987	0.3-5	Experimental determination of energy and angular dependence of scattered molecules

There has been only one study of electron impact dissociative excitation of fragments from carbonyl sulphide (van Brunt and Mumma 1975). Van Brunt and Mumma used time of flight spectroscopy to study the product metastable fragments which were detected by a tantalum surface at 20°C, a brass surface at 20°C and a tantalum surface heated to a temperature just below that at which thermionic emission occurs. The results for both room temperature detectors were the same, while the heated tantalum detector was very sensitive to $CO(a^3\pi)$ fragments. Their time of flight spectra reveals three distinct peaks, however they did not clearly identify the fragments responsible for each peak and consequently were not able to deduce the kinetic energy distributions. The new results obtained in this work will be compared with the results of van Brunt and Mumma and their conclusions re-examined following new data analysis.

7.3 Review of Dissociation of Carbon Dioxide

While the electron impact dissociation of carbonyl sulphide has not been extensively studied, there have been numerous investigations of the electron impact dissociation of carbon dioxide. These two molecules are expected to display similar dissociative features since they both contain a $C=O$ bond.

7.3.1 Studies of the $CO(a^3\pi)$ Fragment

Freund and Klemperer (1967) studied the electron impact dissociation of carbon dioxide by the method of translational spectroscopy. They used incident electron energies of between 12 and 15eV and detected the metastable fragments produced at a heated tantalum surface. Their time of flight spectra indicate that only one metastable fragment was detected. The application of a magnetic field caused a deflection in the product metastable beam from which they deduced that the metastable fragment was polar and therefore was CO^* and not CO_2^*. They proposed that the process occurring was

$$CO_2 + e^- \rightarrow CO(a^3\pi) + O(^3P) + e^- \qquad (1)$$

The efficiency of the detector was assumed to be 5%, giving a cross section of $2 \times 10^{-16}cm^2$, but Freund and Klemperer noted that this value was a sum over several dissociation channels and not the cross section for a single well defined process. A velocity distribution for the CO($a^3\pi$) fragment was deduced from the time of flight spectra and showed a peak velocity of 1kms^{-1} for these fragments. Both the cross section and the peak velocity of the CO($a^3\pi$) fragments determined by Freund and Klemperer have subsequently been shown to be very high. The cross section measured by Freund and Klemperer probably includes cascade from higher lying states such as CO($A^3\Sigma^+$) and CO($d^3\pi$).

Clampitt and Newton (1969) also studied the production of CO($a^3\pi$) from the dissociation of carbon dioxide using translational spectroscopy. They postulated that the process was

$$CO_2 + e^- \rightarrow CO(a^3\pi) + O^- \qquad (2)$$

Clampitt and Newton rejected the process postulated by Freund and Klemperer since the calculated threshold for this process is 11.5eV while they measured the threshold as 10.3eV. Production of a negative oxygen ion was said to require such a lower threshold.

Corvin and Corrigan (1969) measured the rate coefficient for the dissociation of carbon dioxide in the positive column of a d.c. glow discharge. The number of carbon dioxide molecules which were dissociated in collisions was determined by measuring the pressure of the carbon dioxide and the dissociation products and then freezing out the carbon dioxide onto a liquid nitrogen trap and measuring the new pressure. It was then possible to relate the difference in the two pressures to the number of carbon dioxide molecules dissociated. They observed that no condensible products were collected on the liquid nitrogen trap other than non-dissociated carbon dioxide molecules. The dissociation products, therefore, must have been carbon monoxide and atomic oxygen. Furthermore, they deduced that for every two carbon dioxide molecules lost in dissociation, three gas molecules were produced, the most probable reaction being,

$$\begin{aligned} 2\,CO_2 + e^- &\rightarrow 2\,(CO(a^3\pi) + O) + e^- \\ &\rightarrow 2\,CO(a^3\pi) + O_2 + e^- \end{aligned}$$

Freund (1971b) using the same apparatus as Freund and Klemperer re-measured the threshold for production of $CO(a^3\pi)$ to be 11.65 ± 0.03eV in agreement with calculations for process (1). Freund also measured the cross section for this process compared to that for direct electron impact excitation of $CO(a^3\pi)$ from carbon monoxide, assuming the same isotropic angular distribution for both processes. The maximum dissociative cross section obtained by this method was $4 \times 10^{-17}cm^2$ at an incident electron energy of 27eV.

Freund used incident electron energies of 11 to 90eV and detected the fragments at two different surfaces, a warm tantalum surface and a copper-beryllium photodiode. The time of flight spectra for both detectors revealed two peaks. The slow peak was due to the $CO(a^3\pi)$ fragments and Freund proposed that the second, faster, peak was due to $O(^5S)$ metastable fragments.

Wells et al (1972) studied the dissociative excitation of $CO(a^3\pi)$ from carbon dioxide by translational spectroscopy and detected the fragments at a tungsten surface. They measured the threshold for production of metastable fragments as 11.9 ± 0.5eV, in broad agreement with the figure of Freund and of Clampitt and Newton. From the time of flight spectra, Wells et al deduced a mean fragment kinetic energy of 0.3eV, although they did not publish a kinetic energy distribution for the fragments.

At higher incident electron energies, they investigated the possibility of additional fragments contributing to the slower peak. They measured the excitation potentials by detecting the product fragments at four different detecting surfaces, a Cu-Be dynode, two contaminated tungsten surfaces for which the secondary electron emission coefficients differed by a factor of two, and a contaminated magnesium surface. Their assumption was that the secondary electron emission from the surface was dependent on the difference between the work function of the surface and the energy of the metastable state. Since all the measured excitation functions were identical within their experimental error, Wells et al concluded that the $CO(a^3\pi)$ metastable state alone was responsible for this peak in the time of flight spectrum.

Wells et al also determined the cross section for the dissociation process to be 3 x

10^{-18} cm^2/sr at an incident electron energy of 20eV. To measure this differential cross section, they observed both the direct electron impact excitation of $CO(a^3\pi)$ from carbon monoxide and the dissociative excitation from carbon dioxide in the same apparatus. The measured cross section for the direct excitation process of Ajello (1971) was then used to determine the cross section for the dissociative process. The assumptions made in this determination were that the dissociation products were produced with an isotropic distribution and that the lifetime of the $CO(a^3\pi)$ metastable state is 1ms (Borst and Zipf 1971a). This value of the lifetime was used to correct for the number of metastable molecules which decayed before reaching the detector.

Welge and Gilpin (1971) used time of flight spectroscopy to study the photodissociation of carbon dioxide. Wavelengths longer than 105nm (<11.8eV) resulted in the production of low energy (<6eV) metastable fragments which necessitated the use of a low work function caesium coated detector capable of detecting these states. The metastable fragments detected were $O(^1D)$, $O(^1S)$ and $CO(a^3\pi)$ at 1.96, 4.17 and 6.0eV respectively.

7.3.2 Studies of the $O(^5S)$ Fragment

There have been two studies of the $O(^5S)$ fragments produced by dissociative excitation from carbon dioxide, Misakian et al (1975) and Allcock and McConkey (1976). Both these studies used detectors of work function $\leq$6eV, and consequently detected both $O(^5S)$ and $CO(a^3\pi)$ fragments.

Misakian et al used a Bendix channel electron multiplier of work function $\sim$6eV to detect the fragments produced in dissociation. Since this detector was capable of detecting metastable fragments of energy $\geq$6eV their time of flight spectra reveal peaks due to $CO(a^3\pi)$ as well as $O(^5S)$. Their analysis concentrated on the product atomic oxygen fragments. They recorded time of flight spectra at incident electron energies from threshold to 125eV and subsequently converted these to kinetic energy distributions.

The time of flight spectra of the excited oxygen fragments revealed five features. With the aid of the kinetic energy distributions for the oxygen fragments and measurement of their angular distribution, Misakian et al identified the slowest of the these features as being due to $O(^5S)$ produced by predissociation of the $CO_2(\Sigma^+{}_u)$ state into $CO(a^3\pi)$ and $O(^5S)$. They proposed that the next slowest feature was due to Rydberg atoms from a Rydberg state of carbon dioxide.

Allcock and McConkey also used translational spectroscopy to study the excited oxygen peak. They used two detectors, a copper-beryllium diode of work function ~6eV and a silver-oxygen-caesium photodiode of work function <4eV. They recorded time of flight spectra over the incident electron energy range threshold to 100eV. They also concluded that the oxygen peak is due to both metastable oxygen atoms and to Rydberg oxygen atoms. They found good agreement with the results of Misakian et al.

7.4 Review of Dissociation of Carbon Monoxide

Wells et al (1978) investigated the dissociation of carbon monoxide to metastable states of atomic carbon and oxygen. The time of flight spectra recorded over the incident electron energy range 23 - 26eV revealed eight features. Wells et al identified these as Rydberg states of both atomic oxygen and carbon and $O(^5S)$ metastable atoms having kinetic energies in the range 0 - 9eV.

7.5 Dissociation of Carbonyl Sulphide

7.5.1 Tantalum Surface Detector

a) Time of Flight

Time of flight spectra for the dissociative excitation of carbonyl sulphide obtained using the warm tantalum surface detector are shown in figure 7.1.

At an incident electron energy of 15eV, the spectrum consists of only one feature, peak (1), due to fragments with a mean arrival time of 40μs. At an incident electron energy of 20eV, a shoulder develops on the short flight time side of peak (1) and at 35eV this feature dominates the spectrum as peak (2). The fragments responsible for this peak have a mean arrival time at the detector of 23μs. A second shoulder also appears on the short flight time side of peak (2) at an incident electron energy of 30eV. This peak, (3), is due to fragments with a mean arrival time of 14μs and dominates the time of flight spectrum at incident electron energies above 40eV.

These peaks may be ascribed to the metastable species $CO(a^3\pi)$, $O(^5S)$, $S(^5S)$ or to long-lived high Rydberg fragments, all of which have excitation energies above the detection threshold ($\sim$5eV) of the warm tantalum surface.

In the work of van Brunt and Mumma, peak (3) was identified as being due to unspecified Rydberg species, O^{**}, CO^{**} and S^{**}. In the present work, no Rydberg states of carbon monoxide or sulphur were observed in the spectra recorded when using the channel electron multiplier. Comparison of the time of flight spectra for carbonyl sulphide with those for carbon dioxide and carbon monoxide from this work and previous studies suggest that it is due to either $O(^5S)$ metastable fragments or long-lived high Rydberg oxygen fragments, O^{**}. It is difficult to distinguish between these two products. However, earlier work (Wells et al 1978, Freund 1971, Allcock and McConkey 1976) has shown that in many dissociative processes resulting in the production of Rydberg oxygen atoms these cascade down to the $O(^5S)$ state. This is

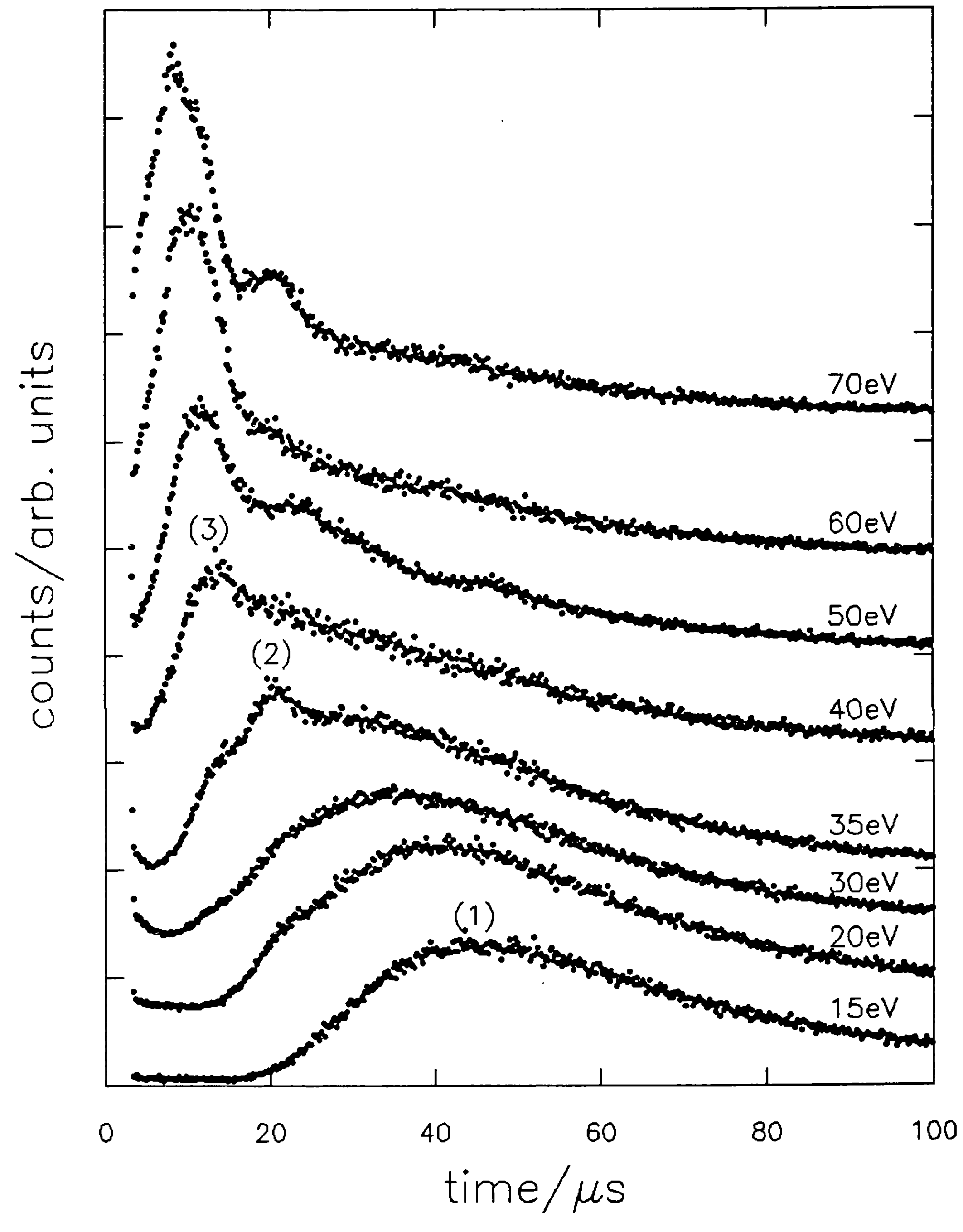

Figure 7.1 Time of flight spectra for the fragments produced in dissociation of carbonyl sulphide for incident electron energies between 15eV and 70eV. The detector was the tantalum surface detector.

also true for the processes in which other excited quintet states of atomic oxygen such as $O(3d^5D_0)$ and $O(3p^5P)$ are produced. It is not possible in this experiment to determine the fraction of O^{**} fragments which decay to $O(^5S)$ atoms before being detected or the fraction which remain in the Rydberg state.

Peak (2) is not so easy to identify. This peak was observed only in the time of flight spectrum recorded by the tantalum surface detector and is therefore due to metastable fragments of excitation energy less than 8eV but greater than 5eV. There is no corresponding feature in the time of flight spectra of carbon dioxide observed by the tantalum detector so the metastable fragments are most probably sulphur atoms. The only metastable state in the required range of excitation energies, $5eV \leq E^* \leq 8eV$, is $S(^5S)$ of excitation energy 6.52eV. The time of flight spectra recorded also reveal that no metastable states of CS or carbonyl sulphide, OCS, are detected, either because the production cross sections are very small, or because the internal energy is below that of the detection threshold of the tantalum surface, 5eV.

b) Kinetic Energy

A consequence of the conversion from time to kinetic energy is that the peak in the kinetic energy distribution corresponds to a position in the tail of the time of flight spectrum. For this reason, it is clear that the only feature in the time of flight spectra recorded by the tantalum surface detector (figure 7.1) which may be replotted successfully in terms of kinetic energy is peak (1), that due to $CO(a^3\pi)$. The time of flight spectra used were those for incident electron energies 15eV and 20eV. These energies are below the threshold for production of $O(^5S)$. To eliminate any contribution from $S(^5S)$ fragments, the region of the spectrum which was converted to kinetic energy was chosen to be that on the long flight time side of the mean arrival time of the $CO(a^3\pi)$ molecules.

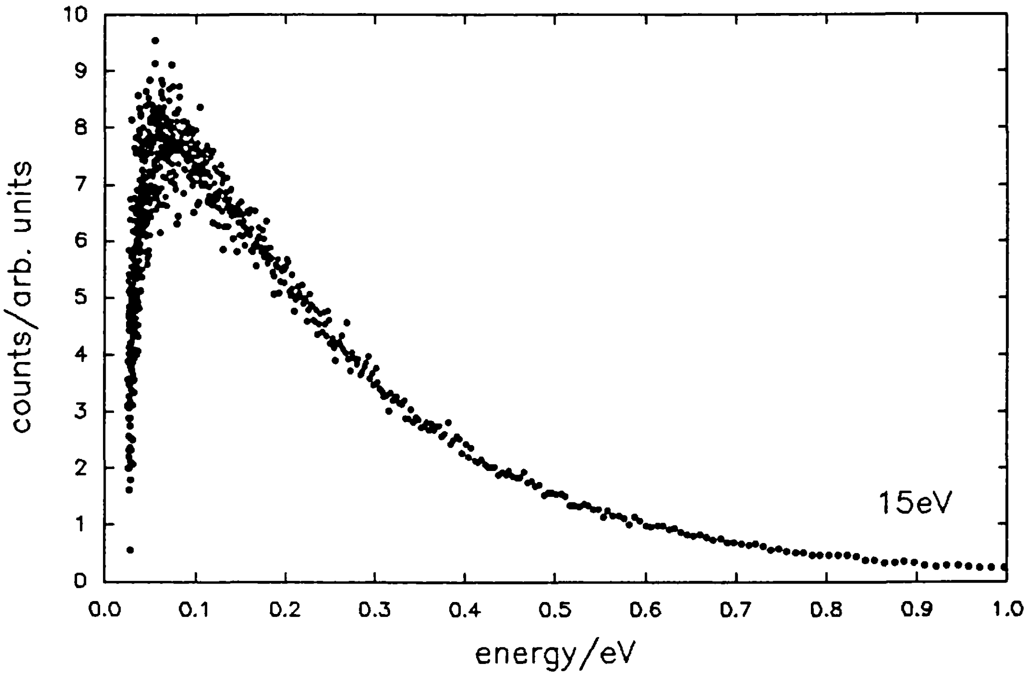

Figure 7.2a Kinetic energy distributions of CO($a^3\pi$) fragments produced in the dissociation of carbonyl sulphide at an incident electron energy of 15eV.

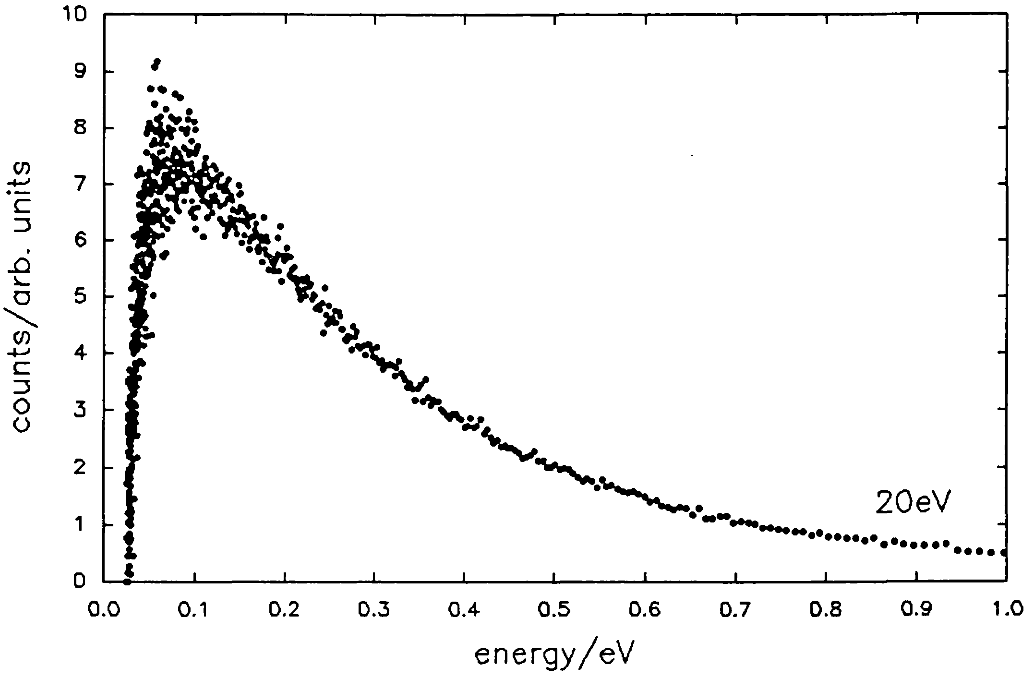

Figure 7.2b Kinetic energy distributions of CO($a^3\pi$) fragments produced in the dissociation of carbonyl sulphide at an incident electron energy of 20eV.

The kinetic energy distributions for the CO($a^3\pi$) fragments at incident electron energies of 15eV and 20eV are shown in figure 7.2. The peak in the 15eV distribution occurs at 0.2eV compared with typical thermal energies of carbon monoxide molecules of ~0.02eV. The position of the peak is in broad agreement with that for the CO($a^3\pi$) fragments produced in dissociation of carbon dioxide determined by Wells et al 1972.

7.5.2 Channel Electron Multiplier

a) Time of Flight

A convenient way to resolve the peaks is to change the detector to one of a different threshold detection energy. The tantalum surface was therefore removed and a bare channel electron multiplier (Mullard B419BL) used in its place. Since the channel electron multiplier has a detection threshold of ~8eV it is unable to detect the CO($a^3\pi$) and S(^5S) fragments which have energies 6.01 and 6.52eV respectively. The only fragments produced in dissociation of carbonyl sulphide that are detected by the channel electron multiplier are expected to be O(^5S) at 9.14eV, a higher lying metastable state of carbon monoxide at ~10eV (Wells et al 1978) or high lying Rydberg states.

A typical time of flight spectrum of the fragments produced in dissociation of carbonyl sulphide detected by the channel electron multiplier is shown in figure 7.3. There is a single peak, mean arrival time 14μs, which corresponds to peak (3) in figure 7.1. There is no evidence of 10eV metastable carbon monoxide fragments, which would have longer flight times than the oxygen fragments, having been produced by dissociative excitation. Neither is there any evidence of long-lived Rydberg states of sulphur or of carbon monoxide.

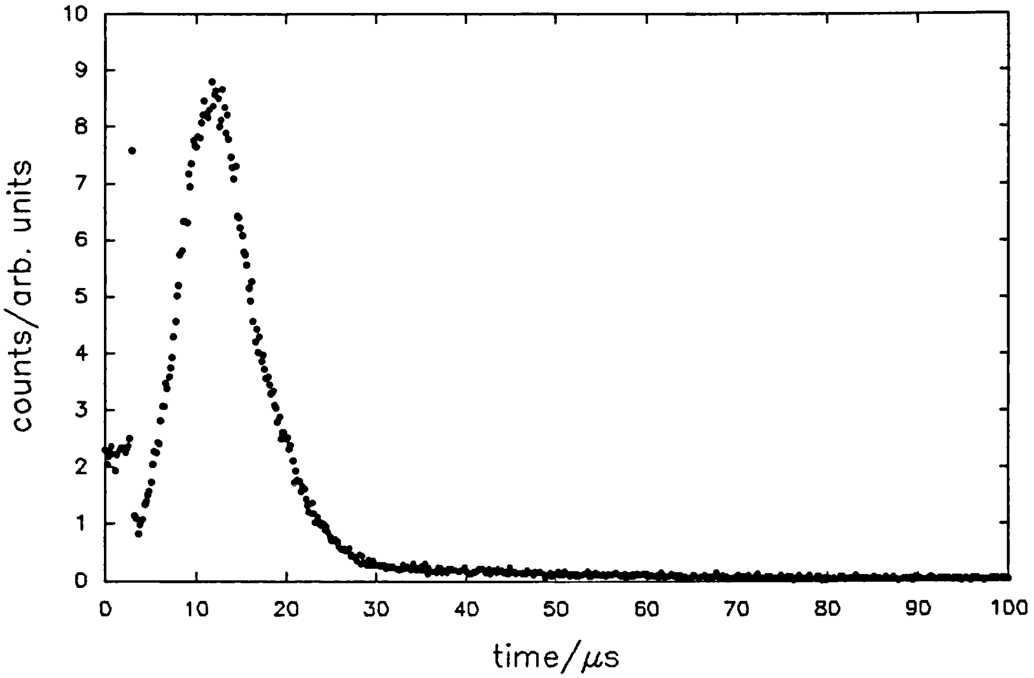

Figure 7.3 Time of flight spectrum for the oxygen fragments produced in the dissociation of carbonyl sulphide at an incident electron energy of 50eV. The detector was a channel electron multiplier.

This assists in the identification of the peaks in figure 7.1. Peak (1) must be due to metastable fragments of energy less than 8eV since the peak was absent in the time of flight spectra recorded by the channel electron multiplier, but of energy greater than 5eV since the peak was present in the time of flight spectra recorded by the tantalum surface detector. These observations are consistent with CO($a^3\pi$) fragments being responsible for peak (1). Peak (3) must be due to metastable fragments of energy greater than 8eV, since this peak was present in spectra recorded by both the tantalum surface detector and the channel electron multiplier.

The use of a channel electron multiplier revealed no evidence for the production of the 10eV metastable state of carbon monoxide (Mason and Newell 1988) in dissociation of carbonyl sulphide by electron impact. Van Brunt and Mumma listed a series of possible dissociation channels involving such a 10eV state and since the present work provides no evidence for such metastable production the possible dissociation channels are reduced to those listed in table 7.3.

Table 7.3 Thresholds for the production of metastable fragments in the dissociation of carbonyl sulphide. Processes involving production of Rydberg states or ions are not included.

Threshold /eV Ashfold et al 1979	Threshold /eV van Brunt and Mumma 1975	Products
3.16		$CO(X^1\Sigma^+) + S(^3P)$
7.30		$CS(X^1\Sigma^+) + O(^3P)$
9.17	9.23	$CO(a^3\pi) + S(^3P)$
	9.74	$CO(X^1\Sigma^+) + S(^5S)$
10.32	10.38	$CO(a^3\pi) + S(^1D)$
10.72		$CS(a^3\pi) + O(^3P)$
	11.09	$CO(X^1\Sigma^+) + S(^5P) \rightarrow CO(X^1\Sigma^+) + S(^5S)$
	11.64	$CO(X^1\Sigma^+) + S(^5D) \rightarrow CO(X^1\Sigma^+) + S(^5S)$
11.92		$CO(a^3\pi) + S(^1S)$
	11.99	$CO(a^3\pi) + S(^5S)$
12.69		$CS(a^3\pi) + O(^1D)$
14.91		$CS(a^3\pi) + O(^1S)$
	15.64	$CS(X^1\Sigma^+) + O(^5S)$
	23.58	$C(^1S) + S(^5S) + O(^3P)$
	24.66	$C(^3P) + S(^1D) + O(^5S)$

b) Kinetic Energy

Although all the recorded time of flight spectra of the oxygen fragments produced by electron impact dissociation of carbonyl sulphide at different incident electron energies are very similar, differences become apparent when the spectra are replotted in terms of the kinetic energy of the fragments. The kinetic energy distributions for the fragments produced at incident electron energies of 40, 50 and 60eV are shown in figure 7.4. Feature (A) in the 40eV spectrum occurs at 1.25eV. As the incident electron energy is increased a second feature, (B), appears at a mean kinetic energy of 1.88eV. Although the peak energy of feature (A) remains the same as the incident electron energy increases, the peak kinetic energy of feature (B) increases to 2.2eV at an incident electron energy of 60eV.

In the only other study of the dissociation of carbonyl sulphide by electron impact (van Brunt and Mumma 1975) no kinetic energy distributions of the fragments were determined. However the electron impact dissociation of carbon dioxide has been widely studied and the kinetic energy distributions of the fragments are well known.

7.6 Dissociation of Carbon Dioxide

For comparison with the kinetic energy distributions for the $O(^5S)$ fragments from carbonyl sulphide, time of flight spectra for the $O(^5S)$ fragments from carbon dioxide were recorded using the channel electron multiplier.

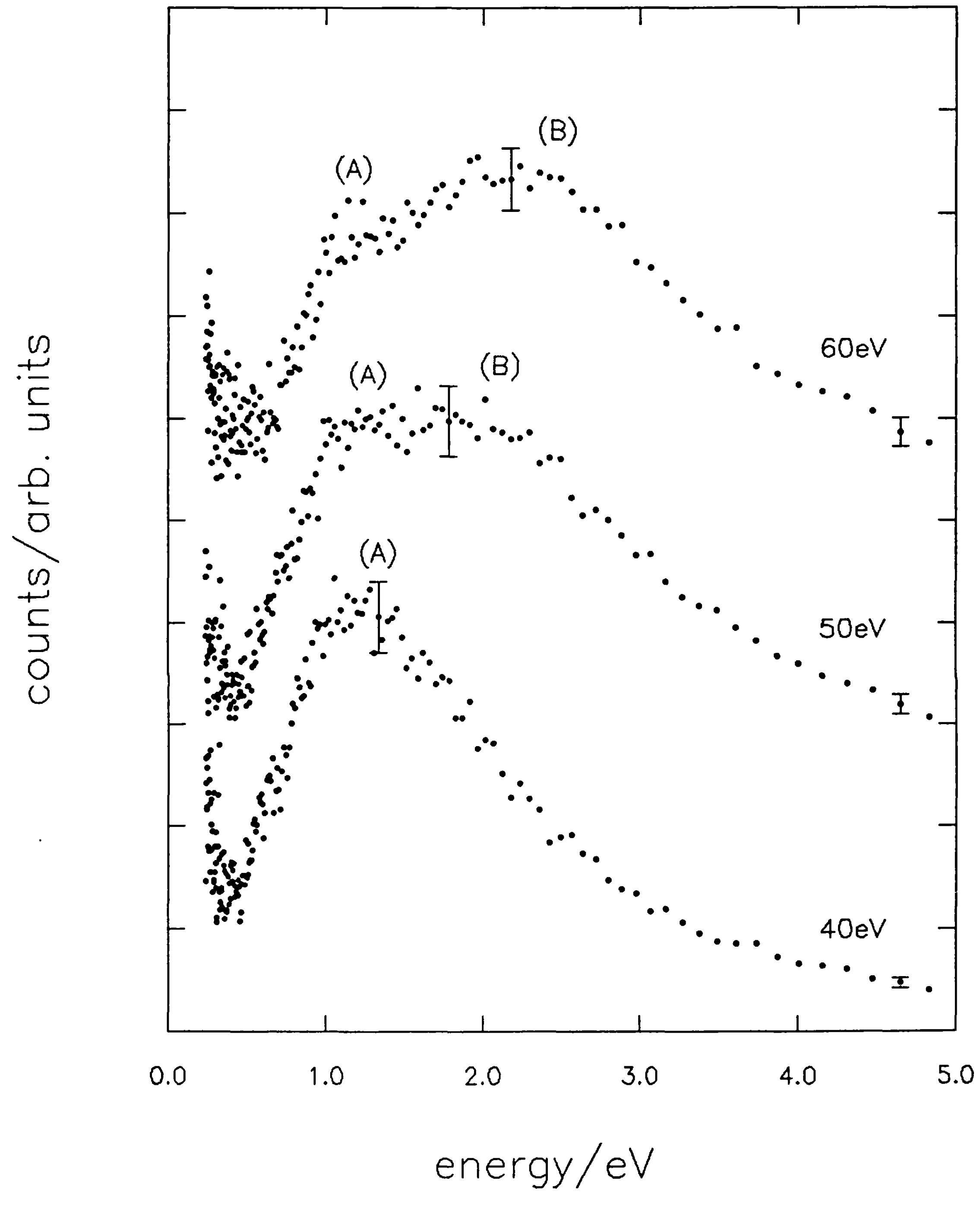

Figure 7.4 Kinetic energy distribution of the oxygen fragments produced in dissociation of carbonyl sulphide at incident electron energies of 40, 50 and 60eV.

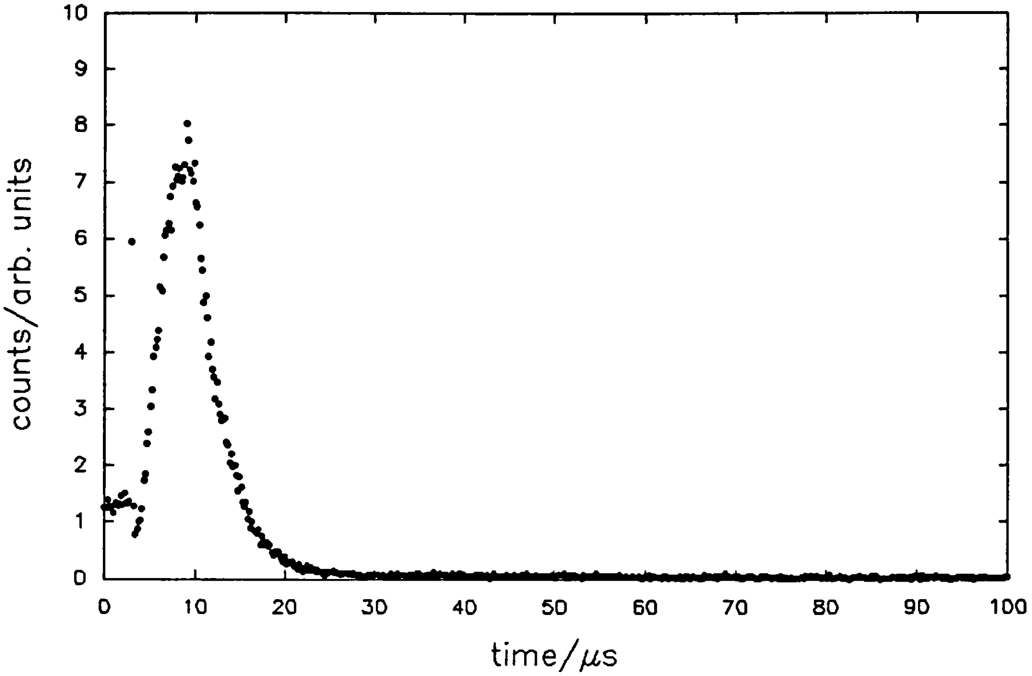

Figure 7.5 Time of flight spectrum for oxygen fragments produced in the dissociation of carbon dioxide at an incident electron energy of 50eV.

a) Time of Flight

The time of flight spectra obtained at incident electron energies of 40, 50 and 60eV were all similar, having a single peak at a mean arrival time of ~10μs, figure 7.5.

b) Kinetic Energy

The kinetic energy distributions of the oxygen fragments from the dissociation of carbon dioxide are shown in figure 7.6. The spectrum for incident electron energy of 40eV shows two features. The first, feature (A), occurs at a mean kinetic energy of 1.89eV, while the second, feature (B), is faster, having a mean kinetic energy of 3.00eV. As the incident electron energy increases, the mean kinetic energy of both features increases. At an incident electron energy of 60eV, the mean kinetic energy of feature (A) is 2.53eV while that of feature (B) is 4.41eV.

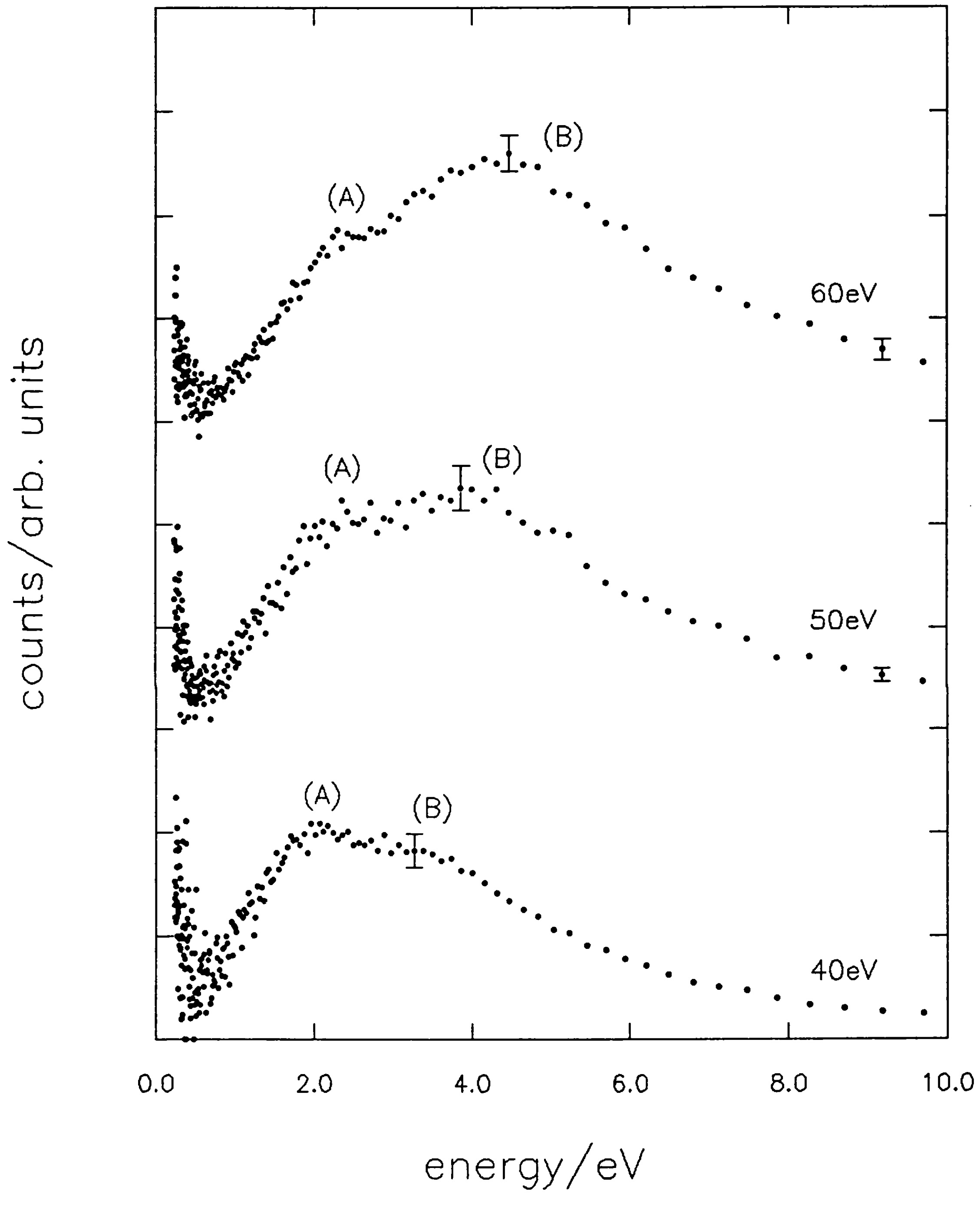

Figure 7.6 Kinetic energy distribution of the oxygen fragments produced in the dissociation of carbon dioxide at incident electron energies of 40, 50 and 60eV.

7.7 Dissociation of Carbon Monoxide

To assist the understanding of the dissociation of carbonyl sulphide, the same method was used to record the time of flight spectra for the O(^{5}S) fragments produced in dissociation of carbon monoxide.

a) Time of Flight

The time of flight spectra of the O(^{5}S) fragments from the dissociation of carbon monoxide at incident electron energies of 40, 50 and 60eV are also all similar, figure 7.7. The mean arrival time of the fragments is $\sim 8\mu s$, faster than the fragments from either carbonyl sulphide or carbon dioxide.

b) Kinetic Energy

The kinetic energy distributions of the oxygen fragments for these incident electron energies are shown in figure 7.8. The kinetic energy distributions for the oxygen fragments from carbon monoxide differ from those fragments from carbonyl sulphide and carbon dioxide in that there is a single peak in the distribution. This feature, (A), shows an increase in the peak kinetic energy from 3.75eV at 40eV to 4.69eV at 60eV incident electron energy.

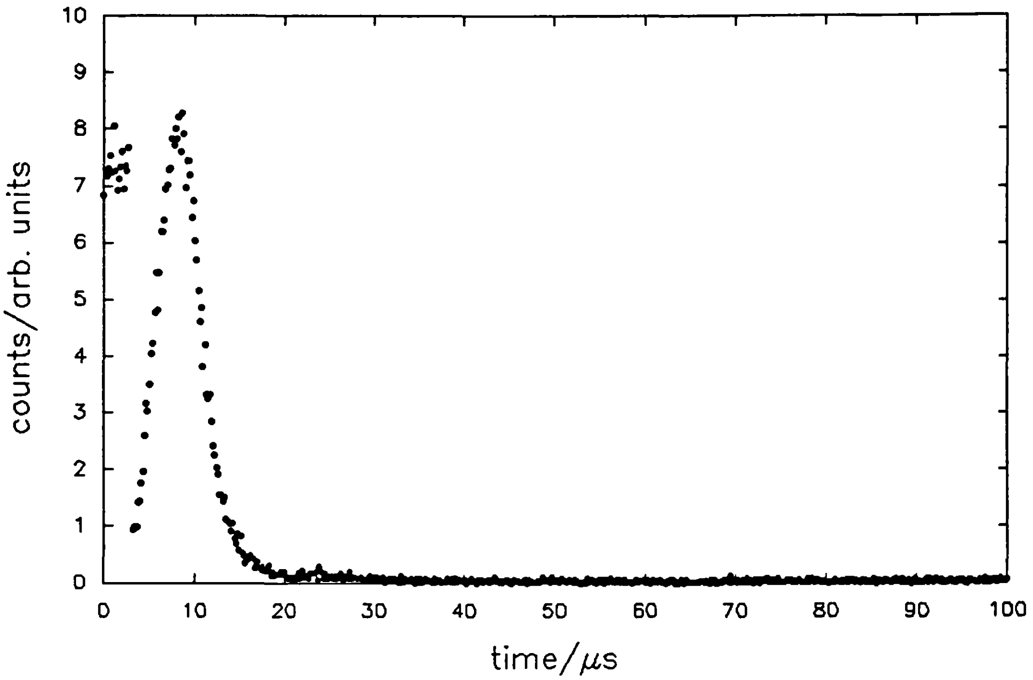

Figure 7.7 Time of flight spectrum for oxygen fragments produced in the dissociation of carbon monoxide at an incident electron energy of 50eV. The detector was a channel electron multiplier.

7.8 Discussion

The kinetic energy distributions of the metastable fragments produced by dissociative excitation allows the nature of the dissociation process to be investigated. Fragments from different parent potential energy states have different characteristic kinetic energy distributions.

Long data collection periods, typically 50 hours, gave good statistics in the peaks, but because of the t^3 dependence in the time to energy conversion, small statistical fluctuations at long flight times give rise to large variations in the low kinetic energy part of the energy distribution. To reduce the error due to the statistical fluctuations in the tail of the metastable peak, a constant background, deduced from the long flight time part of the time of flight spectrum where no metastable molecules reach the detector, was subtracted from the time of flight spectrum. The uncertainty in the position of the kinetic energy peak is typically 10%.

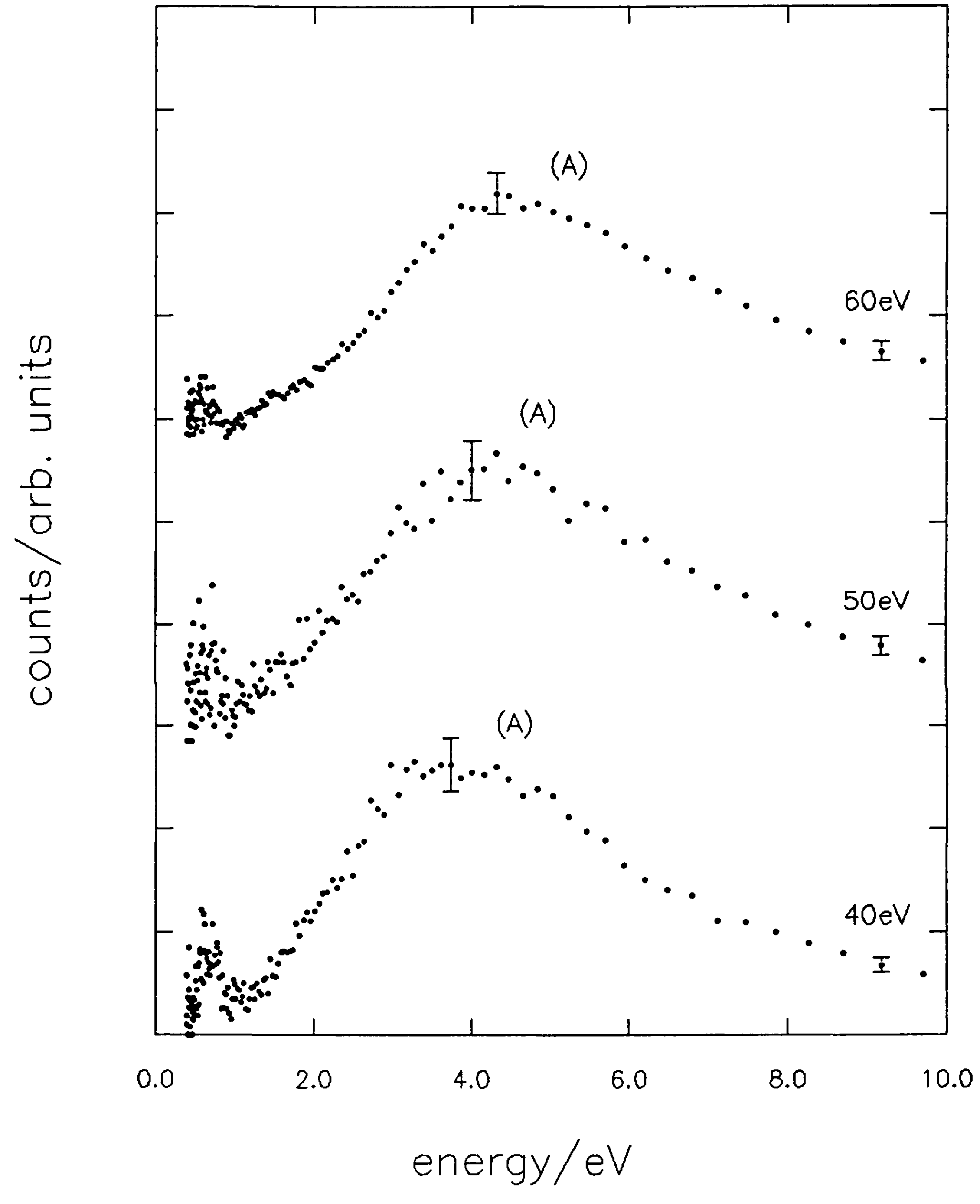

Figure 7.8 Kinetic energy distribution of the oxygen fragments produced in dissociation of carbon monoxide at incident electron energies of 40, 50 and 60eV.

The features of the kinetic energy distributions of the oxygen fragments produced in the electron impact dissociation of carbonyl sulphide, carbon dioxide and carbon monoxide are compared in table 7.4.

Table 7.4 Comparison of features in the kinetic energy distributions of the oxygen fragments produced in the dissociation of carbonyl sulphide, carbon dioxide and carbon monoxide.

Molecule	Fragment	Incident Electron Energy		
		40eV	50eV	60eV
OCS	(A)	1.25 ± 0.10	1.25 ± 0.13	1.25 ± 0.10
	(B)		1.88 ± 0.17	2.19 ± 0.20
	ratio B/A		1.50 ± 0.21	1.75 ± 0.21
CO_2	(A)	1.89 ± 0.13	2.53 ± 0.20	2.53 ± 0.10
	(B)	3.00 ± 0.26	4.03 ± 0.33	4.41 ± 0.26
	ratio B/A		1.59 ± 0.18	1.74 ± 0.12
CO	(A)	3.75 ± 0.53	4.50 ± 0.46	4.69 ± 0.40

The oxygen fragments produced in the dissociation of carbonyl sulphide, carbon dioxide and carbon monoxide are all formed with non-zero kinetic energy distributions and have higher kinetic energies than the $CO(a^3\pi)$ fragments. The oxygen fragments are therefore produced from a purely repulsive potential energy state. Partial potential energy curves could not be constructed due to the difficulties associated with triatomic molecules, nevertheless some qualitative conclusions concerning the dissociation processes may be made.

The $CO(a^3\pi)$ fragments are most likely to be produced from a bound potential energy state. Photodissociation studies (Ashfold et al 1979) suggest that the $OCS(a^1\Pi)$ state may be the molecular parent state even though its excitation is an endothermic process and the production cross section correspondingly low.

It is clear that the nature of electron impact excitation allows different dissociation channels to be followed than in photon excitation. For example electron impact allows excitation to triplet states of the carbonyl sulphide molecule. At present there is little information concerning the triplet states of the carbonyl sulphide molecule or the carbon dioxide molecule; consequently it cannot be determined whether the dissociation proceeds via the $OCS(a^1\Pi)$ state or through a triplet state of unknown nomenclature. Ab initio calculations for the potential energy curves of the lower lying states of carbonyl sulphide and carbon dioxide would be welcome, or semi-empirical calculations similar to those for nitrous oxide (Chutjian and Segal 1972, chapter six). The product molecules may also have considerable internal excitation energy, including vibrational and rotational energy, which due to the different lifetimes of each vibrational level may account for some of the differences in the kinetic energy spectra observed in this work compared with that of Allcock and McConkey.

The oxygen fragments from carbon dioxide, figure 7.6, are faster than the corresponding fragments from the dissociation of carbonyl sulphide, figure 7.4. This is expected since when a molecule dissociates the energy released is shared between the fragments in inverse proportion to their masses. The kinetic energy distributions of Allcock and McConkey (1976) and of Misakian et al (1975) for $O(^5S)$ production from carbon dioxide are shown in figure 7.9. In agreement with the present data, the kinetic energy distribution is found to have structure at higher incident electron energies. In this work, a similar trend was found for oxygen production from carbonyl sulphide, while a single peak was observed in the kinetic energy distribution for oxygen fragments from dissociation of carbon monoxide.

Carbon dioxide and carbonyl sulphide will have similar electronic excited states, the energies of the excited states of carbonyl sulphide being proportionally less than the corresponding states of carbon dioxide but not sharing the symmetry of the carbon dioxide molecule. It is not surprising, therefore, that the kinetic energy distributions for fragments from each are similar, with the thresholds for production of the fragments from carbonyl sulphide being proportionally lower than the corresponding thresholds in carbon dioxide. However, there is no feature in the kinetic energy distribution of oxygen fragments from carbonyl sulphide at an incident electron energy of 40eV which corresponds to the feature (B) in the distribution for oxygen from carbon dioxide at the same incident energy, table 7.4. It is possible that the second feature in carbon dioxide is due to a second electronic state arising from the symmetry of the molecule which is not present in carbonyl sulphide.

Referring again to table 7.4, it can be seen that in both carbon dioxide and carbonyl sulphide the peak kinetic energy of feature (A), figures 5 and 4, remains at the same energy for incident electron energies above 40eV, while feature (B) becomes steadily faster with increasing incident electron energy. However the ratio of the peak kinetic energies of features (A) and (B) are identical, within experimental error, for carbon dioxide and carbonyl sulphide at incident energies of 50eV and 60eV. This indicates that the oxygen fragments are produced from similar repulsive potential energy curves in carbon dioxide and carbonyl sulphide with the cascade contributions to each state essentially the same in both molecules. In the production of oxygen fragments from carbon monoxide a single production mechanism is suggested with increasing cascade contributions at higher incident electron energies.

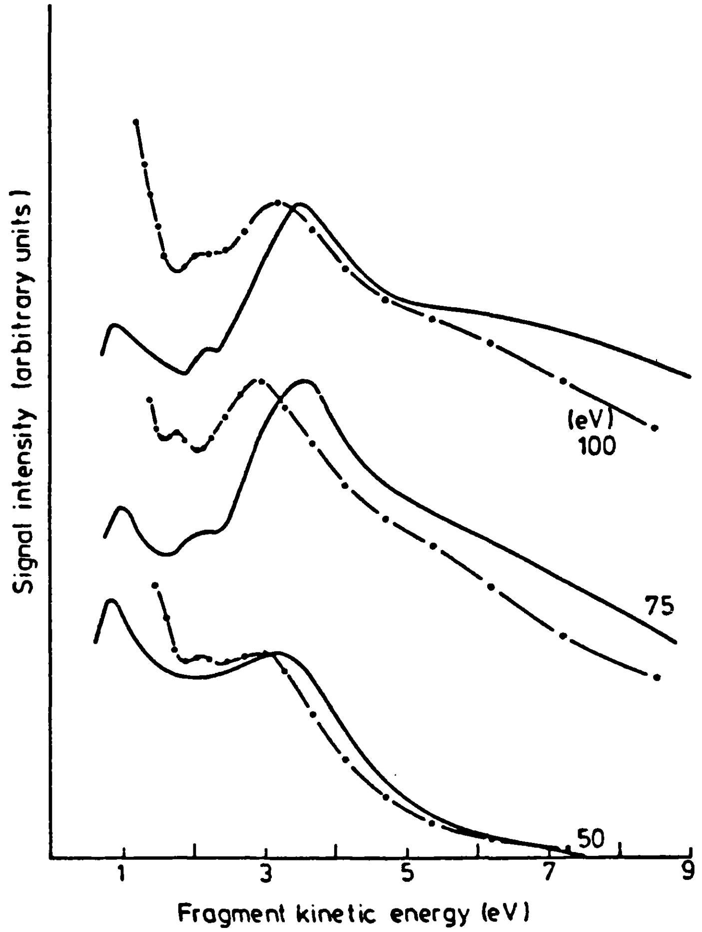

Figure 7.9 Kinetic energy distributions for O(^{5}S) fragments from carbon dioxide determined by Allcock and McConkey (1976) (dotted line) and by Misakian et al (1975) (full line) (Allcock and McConkey 1976).

7.9 Dissociative Excitation of S(^{5}S) from Carbonyl Sulphide

By analogy with the oxygen fragments, the sulphur fragments, S(^{5}S), are also expected to be produced from a purely repulsive potential energy curve. The sulphur fragments would therefore reach the detector before the slower excited carbon monoxide fragments which originate from the repulsive part of a bound potential energy curve.

A recent experiment measured the lifetime of the S(^{5}S) state to be 9.2 ± 1.0 μs (Delalic et al 1990). If this is correct, 92% of the excited sulphur fragments produced in the view cone of the detector would decay before reaching the detector, this compares with 6% of the O(^{5}S) fragments (lifetime 185μs) and <1% of the CO($a^3\pi$) fragments (lifetime ~7ms). In a time of flight spectrum corrected for in-flight decay and assuming the lifetime of S(^{5}S) to be 9.2μs, the sulphur peak would then become eight times the height of the oxygen peak. The production cross section for excited sulphur may be greater than that for oxygen, but it is unlikely to be eight times greater. Erman (1975) in reviewing the high frequency deflection technique used by Delalic et al states that such a method is only applicable for lifetimes up to 10μs. In the determination of the lifetime of the S(^{5}S) state, the experimental method is being pushed to the limit of its sensitivity and consequently the value of 9.2μs should perhaps be regarded as a lower limit. Other lifetime determinations range from 12μs to 30μs and are summarised in table 7.5.

Table 7.5 Experimental and theoretical determinations of the lifetime of the metastable S(^{5}S) state.

Lifetime /μs	Percent Decay[1]	Reference
9.2 ± 1.0	92%	Delalic et al 1990 (expt)
26; 24	12%	Aymar 1973 (expt)
12	85%	Muller 1968 (expt)
17	74%	Lawrence 1967 (calc)
<30	54%	Storey 1991 (provisional calc)

[1] calculated for the path length in this work.

Lifetimes in this range are too long to be measured accurately by optical methods and should be determined by detecting the excited atom directly using the time of flight method (chapter four). In view of the discrepancies in the lifetime determinations for S(^{5}S), both theoretical and experimental studies of electron impact dissociation of carbon disulphide (CS_2) should be undertaken. Once the lifetime of the S(^{5}S) state is measured accurately, the production cross section of this state from carbonyl sulphide may be determined.

7.10 Summary

In this work, fragments produced in the dissociation of carbonyl sulphide, carbon dioxide and carbon monoxide have been studied. In the dissociation of carbonyl sulphide, three distinct peaks appear in the time of flight spectra. It has been suggested that the fragments contributing to these peaks are O(^{5}S), S(^{5}S), CO($a^3\pi$) and high lying Rydberg states of atomic oxygen. The kinetic energy distribution of the CO($a^3\pi$) fragments deduced from the time of flight spectra reveal that these fragments are produced from the repulsive part of a bound potential energy state, possibly OCS($a^1\Pi$). The oxygen fragments produced from dissociation of carbonyl sulphide were compared with those from carbon dioxide and carbon monoxide. The kinetic energy distributions of the oxygen fragments from all these molecules indicate that the fragments are produced from a purely repulsive state. The kinetic energy distributions for the oxygen fragments from carbonyl sulphide and carbon dioxide obtained in this work show similarities and are in agreement with the kinetic energy distributions of the fragments produced from the electron impact dissociation of carbon dioxide in other studies. The kinetic energy distribution of the oxygen fragments from carbon monoxide shows no structure. From the intensity of the S(^{5}S) signal in the present work, it is suggested that the lifetime of this state is $>10\mu$s.

Chapter Eight

Conclusions and Suggestions for Future Work

> *It seems to me to be a superlative thing to know the explanation of everything, why it comes to be, why it perishes, why it is.*
>
> Socrates (Plato *Phædo*)

The dissociation of molecules by electron impact is important in a variety of complex systems and yet it remains one of the least studied inelastic collision processes. In this thesis, the technique of translational spectroscopy has been applied to the study of metastable fragments produced in electron impact dissociation of the simple polyatomic molecules nitrous oxide, carbon dioxide and carbonyl sulphide.

A commercially available channel electron multiplier is both convenient to use and efficient in detecting metastable states of excitation energy ≥8eV. Studies of metastable states with excitation energy <8eV required the development of a tantalum surface detector. Calibration of this detector by the observation of direct electron impact excitation of metastable states in carbon monoxide and molecular nitrogen showed that this detector was efficient in detecting the lower lying electronic states, $N_2(A^3\Sigma^+_u)$, excitation energy 6.17eV, and $CO(a^3\pi)$, excitation energy 6.01eV. The detection efficiency of the tantalum detector was found to be very dependent on the conditions within the vacuum chamber but improved when the tantalum surface was heated gently. These detectors were then used to study the electron impact dissociation of nitrous oxide, carbonyl sulphide, carbon dioxide and carbon monoxide.

In the dissociation of nitrous oxide, both metastable atomic oxygen and metastable molecular nitrogen fragments were observed in the time of flight spectra. The kinetic energy distribution of the molecular nitrogen fragments revealed that they were produced from the repulsive part of a bound potential energy state. Possible parent potential energy levels have been identified as $N_2O(^1\Sigma^-)$, $N_2O(^3\Sigma^+)$ or $N_2O(^3\Delta)$. The kinetic energy distributions also suggest that a substantial proportion of the $N_2(A^3\Sigma^+{}_u)$ metastable molecules are produced by cascade from higher lying states.

In the dissociation of carbonyl sulphide, three metastable species were observed in the time of flight spectra with the tantalum surface detector. The peak corresponding to the slowest fragments has been identified as being due to $CO(a^3\pi)$ metastable molecules. The kinetic energy distribution of these fragments shows that they are produced from the repulsive part of a bound potential energy curve. It is suggested that this parent potential energy state is $OCS(a^1\pi)$. There was no evidence for the production of the 10eV metastable state or Rydberg states being produced in the dissociation process.

The peak corresponding to the fastest fragments has been identified as being due to atomic oxygen fragments. This peak was observed in time of flight spectra when using both the tantalum surface detector and the channel electron multiplier. The kinetic energy distribution of the oxygen fragments produced in dissociation of carbonyl sulphide was compared with those produced in the dissociation of carbon dioxide and carbon monoxide. The kinetic energy distributions of the oxygen fragments produced from carbonyl sulphide and carbon dioxide showed many similarities. The oxygen fragments from all three parent molecules were shown to have been produced in the dissociation of a purely repulsive potential energy state.

The third time of flight peak observed in the dissociation of carbonyl sulphide is suggested to be due to $S(^5S)$ metastable atoms. If this is the case, it is proposed that the lifetime of this metastable state is longer than the current estimates of $<30\mu s$. This uncertainty can be resolved by studying the dissociation of carbon disulphide, CS_2. The only metastable state produced which could be detected on the tantalum surface would be $S(^5S)$. The lifetime of this state could then be determined by recording time of flight spectra at different distances from the interaction region. The finite lifetime of the state would result in the depletion of the long flight time part of the spectrum. If a lifetime is then assumed, the time of flight spectrum can be corrected for decay before being converted to a kinetic energy distribution. If the lifetime assumed is correct, the kinetic energy distributions derived from the time of flight spectra will be the same. Such a method is ideal for metastable states of lifetime in the range 50μs to 150μs since the lifetime effects will be easily distinguishable in the time of flight spectra.

In this thesis, the production of metastable states of excitation energy >6eV from higher lying electronic states of the parent polyatomic molecule has been studied. Most atmospheric and aeronomical processes require a careful study of the production of metastable fragments of low excitation energy. In particular, the study of the terrestrial aurora demands a study of the production mechanisms of O(^{1}S), O^{1}D) and N(^{2}P) atoms.

The detection of such species requires a detector of work function less than those of the transition metals. Several low work function detectors could be investigated. Alkali metals such as sodium and cadmium may be deposited onto a metallic substrate to provide a surface of work function <2eV. A mixture of barium, magnesium and strontium carbonates may also be painted onto a metal surface and activated by heating to produce an oxide layer of work function <3eV. However such detectors are easily poisoned and it would be difficult to maintain a clean surface of constant detection efficiency for the long time periods needed to collect a time of flight spectrum for dissociation.

Alternatively, a state selective detector may be developed. The prototype xenon detector investigated in this work can be improved by cooling the copper finger by use of a cryostat. This can then be used to provide data on the production of O(^{1}S) in the dissociation processes studied in this work. The use of organic materials in the detection of excited species should also be investigated.

Superelastic scattering processes have been reported for electron scattering from sodium and barium and are being extended to the vibrational states of simple polyatomic molecules. The production of excited fragments from the dissociation of vibrationally excited targets may be investigated by heating the gas source. Dissociation of electronically excited targets may also be studied by optical pumping of the ground state.

The results of these experiments may help in the interpretation of the large volume of airglow data accumulated in three decades of space exploration and will aid our understanding of the terrestrial ozone layer, and the evolution of planetary atmospheres.

Appendix

Publications

1. 'Production of the $N_2(A^3\Sigma^+{}_u)$ Metastable State by Electron Impact Dissociative Excitation of N_2O' S.M. Barnett, N.J. Mason and W.R. Newell 1991 Chem Phys **153** 283.

2. 'Dissociative Excitation of Metastable Fragments by Electron Impact on Carbonyl Sulphide, Carbon Dioxide and Carbon Monoxide' S.M. Barnett, N.J. Mason and W.R. Newell 1992 J Phys B **25** accepted for publication.

3. 'Electron Impact Dissociative Excitation of Selected Molecules' S.M. Barnett, N.J. Mason and W.R. Newell 1989 Sixteenth International Conference on the Physics of Electronic and Atomic Collisions, New York, abstracts p349.

4. 'Electron Impact Dissociative Excitation of Selected Aeronomical Molecules' S.M. Barnett, N.J. Mason and W.R. Newell 1989 Third European Conference on Atomic and Molecular Physics, Bordeaux, abstracts p351.

5. 'Detection of the $N_2(A^3\Sigma^+{}_u)$ Metastable State Produced by Direct and Dissociative Excitation' S.M. Barnett, N.J. Mason and W.R. Newell 1990 First National Conference on Atomic, Molecular and Optical Physics, Belfast, abstracts T16.

6. 'Production of Low Lying Metastable States by Dissociative Electron Impact Excitation' S.M. Barnett, N.J. Mason and W.R. Newell 1990 22nd Conference of the European Group for Atomic Spectroscopy, Uppsala, abstracts p63, presented orally.

7. 'Use of a Low Work Function Detector in the Study of Low Lying Metastable States Produced by Direct Electron Impact Excitation' S.M. Barnett, N.J. Mason and W.R. Newell 1990 22nd Conference of the European Group for Atomic Spectroscopy, Uppsala, abstracts p153.

8. 'Production of $O(^5S)$ from CO, CO_2 and OCS by Electron Impact Dissociative Excitation' S.M. Barnett, N.J. Mason and W.R. Newell 1991 Second National Conference on Atomic, Molecular and Optical Physics, Egham, abstracts W6.

9. 'Dissociative Excitation of $CO(a^3\pi)$ by Electron Impact on Carbonyl Sulphide' S.M. Barnett, N.J. Mason and W.R. Newell 1991 Second National Conference on Atomic, Molecular and Optical Physics, Egham, abstracts W7.

10. 'Dissociative Excitation of $CO(a^3\pi)$ by Electron Impact on Carbonyl Sulphide' S.M. Barnett, N.J. Mason and W.R. Newell 1991 23rd International Conference on Phenomena in Ionised Gases, Barga, abstracts p65.

11. 'Production of O(^{5}S) from CO, CO_2 and OCS by Electron Impact Dissociative Excitation' S.M. Barnett, N.J. Mason and W.R. Newell 1991 23rd International Conference on Phenomena in Ionised Gases, Barga, abstracts p67.

12. 'Electron Impact Excitation of Metastable States' S.M. Barnett, J.M. Furlong, N.J. Mason and W.R. Newell 1991 Seventeenth International Conference on the Physics of Electronic and Atomic Collisions, Brisbane, abstracts p265.

13. 'Atoms in Flight' S.M. Barnett and N.J. Mason 1990 Phys Educ **25** 114.

Chemical Physics 153 (1991) 283–295
North-Holland

Production of the $N_2(A\,^3\Sigma_u^+)$ metastable state by electron impact dissociative excitation of N_2O

S.M. Barnett, N.J. Mason and W.R. Newell

Department of Physics and Astronomy, University College London, Gower Street, London WC1E 6BT, UK

Received 2 May 1990; in final form 18 December 1990

Metastable fragments produced by electron impact dissociation of nitrous oxide are investigated using a low work function surface detector. The production of $N_2(A\,^3\Sigma_u^+)$ metastable molecular fragments is shown to be a dominant dissociative process. Kinetic energy spectra of the products are determined by the method of time of flight spectroscopy and used to reveal the various types of dissociative processes involved.

1. Introduction

Dissociation of molecules by electron impact is one of the least studied electron–molecule collision processes. It may be represented by the equation

$$e_E + AB \rightarrow e_{E-\delta E} + A^* + B\,,$$

in which the incident electron provides the energy δE necessary to dissociate the molecule AB and to promote the fragment A to the excited electronic state A^*. This fragment may be produced in a metastable state, which for practical purposes may be defined as an excited state with lifetime in excess of 50 μs. Since the energy of the chemical bond is released as kinetic energy of the fragments, such metastable fragments are both fast moving and long lived. Consequently such dissociation processes contribute greatly to the energy transfer processes occurring in the ionosphere, in aurorae and also in many laboratory induced plasmas.

Experimental results currently available are limited in scope and are often contradictory in their results and conclusions [1]. Particular difficulty has been found in the interpretation of the results of those experiments in which one or more of the fragments are produced in metastable states. The major problems encountered are the calibration of the detector for each metastable state, lifetime effects in time of flight spectra and the small cross sections for the processes.

There is therefore a need for reliable experimental data concerning dissociation processes. Work on the electron impact dissociative excitation of some aeronomically important species has recently been undertaken in this laboratory with the object of resolving some of these earlier discrepancies [2–4].

Theoretical studies have been confined to the dissociative excitation of H_2 into H(2s) and H(2p). Presently, theoretical electronic excitation cross sections for the simple diatomic molecules are being generated using new computational techniques such as the *R*-matrix code [6,7]. These methods are likely to be extended to describe the more complicated electron–polyatomic molecule interactions and may include dissociative excitation.

In this paper we provide new results for the electron impact dissociative excitation of N_2O obtained by time of flight spectroscopy. Nitrous oxide occurs in the upper atmosphere in significant quantities [8] and is one of the gases contributing to the greenhouse effect while also acting as a precursor in the destruction of ozone. Highly reactive excited species, N_2^* and O^*, produced by both electron- and photo-dissociation play a significant role in the processes occurring in the atmosphere. The nitrous oxide laser [9] is an important radiation source in medical applications. The presence of long lived excited species N_2^* and O^*

in the electron induced N_2O discharge must be included in theoretical models developed to describe such systems, as has been the case for the more well known CO and CO_2 lasers [10].

In nitrous oxide, several atomic or molecular metastable species may be excited, depending on the energy of the incident electron, *E*. For example:

$$
\begin{aligned}
e_E + N_2O \rightarrow\; & e_{E-\delta E_1} + N_2(A\,^3\Sigma_u^+ + O(^3P)\,,\\
& e_{E-\delta E_2} + N_2(a\,^1\pi_g) + O(^3P)\,,\\
& e_{E-\delta E_3} + N_2(X\,^1\Sigma_g^+) + O(^1D)\,,\\
& e_{E-\delta E_4} + N_2(X\,^1\Sigma_g^+) + O(^1S)\,,\\
& e_{E-\delta E_5} + N_2(X\,^1\Sigma_g^+) + O(^5S)\,.
\end{aligned}
$$

The notable feature of all these dissociative processes is that the fragments are produced with kinetic energies exceeding the thermal energy of the parent gas molecules. For example, $O(^5S)$ metastable atoms are produced with kinetic energies of 5 eV from the dissociation of N_2O [2]. In general dissociation fragments will be chemically more reactive than the corresponding metastable species which are formed by direct electron impact excitation. In this case the excited species will have kinetic energies associated with the thermal energies in the parent gas beam. Careful study of the kinetic energy spectra of the product metastable fragments produced in dissociation allows the nature of the dissociation process to be investigated and, in some cases, partial potential energy curves to be constructed for the parent molecular state.

Previous work on the dissociative excitation of N_2O has been reported by Freund and Klemperer [11], Clampitt and Newton [12], Allcock and McConkey [13] and Mason and Newell [2]. These experiments have concentrated on a determination of the kinetic energy distribution of the fragments produced but in some cases have failed to determine the precise nature of the fragments. A consequence of this failure to identify the metastable fragments is that the corrections necessary to compensate for the radiative lifetimes cannot be made [14]. If the lifetime of the observed metastable state is comparable to the flight time, the time of flight spectrum will be considerably distorted due to the in-flight decay of those metastable fragments with low kinetic energies. Since the kinetic energy distribution is deduced from the time of flight spectrum, this distortion will also be present in the kinetic energy distribution. Also, if two or more metastable states are produced at the interaction region, the apparent lifetime of the metastable beam will depend on the lifetimes of each of the constituent individual states. The lifetime of the beam as observed at the detector and recorded in the time of flight spectrum will depend not only on the ratio of the states as produced at the interaction region, i.e. the relative cross sections for the production of each state, but also on the relative detection efficiency of the detector to each state. These effects must be taken into account if the time of flight spectra are to be correctly interpreted.

In the present work we calibrated our detector by observing the production of metastable molecular states of nitrogen by direct electron impact excitation of nitrogen. Our detector is shown to detect both the $N_2(a\,^1\pi_g)$ and $N_2(A\,^3\Sigma_u^+)$ states with good efficiency. The electron impact dissociative excitation of N_2O was then studied. By observing both the $N_2(A\,^3\Sigma_u^+)$ and $N_2(a\,^1\pi_g)$ states simultaneously it was possible to determine the relative cross sections of each state in the dissociation process. The present results and those of earlier work [2,13] allow us to determine kinetic energy distributions for the production of $N_2(A\,^3\Sigma_u^+)$ and $N_2(a\,^1\pi_g)$ from N_2O and to determine the dissociative processes responsible for the production of each state.

A reanalysis of earlier experiments shows that the data of Freund and Klemperer [11] is dominated by the $N_2(A\,^3\Sigma_u^+)$ state while that of Clampitt and Newton [12] is in closest agreement with the dominant production of $N_2(a\,^1\pi_g)$. Mason and Newell [2] observed only the $N_2(a\,^1\pi_g)$ state since they used a bare channeltron, with a high work function, ~8 eV, as a detector. Allcock and McConkey [13] used a photomultiplier tube as a metastable detector placed 41 cm from the interaction region. Analysis of the kinetic energy distribution for $N_2(a\,^1\pi_g)$ [2] together with knowledge of the lifetime of the state shows that 98% of the $N_2(a\,^1\pi_g)$ state would have decayed before reaching the detector in the work of Allcock and McConkey [13]. Therefore their observed kinetic energy spectrum should be that of the $N_2(A\,^3\Sigma_u^+)$ state only. The good agreement between the results presented here and those of Allcock and McConkey support this hypothesis and provide evidence that the dissociative excitation cross section for production of $N_2(A\,^3\Sigma_u^+)$ from N_2O is greater than that for the production of $N_2(a\,^1\pi_g)$ from N_2O.

2. Apparatus

The apparatus used in the present study of the electron impact dissociative excitation of nitrous oxide is relatively simple. A schematic diagram of the apparatus is shown in fig. 1. The apparatus consists of a preselective electron gun, a hypodermic needle gas source and a surface detection system. The detection system will be described in detail.

The electron gun has been described in detail previously [15]. The central element of the einzel lens situated in the middle of the electron gun, has two functions. The first is to allow only electrons in a 0.5 eV energy range to pass through, thus producing an energy filtered electron beam, the second is to pulse the electron beam to allow time of flight spectroscopy of the collision products. This pulsed electron gun provided a time-averaged current of typically 1.5 nA at the interaction region. The molecular gas target beam is introduced into the experimental chamber by a hypodermic needle driven from a constant pressure gas source. The pressure behind the hypodermic needle was slightly above atmospheric pressure and that of the target gas beam was estimated to be 2–3×10^{-2} Torr with a background pressure in the vacuum chamber typically $<1\times10^{-7}$ Torr. The electron beam was crossed perpendicularly with this gas beam. Spectroscopic grade gas was used in all experiments.

The interaction region is defined by the overlap of the electron beam, the molecular gas beam and the field of view of the detector. A small fraction of the collision products from the interaction region are collimated by a flight tube situated between the interaction region and the detector and placed perpendicularly to the electron beam. The distance between the interaction region and detector was ~ 7 cm. The scattered electrons and product ions were prevented from

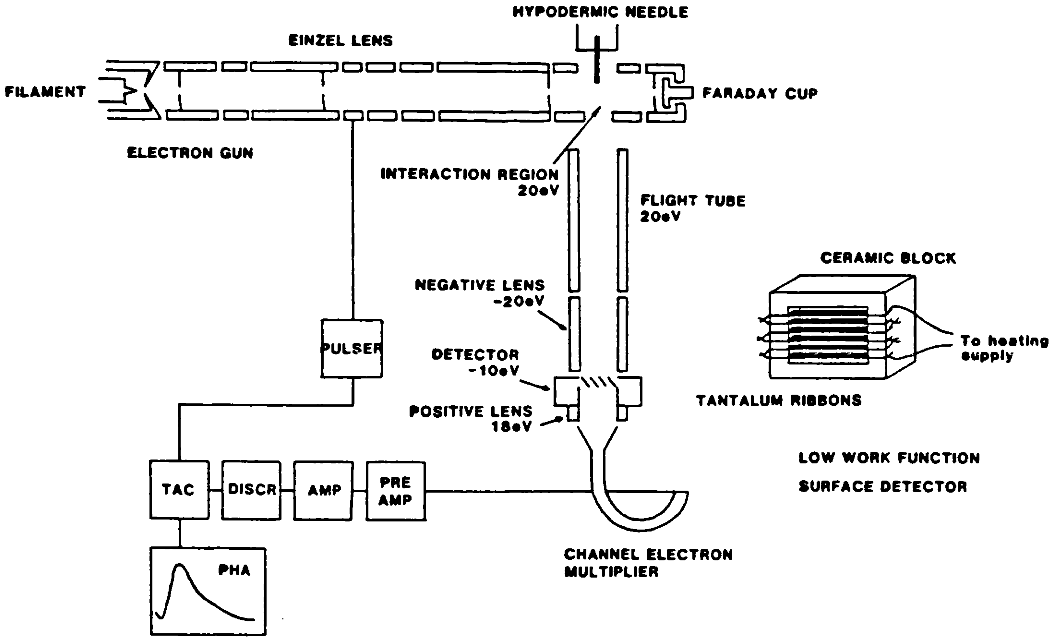

Fig. 1. Schematic diagram of the complete apparatus. Typical potentials for the detection of metastable N_2 at an incident electron energy of 20 eV are indicated. Not to scale.

reaching the surface detector by the application of electrostatic fields along the flight tube. The photons arrive at the detector almost instantaneously and can therefore be discriminated against by the timing electronics. Only the metastable fragments are registered in the detection electronics, as pulses from the channel electron multiplier. The detector itself discriminates against the ground state atoms or molecules.

The electronic pulsing of the electron beam, necessary for performing time of flight spectroscopy, is achieved by applying a square wave of 15 V amplitude and 50 ns risetime to the einzel lens. For the study of the time of flight of the dissociation fragments the pulses were typically $\leqslant 2$ µs wide and had a repetition rate of 5 kHz. This gives a duty cycle of $\leqslant 1$%. The pulse from the channel electron multiplier caused by the arrival of a metastable molecule is used as the stop pulse to a time to amplitude converter (TAC). The start pulse for the TAC is derived from the pulse applied to the electron beam to turn the beam on. A delay can be introduced between these two pulses allowing discrimination of those events arriving instantaneously. the time between these two pulses, the time of flight of the metastable fragment, is converted to a voltage by the TAC. This output is then monitored by a pulse height analyser (PHA) and the data is stored directly from the PHA onto a BBC model B and subsequently transfered to a mainframe computer system for data analysis. All the pulse counting electronics and the PHA were commercially available EG&G Ortec units.

The principle used in detection is that metastable atomic and molecular species impinging upon a metal surface will cause secondary electron ejection. These secondary electrons can then be focused by electrostatic fields into a Mullard type B419L channel electron multiplier for further amplification and pulse counting.

This ability of metastable atoms to cause secondary ejection was first noticed by Webb [16] and Oliphant [17], with later studies of the phenomenon, and how it depended on the condition of the metal surface, being carried out by Sonkin [18], MacLennan [19] and Varney [20]. Stebbings [21] determined the secondary emission coefficient for $He(2\,^3S)$ metastable atoms incident upon a gold surface to be 0.29 ± 0.03. This work was extended by Dunning et al. [22] who used a range of metal surfaces to detect metastable states of the noble gases. They confirmed Sonkin's observations that the detection efficiency increases with contamination of the surface, and in some cases measured the emission coefficient to be > 1. To explain this they proposed a mechanism in which the impurities adsorbed onto the metal surface undergo Penning ionisation by the incoming metastable atoms. The mechanism of secondary ejection is not yet well understood, but while it is not necessary to make absolute measurements, this method of metastable detection is useful and has been widely adopted [23,24]. The arrangement used in the present work is based on that of Zubek and King [25] and is shown schematically in fig. 1.

The detecting surface itself consists of ribbons of tantalum. Tantalum was used since it has a low work function, ~4 eV, and has been shown to be effective in the detection of the 6 eV $N_2(A\,^3\Sigma_u^+)$ metastable state [26]. The ribbons have dimensions $3 \times 15 \times 0.01$ mm and six are arranged at 45° to the flight path, effectively providing a continuous surface of 8×15 mm to the incoming metastable species. The secondary electrons ejected from the metal surface are focused by the negative and the positive electrostatic lenses into the channel electron multiplier.

Many workers have tried to quantify the effects of impurities adsorbed onto the surface of a metal and the treatments necessary to clean the surface [18,22]. However, an extensive survey of the literature has lead the authors to the conclusion that although an atomically clean surface is the only truly reproducible surface, it will not necessarily be the most efficient surface for the detection of the metastable species being studied. Therefore certain concessions must be made. It will not, for example, be possible to make absolute measurements, since the number of electrons ejected per incident metastable atom or molecule depends on the adhesion coefficient of the metastable species, the temperature and the purity of the surface and the background residual gas pressure. In our studies of direct excitation of nitrogen and the dissociative excitation of nitrous oxide it was found that the metastable products were most efficiently detected while the tantalum surface was being heated at a temperature well below that at which thermionic emission occurs from the surface. If the surface was not heated at all, the efficiency steadily dropped, presumably as the surface adsorbed nitrogen. oxygen and nitrous oxide.

However it was also found that heating to temperatures just below that at which thermionic emission occurs leads to a drop in detection efficiency, perhaps because the impurities were evaporated from the surface [22]. The surface was allowed to reach a steady state while being bombarded by gas molecules and metastable species. It was necessary periodically to stop the gas beam and heat the surface to a temperature close to that at which thermionic emission occurs to remove any excess surface coating that had developed during long data collection periods.

For the purpose of this work it was necessary to develop a detector with a work function sufficiently low to detect $N_2(A\,^3\Sigma_u^+)$ at 6.17 eV but also to detect $N_2(a\,^1\pi_g)$ and $N_2(E\,^3\Sigma_g^+)$ at 8.55 and 12.2 eV respectively. A state selective detector as described by Kume et al. [27] would not have allowed us to study the complete dissociation process. To ensure that the detector was capable of detecting both $N_2(A\,^3\Sigma_u^+)$ and $N_2(a\,^1\pi_g)$ states, direct electron impact excitation of N_2 to these states was observed. Details of this are given in section 3.

It was also necessary to ensure that the relative detection efficiency of each state remained constant over the data collection period. This period could span several days. Consequently the spectra were recorded every few hours and each spectrum could be superimposed onto previous spectra. Examination of such plots shows that there is no observable change in the detection efficiencies. This is best illustrated in the 40 eV electron impact dissociation spectrum of N_2O, shown in fig. 2. It can be seen that there was no measurable change in the relative heights of the nitrogen, N_2^*, and oxygen, O^*, peaks. Any change in the relative detection efficiency of the surface to the $N_2(A\,^3\Sigma_u^+)$ and $N_2(a\,^1\pi_g)$ states would have resulted in a change in the height of the metastable nitrogen peak relative to the oxygen peak. Therefore the relative detection efficiency of the metal surface to each metastable species must have remained constant. The overall count rate monitored, however, did fluctuate during data collection periods.

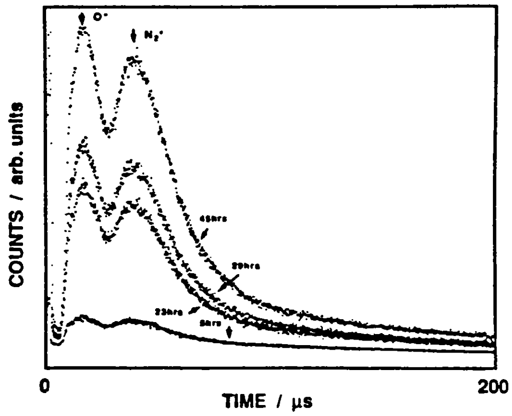

Fig. 2. Time of flight spectra for the dissociative excitation of N_2O at an incident electron energy of 40 eV. These spectra were recorded after 5, 23, 29 and 45 hours and show the constant relative detection efficiency of the tantalum surface to the species N_2^* and O^*.

3. Direct excitation of N_2

The detector was calibrated by observing the direct excitation of N_2 to $N_2(A\,^3\Sigma_u^+)$, $N_2(a\,^1\pi_g)$ and $N_2(E\,^3\Sigma_g^+)$ over a range of incident electron energies from threshold to 21 eV.

The molecules in the parent gas beam have thermal velocities described by a modification of the Maxwellian distribution. It is assumed that the molecules in the metastable beam have the same velocity distribution as the molecules in the parent gas beam and can also be described by such a distribution [28]. The modified Maxwellian distribution may be written:

$$P(t) = \frac{C}{t^g} \exp\left(\frac{-mL^2}{2kTt^2}\right) \exp\left(\frac{-t}{\tau}\right), \tag{1}$$

where C is a normalising constant, t is time taken by a molecule of velocity v to reach the detector, m is the mass of the metastable molecule, L is the path length between the interaction region and the detector, T is the temperature of the gas, k is Boltzmann's constant, τ is the lifetime of the metastable state and g is a real number such that $4 < g < 5$.

The modification of the Maxwellian distribution is obtained by including a variable parameter g which is simply dependent on the dynamics of the gas beam. A perfectly diffuse gas beam would be a good approximation to the pure Maxwellian distribution and in this case g would have a value of 4. However as the degree of collimation increases the value of g rises to around 5 [11].

An accurate determination of the path length, L, between the interaction region and the detector was made by recording a time of flight spectrum of the excitation of the $(3p^5 4s)^3P_{0,2}$ states of argon. the lifetime of these states has been reported as 3 s or longer [29,30] hence the lifetime term $\exp(-t/\tau)\approx 1$ in eq. (1). The value of g for argon in the apparatus is unknown, however by using a direct measurement of the path length, 0.07 m, the experimental data was compared to eq. (1) and a first approximation of g obtained as 4.5. This was then used to obtain a new value of the pathlength. A refined value for L was found by an iterative procedure to be 0.071 ± 0.002 m.

It was assumed that the parent gas beam did not cool significantly on admittance to the chamber and therefore the temperature of the metastable beam was assumed to be 293 K.

In the present work the appropriate value of g associated with the nitrogen beam was determined by comparing the N_2 metastable time of flight spectrum produced at an incident electron energy of 8.5 eV with eq. (1). At this incident energy, only the $N_2(A\,^3\Sigma_u^+)$ metastable state which has a threshold of 6.17 eV will be present. The higher metastable states, $N_2(a\,^1\pi_g)$ and $N_2(E\,^3\Sigma_u^+)$, have thresholds of 8.55 eV and 12.2 eV, respectively and so will not be populated. The lifetime of the $N_2(A\,^3\Sigma_u^+)$ metastable state has been reported as 1.4 s [31]. This value of the lifetime and the path length and temperature determined above were used to obtain a value of g of 4.94.

This value of g was then used to fit the other direct electron impact excitation spectra to determine the apparent lifetime of the metastable beam at each excitation energy. A typical time of flight spectrum for direct excitation of N_2 is shown in fig. 3, together with the theoretical curve from which the lifetime was estimated.

The lifetime derived from the time of flight spectrum depends on (1) the proportion of each metastable state present in the beam, (2) the lifetimes of these metastable states and (3) the relative detection efficiency of the metal surface to each state. Consequently when several metastable species are present, the lifetime term of eq. (1) can be replaced by

$$K_T \exp(-t/\tau) = \sum_i K_i \exp(-t/\tau_i)\,, \qquad (2)$$

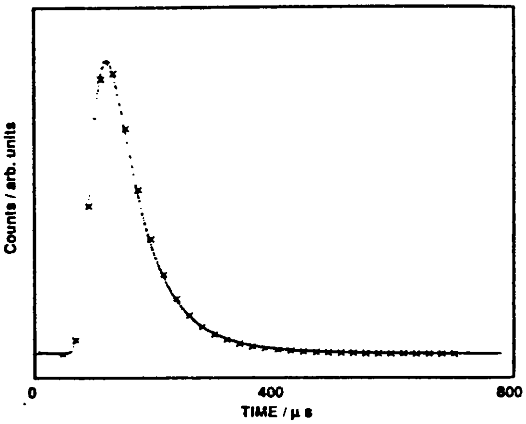

Fig. 3. A time of flight spectrum for direct excitation of N_2 at an incident electron energy of 21 eV. The calculated curve (×) reveals an apparent lifetime for the metastable beam of 288 µs.

where τ is the apparent lifetime of the metastable beam, τ_i are the lifetimes of each metastable state in the beam and the K_i are parameters depending on the detection efficiency and excitation cross section of each metastable state in the beam, K_T is a parameter depending on the total excitation cross section and the detection efficiency of the surface to each metastable state. Considering the production of the metastable states of nitrogen, eq. (2) becomes:

$$K_T \exp(-t/\tau) = K_A \exp(-t/\tau_A) + K_a \exp(-t/\tau_a) + K_E \exp(-t/\tau_E)\,. \qquad (3)$$

Alternatively, if σ_A, σ_a and σ_E are the cross sections for the production of the $N_2(A\,^3\Sigma_u^+)$, $N_2(a\,^1\pi_g)$ and $N_2(E\,^3\Sigma_g^+)$ states with lifetimes τ_A, τ_a and τ_E respectively, this may be written assuming 100% detection efficiency of each state as

$$\sigma_T \exp(-t/\tau) = \sigma_A \exp(-t/\tau_a) + \sigma_a \exp(-t/\tau_a) + \sigma_E \exp(-t/\tau_E)\,, \qquad (4)$$

where σ_T is the total excitation cross section.

For each of the incident electron energies used the apparent lifetime of the metastable beam was determined, as shown in table 1.

Total excitation cross sections for the $N_2(A\,^3\Sigma_u^+)$, $N_2(a\,^1\pi_g)$ and $N_2(E\,^3\Sigma_u^+)$ states have been found experimentally by Borst [32]. Borst et al. [33] and by

Table 1

Incident electron energy (eV)	Apparent lifetime of beam
8.5	1.4 s
10	1 ms
12	175 μs
13	376 μs
15	456 μs
17	479 μs
21	288 μs

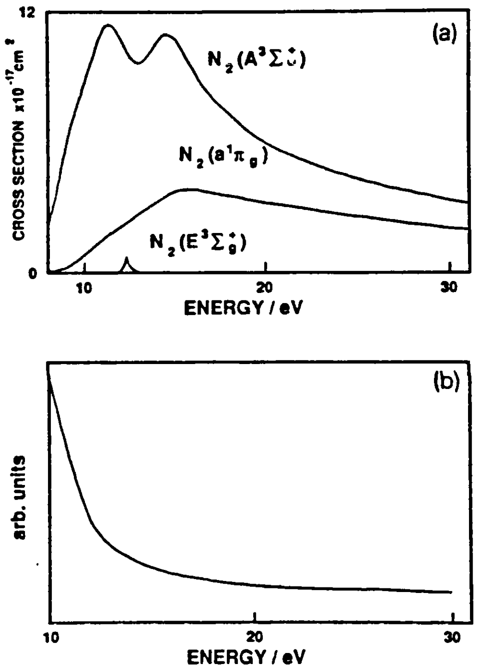

Fig. 4. (a) Direct excitation cross sections for the metastable states $N_2(A\,^3\Sigma_u^+)$, $N_2(a\,^1\pi_g)$ and $N_2(E\,^3\Sigma_g^+)$ of nitrogen as determined by Borst [32]. (b) The ratio of the cross sections σ_A/σ_a.

Cartwright et al. [34]. The cross sections of the $N_2(A\,^3\Sigma_u^+)$ and $N_2(a\,^1\pi_g)$ states, shown in fig. 4a, were constructed from the tables given by Borst [32]. The cross section of the $N_2(E\,^3\Sigma_g^+)$ state is taken from Borst et al. [33].

The ratio of the cross sections of the $N_2(A\,^3\Sigma_u^+)$ and $N_2(a\,^1\pi_g)$ states obtained from this data is shown in fig. 4b. The apparent lifetimes determined for each incident electron energy in the present work can be qualitatively explained using the cross sections in fig. 4. At incident electron energies below 8.55 eV only the $N_2(A\,^3\Sigma_u^+)$ metastable state will be present, and the apparent lifetime of the metastable beam will be the same as the lifetime of the $N_2(A\,^3\Sigma_u^+)$ state, 1.4 s. As the incident electron energy passes through the threshold for $N_2(a\,^1\pi_g)$ production, 8.55 eV, the apparent lifetime of the metastable beam is reduced since the lifetime of the $N_2(a\,^1\pi_g)$ state is 115 ± 10 μs [35]. The cross section of the $N_2(a\,^1\pi_g)$ state rises very slowly close to its threshold and this is reflected in the gradual reduction of the apparent lifetime of the metastable beam. At incident electron energies greater than ~ 16 eV the ratio of the $N_2(A\,^3\Sigma_u^+)$ state to the $N_2(a\,^1\pi_g)$ state in the beam decreases slowly and steadily and so the apparent lifetime of the beam is expected also to decrease slowly. It should be remembered that the values of K_T and K_i in eq. (2) depend not only on the cross sections for the production of each state but also on the detection efficiency of the metal surface to each state. The ratio of the $N_2(A\,^3\Sigma_u^+)$ and $N_2(a\,^1\pi_g)$ states as observed at the tantalum detector will therefore be different to the ratios as measured by Borst. However, the apparent lifetimes measured in this study follow the trends that would be expected from the cross sections of Borst. The deviation at 12 eV can be explained by the production of $N_2(E\,^3\Sigma_u^+)$. This metastable state has a sharp cross section centered at 12.2 eV, fig. 4a, and a lifetime of 190 ± 30 μs [36]. The presence of this third state in the metastable beam will further reduce the apparent lifetime.

The $N_2(a\,^1\pi_g)$ state is not populated by cascade from higher lying states to any significant degree; the direct excitation cross section has therefore been reliably determined and agreed upon by several workers [32,35]. Using the published excitation cross section of Mason and Newell [35] and the function σ_T determined in the present work, the shape of the cross section for the excitation of the $N_2(A\,^3\Sigma_u^+)$ state was deduced. It was found that the cross section for the production of the $N_2(A\,^3\Sigma_u^+)$ state thus determined followed the same shape as that observed by Borst, but that is was smaller in magnitude relative to the $N_2(a\,^1\pi_g)$ state. This suggests that our tantalum surface detects the $N_2(a\,^1\pi_g)$ state more efficiently than the $N_2(A\,^3\Sigma_u^+)$ state.

This study of direct electron impact excitation of N_2 demonstrates that the tantalum detector, although being more sensitive to the $N_2(a\,^1\pi_g)$ state, could detect efficiently both the $N_2(A\,^3\Sigma_u^+)$ and $N_2(a\,^1\pi_g)$ states. Consequently it was possible to use this detection system to study production of both of these states of N_2 by dissociative excitation of N_2O.

4. Dissociation of N_2O

The time of flight spectra for the dissociative excitation of N_2O are shown in fig. 5. The kinetic energy of the fragments can be deduced from the time of flight spectra. The energy of the metastable molecule arriving at the detector at time t is given by:

$$\epsilon = \tfrac{1}{2}m(L/t)^2\,,$$

where L is the path length between the interaction region and the detector, and m is the mass of the metastable molecule.

If $T(t)$ is the number of counts in each time channel of width $\mathrm{d}t$ in the time of flight spectrum and $D(\epsilon)$ is the number of counts in each energy channel of width $\mathrm{d}\epsilon$ in the kinetic energy spectrum these are related by

$$\int D(\epsilon)\,\mathrm{d}\epsilon = \int T(t)\,\mathrm{d}t\,,$$

therefore

$$D(\epsilon) \propto t^3\,T(t)\,. \qquad (5)$$

Long data collection periods, typically 50 hours, gave good statistics in the peaks, but because of the t^3 dependence, small statistical fluctuations at long flight times give rise to large variations in the low kinetic energy part of the energy distribution. A constant background was deduced from the long flight time part of the time of flight spectrum where no metastable molecules reach the detector. To reduce the error due to the statistical fluctuations in the tail of the metastable peak, the constant background was subtracted from the data and a smooth curve fitted to the tail before the time data was converted to kinetic energy data. This fitting process resulted in an uncertainty in the position of the kinetic energy peak of typically 9%. Point to point conversion of the time of flight data to a kinetic energy spectrum was performed for the region of the spectrum in which the nitrogen peak dominated over the oxygen peak.

The determination of the kinetic energy distribution for the oxygen peak gave results in agreement with those of Mason and Newell [2]. The kinetic energy distributions obtained for the nitrogen peak are shown in fig. 6. The energy at which each curve peaks and the half height energy are given in table 2.

It can be seen from the kinetic energy spectra in fig. 6 that as the incident electron energy increases the nitrogen kinetic energy spectrum shifts to higher energy and increases in width. The increase of the peak kinetic energy in the first five eV above threshold occurs as the Franck–Condon overlap region is exceeded. The broadening at higher energies is due to an increased number of dissociation processes contributing to the metastable nitrogen peak by cascade from higher lying excited states.

In fig. 7a we reproduce the 12 eV and 75 eV spectra of Allcock and McConkey, and in fig. 7b the 13 eV and 60 eV spectra from the present work. The two sets of data correspond very closely. The present 60 eV kinetic energy spectrum peaks at 0.292 eV whereas the 75 eV spectrum of Allcock and McConkey peaks at 0.27 eV but is not as broad. Such a difference could be due to the presence of the $N_2(a\,^1\pi_g)$ state in the present work but which was absent in the work of Allcock and McConkey. The 12 eV and 13 eV spectra are, however, in excellent agreement.

Fig. 7d shows the kinetic energy spectra for an incident electron energy of 20 eV from the present work compared to that of Mason and Newell, reproduced in fig. 7c. These spectra peak at 0.162 ± 0.016 eV and 0.125 ± 0.009 eV respectively. The difference is due to the different processes being observed. Mason and Newell [35] selectively detected only the $N_2(a\,^1\pi_g)$ metastable state while we detected a mixture of both the $N_2(A\,^3\Sigma_u^+)$ and the $N_2(a\,^1\pi_g)$ states. Since our results agree more closely with those of Allcock and McConkey [13] than those of Mason and Newell [35] it is reasonable to conclude that we are detecting mainly the $N_2(A\,^3\Sigma_u^+)$ fragments. In the present study of direct electron impact excitation of molecular nitrogen, it was demonstrated that the tantalum

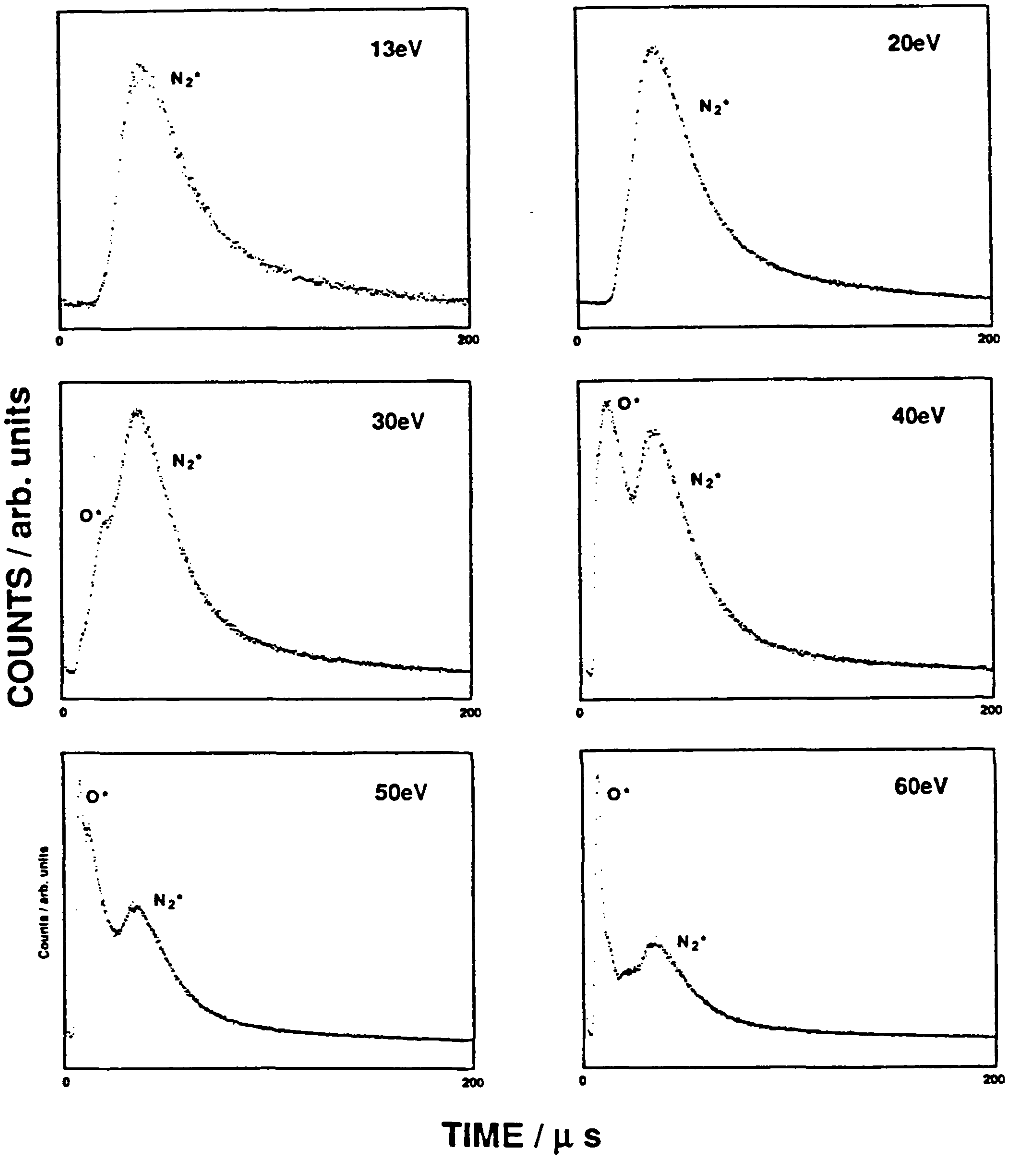

Fig. 5. Time of flight spectra for the dissociative excitation of N_2O.

surface detector is preferentially sensitive to the $N_2(a\ ^1\pi_g)$ metastable state. Therefore the dominance of the $N_2(A\ ^3\Sigma_u^+)$ metastable state in the time of flight spectra in the present work indicates that the dissociative excitation cross section for $N_2(A\ ^3\Sigma_u^+)$ (is substantially greater than that for $N_2(a\ ^1\pi_g)$ production.

The kinetic energy spectra of the product metastable fragments produced in dissociative excitation allow the nature of the dissociation process to be in-

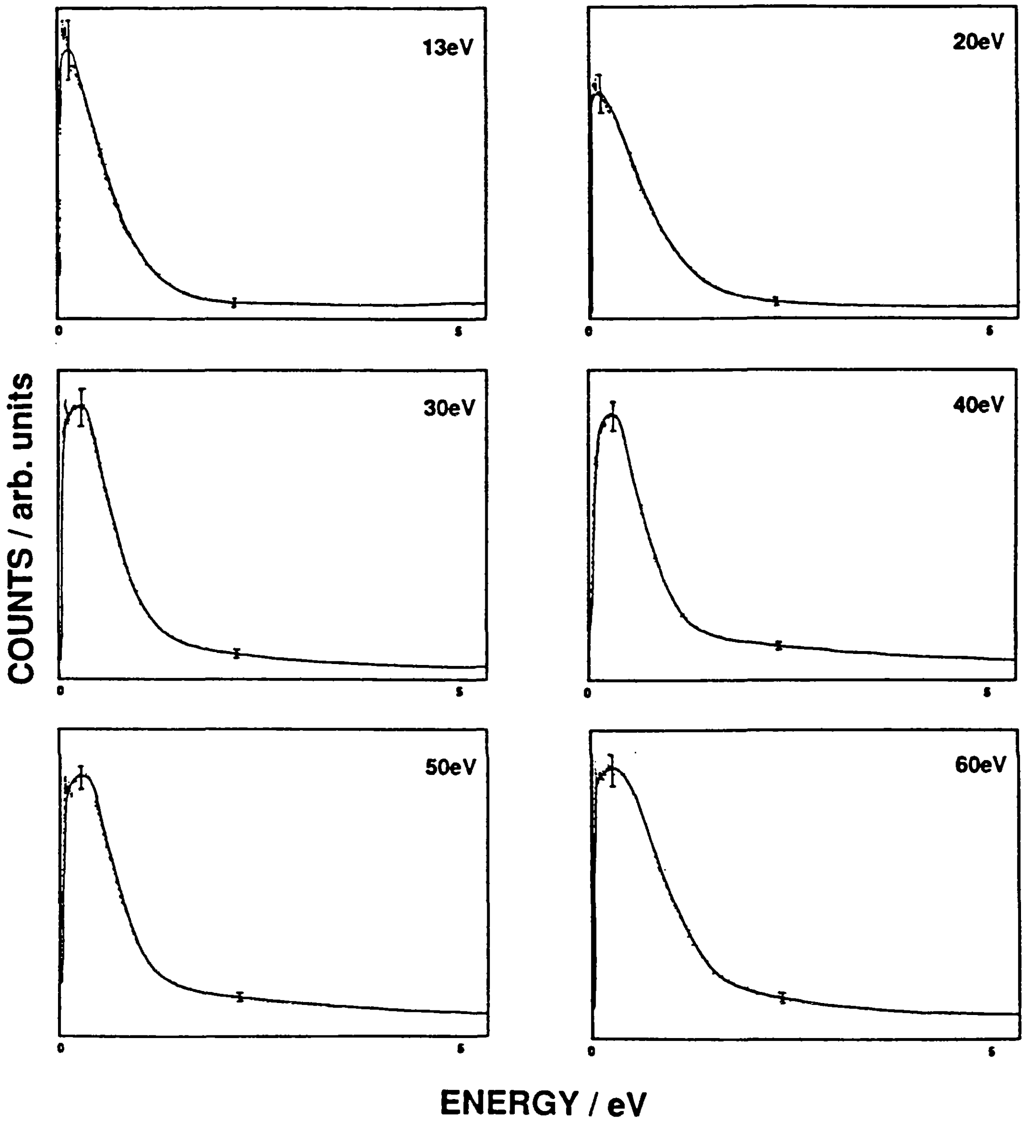

Fig. 6. Kinetic energy distributions for the nitrogen metastable peak deduced from the time of flight spectra shown in fig. 5.

vestigated. Fragments with finite minimum kinetic energy, fig. 8a, are produced from a purely repulsive potential energy curve. The production of some of the fragments with near zero kinetic energies indicates dissociation from the repulsive part of a bound molecular potential energy curve, fig. 8b. The kinetic energy spectra in fig. 6 show evidence of near zero energy fragments, revealing that the metastable nitrogen fragments formed in dissociative excitation of nitrous oxide are produced from a bound potential energy curve or curves.

The steady broadening of the kinetic energy distri-

Table 2

Incident electron energy (eV)	Peak intensity (eV) ±0.016	Half height energy (eV) ±0.016
13	0.130	0.649
15	0.146	0.698
20	0.162	0.682
25	0.195	0.746
30	0.244	0.731
40	0.292	0.779
50	0.292	0.747
60	0.292	1.039

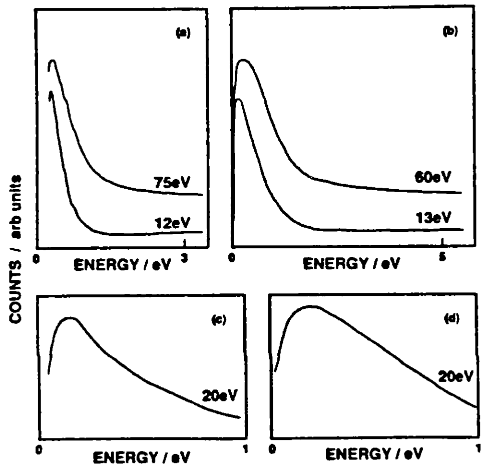

Fig. 7. Comparison of the kinetic energy spectra obtained in the present work with previous experiments: (a) the kinetic energy distributions of Allcock and McConkey [13] at incident energies of 12 eV and 75 eV and (b) those at 13 eV and 60 eV from the present work; (c) kinetic energy spectra for incident electron energy 20 eV from Mason and Newell [15] and (d) from this work.

bution between threshold and 60 eV indicates a cascade contribution to the observed metastable molecular nitrogen flux. It has previously been confirmed that cascade contributions to the $N_2(a\,^1\pi_g)$ state are small [2,35]. Therefore in this case the broadening must be due to cascade to the $N_2(A\,^3\Sigma_u^+)$ state. Excitation of the $N_2(A\,^3\Sigma_u^+)$ state by electron impact upon molecular nitrogen revealed substantial cascade from both the $N_2(B\,^2\pi_g)$ and $N_2(C\,^3\pi_u)$ states.

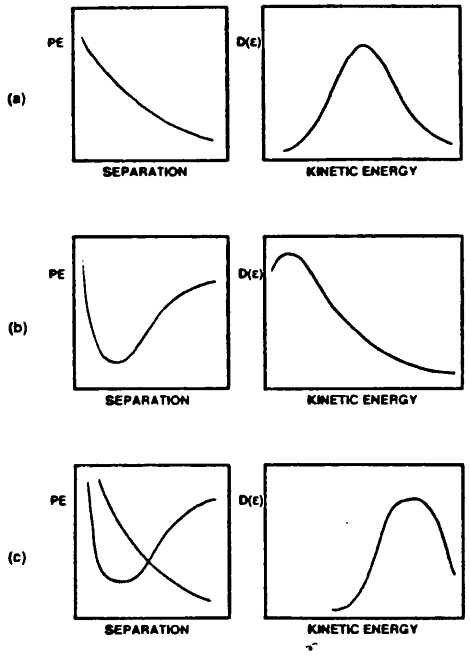

Fig. 8. The relationship between the parent molecular potential energy curve and the kinetic energy distributions of the product fragments is illustrated. Distributions are shown for dissociation from (a) a purely repulsive potential energy curve, (b) the repulsive part of a bound potential energy curve, (c) perturbation of a bound state by crossing of a repulsive state as in predissociation.

It is therefore necessary to consider the following processes in dissociative excitation:

$$e^- + N_2O \rightarrow N_2(A\,^3\Sigma_u^+) + O(^3P)$$

$$\rightarrow N_2(B\,^3\pi_g) + O(^3P) \rightarrow N_2(A\,^3\Sigma_u^+) + O(^3P)$$

$$\rightarrow N_2(C\,^3\pi_u) + O(^3P) \rightarrow N_2(A\,^3\Sigma_u^+) + O(^3P)\,.$$

Such two step processes are not unusual in dissociative excitation as recent studies of dissociative excitation in molecular oxygen have revealed [3].

Partial potential energy curves for the repulsive part of the bound state cannot be constructed from the kinetic energy spectra determined in the present work because of this significant cascade contribution. Such partial potential energy curves have been deduced for fragments from diatomic molecules such as O_2 [37,38] in which the potential of the ground state is well established. However, to apply the same technique to a triatomic molecule requires knowledge of a ground state potential surface and extension of two dimensional arguments to a three dimensional problem. However, earlier calculations of the energies and potential surfaces of the lowest excited electronic states of nitrous oxide may be reconsidered in the light of the present results.

Semi-empirical calculations for potential energy curves of the lower lying states of nitrous oxide are reproduced in fig. 9 [39]. A Σ^- state, threshold 4 eV, is predicted to be responsible for the production of $N_2(A\,^3\Sigma_u^+)$ and $O(^3P)$ fragments at a dissociative excitation energy of 7.89 eV, while a $^3\Delta$ or $^3\Sigma^+$ state is responsible for production of $N_2(B\,^3\pi_g)$ and $O(^3P)$ fragments. In fig. 9 both these states are bound, in agreement with the present results. A third production channel from the $N_2O(2\,^1\pi)$ repulsive state must therefore have a low excitation cross section, at least at incident electron energies less than 20 eV. There is the possibility of purely repulsive states overlapping both the $^1\Sigma^-$ and $^3\Delta$ or $^3\Sigma^+$ states and allowing predissociation. The kinetic energy distributions of fragments produced by predissociation would have a shape such as that shown in fig. 8c. The kinetic energy distributions obtained in the present work do not have these characteristics. No calculations of the electronic state of N_2O yielding $N_2(C\,^3\pi_u)$ and $O(^3P)$ fragments are available.

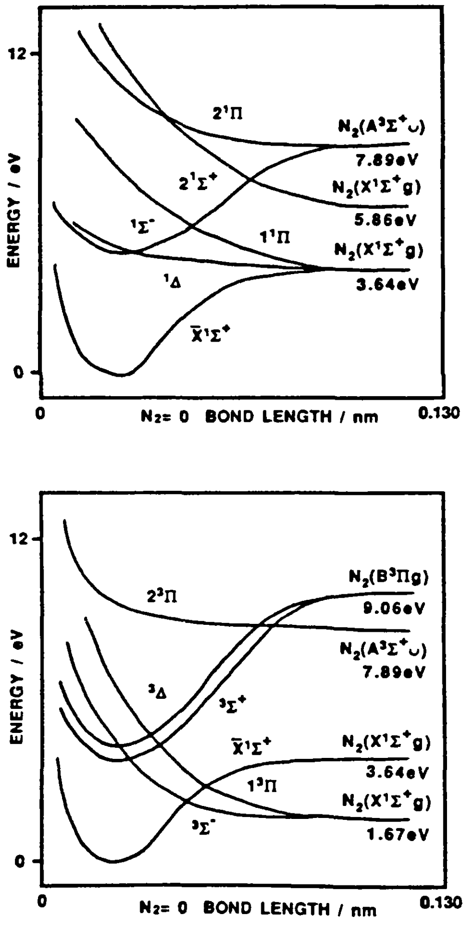

Fig. 9. Potential energy curves for low lying states of nitrous oxide calculated using a semi-empirical technique [39].

5. Conclusions

In this paper we have discussed some of the considerations required for a detailed and accurate analysis of metastable time of flight spectroscopy. By the careful analysis of our time of flight spectra for the direct excitation of the metastable states of N_2, we found the apparent lifetime of the metastable beam over an incident energy range of 8.5–21 eV. From this, we further deduced that the tantalum surface detected the $N_2(A\,^3\Sigma_u^+)$ state less efficiently than the $N_2(a\,^1\pi_g)$ state. It was also observed that the relative detection efficiency of each state remained constant.

Knowledge of the properties of the detector allowed a new investigation of the electron impact dissociation of N_2O to be performed in which both the $N_2(A\,^3\Sigma_u^+)$ and $N_2(a\,^1\pi_g)$ states were observed simultaneously. Comparison of the results obtained in the present work with previous experiments leads us to conclude that the production of the $N_2(A\,^3\Sigma_u^+)$ state dominates in the dissociation process. This conclusion is further endorsed by the knowledge that our detector was preferentially sensitive to the $N_2(a\,^1\pi_g)$ state.

The metastable fragments appear to be produced from the repulsive part of a bound molecular potential energy curve. There is also evidence that several competing dissociative channels populate the $N_2(A\,^3\Sigma_u^+)$ state by cascade at the higher energies.

In view of the many applications we hope to extend our studies of dissociative excitation to other di- and polyatomic molecules which are important in gaseous discharges and aeronomical phenomena.

Acknowledgments

We are indebted to Messrs E.J.C. Oldfield and I. Rangué for their skilled technical assistance. SMB acknowledges receipt of a SERC studentship. NJM acknowledges the award of a Royal Society Fellowship.

References

[1] E.C. Zipf, Dissociation of Molecules by Electron Impact Electron–Molecule Interactions and Their Applications. Vol. 1, Ch. 4 (Academic Press, New York, 1982).
[2] N.J. Mason and W.R. Newell, J. Phys. B 22 (1989) 2297.
[3] N.J. Mason and W.R. Newell, J. Phys. B 23 (1990) 464.
[4] S.M. Barnett, N.J. Mason and W.R. Newell, XVI ICPEAC, New York, Abstracts (1989) p. 349.
[5] S. Chung and C.D. Lin, Phys. Rev. A 17 (1978) 1874.
[6] S.E. Branchett and J. Tennyson, Phys. Rev. Letters 64 (1990).
[7] P.G. Burke, C.J. Noble and P. Scott, Proc. Roy. Soc. A 410 (1987) 289.
[8] R.G. Prinn, P.G. Simmonds, R.A. Rasmussen, R.D. Rosen, F.H. Alyea, A.J. Cardelino, A.J. Crawford, D.M. Cunnold, P.J. Fraser and J.E. Lovelock, J. Geophys. Res. 88 (1983) 8353.
[9] K.E. Fox and J. Reid, J. Opt. Soc. Am. B 2 (1985) 807.
[10] C.E. Little and P.G. Browne, J. Phys. B 21 (1988) 2675; ibid., J. Phys. B 22 (1989) 1269.
[11] R.S. Freund and W. Klemperer, J.Chem. Phys. 47 (1967) 2897.
[12] R. Clampitt and A.S. Newton, J. Chem. Phys. 50 (1969) 1997.
[13] G. Allcock and J.W. McConkey, chem. Phys. 34 (1978) 169.
[14] N.J. Mason, Meas. Sci. Technol. 1 (1990) 396.
[15] N.J. Mason and W.R. Newell, J. Phys. E 19 (1986) 722.
[16] H.W. Webb, Phys. Rev. 24 (1924) 113.
[17] M.L.E. Oliphant, Proc. Roy. Soc. A 124 (1929) 228.
[18] S. Sonkin, Phys. Rev. 43 (1933) 788.
[19] D.A. MacLennan, Phys. Rev. 148 (1966) 218.
[20] R.N. Varney, Phys. Rev. 175 (1968) 98.
[21] R.F. Stebbings, Proc. Roy. Soc. A 241 (1957) 270.
[22] F.B. Dunning, A.C.H. Smith and R.F. Stebbings, J. Phys. B 4 (1971) 1683.
[23] W. Lichten, J. Chem. Phys. 26 (1957) 306.
[24] J.C. Hemminger, B.G. Wicke and W. Klemperer, J. Chem. Phys. 65 (1976) 2798.
[25] M.Zubek and G.C. King, J. Phys. E 15 (1982) 511.
[26] D.S. Newman, M. Zubek and G.C. King, J. Phys. B 16 (1983) 2247.
[27] H. Kume, T. Kondow and K. Kuchitsu, J. Phys. Chem. 90 (1986) 5146; ibid., J. Chem. Phys. 84 (1986) 4031.
[28] S.M. Barnett and N.J. Mason, Phys. Educ. 25 (1990) 114.
[29] N.E. Small-Warren and L.Y.C. Chui, Phys. Rev. A 11 (1975) 1777.
[30] R.S. van Dyck Jr., C.E. Johnson and H.A. Shugart, Phys. Rev. A 5 (1972) 991.
[31] D.E. Shemansky and N.P.Carleton, J. chem. Phys. 51 (1969) 682.
[32] W.L. Borst, Phys. Rev. A 5 (1972) 648.
[33] W.L. Borst, W.C. Wells and E.C. Zipf, Phys. Rev. A 5 (1972) 1744.
[34] D.C. Cartwright, S. Trajmar, A. Chutjian and W. Williams, Phys. Rev. A 16 (1977) 1041.
[35] N.J. Mason and W.R. Newell, J. Phys. B 20 (1987) 3913.
[36] W.L. Borst and E.C. Zipf, Phys. Rev. A 3 (1971) 979.
[37] W.L. Borst and E.C. Zipf, Phys. Rev. A 4 (1971) 153.
[38] R.S. Freund, J. Chem. Phys. 54 (1971) 3125.
[39] A. Chutjian and G.A. Segal, J. Chem. Phys. 57 (1972) 3069.

IOP J Phys B Batch 228 Galley 1 K31
J. Phys. B: At. Mol. Opt. Phys. 25 (1992) 1307-20 Printed in the UK

Dissociative excitation of metastable fragments by electron impact on carbonyl sulphide, carbon dioxide and carbon monoxide

S M Barnett, N J Mason and W R Newell

Department of Physics and Astronomy, University College London, Gower Street, London WC1E 6BT, UK

Received 6 September 1991, in final form 23 December 1991

Abstract. Metastable fragments produced in the electron impact dissociation of carbonyl sulphide, carbon dioxide and carbon monoxide have been studied by the technique of time-of-flight spectroscopy. Three metastable fragments were identified in the time-of-flight spectra for dissociation of carbonyl sulphide and have been classified as $O(^5S)$, $S(^5S)$ and $CO(a\,^3\Pi)$. From the time-of-flight spectra, the kinetic energy distributions of the fragments have been deduced. The production of $CO(a\,^3\Pi)$ from carbonyl sulphide has been compared with its production from carbon dioxide; the production of $O(^5S)$ from dissociation of carbonyl sulphide, carbon dioxide and carbon monoxide is also compared.

1. Introduction

Dissociation of molecules by electron impact is one of the least studied electron-molecule collision processes. It may be represented by the equation

$$e_E + AB \rightarrow e_{E-\delta E} + A^* + B$$

in which the incident electron provides the energy δE necessary both to dissociate the molecule AB and to promote the fragment A to the excited electronic state A^* where A may be an atomic or a molecular fragment. This excited fragment may be produced in a metastable state, which in the present experimental work will be defined as an excited state with lifetime in excess of 50 μs. Since the energy of the chemical bond is released as kinetic energy of the fragments, such metastable fragments are fast moving as well as long lived. Consequently such dissociation processes contribute greatly to the energy transfer in the terrestrial ionosphere, aurorae and many laboratory induced plasmas.

Experimental results for such dissociative processes are limited in scope and have often been contradictory in their results and conclusions (Zipf 1982). Particular difficulty has been found in the interpretation of the results of those experiments in which one, or more, of the fragments is produced in a metastable state. The major experimental problems encountered are: (i) the calibration of the detector for each metastable state, (ii) lifetime effects in time-of-flight spectra and (iii) the small cross sections for each of the processes. There is therefore a need for reliable experimental data concerning dissociation processes. Theoretical studies of dissociative excitation are currently confined to molecular hydrogen (Chung and Lin 1978), however new computational techniques such as the R-matrix code (Branchett and Tennyson 1991,

0953-4075/92/000000+00$04.50

Burke *et al* 1987) are likely to be extended to describe the dissociation of some simple diatomics. Consequently, more quantitative experimental data will be required for comparison.

Carbonyl sulphide is the predominant sulphur bearing compound in the terrestrial atmosphere. It is present in the troposphere (Crutzen 1976) and in the stratosphere (Inn *et al* 1979), the carbonyl sulphide concentration in the stratosphere being maintained by diffusion of carbonyl sulphide from the troposphere (Turco *et al* 1981 and references therein). Dissociation of carbonyl sulphide is an initial step in the formation of stratospheric sulphate aerosol particles (Crutzen 1976) which affect the earth's radiation balance and climate. Like carbon dioxide, carbonyl sulphide contributes to the 'greenhouse effect' in which far infrared radiation from the earth's surface is trapped, resulting in heating of the atmosphere. Carbonyl sulphide is also present in significant quantities in the interstellar medium (Hollis and Ulich 1977) and transitions in carbonyl sulphide have been observed in the interstellar clouds SGR B2 (OH) and W51 (Hollis and Ulich 1977).

In the dissociation of carbonyl sulphide several atomic or molecular metastable species may be excited, depending on the energy, *E*, of the incident electron. Some dissociative modes relevant to this work are described by the equations:

$$\begin{array}{rl} & \underline{\mathrm{CO}(\mathrm{a}\,^3\Pi})+\mathrm{S}(^3\mathrm{P})+\mathrm{e}^-_{(E-\delta E1)} \\ \mathrm{e}^-_E+\mathrm{OCS}\rightarrow & \mathrm{CS}(\mathrm{X}\,^1\Sigma)+\underline{\mathrm{O}}(^5\underline{\mathrm{S}})+\mathrm{e}^-_{(E-\delta E2)} \\ & \mathrm{CO}(\mathrm{X}\,^1\Sigma)+\underline{\mathrm{S}}(^5\underline{\mathrm{S}})+\mathrm{e}^-_{(E-\delta E3)} \end{array}$$

in which the metastable fragment produced in each case is underlined. In addition, long-lived high Rydberg fragments, S^{**} and O^{**}, will be formed and, under certain experimental conditions, will be detected simultaneously with the metastable fragments.

The notable feature of all these dissociative processes is that the fragments are produced with kinetic energies exceeding the thermal energy of the parent gas molecules. Consequently, in general, the dissociation fragments are chemically more reactive than the corresponding metastable species which are formed by direct electron impact excitation in which the excited species have kinetic energies associated with the values of the thermal energies in the parent gas beam. Careful study of the kinetic energy spectra of the product metastable fragments produced in dissociation allows the nature of the dissociation process to be investigated and, in some cases, partial potential energy curves to be constructed for the parent molecular state.

Previous work on the photodissociation of carbonyl sulphide has been limited to experiments which employed wavelengths in the range 60 to 200 nm (<18 eV) (e.g. Ashfold *et al* 1979, Strauss *et al* 1989) to measure dissociation rates and cross sections. Several electron energy loss studies have been performed (Szmytkowski 1983, Sohn *et al* 1987, Lynch *et al* 1979) but there has been only one study of dissociation by electron impact (van Brunt and Mumma 1975). Van Brunt and Mumma studied the product fragments by time-of-flight spectroscopy but did not clearly identify the fragments and consequently were not able to deduce the kinetic energy distributions. The new results obtained in this work will be compared with the results of van Brunt and Mumma and their conclusions re-examined.

While the electron impact dissociation of carbonyl sulphide has not been extensively studied, there have been numerous investigations of the electron impact dissociation of carbon dioxide. These two molecules are expected to display similar dissociative features since they both contain a C=O bond. The present results for the dissociative excitation of the oxygen fragments from carbonyl sulphide will be compared with previous results for dissociative excitation of O(^{5}S) from carbon dioxide (e.g. Misakian *et al* 1975, Allcock and McConkey 1976). Similarities in the kinetic energy distributions for the oxygen fragments produced by dissociative excitation of carbonyl sulphide and of carbon dioxide are discussed. The production of oxygen fragments in the dissociation of carbon monoxide has also been studied for comparison.

2. Experimental details

The apparatus used in the present study of electron impact dissociative excitation has been described in detail elsewhere (Barnett *et al* 1991). A pulsed electron beam of time averaged current ~3 nA and tunable in the range 10–70 eV is crossed perpendicularly with a molecular gas beam. The time taken for the product metastable fragments to travel from the interaction region to the detector is recorded as a time-of-flight spectrum. In this work two different metastable detectors were used, each with different detection thresholds. One of the detectors uses the principle of Auger ejection from a metal surface and was based on the design of Zubek and King (1986). This detector consisted of tantalum strips arranged at 45° to the incident metastable beam and maintained at a temperature of ~40-70 °C by ohmic heating. The detection threshold of the warm tantalum surface was ~5 eV. Its operation has been described in detail previously (Barnett *et al* 1991). The second detector was a bare Mullard type B419BL channel electron multiplier which was used to detect selectively the product metastable species of energy greater than 8 eV (Brunt *et al* 1978, Mason and Newell 1987). The pathlength in these experiments was 0.070 m and 0.080 m for the tantalum surface detector and the channel electron multiplier respectively.

3. Results

Time-of-flight spectra for the dissociative excitation of carbonyl sulphide obtained using the warm tantalum surface detector are shown in figure 1.

At an incident electron energy of 15 eV, the spectrum consists of only one feature, peak 1, due to fragments with a mean arrival time of 40 μs. At an incident electron energy of 20 eV, a shoulder develops on the short flight time side of peak 1 and at 35 eV this feature dominates the spectrum as peak 2. The fragments responsible for this peak have a mean arrival time at the detector of 23 μs. A second shoulder also appears on the short flight time side of peak 2 at an incident electron energy of 30 eV. This peak, 3, is due to fragments with a mean arrival time of 14 μs and dominates the time-of-flight spectrum at incident electron energies above 40 eV.

These peaks may be ascribed to the metastable species CO(a $^3\Pi$), O(^{5}S), S(^{5}S) or to long-lived high Rydberg fragments, all of which have excitation energies above the detection threshold (~5 eV) of the warm tantalum surface. A convenient way to resolve the peaks is to change the detector to one of a different threshold detection energy. The tantalum surface was therefore removed and a bare channel electron multiplier (Mullard B419L) used in its place. Since the channel electron multiplier has a detection threshold of ~8 eV it is unable to detect the CO(a $^3\Pi$) and S(^{5}S) fragments which have energies 6.01 and 6.52 eV respectively. The only fragments produced in dissociation

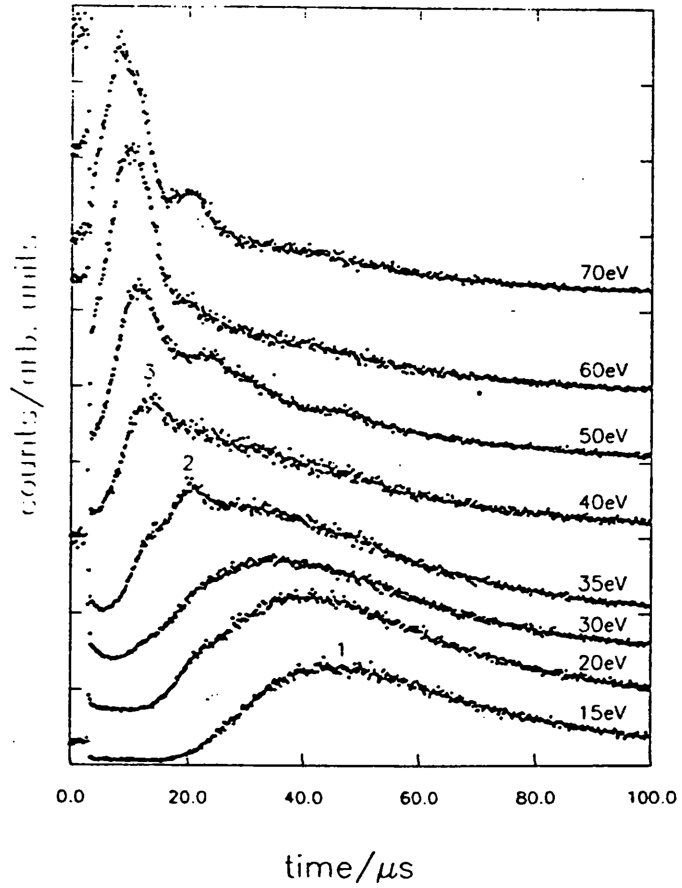

Figure 1. Time-of-flight spectra for fragments produced in dissociation of carbonyl sulphide. The detector used was warm tantalum, work function ~5 eV. The spectra were normalized and given an arbitrary zero offset. The signal at flight times <3 μs is due to photons produced during the electron pulse.

of carbonyl sulphide that can be detected by the channel electron multiplier are expected to be O(^{5}S) at 9.14 eV, a higher lying metastable state of carbon monoxide at ~10 eV (Wells *et al* 1978) or high lying Rydberg states.

A typical time-of-flight spectrum of the fragments produced in dissociation of carbonyl sulphide detected by the channel electron multiplier is shown in figure 2. There is a single peak, mean arrival time 14 μs, which corresponds to peak 3 in figure 1. There is no evidence of 10 eV metastable carbon monoxide fragments, which would have longer flight times than the oxygen fragments, having been produced by dissociative excitation. Neither is there any evidence of long-lived Rydberg states of sulphur or of carbon monoxide.

Peak 1 must be due to metastable fragments of energy less than 8 eV since the peak was absent in the time-of-flight spectra recorded by the channel electron multiplier, but of energy greater than 5 eV since the peak was present in the time-of-flight spectra recorded by the tantalum surface detector. These observations are consistent with the assignment of CO(a $^3\Pi$) fragments being responsible for peak 1. Peak 3 must be due to metastable fragments of energy greater than 8 eV, since this peak was present in

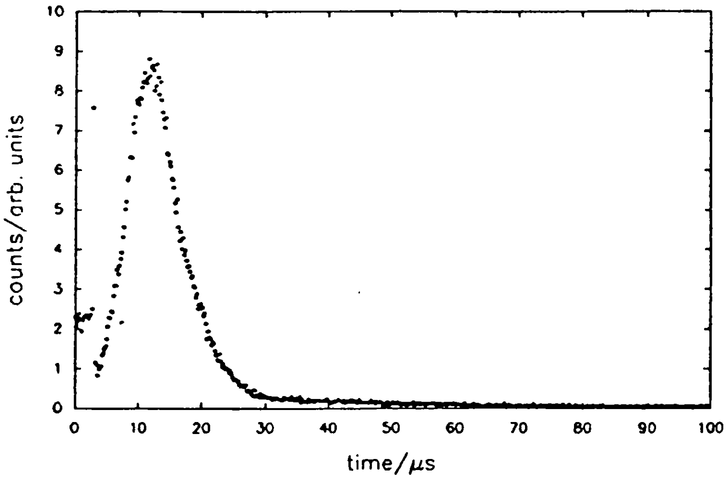

Figure 2. Time-of-flight spectra for oxygen fragments produced in the dissociation of carbonyl sulphide. The detector was a bare channel electron multiplier, work function ~8 eV.

spectra recorded by both the tantalum surface detector and the channel electron multiplier.

In the work of van Brunt and Mumma, peak 3 was identified as being due to unspecified Rydberg species. The present work suggests that it is due to either $O(^5S)$ metastable fragments or long-lived high Rydberg oxygen fragments, O^{**}. It is difficult to distinguish between these two products, however earlier work (Wells *et al* 1978, Freund 1971, Allcock and McConkey 1976) has shown that in many dissociative

Table 1. Thresholds for the production of metastable fragments. Note: processes involving the production of Rydberg states or ions are not included in the table.

Threshold (eV) (Ashfold *et al*)	Threshold (eV) (van Brunt and Mumma)	Products
3.16		$CO(x\,^1\Sigma^+)+S(^3P)$
7.30		$CS(x\,^1\Sigma^+)+O(^3P)$
9.17	9.23	$CO(a\,^3\Pi)+S(^3P)$
	9.74	$CO(x\,^1\Sigma^+)+S(^5S)$
10.32	10.38	$CO(a\,^3\Pi)+S(^1D)$
10.72		$CS(a\,^3\Pi)+O(^3P)$
	11.09	$CO(x\,^1\Sigma^+)+S(^5P)\rightarrow S(^5S)$
	11.64	$CO(x\,^1\Sigma^+)+S(^5D)\rightarrow S(^5S)$
11.92		$CO(a\,^3\Pi)+S(^1S)$
	11.99	$CO(a\,^3\Pi)+S(^5S)$
12.69		$CS(a\,^3\Pi)+O(^1D)$
14.91		$CS(a\,^3\Pi)+O(^1S)$
	15.64	$CS(x\,^1\Sigma^+)+O(^5S)$
	23.58	$C(^1S)+S(^5S)+O(^3P)$
	24.66	$C(^3P)+S(^1D)+O(^5S)$

processes resulting in the production of Rydberg oxygen atoms these cascade down to the $O(^5S)$ state. This is also true for the processes in which other excited quintet states of atomic oxygen such as $O(3d\ ^5D_0)$ and $O(3p\ ^5P)$ are produced. It is not possible in this experiment to determine the fraction of O^{**} fragments which decay to $O(^5S)$ atoms before being detected or the fraction which remain in the Rydberg state.

Peak 2 is not so easy to identify. This peak was observed only in the time-of-flight spectrum recorded by the tantalum surface detector and is therefore due to metastable fragments of excitation energy less than 8 eV but greater than 5 eV. There is no corresponding feature in the time-of-flight spectra of carbon dioxide observed by the tantalum detector so the metastable fragments are most probably sulphur atoms. The only metastable state in the required range of excitation energies, $5\ \mathrm{eV} \leqslant E^* \leqslant 8\ \mathrm{eV}$, is $S(^5S)$ of excitation energy 6.52 eV. The time-of-flight spectra recorded also reveal that no metastable states of CS or carbonyl sulphide, OCS, are detected, either because the production cross sections are very small, or because the internal energy is below that of the detection threshold of the tantalum surface, 5 eV.

The use of a channel electron multiplier revealed no evidence for the production of the 10 eV metastable state of carbon monoxide (Mason and Newell 1988) in dissociation of carbonyl sulphide by electron impact. Van Brunt and Mumma listed a series of possible dissociation channels involving such a 10 eV state and since the present work provides no evidence for such metastable production the possible dissociation channels are reduced to those listed in table 1.

4. Discussion

The kinetic energy distributions of the metastable fragments produced by dissociative excitation allows the nature of the dissociation process to be investigated.

The kinetic energy distributions of the fragments can be deduced from the recorded time-of-flight spectra. The energy of the metastable fragment arriving at the detector at time t is given by:

$$\varepsilon = \tfrac{1}{2}m(L/t)^2$$

where L is the pathlength between the interaction region and the detector, and m is the mass of the metastable molecule.

If $T(t)$ is the number of counts in each time channel of width $\mathrm{d}t$ in the time-of-flight spectrum and $D(\varepsilon)$ is the number of counts in each energy channel of width $\mathrm{d}\varepsilon$ in the kinetic energy spectrum these are related by

$$\int D(\varepsilon)\,\mathrm{d}\varepsilon = \int T(t)\,\mathrm{d}t$$

giving

$$D(\varepsilon) \propto t^3 T(t).$$

Long data collection periods, typically 50 h, gave good statistics in the peaks, but because of the t^3 dependence in the time to energy conversion, small statistical fluctuations at long flight times give rise to large variations in the low kinetic energy part of the energy distribution. To reduce the error due to the statistical fluctuations in the tail of the metastable peak, a constant background, deduced from the long flight time part of the time-of-flight spectrum where no metastable molecules reach the detector, was subtracted from the time-of-flight spectrum. The uncertainty in the position of the kinetic energy peak is typically 5–10%.

A consequence of the conversion from time to kinetic energy is that the peak in the kinetic energy distribution corresponds to a position in the tail of the time-of-flight spectrum. For this reason, it is clear that the only feature in the time-of-flight spectra recorded by the tantalum surface detector (figure 1) which may be replotted successfully in terms of kinetic energy is peak 1, that due to CO(a $^3\Pi$).

The kinetic energy distributions for the CO(a $^3\Pi$) fragments at incident electron energies of 15 eV and 20 eV are shown in figure 3. The peak in the 15 eV distribution occurs at 0.2 eV compared with typical thermal energies of carbon monoxide molecules of ~0.02 eV. There is a finite probability of the fragments being formed with zero kinetic energy. This is the characteristic kinetic energy distribution for fragments produced from the repulsive part of a bound potential energy curve.

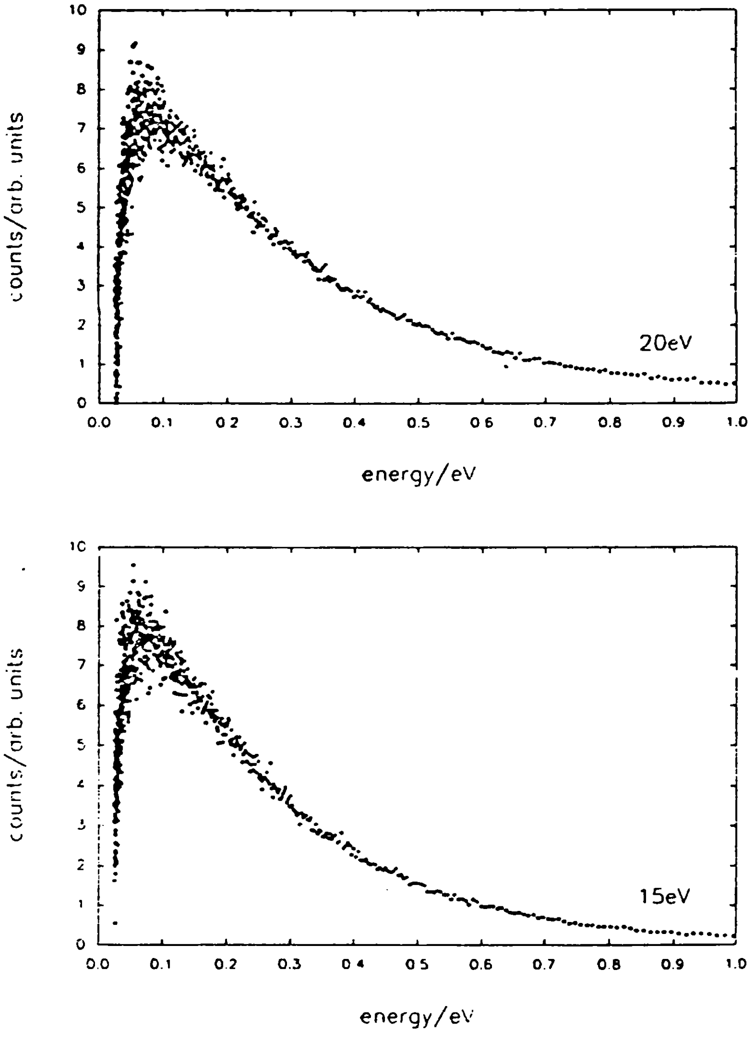

Figure 3. Kinetic energy distributions for CO(a $^3\Pi$) fragments produced in the dissociation of carbonyl sulphide, detected by tantalum surface.

Although all the recorded time-of-flight spectra of the oxygen fragments produced by electron impact dissociation of carbonyl sulphide at different incident electron energies are very similar, differences become apparent when the spectra are replotted in terms of the kinetic energy of the fragments. The kinetic energy distributions for the fragments produced at incident electron energies of 40, 50 and 60 eV are shown in figure 4. Feature A in the 40 eV spectrum occurs at 1.25 eV. As the incident electron energy is increased a second feature, B, appears at a mean kinetic energy of 1.88 eV. Although the peak energy of feature A remains the same as the incident electron energy increases, the peak kinetic energy of feature B increases to 2.2 eV at an incident electron energy of 60 eV.

In the only other study of the dissociation of carbonyl sulphide by electron impact (van Brunt and Mumma 1975) no kinetic energy distributions of the fragments were determined. However the electron impact dissociation of carbon dioxide has been widely studied and the kinetic energy distributions of the fragments are well known.

For comparison with the kinetic energy distribution for oxygen fragments from carbonyl sulphide, time-of-flight spectra for the oxygen fragments from carbon dioxide were recorded using the channel electron multiplier and the corresponding kinetic energy distributions are shown in figure 5. The spectrum for incident electron energy

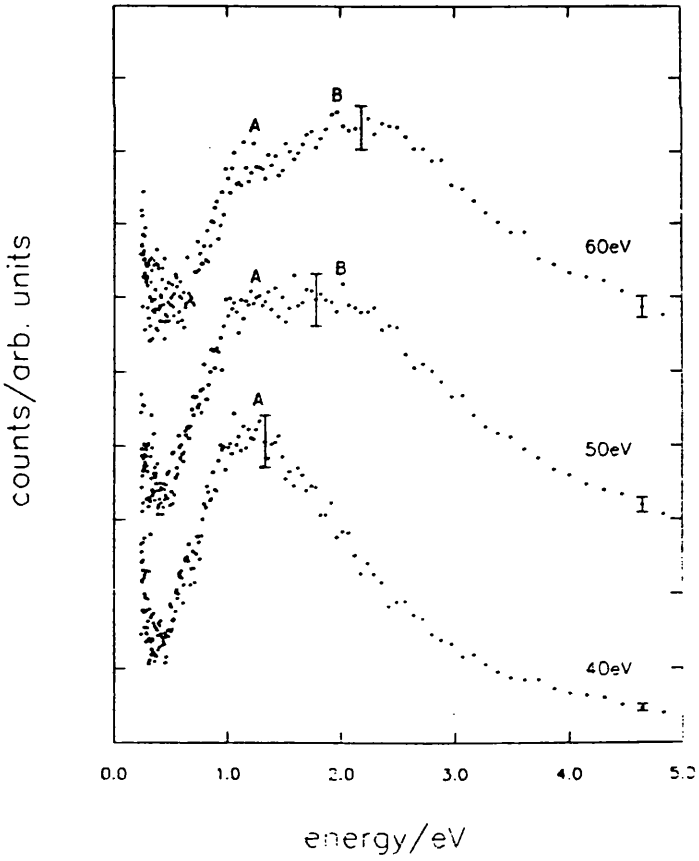

Figure 4. Kinetic energy distribution of the oxygen fragments produced in dissociation of carbonyl sulphide. The spectra were normalized and given an arbitrary zero offset.

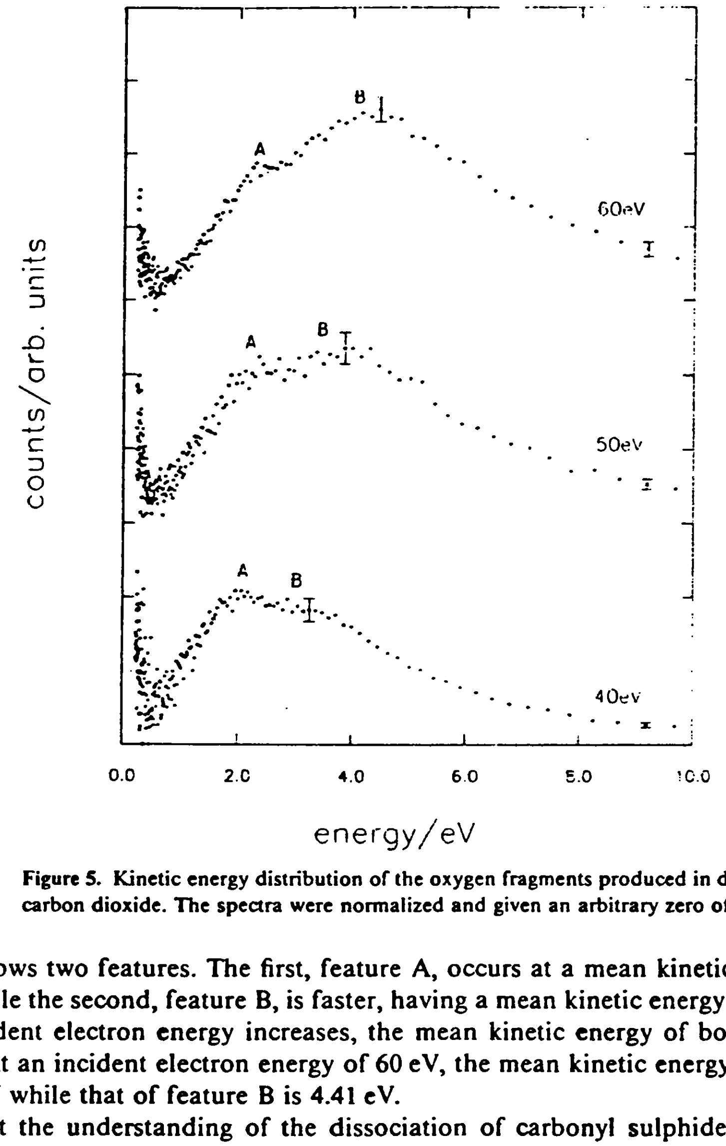

Figure 5. Kinetic energy distribution of the oxygen fragments produced in dissociation of carbon dioxide. The spectra were normalized and given an arbitrary zero offset.

of 40 eV shows two features. The first, feature A, occurs at a mean kinetic energy of 1.89 eV, while the second, feature B, is faster, having a mean kinetic energy of 3.00 eV. As the incident electron energy increases, the mean kinetic energy of both features increases. At an incident electron energy of 60 eV, the mean kinetic energy of feature A is 2.53 eV while that of feature B is 4.41 eV.

To assist the understanding of the dissociation of carbonyl sulphide, the same method was used to record the time-of-flight spectra for the oxygen fragments produced in dissociation of carbon monoxide at incident electron energies of 40, 50 and 60 eV. The kinetic energy distributions of the oxygen fragments for these incident electron energies are shown in figure 6. The kinetic energy distributions for the oxygen fragments from carbon monoxide differ from those fragments from carbonyl sulphide and carbon dioxide in that there is a single peak in the distribution. This feature, A, shows an increase in the peak kinetic energy from 3.75 eV at 40 eV to 4.69 eV at 60 eV incident electron energy.

The features of the kinetic energy distributions of the oxygen fragments produced in the electron impact dissociation of carbonyl sulphide, carbon dioxide and carbon monoxide are compared in table 2.

The oxygen fragments produced in the dissociation of carbonyl sulphide, carbon dioxide and carbon monoxide are all formed with non-zero kinetic energy distributions

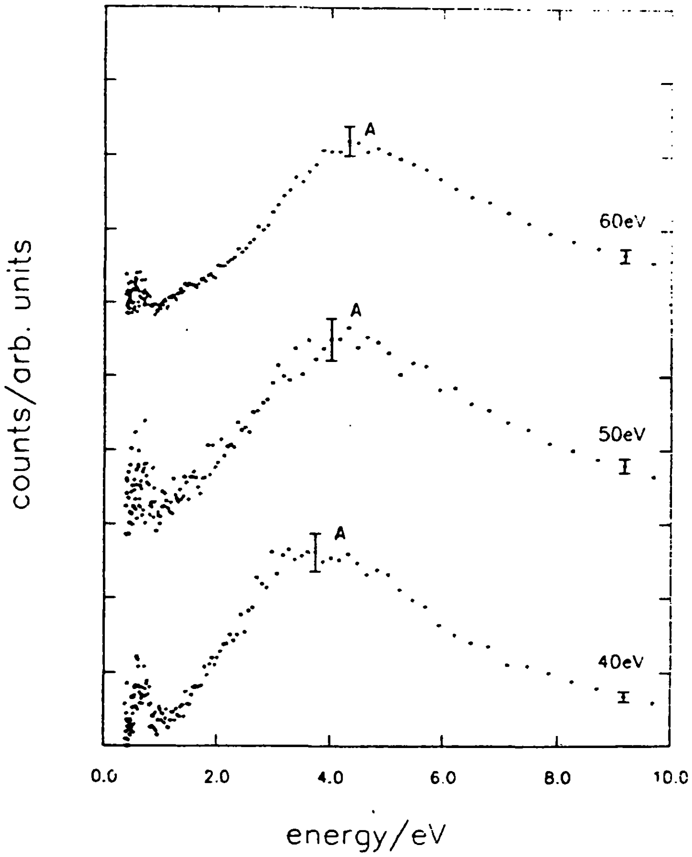

Figure 6. Kinetic energy distribution of the oxygen fragments produced in dissociation of carbon monoxide. The spectra were normalized and given an arbitrary zero offset.

Table 2. Peak energies in the kinetic energy distributions of oxygen fragments (figures 4–6). Energies are expressed in eV.

		Incident electron energy		
Molecules	Feature	40 eV	50 eV	60 eV
OCS	feature A	1.25 ± 0.10	1.25 ± 0.13	1.25 ± 0.10
	feature B		1.88 ± 0.17	2.19 ± 0.20
	ratio B/A		1.50 ± 0.21	1.75 ± 0.21
CO_2	feature A	1.89 ± 0.13	2.53 ± 0.20	2.53 ± 0.10
	feature B	3.00 ± 0.26	4.03 ± 0.33	4.41 ± 0.26
	ratio B/A		1.59 ± 0.18	1.74 ± 0.12
CO	feature A	3.75 ± 0.53	4.50 ± 0.46	4.69 ± 0.40

and have higher kinetic energies than the CO(a $^3\Pi$) fragments. The oxygen fragments are therefore produced from a purely repulsive potential energy state.

Partial potential energy curves for the repulsive part of the bound state cannot be constructed from the kinetic energy spectra determined in the present work because of the possible cascade contribution and the difficulties associated with polyatomic molecules. Such partial potential energy curves have been deduced for fragments from diatomic molecules for which the potential of ground state has been well established, e.g. molecular oxygen (Borst and Zipf 1971, Freund 1971). To apply the same technique to a triatomic molecule, knowledge of the ground state potential surface and an extension of two-dimensional arguments to a three-dimensional problem is required. Nevertheless some qualitative conclusions concerning the dissociation processes may be made.

The CO(a $^3\Pi$) fragments are most likely to be produced from a bound potential energy curve. Photodissociation studies (Ashfold *et al* 1979) suggest that the OCS(a $^1\Pi$) state may be the molecular parent state even though its production cross section is low because of the endothermic nature of the process.

It is clear that the nature of electron impact excitation allows different dissociation channels to be followed than in photon excitation. For example the electron impact may allow excitation to triplet states of the carbonyl sulphide molecule. At present there is little information concerning the triplet states of the carbonyl sulphide molecule or the carbon dioxide molecule; consequently we cannot determine whether the dissociation proceeds via the OCS(a $^1\Pi$) state or through a triplet state of unknown nomenclature. *Ab initio* calculations for the potential energy curves of the lower lying states of carbonyl sulphide and carbon dioxide would be welcome, or semi-empirical calculations similar to those for nitrous oxide (Chutjian and Segal 1972). The product molecules may also have considerable internal excitation energy, including vibrational and rotational energy, which due to the varying lifetimes of each vibrational level may account for some of the differences in our observed kinetic energy spectra in carbon dioxide with those of Allcock and McConkey.

The oxygen fragments from carbon dioxide, figure 5, are faster than the corresponding fragments from the dissociation of carbonyl sulphide, figure 4. This is expected since when a molecule dissociates the energy of the chemical bond is shared between the fragments according to the masses of the fragments. The kinetic energy distributions of Allcock and McConkey (1976) and of Misakian *et al* (1975) for O(^{5}S) production from carbon dioxide are shown in figure 7. In agreement with the present data the kinetic energy distribution is found to have structure at higher incident electron energies. In this work, a similar trend was found for oxygen production from carbonyl sulphide, while a single peak was observed in the kinetic energy distribution for oxygen fragments from dissociation of carbon monoxide.

Carbon dioxide and carbonyl sulphide will have similar electronic excited states, the energies of the excited states of carbonyl sulphide being proportionally less than the corresponding states of carbon dioxide but not sharing the symmetry of the carbon dioxide molecule. It is not surprising, therefore, that the kinetic energy distributions for fragments from each are similar, with the thresholds for production of the fragments from carbonyl sulphide being proportionally lower than the corresponding thresholds in carbon dioxide. However, we find no feature in the kinetic energy distribution of oxygen fragments from carbonyl sulphide at an incident electron energy of 40 eV which corresponds to the feature B in the distribution for oxygen from carbon dioxide at the same incident energy, see table 2. It is possible that the second feature in carbon

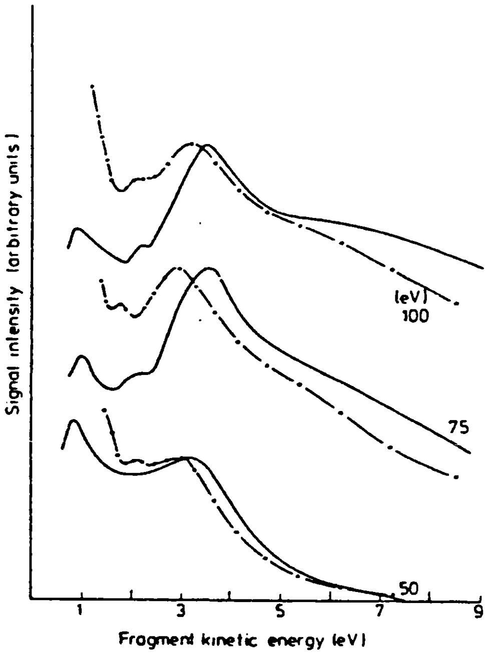

Figure 7. Kinetic energy distributions for oxygen fragments from carbon dioxide determined by Allcock and McConkey (1976) (dotted curve) and by Misakian *et al* (1975) (full curve). (Reproduced with permission of IOP Publishing.)

dioxide is due to the second electronic state arising from the symmetry of the molecule which is not present in carbonyl sulphide.

Referring again to table 2, it can be seen that in both carbon dioxide and carbonyl sulphide the peak kinetic energy of feature A, figures 4 and 5, remains at the same energy for incident electron energies above 40 eV, while feature B becomes steadily faster with increasing incident electron energy. However the ratio of the peak kinetic energies of features A and B are identical, within experimental error, for carbon dioxide and carbonyl sulphide at incident energies of 50 eV and 60 eV. This indicates that the oxygen fragments are produced from similar repulsive potential energy curves in carbon dioxide and carbonyl sulphide with the cascade contributions to each state essentially the same in both molecules. This perhaps adds further evidence that a single fragment, O(^{5}S), is detected. In the production of oxygen fragments from carbon monoxide a single production mechanism is suggested with increasing cascade contributions at higher incident electron energies.

By analogy with the oxygen fragments, the sulphur fragments, S(^{5}S), are also expected to be produced from a purely repulsive potential energy curve. The sulphur fragments would therefore reach the detector before the slower excited carbon monoxide fragments which originate from the repulsive part of a bound potential energy curve.

A recent experiment measured the lifetime of the S(^{5}S) state to be $9.2 \pm 1.0\ \mu$s (Delalic *et al* 1990). If this is correct, 92% of the excited sulphur fragments produced in the view cone of the detector would decay before reaching the detector, this compares with 6% of the O(^{5}S) fragments (lifetime 185 μs) and 1% of the CO(a $^3\Pi$) fragments (lifetime ~1 ms). In a time-of-flight spectrum corrected for inflight decay (Mason 1990) and assuming the lifetime of $S(^5S)$ to be 9.2 μs, the sulphur peak would then become eight times the height of the oxygen peak. The production cross section for excited sulphur may be greater than that for oxygen, but it is unlikely to be eight times greater. Erman (1975) in reviewing the high frequency deflection technique used by Delalic *et al* states that such a method is only applicable for lifetimes up to 10 μs. In the determination of the lifetime of the $S(^5S)$ state, the experimental method is being pushed to the limit of its sensitivity and consequently the value of 9.2 μs should perhaps be regarded as a lower limit. Other lifetime determinations range from 12 μs to 30 μs and are summarized in table 3.

Table 3. Lifetime determinations of $S(^5S)$.

Lifetime (μs)	Percentage decaying†	Reference
9.2 ± 1.0	92	Delalic (1990) (expt.)
26; 24	12	Aymar (1973) (expt.)
12	85	Müller (1968) (expt.)
17	74	Lawrence (1967) (calc.)
<30	54	Storey (1991) (calc.) (provisional)

† For the pathlength and solid angle of the detector in this work.

Lifetimes in this range are too long to be accurately measured by optical methods and should be determined by detecting the excited atom directly using the time-of-flight method (Barnett and Mason 1990). In view of the discrepancies in the lifetime determinations for $S(^5S)$, both theoretical and experimental studies of electron impact dissociation of carbon disulphide (CS_2) should be undertaken. Once the lifetime of the $S(^5S)$ state is measured accurately, the production cross section of this state from carbonyl sulphide may be determined. Electron impact dissociation of carbonyl sulphide and carbon disulphide producing $S(^5S)$ is potentially a useful laboratory source of this astrophysically important species; knowledge of the cross sections for production of this state from carbonyl sulphide will enable the feasibility of such a source to be established. New collision experiments complementary to those using the $O(^5S)$ species (Kiefl and Fricke 1980) could then be undertaken.

5. Conclusion

In this work, fragments produced in the dissociation of carbonyl sulphide, carbon dioxide and carbon monoxide have been studied. In the dissociation of carbonyl sulphide, three distinct peaks appear in the time-of-flight spectra. It has been suggested that the fragments contributing to these peaks are $O(^5S)$, $S(^5S)$, $CO(a\,^3\Pi)$ and high lying Rydberg states of atomic oxygen. The kinetic energy distribution of the $CO(a\,^3\Pi)$ fragments deduced from the time-of-flight spectra reveal that these fragments are produced from the repulsive part of a bound potential energy state, possibly $OCS(a\,^1\Pi)$.

The oxygen fragments produced from dissociation of carbonyl sulphide were compared with those from carbon dioxide and carbon monoxide. The kinetic energy distributions of the oxygen fragments from all these molecules indicate that the fragments are produced from a purely repulsive state. The kinetic energy distributions for the oxygen fragments from carbonyl sulphide and carbon dioxide obtained in this work show similarities and are in agreement with the kinetic energy distributions of the fragments produced from the electron impact dissociation of carbon dioxide in other studies. The kinetic energy distribution of the oxygen fragments from carbon monoxide shows no structure. From the intensity of the S(^{5}S) signal in the present work, it is suggested that the lifetime of this state is $>10\,\mu$s.

Acknowledgments

We are indebted to Messrs E J C Oldfield and I Rangué for their skilled technical assistance. We would also like to thank Dr P Storey for calculating the lifetime of S(^{5}S) for us, and Dr J Tennyson for useful discussions. SMB acknowledges receipt of a SERC studentship. NJM acknowledges the award of a Royal Society University Fellowship.

References

Allcock G and McConkey J W 1976 *J. Phys. B: At. Mol. Phys.* **9** 2127-39

Ashfold M N R, Macpherson M T and Simons J P 1979 *Top. Current Chem.* **86** 3-80

Aymar M 1973 *Physica* **66** 364-79 (in French)

Barnett S M and Mason N J 1990 *Phys. Educ.* **25** 114-9

Barnett S M, Mason N J and Newell W R 1991 *Chem. Phys.* **153** 283-95

Borst W L and Zipf E C 1971 *Phys. Rev.* A **4** 153-61

Branchett S E and Tennyson J 1990 *Phys. Rev. Lett.* **64** 2889-92

Brunt J N H, King G C and Read F H 1978 *J. Phys. B: At. Mol. Phys.* **11** 173-92

Burke P G, Noble C J and Scott P 1987 *Proc. R. Soc.* A **410** 289-310

Chung S and Lin C C 1978 *Phys. Rev.* A **17** 1874-91

Chutjian A and Segal G A 1972 *J. Chem. Phys.* **57** 3069-82

Crutzen P J 1976 *Geophys. Res. Lett.* **3** 73-6

Delalic Z, Erman P and Kallne E 1990 *Phys. Scr.* **42** 540-2

Erman P 1975 *Phys. Scr.* **11** 65-78

Freund R S 1971 *J. Chem. Phys.* **54** 3125-41

Hollis and Ulich 1977

Inn E C Y, Vedder J F, Tyson B J and O'Hara D 1979 *Geophys. Res. Lett.* **6** 191-3

Kiefl H U and Fricke J 1980 *J. Phys. B: At. Mol. Phys.* **13** 1185-93

Lawrence G M 1967 *Astrophys. J.* **148** 261-8

Lynch M G, Dill D, Siegel J and Dehmer J L 1979 *J. Chem. Phys.* **71** 4249-54

Mason N J 1990 *Meas. Sci. Technol.* **1** 596-600

Mason N J and Newell W R 1987 *J. Phys. B: At. Mol. Phys.* **20** 3913-21

—— 1988 *J. Phys. B: At. Mol. Opt. Phys.* **21** 1293-302

Misakian M, Mumma M J and Faris J F 1975 *J. Chem. Phys.* **62** 3442-53

Muller D 1968 *Z. Naturf.* A **23** 1707-16 (in German)

Sohn W, Kochem K-H, Scheuerlein K M, Jung K and Ehrhardt H 1987 *J. Phys. B: At. Mol. Phys.* **20** 3217-36

Storey P 1991 Private communication

Strauss C E, McBane G C, Houston P L, Burak I and Hepburn J W 1989 *J. Chem. Phys.* **90** 5364-72

Szmytkowski Cz 1983 *Proc. 13th Int. Conf. on the Physics of Electronic and Atomic Collisions (Berlin)* (Amsterdam: North-Holland) Abstracts p 242

Turco R P, Cicerone R J, Inn E C Y and Capone L A 1981 *J. Geophys. Res.* **86** 5373-7

van Brunt R J and Mumma M J 1975 *J. Chem. Phys.* **62** 3210-5

Wells W C, Borst W L and Zipf E C 1978 *Phys. Rev.* A **17** 1357-65

Zipf E C 1982 *Electron-Molecule Interactions and their Applications* vol 1, ed L G Christophorou (New York: Academic) ch 4

Zubek M and King G C 1982 *J. Phys. E: Sci. Instrum.* **15** 511-3

References

Aarts J F M and de Heer F J 1971 Physica **52** 45

Ajello J M 1970 J Chem Phys **53** 1156

Ajello J M 1971 J Chem Phys **55** 3158

Ajello J M and Shemansky D E 1985 J Geophys Res **90** 9845

Allison W, Dunning F B and Smith A C H 1972 J Phys B **5** 1175

Allcock G and McConkey J W 1976 J Phys B **9** 2127

Allcock G and McConkey J W 1978 Chem Phys **34** 169

Ashfold M N R, MacPherson M T and Simons J P 1979 Topics in Current Chemistry **86** 3

Aymar M 1973 Physica **66** 364 (French)

Barth C A 1969 Science **165** 1004

Barth C A, Stewart A J, Hord C W and Lane A L 1972 Icarus **17** 457

Berrington K A, Burke P G, Freitas L C G and Kingston A E 1985 J Phys B **18** 4135

Black G, Sharpless R L, Slanger T G and Lorents D C 1975 J Chem Phys **62** 4274

Boiziau C, Garot C, Nuvolone R and Roussel J 1980 Surf Sci **91** 313

Born J 1926 Z Phys **38** 803

Borst W L 1969 Phys Rev **181** 357

Borst W L 1971 Rev Sci Instrum **42** 1543

Borst W L 1972 Phys Rev A **5** 648

Borst W L, Wells W C and Zipf E C 1972 Phys Rev A **5** 1744

Borst W L and Zipf E C 1971a Phys Rev A **3** 979

Borst W L and Zipf E C 1971b Phys Rev A **4** 153

Bozso F, Yates J T, Arias J, Metiu H and Martin R M 1983 J Chem Phys **78** 4256

Branchett S E and Tennyson J 1990 Phys Rev Letters **64** 2889

Branchett S E, Tennyson J and Morgan L A 1991 J Phys B **24** 3479

Bransden B H and McDowell M R C 1978 Phys Rep **46** 249

Brinkman R T and Trajmar S 1970 Ann Geophys **26** 201

Brunger M J, Teubner P J O and Buckman S J 1988 Phys Rev A **37** 3570

Brunt J N H, King G C and Read F H 1976 J Phys E Sci Instrum **10** 134

Brunt J N H, King G C and Read F H 1978 J Phys B **11** 173

van Brunt R J and Mumma M J 1975 J Chem Phys **62** 3210

Burke P G, Noble C J and Scott P 1987 Proc Roy Soc **410A** 289

Cameron W H B 1926 Phil Mag **1** 405

Carleton N P and Oldenberg O 1961 J Chem Phys **36** 3460

Cartwright D C 1970 Phys Rev A **2** 1331

Cartwright D C 1972 Phys Rev A **5** 1974

Cartwright D C, Trajmar S, Chutjian A and Williams W 1977 Phys Rev A **16** 1041

Cermak V 1966 J Chem Phys **44** 1318

Ching B K, Cook G R and Becker R A 1967 J Quant Spectrosc and Radiat Transfer **7** 323

Chung S and Lin C C 1972 Phys Rev A **6** 988

Chung S and Lin C C 1978 Phys Rev A **17** 1874

Chutjian A, Segal G A 1972 J Chem Phys **57** 3069

Clampitt R and Newton A S 1969 J Chem Phys **50** 1997

Compton K T 1922 Phys Rev **20** 283

Compton R N and Bardsley J N 1984 in *Electron-Molecule Collisions* edited by I Shimamura and K Takayanagi (New York, Plenum), Chapter 3

Conrad H, Ertl G, Kuppers J, Wang S-W, Gerard K and Haberland H 1979 Phys Rev Letters **42** 1082

Corr J J, Khakoo M A and McConkey J W 1987 J Chem Phys B **20** 2597

Corvin K K and Corrigan S J B 1969 J Chem Phys **50** 2570

Couliette J H 1928 Phys Rev **32** 636

Cox R A and Derwent R G 1981 Gas Kinetics and Energy Transfer Specialist Periodical Reports of the Chemistry Society **4** 189

Crutzen P J 1976 Geophys Res Letters **3** 73

Csanak G, Cartwright D C, Srivastava S K and Trajmar S 1984 in *Electron-Molecule Interactions and their Applications* vol 1 edited by L G Christophorou (London, Academic Press), Chapter 1

Curtis L J and Erman P 1977 J Opt Soc Am **67** 1218

Dahl F and Oddershede J 1986 Physica Scripta **33** 135

Delalic Z, Erman P and Kallne E 1990 Physica Scripta **42** 540

Delchar T A, MacLennan D A and Landers A M 1969 J Chem Phys **50** 1779

Donnelly D P, Pearl J C and Zorn J C 1971 American Journal of Physics **39** 983

Donovan R J and Husain D 1967 Trans Faraday Soc **63** 2879

Dorrestein R 1942 Physica **5** 447

Drake G W F, Victor G A and Dalgarno A 1969 Phys Rev **180** 25

Dunn G H 1962 Phys Rev Letters **8** 62

Dunning F B 1972 J Phys E **5** 263

Dunning F B, Cook T B, West W P and Stebbings R F 1975b Rev Sci Instrum **46** 1072

Dunning F B, Rundel R D and Stebbings R F 1975a Rev Sci Instrum **46** 697

Dunning F B and Smith A C H 1970a J Phys B **3** L60

Dunning F B and Smith A C H 1970b Phys Letters **32A** 287

Dunning F B and Smith A C H 1971 J Phys B **4** 1696

Dunning F B, Smith A C H and Stebbings R F 1971 J Phys B **4** 1683

van Dyck R S, Johnson C E and Shugart H A 1970 Phys Rev Letters **25** 1403

van Dyck R S, Johnson C E and Shugart H A 1972 Phys Rev A **5** 991

Erman P 1975 Physica Scripta **11** 65

Ertl G 1986 Phil Trans R Soc Lond **A318** 51

Estrup P J and Anderson J 1968 J Chem Phys **49** 523

Fairbairn A R 1970 J Quant Spectrosc and Radiat Transfer **10** 1321

Field F H and Franklin J L 1970 *Electron Impact Phenomena and the Properties of Gaseous Ions* (Academic Press, New York)

Finn T G and Doering J P 1976 J Chem Phys **64** 4490

Fliflet A W, McKoy V and Rescigno T N 1979 J Phys B **12** 3281

Fox J L and Dalgarno A 1979 J Geophys Res **84** 7315

Fox K E and Reid J 1985 J Opt Soc Am B **2** 807

French J B and Locke J W 1967 in *Rarefied Gas Dynamics* edited by C L Brundin (New York, Academic Press) p1461

Freund R S 1969 J Chem Phys **50** 3734

Freund R S 1971a J Chem Phys **54** 3125

Freund R S 1971b J Chem Phys **55** 3569

Freund R S and Klemperer W 1967 J Chem Phys **47** 2897a

Freund R S, Schiavone J A and Brader D F 1976 J Chem Phys **64** 1122

Garstang R H 1961 Proc Camb Phil Soc **57** 115

Gilmore F R 1965 J Quant Spectrosc Rad Trans **5** 369

Gilpin R and Welge K H 1971 J Chem Phys **55** 975

Golden D E, Burns D J and Sutcliffe V C 1974 Phys Rev A **10** 2123

Griem H R 1969 Astrophys J **156** L103

Haddad G N and Elford M T 1979 J Phys B **12** L743

Hagstrum H D 1954 Phys Rev **96** 336

Hagstrum H D 1956 Phys Rev **104** 1516

Hagstrum H D 1978 in *Electron and Ion Spectroscopy of Solids* edited by L Fiermans, J Vennik and W Dekeyser (New York, Plenum), Chapter 7

Hagstrum H D 1979 Phys Rev Letters **43** 1050

Hansche G E 1940 Phys Rev **57** 289

Harting E and Read F H 1976 *Electrostatic Lenses* (Amsterdam, Elsevier)

Hasted J B 1959 J Appl Phys **30** 23

Hasted J B and Mahadevan P 1959 Proc Roy Soc **A249** 42

de Heer F J and Jansen R H J 1977 J Phys B **10** 3741

Hemminger J C, Wicke B G and Klemperer W 1976 J Chem Phys **65** 2798

Herzberg G 1966 *Molecular Spectra and Molecular Structure* vol 1 (New York, van Nostrand)

Holland R F 1969 J Chem Phys **51** 3940

Holley T K, Chung S and Lin C C 1981 Phys Rev A **24** 2946

Hollis J M and Ulich B L 1977 Astrophys J **214** 699

Hotop H and Niehaus A 1970 J Mass spectr Ion Phys **5** 415

Hughes A L and DuBridge L A 1932 *Photoelectric Phenomena* (New York, McGraw Hill)

Inn E C Y, Vedder J F, Tyson B J and O'Hara D 1979 Geophys Res Letters **6** 191

James T C 1971 J Chem Phys **55** 4118

Johnson C E 1970 J Chem Phys **57** 576

Johnson C E 1972 Phys Rev A **5** 2688

Johnson C E and van Dyck R S 1972 J Chem Phys **56** 1506

Johnson P D and Delchar T A 1978 Surf Sci **77** 400

Kaminsky M 1965 *Atomic and Ionic Impact Phenomena on Metal Surfaces* (New York, Academic Press Inc)

Kannerstine F M 1924 Phys Rev **23** 108

Kiefl H U and Fricke J 1980 J Phys B **13** 1185

Kiefl H U, Karl E and Fricke J 1983 J Phys B **16** 4165

Klemm R B, Glicker S, Stief L J 1975 Chem Phys Letters **33** 512

Klemperer O 1974 *Electron Optics* (Cambridge, University Press)

Kume H, Kondow T and Kuchitsu K 1986a J Chem Phys **84** 4031

Kume H, Kondow T and Kuchitsu K 1986b J Phys Chem **90** 5146

Kurzweg L, Egbert G T and Burns D J 1973 Phys Rev A **7** 1966

Kuyatt C E 1979 Private Communication referednced in Chutjian A and Cartwright D C 1981 Phys Rev **A23** 2178

Lai S, McNeil W J and Murad E 1988 J Geophys Res **93** 5871

Lawrence G M 1967 Astrophys J **148** 261

Lawrence G M 1971 Chem Phys Letters **9** 575

Leclerc B, Poulin A, Roy D, Hubin-Franskin M-J and Delwiche J 1981 J Chem Phys **75** 5329

Lee L C and Chiang C C 1982 Chem Phys Letters **92** 425

Lee L C and Judge D L 1975 J Chem Phys **63** 2782

Leming C W and Pollack G L 1970 Phys Rev B **2** 3323

Lichten W 1957 J Chem Phys **26** 306

Little C E and Browne P G 1987 Chem Phys Letters **134** 560

Little C E and Browne P G 1988 J Phys B **21** 2675

Little C E and Browne P G 1989 J Phys B **22** 1269

Lofthus A and Krupenie P H 1977 J Phys Chem Ref Data **6** 113

Lynch M G, Dill D, Siegel J and Dehmer J L 1979 J Chem Phys **71** 4249

MacLennan D A 1966 Phys Rev **148** 218

Marinelli W J, Kessler W J, Green B D and Blumberg W A M 1989 J Chem Phys **91** 701

Mason N J 1990 Meas Sci and Technol **1** 596

Mason N J and Newell W R 1986 J Phys E **19** 722

Mason N J and Newell W R 1987a J Phys B **20** 1357

Mason N J and Newell W R 1987b J Phys B **20** 3913

Mason N J and Newell W R 1988 J Phys B **21** 1293

Mason N J and Newell W R 1989 J Phys B **22** 2297

Mason N J and Newell W R 1990a J Phys B **23** 4641

Mason N J and Newell W R 1990b Meas Sci Technol **1** 983

Massey H S W and Mohr C B O 1932 Proc Roy Soc **A135** 258

Mazeau J, Hall R I, Joyez G, Landau M and Reinhardt J 1973 J Phys B **6** 873

McEwan M J, Lawrence G M and Poland H M 1974 J Chem Phys **61** 2857

Messenger H A 1926 Phys Rev **28** 962

Metherell A J F and Cook R F 1971 Optik **34** 535

Meyer J A, Klosterboer D H and Setser D W 1971 J Chem Phys **55** 2084

Misakian M, Mumma M J and Faris J F 1975 J Chem Phys **62** 3442

Muller D 1968 Naturforschung Z **23A** 1707 (German)

Munakata T, Hirooka T and Kuchitsu K 1978 J Electron Spectrosc **13** 219

Newman D S, Zubek M and King G C 1983 J Phys B **16** 2247

Newman D S, Zubek M and King G C 1985 J Phys B **18** 985

Nicholls R W 1964 Ann Geophys **20** 144

Nicholls R W and Hasson W V 1971 J Phys B **4** 681

Nowak G, Borst W L and Fricke J 1978 Phys Rev A **17** 1921

Ohshima S, Kondow T and Kuchitsu K 1985 Bull Chem Soc Japan **58** 1833

Oliphant M L E 1929 Proc Roy Soc **A124** 228

Oliphant M L E and Moon P B 1930 Proc Roy Soc **A127** 388

Olmsted J, Newton A S and Street K 1965 J Chem Phys **42** 2321

Ondrey G S, Kanfer S and Bersohn B 1983 J Chem Phys **79** 179

Papaliolios C 1965 PhD Thesis referenced in Lawrence G M 1971 Chem Phys Letters **9** 575

Pearl A S 1970 Phys Rev Letters **24** 703

Petley C H 1971 Mullard Tech Rev **24** 130

Phillips M H, Anderson L W and Lin C C 1981b Phys Rev **A23** 2751

Phillips M H, Anderson L W and Lin C C 1985 Phys Rev **A32** 2117

Phillips M H, Anderson L W, Lin C C and Miers R E 1981a Phys Letters **82A** 404

Pierce J R 1940 J Appl Phys **11** 548

Pilling M J, Bass A M and Braun W 1971 J Quant Spectrosc and Radiat Transfer **11** 1593

Poland H M and Lawrence G M 1973 J Chem Phys **58** 1425

Powell H T, Murray J R and Rhodes C K 1974 Appl Phys Letters **25** 730

Prinn R G, Simmonds P G, Rasmussen R A, Rosen R D, Alyea F H, Cardelino A J, Crawford A J, Cunnold D M, Fraser P J and Lovelock J E 1983 J Geophys Res **88** 8353

Raitt W J, Siskind D E, Banks P M and Williamson P R 1984 Planet Space Sci **32** 457

Rogers W A and Biondi M A 1964 Phys Rev **134A** 1215

Rescigno T N, McCurdy C W, McCoy V and Bender C F 1976 Phys Rev A **13** 216

Rozsnyai B F 1967 J Chem Phys **47** 4102

Rudolph R N and Inn E C Y 1981 J Geophys Res **86** 9891

Rundel R D, Aitken K L and Harrison M F A 1969 J Phys B **2** 954

Rundel R D and Stebbings R F 1972 in *Case Studies in Atomic Collision Physics* vol 2 edited by E W McDaniel and M R C McDowell (Amsterdam, North Holland), Chapter 8

Sasaki V N and Nakao T 1935a Proc Imp Acad Japan **11** 138

Sasaki V N and Nakao T 1935b Proc Imp Acad Japan **11** 413

Sasaki V N and Nakao T 1941 Proc Imp Acad Japan **17** 75

Schultz G J and Fox R E 1956 Phys Rev **106** 1179

Schohl S, Klar D, Kraft T, Meijer H A J, Ruf M-W, Schmitz U, Smith S J and Hotop H 1991 Z Phys D **21** 25

Sesselmann W, Woratschek B, Kuppers J, Ertl G and Haberland H 1987 Phys Rev B **35** 1547

Shekhter S S 1937 J Expt Theoret Phys (USSR) **7** 750

Shemansky D E 1969 J Chem Phys **51** 5487

Shemansky D E and Carleton N P 1969 J Chem Phys **51** 682

Sholette W P and Muschlitz E E 1962 J Chem Phys **36** 3368

Skerbele A and Lassettre E N 1970 J Chem Phys **53** 3806

Slangar T G and Black G 1971 J Chem Phys **55** 2164

Small-Warren N E and Chui L Y C 1975 Phys Rev A **11** 1777

Sohn W, Kochem K-H, Scheuerlein K M, Jung K and Ehrhardt H 1987 J Phys B **20** 3217

Sonkin S 1933 Phys Rev **43** 788

Stebbings R F 1957 Proc Roy Soc **A241** 270

Stedman D D, Meyer J A and Setser D W 1968 J Am Chem Soc **90** 6856

Stern R M 1964 Appl Phys Letters **5** 218

Storey P 1991 Private Communication

Strauss C E, McBane G C, Houston P L, Burak I and Hepburn J W 1989 J Chem Phys **90** 5364

Strobel D F 1982 J Geophys Res **87** 1361

Szmytkowski C 1983 Proceedings of 13th International Conference on the Physics of Electronic and Atomic Collisions, Berlin (Amsterdam, North Holland), Abstracts p242

Szmytkowski C, Karwasz G and Maciag K 1984 Chem Phys Letters **107** 481

Szmytkowski C, Maciag K, Karwasz G and Filipovic D 1989 J Phys B **22** 525

Szmytkowski C and Zubek M 1978 Chem Phys Letters **57** 105

Taylor N J 1964 Surf Sci **2** 544

Teubner P J O, Riley J L, Tonkin M C, Furst J E and Buckman S J 1985 J Phys B **18** 3641

Trajmar S and Cartwright D C 1984 in *Electron-Molecule Interactions and their Applications* vol 1 edited by L Christophorou (Academic Press Inc, New York), Chapter 2

Turco R P, Cicerone R J, Inn E C Y and Capone L A 1981 J Geophys Res **86** 5373

Turco R P, Whitten R C, Toon O B, Pollack J B and Hamill P 1980 Nature **283** 283

Vance D W 1967 Phys Rev **164** 372

Varnerin L J 1953 Phys Rev **91** 859

Varney R N 1968 Phys Rev **175** 98

Webb H W 1924 Phys Rev **24** 113

Weissmann G, Ganz J, Siegel A, Waibel H and Hotop H 1984 Optics Comunications **49** 335

Welge K H and Gilpin R 1971 J Chem Phys **54** 4225

Wells W C, Borst W L and Zipf E C 1972 J Geophys Res **77** 69

Wells W C, Borst W L and Zipf E C 1973 Phys Rev A **8** 2463

Wells W C, Borst W L and Zipf E C 1978 Phys Rev A **17** 1357

Wells W C and Zipf E C 1972 Trans Am Geophys Union **53** 1068

Wells W C and Zipf E C 1974 Phys Rev A **9** 568

Wigner E 1927 Gott Nachr **1** 275

Young R A, Black G and Slanger T G 1968 J Chem Phys **48** 2067

Young R A, Black G and Slanger T G 1969 J Chem Phys **50** 303

Zipf E C 1963 J Chem Phys **38** 2034, erratum 1963 J Chem Phys **39** 3534

Zipf E C 1984 in *Electron-Molecule Interactions and their Applications* vol 1 edited by L Christophorou (Academic Press Inc, New York), Chapter 4

Zipf E C and Wells W C 1980 Planet Space Sci **28** 859

Zubek M 1986 J Phys E **19** 463

Zubek M and King G C 1982 J Phys E **15** 511

Zubek M and King G C 1987 J Phys B 20 1135